GA-A14771
UC-77

GAS-COOLED FAST BREEDER REACTOR

QUARTERLY PROGRESS REPORT FOR THE PERIOD NOVEMBER 1, 1977 THROUGH JANUARY 31, 1978

by
PROJECT STAFF

Prepared under
Contract EY-76-C-03-0167
Project Agreement No. 23
for the San Francisco Operations Office
Department of Energy

GENERAL ATOMIC PROJECT 3228
DATE PUBLISHED: FEBRUARY 1978

GENERAL ATOMIC COMPANY

PROGRESS REPORT SERIES

GA-5537	November 1, 1963 through July 31, 1964
GA-6667	August 1, 1964 through July 31, 1965
GA-7645	August 1, 1965 through July 31, 1966
GA-8107	August 1, 1966 through July 31, 1967
GA-8787	August 1, 1967 through July 31, 1968
GA-8895	August 1, 1968 through October 31, 1968
GA-9229	November 1, 1968 through January 31, 1969
GA-9359	February 1, 1969 through April 30, 1969
GA-9639	May 1, 1969 through July 31, 1969
GA-9811	August 1, 1969 through October 31, 1969
GA-9838	November 1, 1969 through January 31, 1970
GA-10517	February 1, 1970 through January 31, 1971
GA-10645	February 1, 1971 through April 30, 1971
GA-A10803	May 1, 1971 through July 31, 1971
GA-A10906	August 1, 1971 through July 31, 1972
GA-A12003	November 1, 1971 through January 31, 1972
GA-A12165	February 1, 1972 through April 30, 1972
GA-A12252	May 1, 1972 through July 31, 1972
GA-A12421	August 1, 1972 through October 31, 1972
GA-A12530	November 1, 1972 through January 31, 1973
GA-A12635	February 1, 1973 through April 30, 1973
GA-A12728	May 1, 1973 through July 31, 1973
GA-A12824	August 1, 1973 through October 31, 1973
GA-A12894	November 1, 1973 through January 31, 1974
GA-A13021	February 1, 1974 through April 30, 1974
GA-A13148	May 1, 1974 through July 31, 1974
GA-A13238	August 1, 1974 through October 31, 1974
GA-A13379	November 1, 1974 through January 31, 1975
GA-A13458	February 1, 1975 through April 30, 1975
GA-A13565	May 1, 1975 through July 31, 1975

GA-A13766	August 1, 1975 through October 31, 1975
GA-A13815	November 1, 1975 through January 31, 1976
GA-A13868	February 1, 1976 through April 30, 1976
GA-A13975	May 1, 1976 through July 31, 1976
GA-A14112	August 1, 1976 through October 31, 1976
GA-A14240	November 1, 1976 through January 31, 1977
GA-A14358	February 1, 1977 through April 30, 1977
GA-A14492	May 1, 1977 through July 31, 1977
GA-A14613	August 1, 1977 through October 31, 1977

ABSTRACT

The tasks of the gas-cooled fast breeder reactor (GCFR) program which are supported by the Department of Energy include development of GCFR fuel, blanket, and control assemblies; development of the pressure equalization system for GCFR fuel; out-of-pile loop facility test programs; fuels and materials development; fuel, blanket, and control rod analyses and development; nuclear analysis and reactor physics for GCFR core design; shielding requirements for the GCFR; reactor engineering to assess the thermal, hydraulic, and structural performance of the core and the core support structure; plant systems control; systems engineering; development of reactor components, including reactor vessel, control and locking mechanisms, fuel handling equipment, core support structure, shielding assemblies, main helium circulator, steam generator, circulator test facility, and auxiliary circulator; development of a helium circulator test facility; reactor safety, environment, and risk analyses, including planning and support of an in-pile and out-of-pile safety test program; nuclear island engineering design; and development of a reliability data bank.

CONTENTS

FIGURES

TABLES

1. INTRODUCTION

The various tasks of the gas-cooled fast breeder reactor (GCFR) program for the period November 1, 1977 through January 31, 1978 sponsored by the Department of Energy (DOE) are discussed in this quarterly progress report. The GCFR utility program, which is sponsored by a large number of electric utility companies, rural electric cooperatives, and General Atomic (GA), is primarily directed toward the development of a GCFR demonstration plant. The utility-sponsored work and the DOE-sponsored work are complementary.

Analytical, experimental, and fabrication development is being accomplished under the core assembly development task to establish the basis for the design of GCFR fuel, blanket, and control assemblies. Methods development for structural, thermal-hydraulic, and mechanical analyses is discussed, and the results of structural analysis of the fuel assembly components and thermal-hydraulic analysis of the blanket assembly during low power are presented. Current progress on rod-spacer interaction tests, fuel assembly seismic and vibration test planning, and development of assembly fabrication techniques is also presented. The various subtasks of core assembly development and the work accomplished during this reporting period are discussed in Section 2.

The technology to support the design and construction of the pressure equalization system (PES) for GCFR fuel is being developed. This includes (1) the development of analytical models and computer codes which will be verified by test programs and testing of materials and seals and (2) the development of fabrication processes for the PES. These are discussed in Section 3.

To demonstrate the ability of GCFR fuel, control, and blanket assembly designs to meet design goals and verify predictions of analytical models, a

series of out-of-pile simulation tests will be performed. The emphasis of the tests will be on obtaining thermal-structural data for steady-state, transient, and margin conditions using electrically heated rod bundles in a dynamic helium loop. These are discussed in Section 4.

In the fuels and materials development program, thermal flux and fast flux irradiation studies are being conducted to establish conditions and design features specific to GCFR fuel rods, such as vented fuel, fission product traps, and surface-roughened cladding. In addition, an irradiation test program of smooth and surface-roughened GCFR cladding specimens is being conducted to determine how these materials behave under irradiation. The fuels and materials tests, the analytical studies, and the results to date are presented in Section 5.

Under the fuel rod engineering task, performance of the fuel and blanket rods under steady-state and transient conditions is being evaluated to determine performance characteristics, operating limits, and design criteria. In addition, surveillance of the fuel rod and blanket rod technology of other programs is being carried out. These studies are presented in Section 6.

The objectives of the nuclear analysis and reactor physics task are to verify and validate the nuclear design methods which will be applied to the GCFR core design. Data from a critical assembly experimental program at the ZPR-9 facility at Argonne National Laboratory (ANL) are being used for this purpose. Critical assembly design, analysis, and methods development are discussed in Section 7.

Verification of the physics and engineering analytical methods and the data for design of the GCFR shields is being conducted under the shielding requirements task along with an evaluation of the effectiveness of various shield configurations. The results of radial shield analyses and the work being done on structural analysis are presented in Section 8.

Section 9 discusses systems engineering for the GCFR. This includes systems integration; coordination of interface requirements between plant systems; and development and implementation of effective documentation management.

Section 10 discusses the evaluation and development of the main components of the GCFR, including reactor vessel, control and locking machanisms, fuel handling, core support structure, shielding assemblies, main helium circulator, steam generator, auxiliary circulator, and helium processing components. Section 11 is concerned with the engineering required to design and develop the circulator test facility, and Section 12 reports on the development of control systems and the assessment of seismically induced and flow-induced vibration behavior for the GCFR demonstration plant.

The reactor safety task, which is discussed in Section 13, includes (1) maintenance of liaison between GA and other organizations and integration of the overall GCFR safety analysis effort; (2) formulation and review of the GCFR safety program plan; (3) performance of detailed safety, environmental, and risk analyses of the GCFR; (4) evaluation of the post-accident fuel containment (PAFC) capability of the GCFR; (5) integration of the results of DOE safety studies into the licensing reviews; and (6) evaluation of probabilistic design methods for use in the GCFR program. Procurement, supply, and storage of reliability data are also reported along with estimates in support of probabilistic analyses of accident events being analyzed for gas-cooled reactors.

Section 14 discusses the safety test program, which involves quantification of fuel and cladding behavior during accidents leading to core damage and identification of safety test information required for licensing and commercialization of the GCFR. The GRIST-2 and duct melting and fall-away test programs (DMFT) are also examined.

Section 15 discusses the nuclear island. The purposes of this task are to accomplish engineering design work on the nuclear island portion

of the demonstration plant and to resolve the interface requirements of major nuclear steam supply (NSSS) and balance of plant (BOP) systems.

Development of an alternate design concept for the NSSS and related BOP facilities and equipment is discussed in Section 16, and the characteristics of a GCFR fueled with combinations of U-233, U-235, U-238, plutonium, and thorium are reported in Section 17.

2. CORE ASSEMBLY DEVELOPMENT (189a No. 00582)

2.1. CORE ASSEMBLY THERMAL-HYDRAULIC ANALYSIS

2.1.1. Introduction

Experimental data are being evaluated to develop the analytical basis for the design and development of the GCFR fuel, control, and blanket assemblies. Because complete prototype in-pile tests cannot be conducted, a strong analytical base supported by development tests is required to design the core assemblies. The current effort is devoted to the development of an adequate steady-state and transient analysis capability in the areas of thermal-hydraulic and structural analysis to provide a basis for assembly design criteria and specific test requirements. The main efforts have focused on improvement of thermal-hydraulic correlations and development of methods for applying the correlations to the design and analysis of GCFR core assemblies.

2.1.2. Fuel Assembly Analysis

The following modifications were recently incorporated in the COBRA-IIIC code (Ref. 2-1); the details of these modifications are described in Ref. 2-2.

1. Use of R and G functions (i.e., correlations for velocity and temperature distributions).

2. Method to calculate friction factor and Stanton number in the wall channels by inverse Dalle Donne transformation.

3. Method to apply Biot number correction based on local heat transfer coefficient.

4. Option to use variable nodal lengths.

Analyses using this modified version, called COBRA*GCFR, were verified by comparison with

1. Analyses of a 19-rod bundle (Ref. 2-3) by the SCRIMP (Ref. 2-4) and SAGAPO codes (Ref. 2-5).

2. Experimental results for BR-2 calibration element III (Ref. 2-6).

The configuration of the 19-rod bundle analyzed is shown in Fig. 2-1. Because of symmetry of the bundle and the spacers, analysis of a one-twelfth-bundle is adequate. Figure 2-2 shows the subchannel model used for the COBRA*GCFR analysis. The test bundle and experimental conditions are summarized in Table 2-1. Heat transfer and friction factor correlations for the smooth portion were obtained from Ref. 2-7. Table 2-2 compares the COBRA*GCFR results for the 19-rod bundle with results from the SCRIMP and SAGAPO codes.

The friction factors obtained by COBRA*GCFR in the smooth portion (level I) are within 3% to 4% of the SAGAPO results. There is closer agreement for the flow distribution obtained by the different codes, and the film drops are within 2% of each other. In the rough portion of the bundle, all parameters are within 3% of each other except for the friction factors in the wall channel (which are within 7% of the SAGAPO results). This comparison is more difficult than that for the smooth portion since the friction and Stanton numbers for the rough portion are calculated by integration in the code; this procedure involves checking out the basic correlation and the integration method used in the code. In the smooth portion these quantities are calculated by correlations which are input

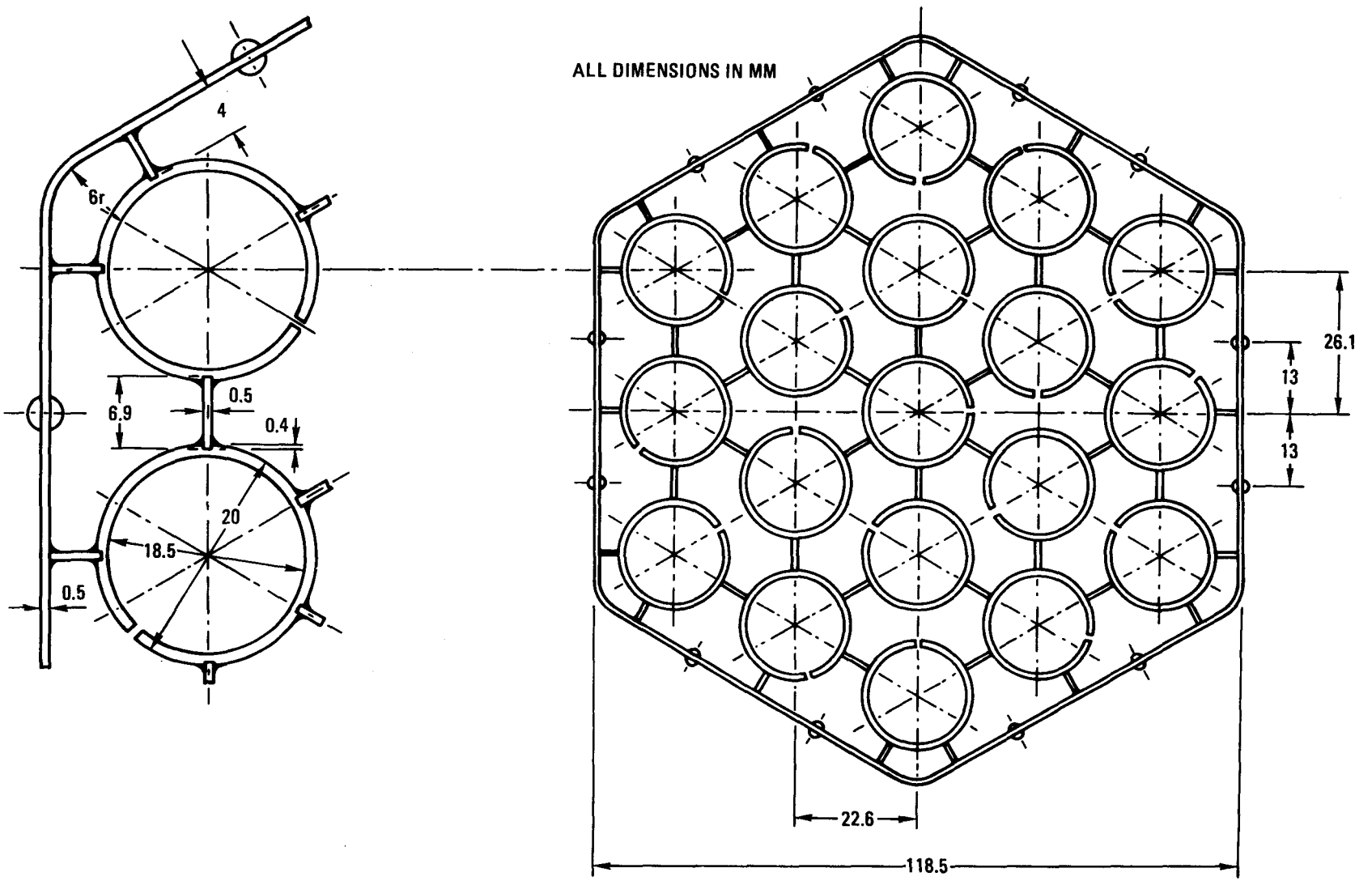

Fig. 2-1. 19-rod bundle tested at Institut für Neutronenphysik

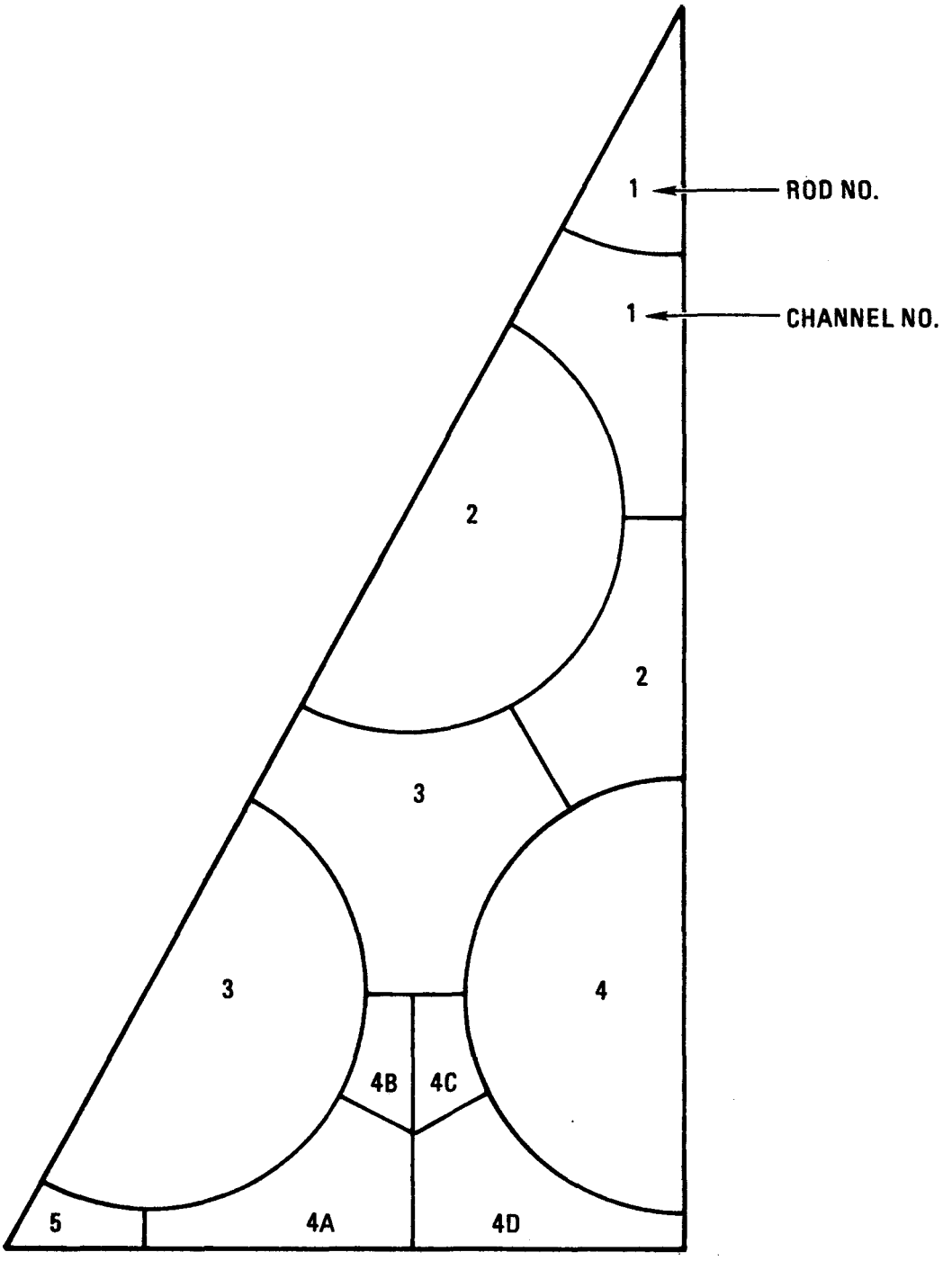

Fig. 2-2. COBRA*GCFR model for 19-rod bundle

TABLE 2-1
GEOMETRY, TEST CONDITIONS, AND CORRELATIONS
FOR 19-ROD BUNDLE

Geometry	
19-rod bundle, hexagonal shroud	
O.D. of smooth rods	18.3 mm
O.D. of rough rods	18.9 mm
Volumetric diameter of rough rods	18.37 mm
Pitch of rods	26.1 mm
Distance from shroud wall to center of external rods	14.79 mm
Roughness: square ribs	
Height	0.3 mm
Width	0.3 mm
Pitch	2.7 mm
Test conditions	
Inlet pressure	3.991 MPa
Inlet gas temperature	189.89°C
Mass flow rate	1.2072 kg/s
Heat power per unit length of each rod	101.63 W/cm

TABLE 2-1 (Continued)

Correlations for rough region

$$R(h^+) = 2.71 + \frac{5100}{(h_w^+)^3} + 0.4 \ln\left(\frac{h_R}{0.01\ (r_0 - r_1)}\right) + \frac{5}{\sqrt{h_w^+}}\left(\frac{T_w}{T_b} - 1\right)^2 ,$$

$$G(h^+) = 3.813\ (h_w^+)^{0.274}\ Pr^{0.44}\left(\frac{T_w}{T_B}\right)^{0.5}\ \left(\frac{h_R}{0.001\ (r_2 - r_1)}\right)^{0.053} ,$$

where h_R = height of ribs,
T_w = wall temperature,
T_B = bulk temperature of whole annulus,
T_b = bulk temperature of zone inside r_0 line,
r_0 = radius of zero shear line,
r_1 = volumetric radius of rods,
r_2 = inner radius of outer tube (annulus),
R = parameter in velocity profile,
G - parameter in temperature profile,
h^+ = roughness Reynolds number.

TABLE 2-2
RESULTS FOR TURBULENT CASE, SMOOTH PART[a]

Channel No.	COBRA*GCFR[b]			SAGAPO			SCRIMP		
	f	$\dot{m}$ (g/s)	ΔT (K)	f	$\dot{m}$ (g/s)	ΔT (K)	f	$\dot{m}$ (g/s)	ΔT (K)
Axial Level 1 (868 mm)									
1	0.01788	13.56	76.7	0.01758	13.60	76.5	0.01780	13.70	71.8
2	0.01788	13.56	76.4	0.01756	13.60	76.4	0.01780	13.69	71.8
3	0.01788	27.11	76.5	0.01759	27.13	76.5	0.01780	27.39	71.8
4	0.01799	40.63	82.7	0.01725	40.72	81.9	0.01750	40.45	82.2
5	0.02022	5.65	94.7	0.02061	5.55	93.1	0.01995	5.37	97.1
Axial Level 4 (1658 mm)									
1	0.1248	12.68	35.8	0.12161	12.5	34.9	0.1227	12.03	36.1
2	0.1248	12.67	35.8	0.12161	12.5	34.9	0.1228	12.04	36.1
3	0.1248	25.34	35.8	0.12159	25.1	34.9	0.1232	24.36	35.8
4	0.0678	43.64	38.0	0.06338	44.2	36.1	0.0698	45.53	35.8
5	0.0605	6.15	36.4	0.05810	6.34	37.3	0.0607	6.64	38.6
Axial Level 6 (2128 mm)									
1	0.1248	11.90	35.8	0.12160	11.9	36.2	0.1251	11.77	36.6
2	0.1248	11.91	35.8	0.12160	11.9	36.2	0.1251	11.80	36.5

TABLE 2-2 (Continued)

Channel No.	COBRA*GCFR[b]			SAGAPO			SCRIMP		
	f	$\dot{m}$ (g/s)	ΔT (K)	f	$\dot{m}$ (g/s)	ΔT (K)	f	$\dot{m}$ (g/s)	ΔT (K)
3	0.1248	23.92	35.8	0.12160	24.2	36.2	0.1249	24.02	36.1
4	0.0676	46.22	38.0	0.06326	46.0	35.0	0.0675	46.36	35.3
5	0.0604	6.54	36.4	0.05795	6.62	35.8	0.0613	6.64	38.5

(a)

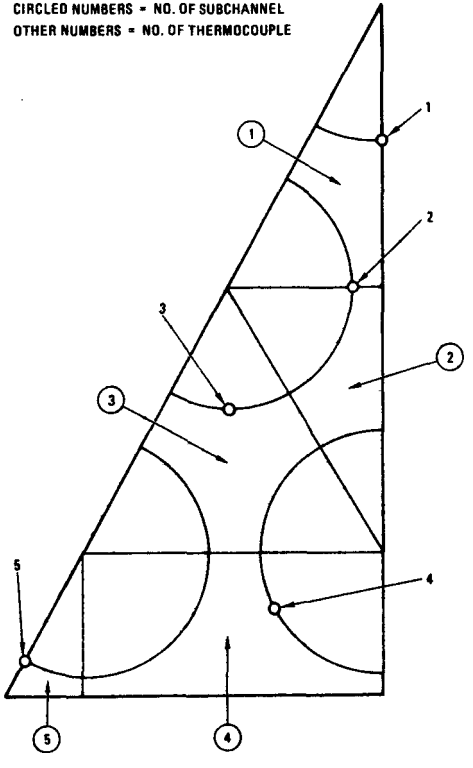

(b) f = friction factor,

$\dot{m}$ = mass flow per channel,

ΔT = difference between surface and bulk temperature.

to the code. In addition, since the hot spot temperature occurs in the rough portion, the temperatures in this region are more important for safe plant operation. Since the SAGAPO results have already been compared with experimental results (Ref. 2-3), comparison of the current analysis with experiments is not reported.

Heat transfer calibration tests on 12-rod bundles were performed in the high-pressure helium loop of the Heat Transfer Laboratory of the Institute of Neutron Physics and Reactor Engineering at the Karlsruhe Nuclear Research Center. The test apparatus, test bundle, and results for a turbulent flow test are described in Ref. 2-6. The average Reynolds number of the flow for the test under consideration was $\sim 7 \times 10^4$. Figure 2-3 shows the 12-rod KE III bundle including the rod numbers. Because of the symmetry (Fig. 2-4), it is sufficient to analyze one-third of the bundle. Figure 2-5 shows the COBRA*GCFR model. The geometry, test conditions, and correlations in the rough portion are given in Table 2-3. The correlations in the smooth portion of the bundle were obtained from Ref. 2-7.

The experiment under consideration was at fully turbulent flow conditions ($Re \simeq 7 \times 10^4$), and the average film drop was about 230°C. Figure 2-6 compares the pressure drop obtained in the experiment with that obtained in this analysis. The total pressure drop predicted is within less than 2% of the experimental results. Figures 2-7 through 2-9 compare the measured and predicted temperatures at the thermocouple locations. In most cases the agreement is within less than 10°C, which is equal to 4.3% of the film drop, or 2.5% of the total temperature rise to the location of the thermocouple. At two thermocouple locations (rods 42 and 78) there is a larger difference between the predicted and measured temperatures. Taking symmetry into consideration makes it obvious that this difference is due to a possible error in the measurement rather than in the analysis.

As a result of this study it is concluded that the COBRA*GCFR code can correctly perform the thermal-hydraulic analysis of roughened rod

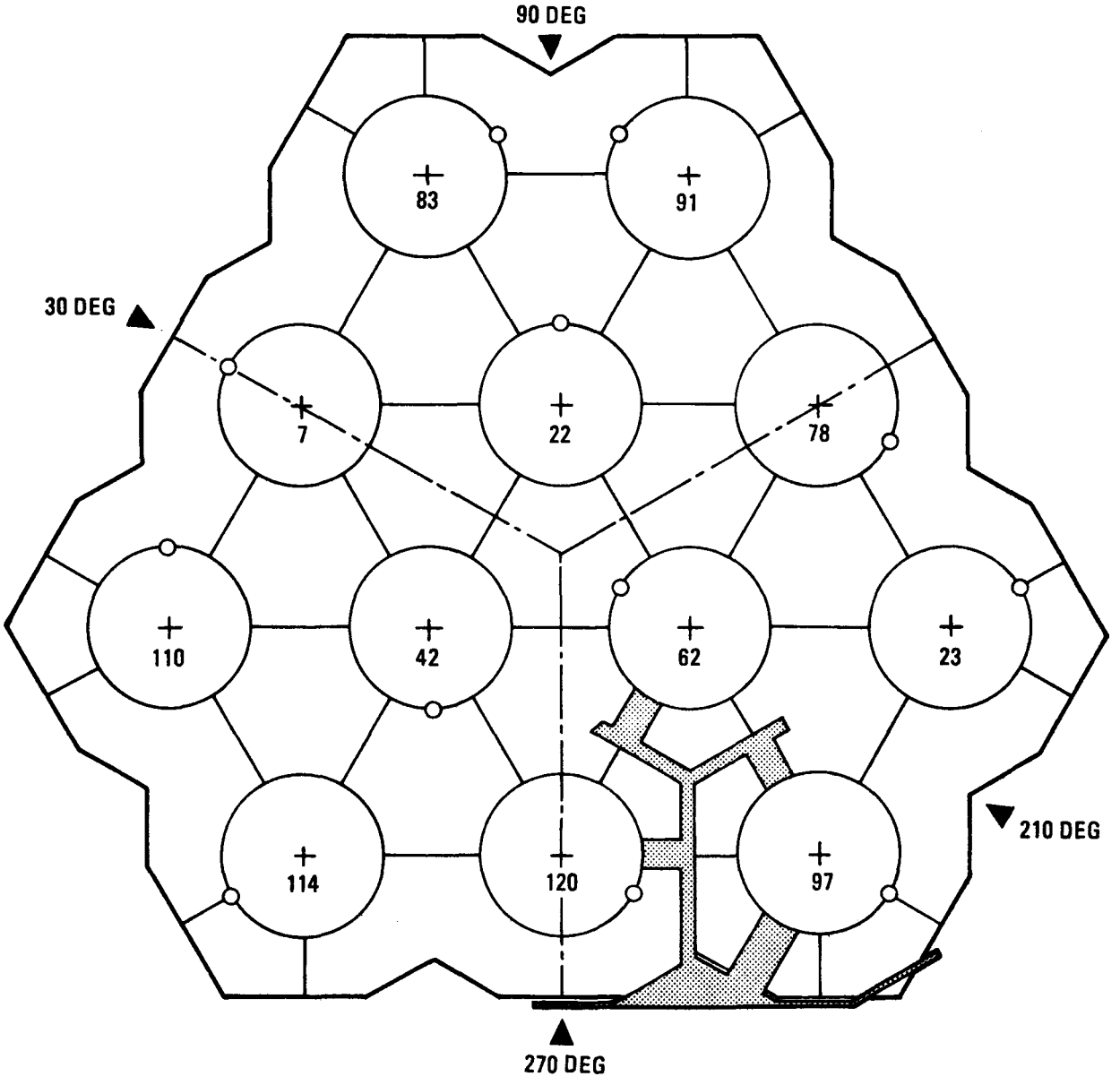

Fig. 2-3. BR-2 calibration bundle III with rod numbers

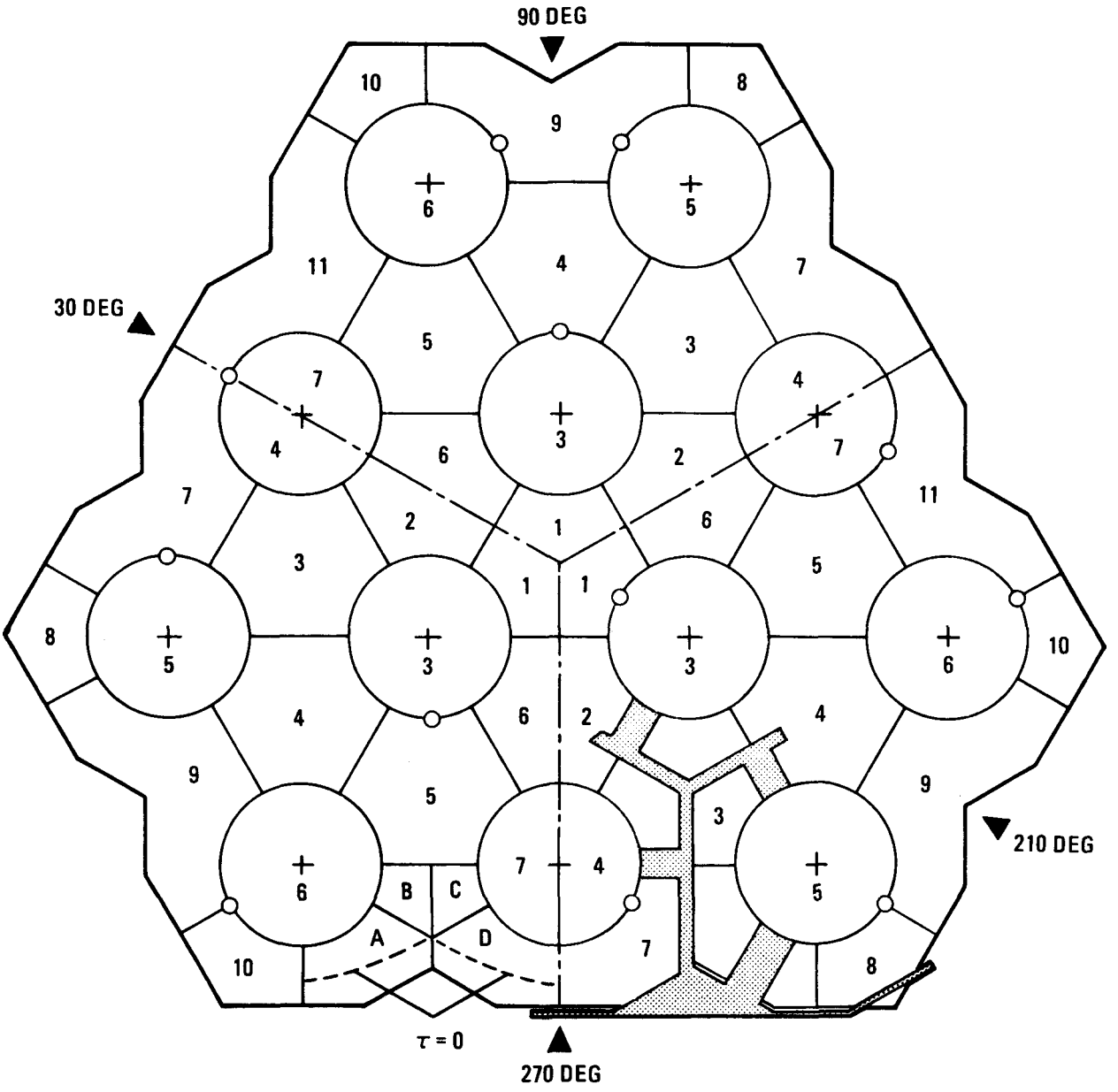

Fig. 2-4. Cross section of BR-2 bundle with symmetry

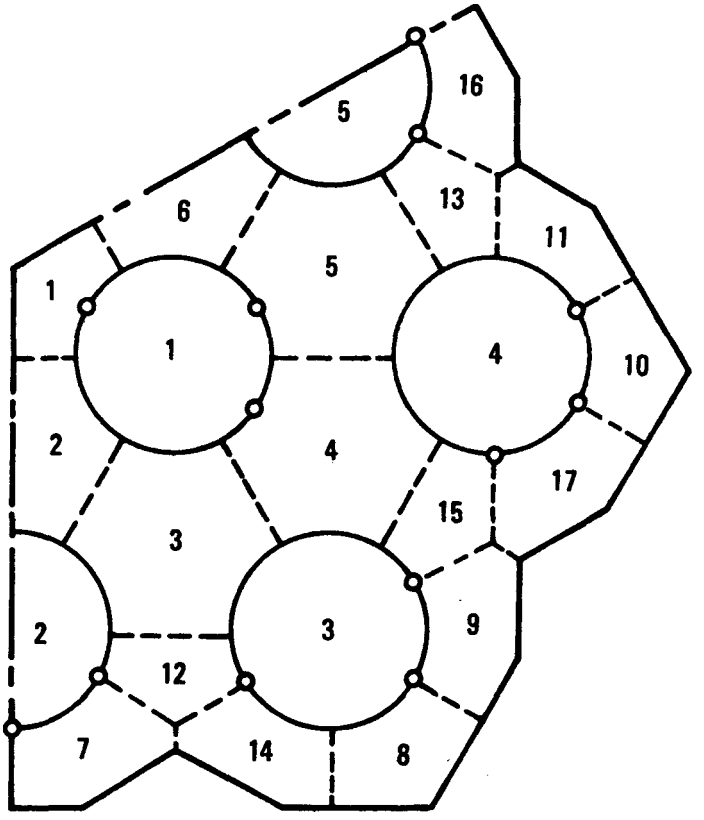

Fig. 2-5. COBRA model for BR-2 analysis

TABLE 2-3
GEOMETRY, TEST CONDITIONS, AND CORRELATIONS FOR
BR-2 CALIBRATION ELEMENT III

Geometry	
12-rod bundle, BR-2 calibration tests (KE III)	
O.D. of smooth rods	8.0 mm
O.D. of rough rods	8.0 mm
Volumetric diameter of rough rods	7.86 mm
Pitch of rods	11.1 mm
Distance from shroud wall to center of external rods	6.0 mm
Height of blocking triangle	1.57 mm
Base angle of blocking triangle	30 deg
Roughness: trapezoidal ribs	
Height	0.112 mm[(a)]
Width at tip	0.332 mm[(a)]
Width at base	0.548 mm[(a)]
Pitch	1.214 mm[(a)]
Test conditions	
Inlet pressure	3.9325 MPa
Inlet gas temperature	201.8°C
Mass flow rate	0.16702 kg/s
Heat power per unit length of each rod	307.48 W/cm

Correlations for rough region[(b)]

$$R(h^+) = 4.7 + \frac{359}{(h_w^+)^2} + 0.4 \ln\left(\frac{h_R}{0.01\ (r_0 - r_1)}\right) + \frac{5}{h_w^+}\left(\frac{T_w}{T_b} - 1\right)^2 ,$$

TABLE 2-3 (Continued)

$$G(h^+) = g_o Pr^{0.44} \left(\frac{T_W}{T_B}\right)^{0.5} \left(\frac{h_R}{0.01\ (r_0 - r_1)}\right)^{0.053} ,$$

$$g_o = 4.4\ (h_w^+)^{0.24} \text{ if } g_o > 10 ,$$

$$= 10 \text{ if } g_o < 10 .$$

(a) Mean value.

(b) See Table 2-1 for definitions of symbols.

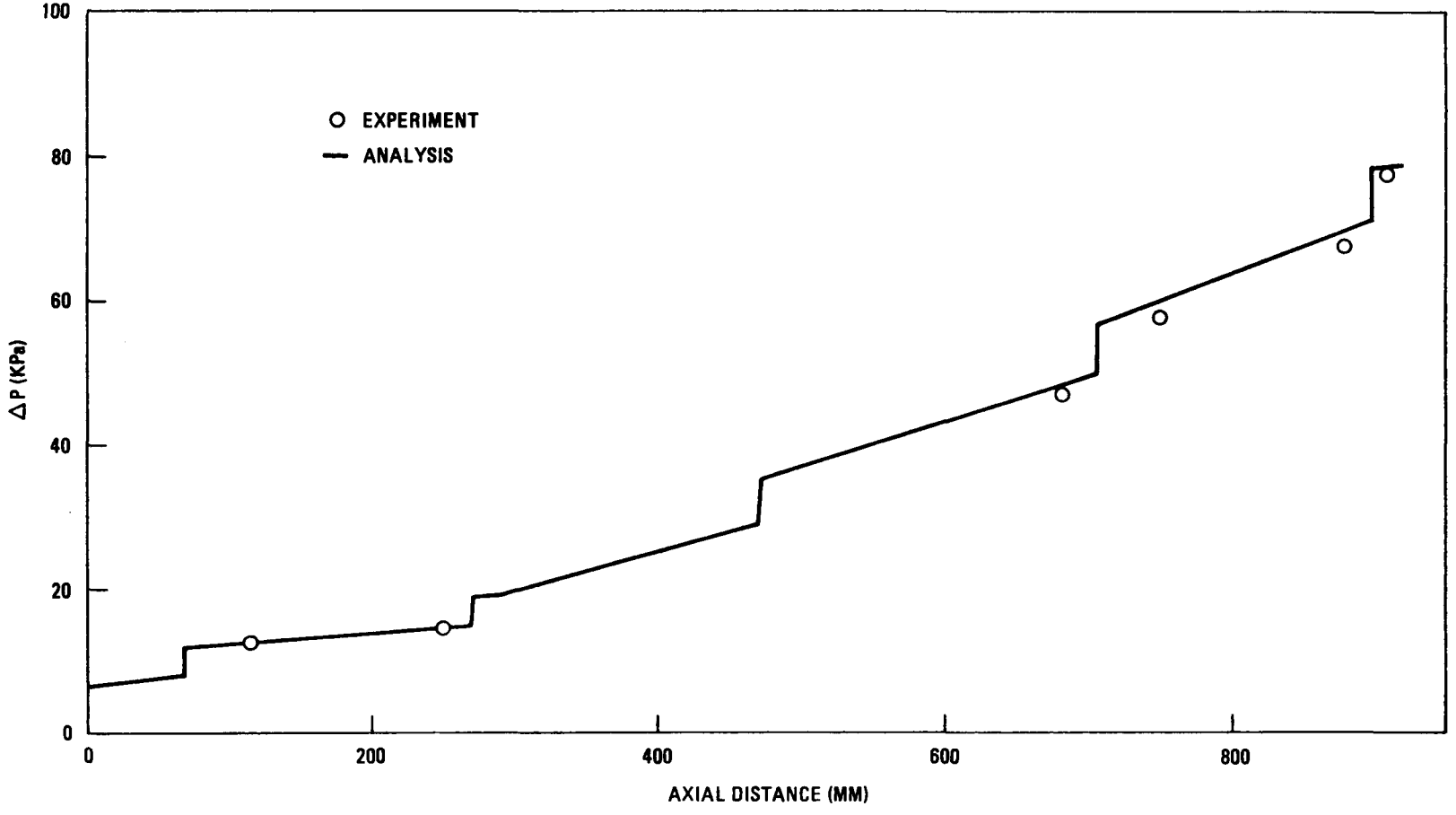

Fig. 2-6. Comparison of BR-2 experiment and COBRA*GCFR analysis

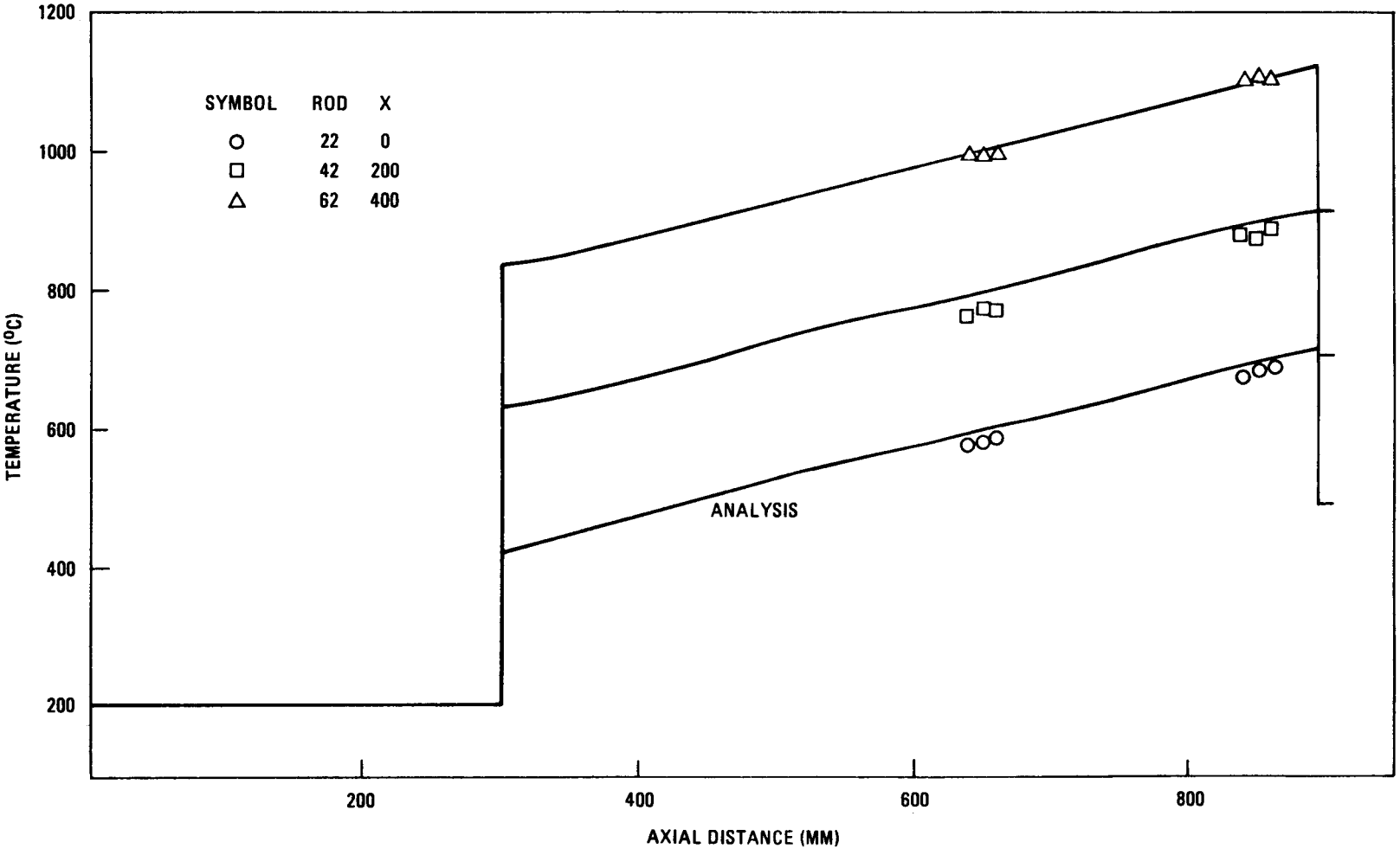

Fig. 2-7. Comparison of BR-2 experiment and COBRA*GCFR analysis in central channels

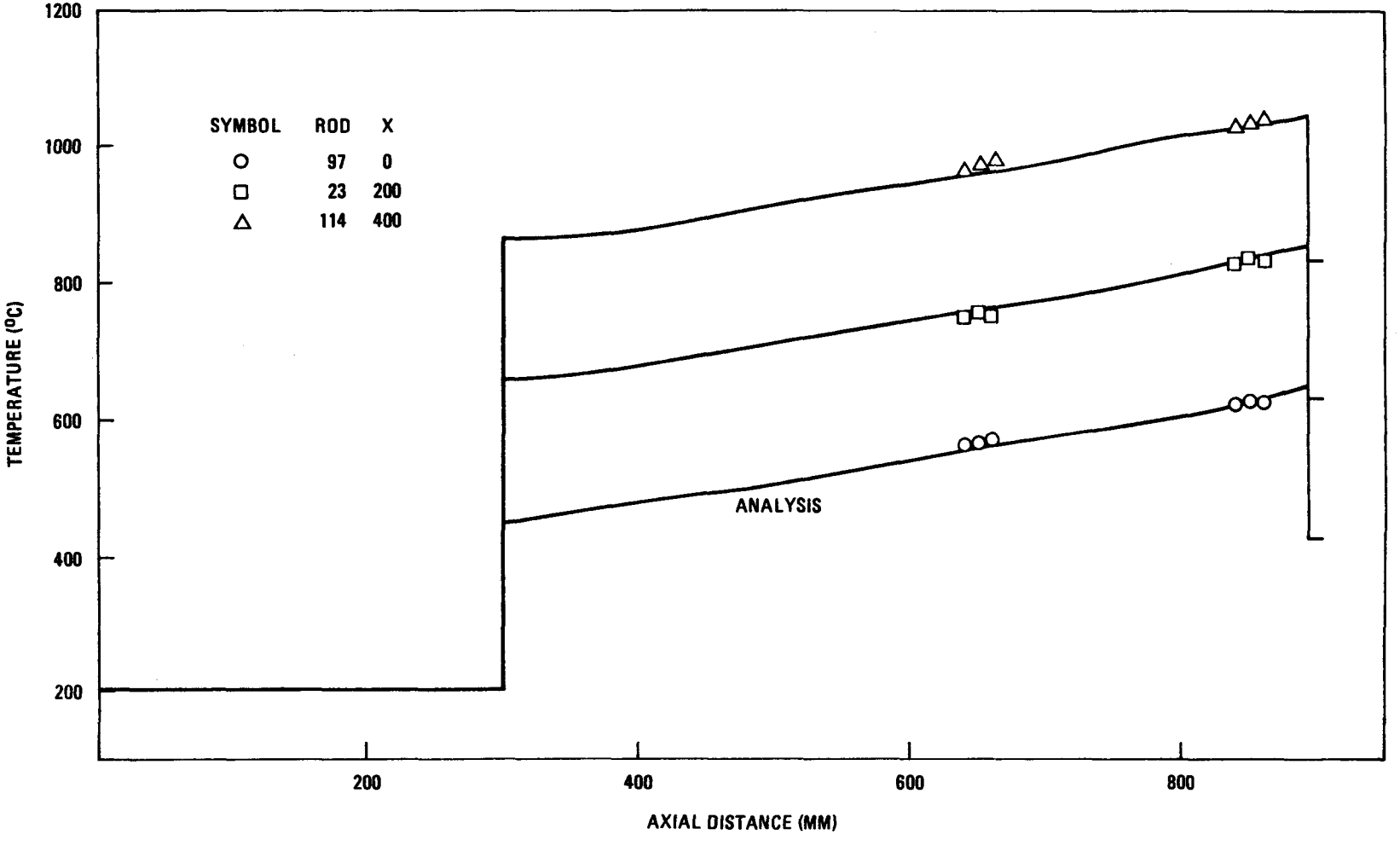

Fig. 2-8. Comparison of BR-2 experiment and COBRA*GCFR analysis in corner channels

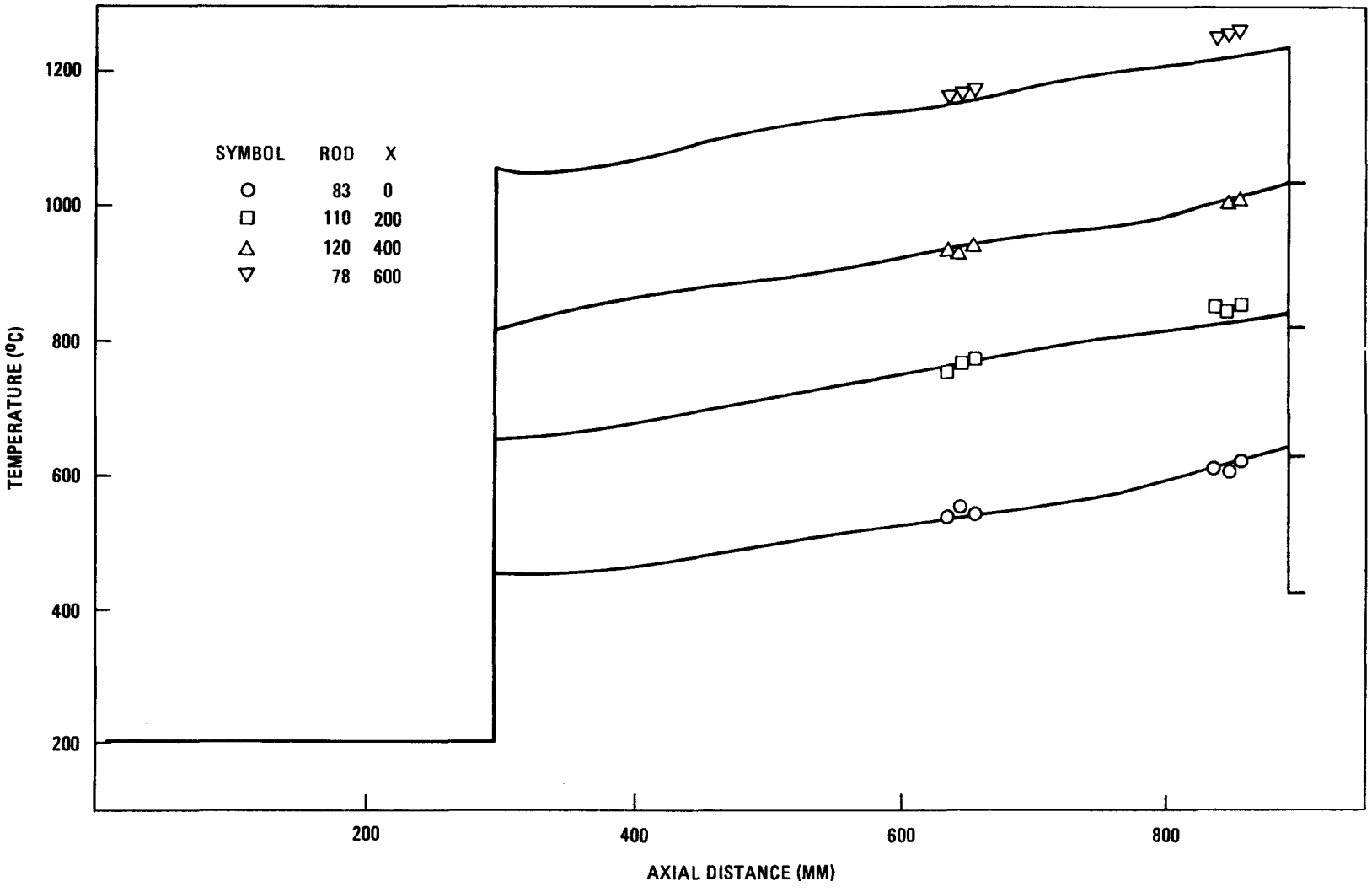

Fig. 2-9. Comparison of BR-2 experiment and COBRA*GCFR analysis in wall channels

bundles for turbulent flow conditions. In addition, the COBRA*GCFR code is much cheaper to run compared with other existing codes (e.g., SAGAPO, SCRIMP) and hence is preferred over the other codes.

2.1.3. Control Assembly Analysis

There was no activity on the analysis of the control assembly during this quarter.

2.1.4. Radial Blanket Assembly Analysis

2.1.4.1. Effect of Cladding Axial Conduction Under Steady-State Operating Conditions. Because of the variation in the axial power profile in a typical radial blanket rod, some rather large cladding axial temperature gradients have been calculated. To determine the effect of axial conduction in the cladding on these temperature gradients, a large step change in axial power was imposed on a rod of the radial blanket configuration, and analyses were performed with and without conduction in the model. Even with this extreme operating condition, it was found that axial conduction had a negligibly small effect on nominal and hot spot cladding temperatures. In addition, a 6% increase in COBRA iteration time was observed as a result of including conduction in the model. Therefore, this option will not be used for analyses of the radial blanket under nominal steady-state operating conditions.

2.1.4.2. Hot Spot Factor for Cladding Circumferential Heat Transfer Coefficient Variation. Preliminary values for coolant, film, and cladding hot spot factors have been developed (Ref. 2-8). Because of large uncertainties in the circumferential variation of the heat transfer coefficient around the rod, a conservative value of 1.8 had been selected for this factor. Recent data (Ref. 2-9) indicate that the overall film hot spot factor can be significantly reduced. Tests were performed on a 61-rod wire-wrapped rod bundle simulating the GCFR radial blanket assembly.

Circumferential surface temperatures of heated rods in the bundle were measured, and local values of the heat transfer coefficient were calculated. Values for the ratio of average-to-minimum heat transfer coefficient were plotted as a function of Reynolds number and were found to range from 1.2 to 1.4 in the turbulent flow regime for the various test rods. Since no measurements were made at the precise hot spot location, a point immediately downstream of a wire, and in the gap between the rods, a number of these tests will be rerun. Larger heat transfer coefficient ratios are expected. However, as discussed in Ref. 2-10, circumferential cladding conduction reduces the ratio of maximum-to-average film temperature difference (film hot spot factor) to a value substantially lower than that of the coefficient ratio. Therefore, until the new data are available, a hot spot factor of 1.4 for the cladding circumferential heat transfer coefficient variation will be used for radial blanket assembly analyses.

2.1.4.3. Axial and Radial Power Profiles. The axial and radial power distributions in the radial blanket assemblies have a direct effect on the cladding temperatures in the maximum-powered assembly and consequently on the coolant flow requirements in the blanket assemblies. In an effort to use the most recent information on radial and axial power distributions, a review of the subject was performed and nuclear analysis data were curve fitted and the resulting power profiles normalized.

The most recent information available on radial power distributions in the radial blankets was for the 0.224-MPa pressure drop core with 121 fuel and control assemblies (Ref. 2-2). Although the current GCFR design specifies a 0.29-MPa pressure drop core with 127 fuel and control assemblies, these data are considered adequate for preliminary design analyses. The radial power distributions for various cycles in the blanket management scheme indicate that for the first row of blankets, the maximum power levels are predicted for the end of the equilibrium cycle (EOC), and the largest power gradients are predicted for the beginning of the equilibrium cycle (BOC). Curve fits were performed using the radial power distributions for BOC 5 and EOC 6, assuming exponential profiles in the first

blanket row, which is more significant from a maximum power standpoint. Excellent curve fits were obtained with coefficients of determination of 0.997 and 0.998 for BOC 5 and EOC 6, respectively. Next, average power values were determined by integration and used to normalize the power distributions. Thus, the following relations were obtained for the normalized radial power distributions:

$$\frac{P}{P_{avg}} = 2.139e^{-1.7773r/R} \text{ for BOC} \quad ,$$

$$\frac{P}{P_{avg}} = 1.724e^{-1.210r/R} \text{ for EOC} \quad ,$$

where r is the distance from the core-blanket interface, and R is the thickness of the first row of blankets (in the radial direction). Although the magnitude of gamma ray heating at the core-blanket interface is small compared with that of other power components and the radial decay is steeper, as can be seen from Fig. 2-10, the gamma ray heating contribution is still significant for the blanket rod nearest the core in the maximum-powered assembly.

2.1.4.4. COBRA-IV Code Development. The reference version of the COBRA-IV subchannel analysis computer program (Ref. 2-11) accepts system pressure as input and calculates a coolant property table as a function of temperature at that pressure level. This table is then used throughout the bundle even though the local pressure is lower than the input reference pressure. Even though the effect of pressure on helium properties at nominal radial blanket operating temperatures is negligible, it becomes significant as the temperature level falls. A modification of the COBRA-IV implicit solution scheme was made to recalculate the helium property table at each axial node, and the requirement for an input helium "saturation" property table was removed. This modification permits the execution of transients in which the system pressure varies as a function of time.

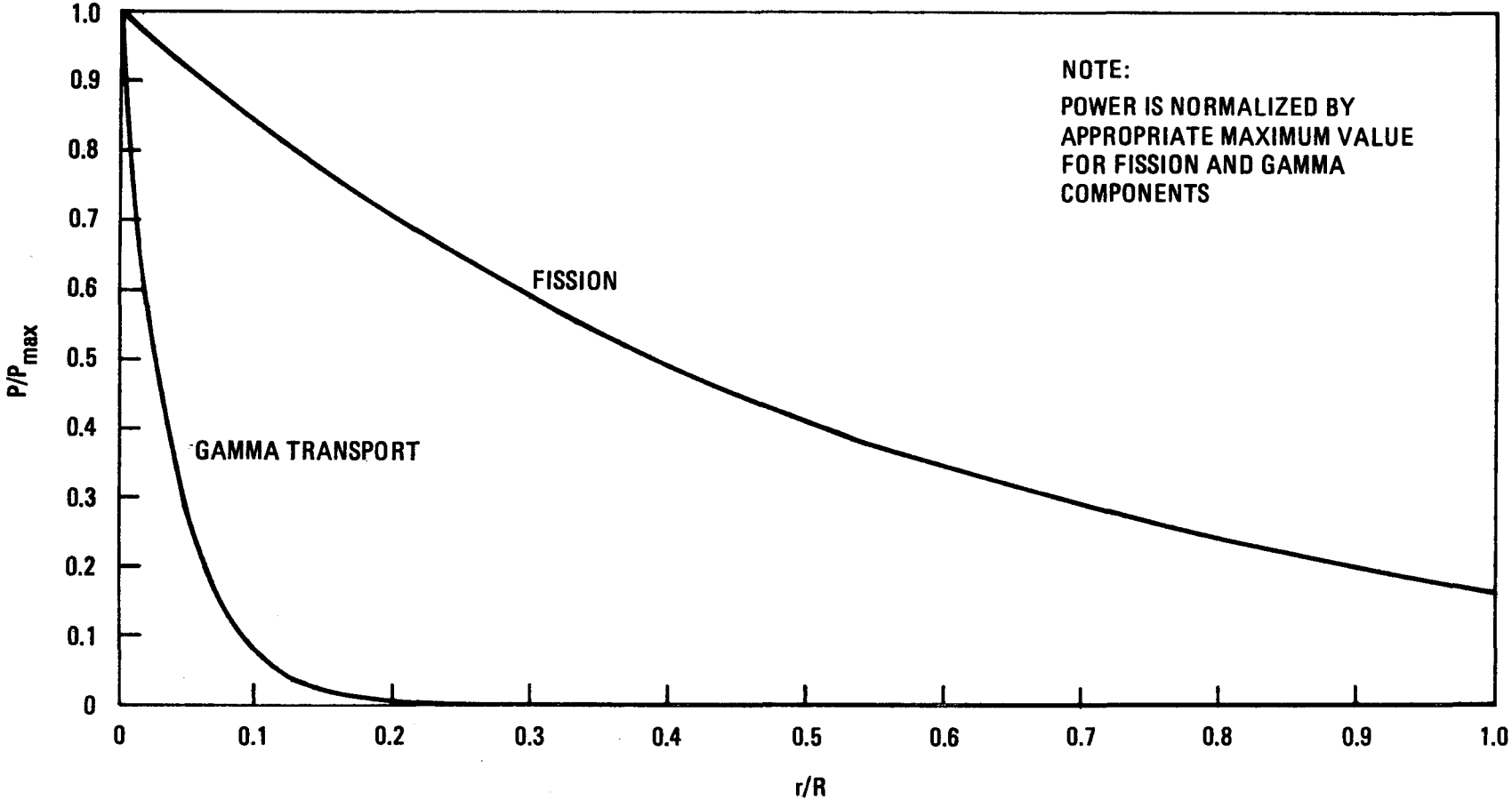

Fig. 2-10. Radial power distribution in first row of radial blankets

The capability of inputting hot spot factors and calculating hot spot temperatures was also incorporated into the code, and separate factors were applied to the coolant bulk, surface film, and radial cladding temperature profiles to arrive at the maximum midwall temperature. This procedure is necessary for determination of the assembly coolant flow rate required for limiting the maximum cladding midwall temperature to a specified value.

2.2. CORE ASSEMBLY MECHANICAL ANALYSIS

2.2.1. Core Distortion Analysis

The relative swelling distortions of the principle GCFR core assembly components, i.e., fuel rod cladding, grid spacers, and flow duct, were re-evaluated, and the effect of swelling on cladding-spacer interaction was studied. Thermal-hydraulic data were obtained from the CALIOP code (Ref. 2-12) for a 0.29-MPa pressure drop core and 320° and 585°C inlet and outlet temperatures, respectively. This represents a worst-case assembly condition. Physics data were obtained from Ref. 2-13. These data were for the central assembly, since swelling effects will be most severe there. Revision 5 of the swelling equation from Ref. 2-14 for 20% cold-worked 316 stainless steel was used. Thermal bowing, swelling-induced bowing, and pressure-induced dilation were not considered. Steady-state operation throughout life was assumed.

The results are given in Figs. 2-11 and 2-12. In all cases the change in diameter due to swelling is plotted against distance from the grid manifold. Each figure consists of an o.d. (rod or spacer) and a containing envelope (spacer or duct); potential interference is denoted by a cross-hatched area. Figure 2-11 shows the locus of the spacer outer diameters and the profile of the duct i.d. at the end of life (EOL). The initial gap of 0.2 mm is sufficient to preclude swelling interference. However, as much as 6.6 mm diametral interference would be experienced if an attempt were

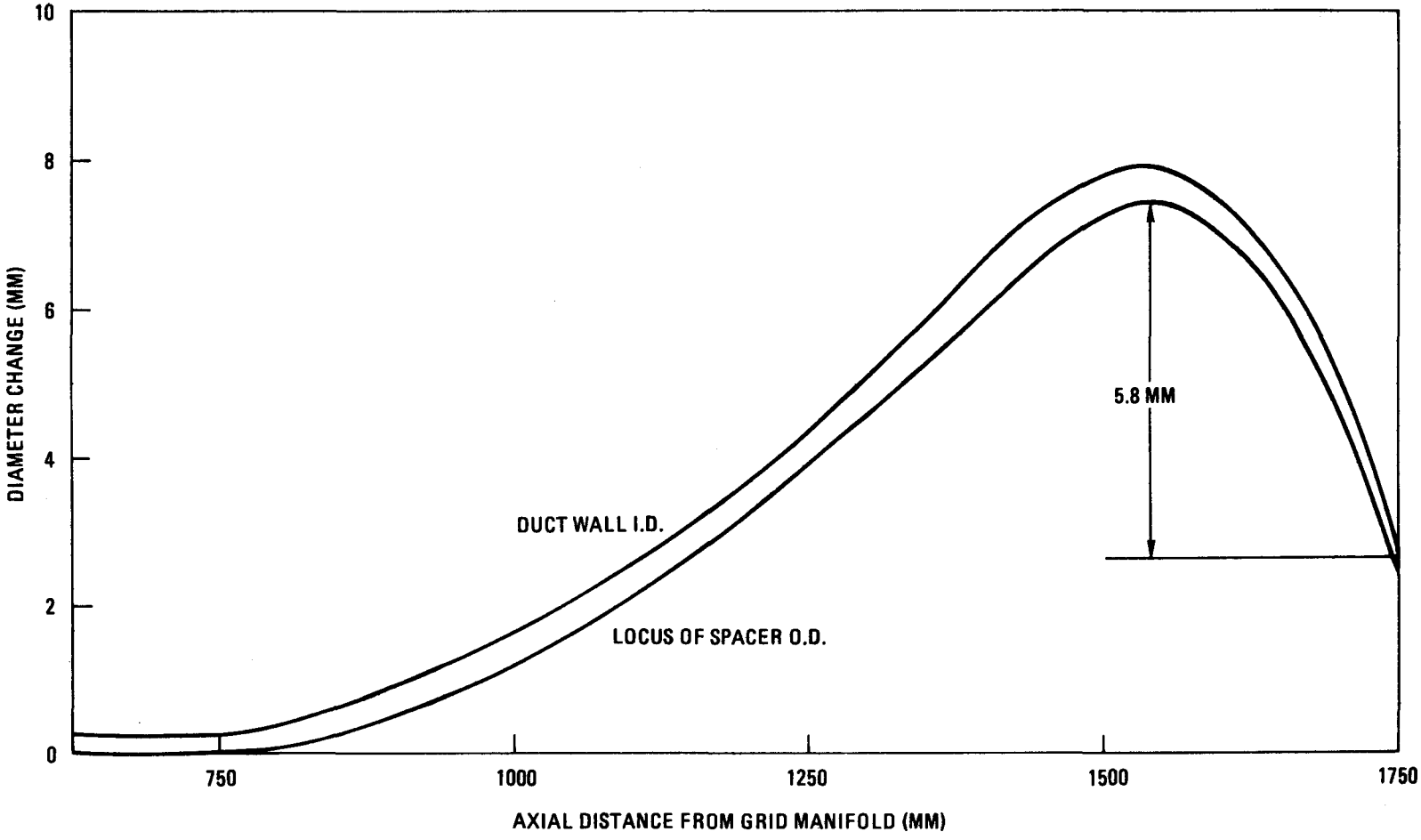

Fig. 2-11. Comparison of swelling distortions of grid spacers and duct (time = 18,000 hr)

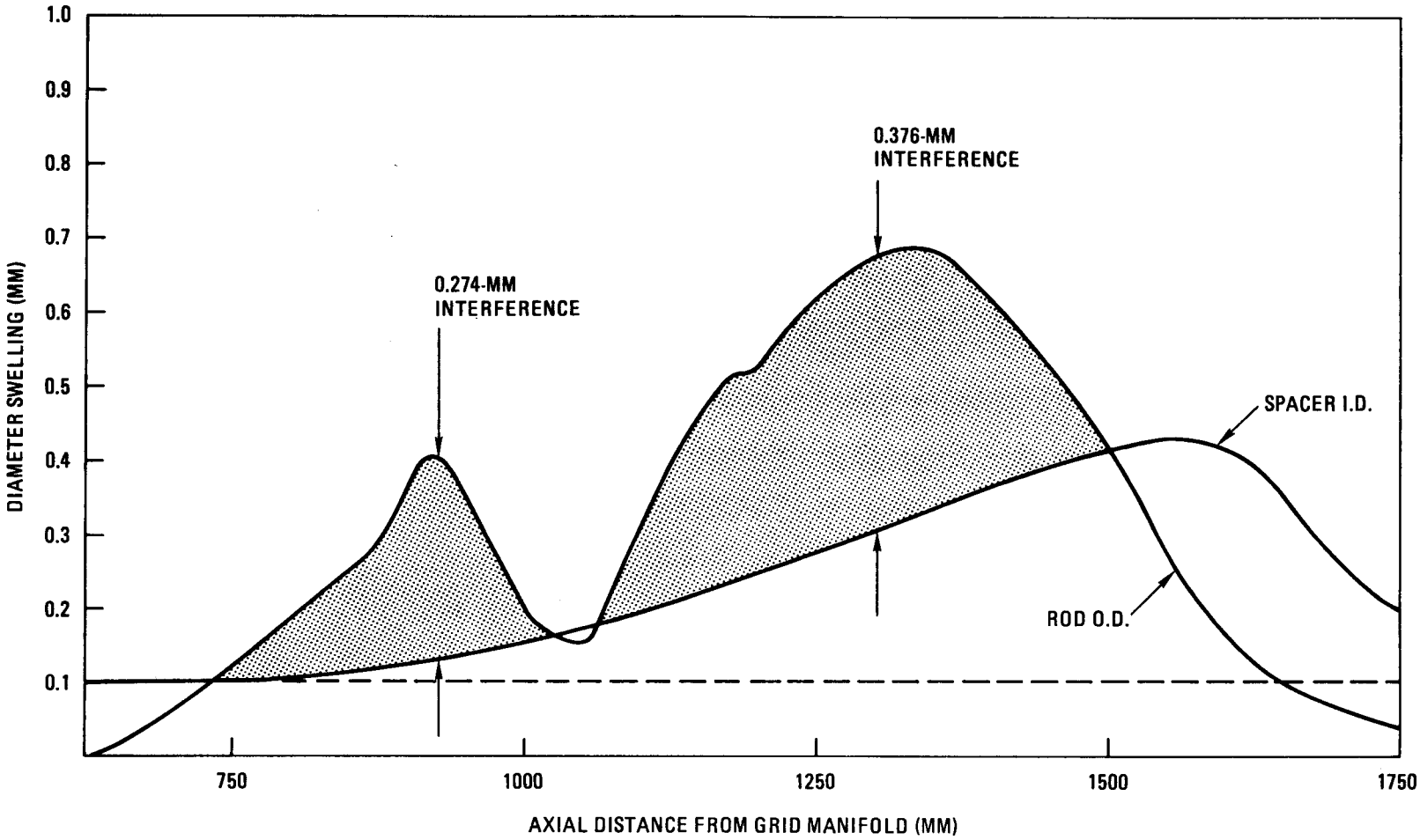

Fig. 2-12. Comparison of swelling distortions of rod and spacer cell (time = 18,000 hr)

made to remove the bundle from the duct in addition to any other interference due to bowing. As shown in Fig. 2-11, almost the entire lower half of the bundle will be swollen more than the outlet end. Obviously, sliding the bundle out of the duct at EOL will not be feasible.

Figure 2-12 demonstrates the potential rod-spacer interference at 18,000 hr. Interference occurs early in life and becomes excessive and extensive before two cycles of operation are complete. Figure 2-11 shows that diametral swelling of the duct is almost 8 mm, or 4 mm radially at the worst location. Since this is somewhat more severe than predicted in previous studies (Ref. 2-15), the duct dilation problem was re-evaluated. Duct dilation is a complex interaction of temperature and neutron flux involving irradiation creep and swelling. To arrive at some design alternatives which would mitigate assembly interaction due to large duct dilations, four parameters were investigated: duct wall dimension, maximum assembly outlet temperature, interassembly gap, and maximum assembly life.

Figures 2-13 through 2-15 present the results of the parametric study; each figure is for a specified wall thickness and contains duct dilations as a function of time for five different outlet temperatures. The limit lines labeled "available gap" represent the remaining interassembly space as a function of time, assuming that the adjacent element is in its second cycle of operation and has an outlet temperature of 585°C. The current design has a 3.8-mm wall and a 6.5-mm interassembly gap. Figure 2-14 indicates that for the current worst-case assembly (outlet temperature = 585°C), this gap is not sufficient to accommodate the dilation.

The conclusions drawn from this study are as follows:

1. The present rod-spacer clearance is insufficient, and either the diametral clearance should be increased to 0.5 mm, or the spacer should be replaced with a noninterfering design such as a rhombic spacing system.

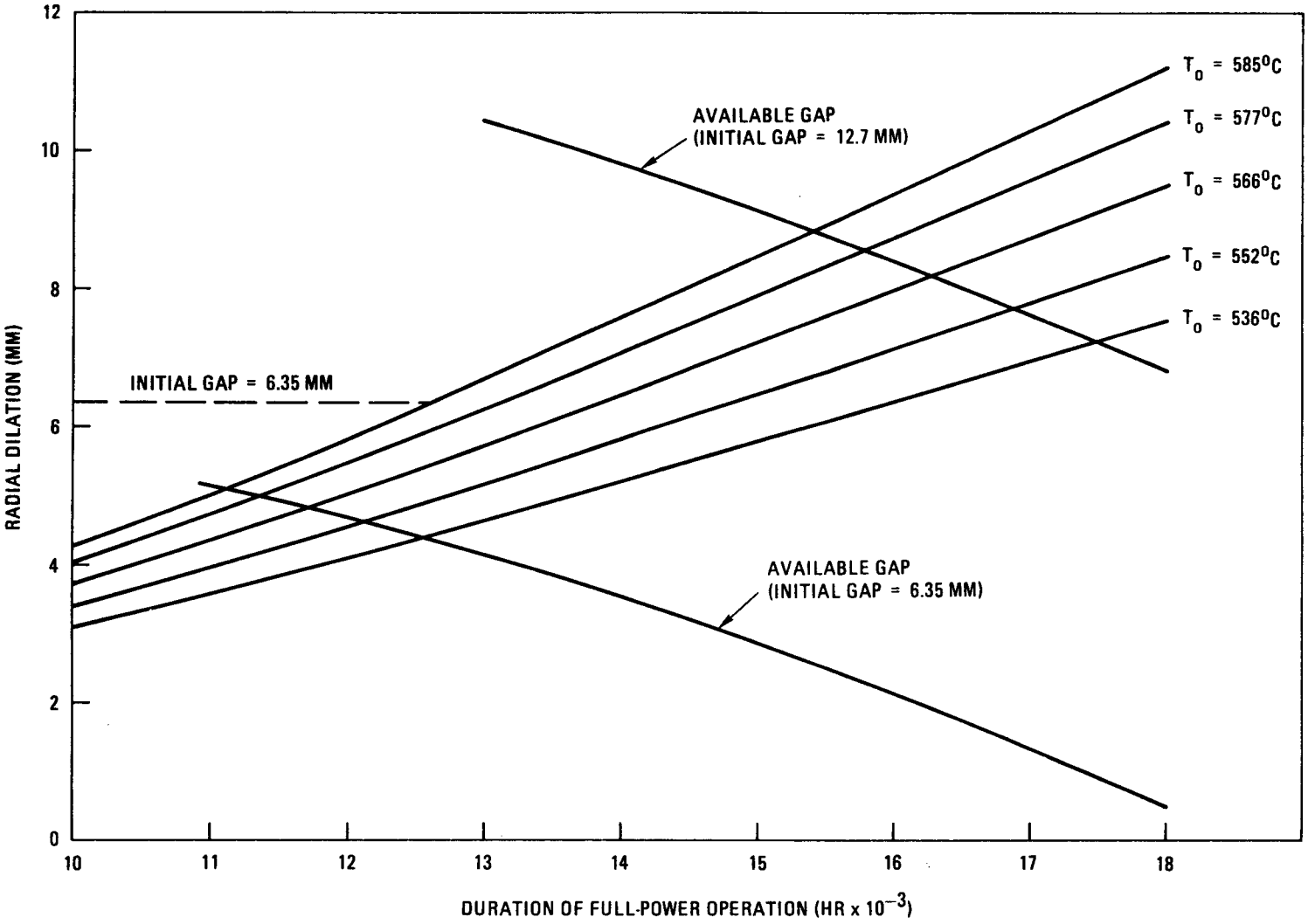

Fig. 2-13. Parametric study of duct wall dilation for a wall thickness of 2.54 mm

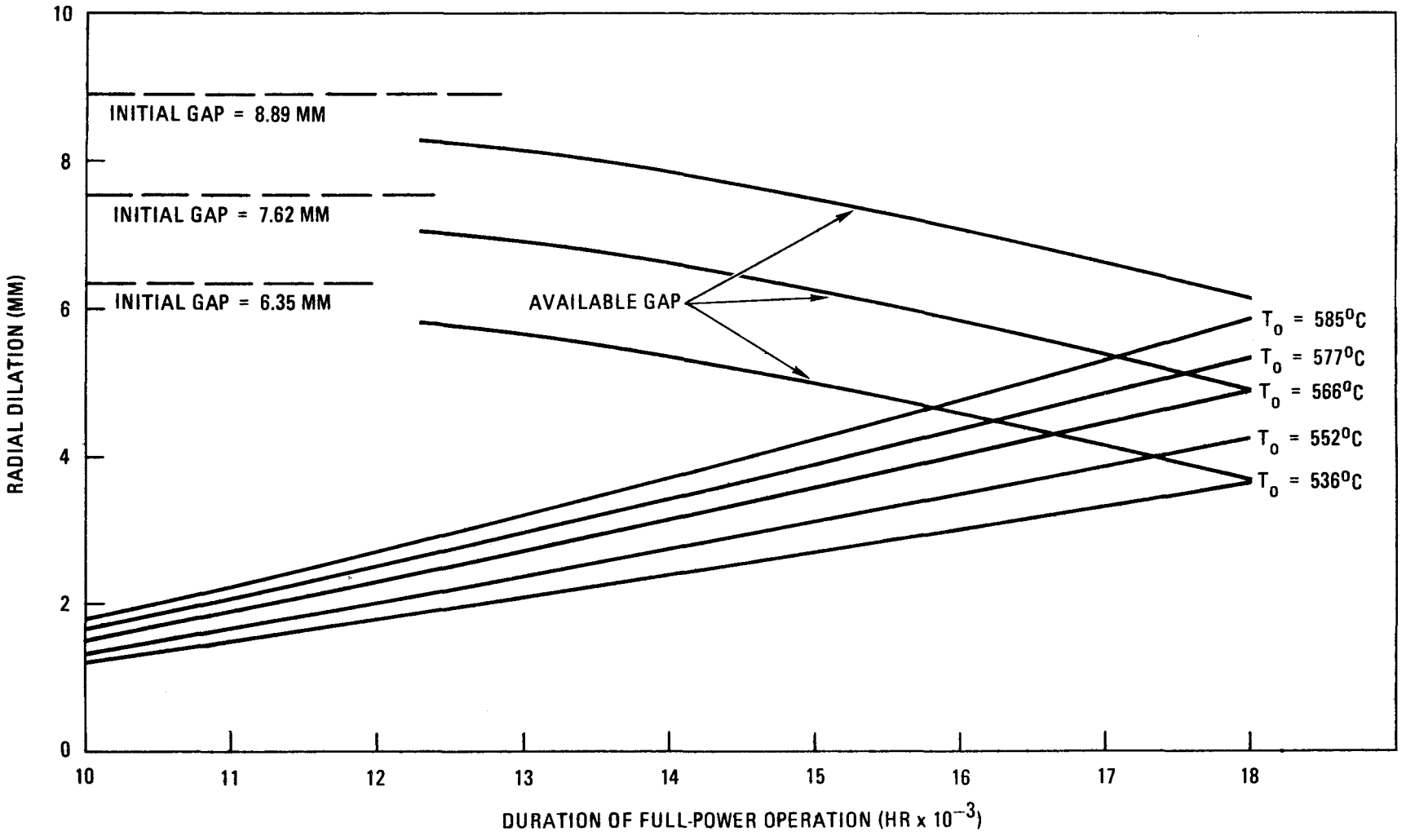

Fig. 2-14. Parametric study of duct wall dilation for a wall thickness of 3.81 mm

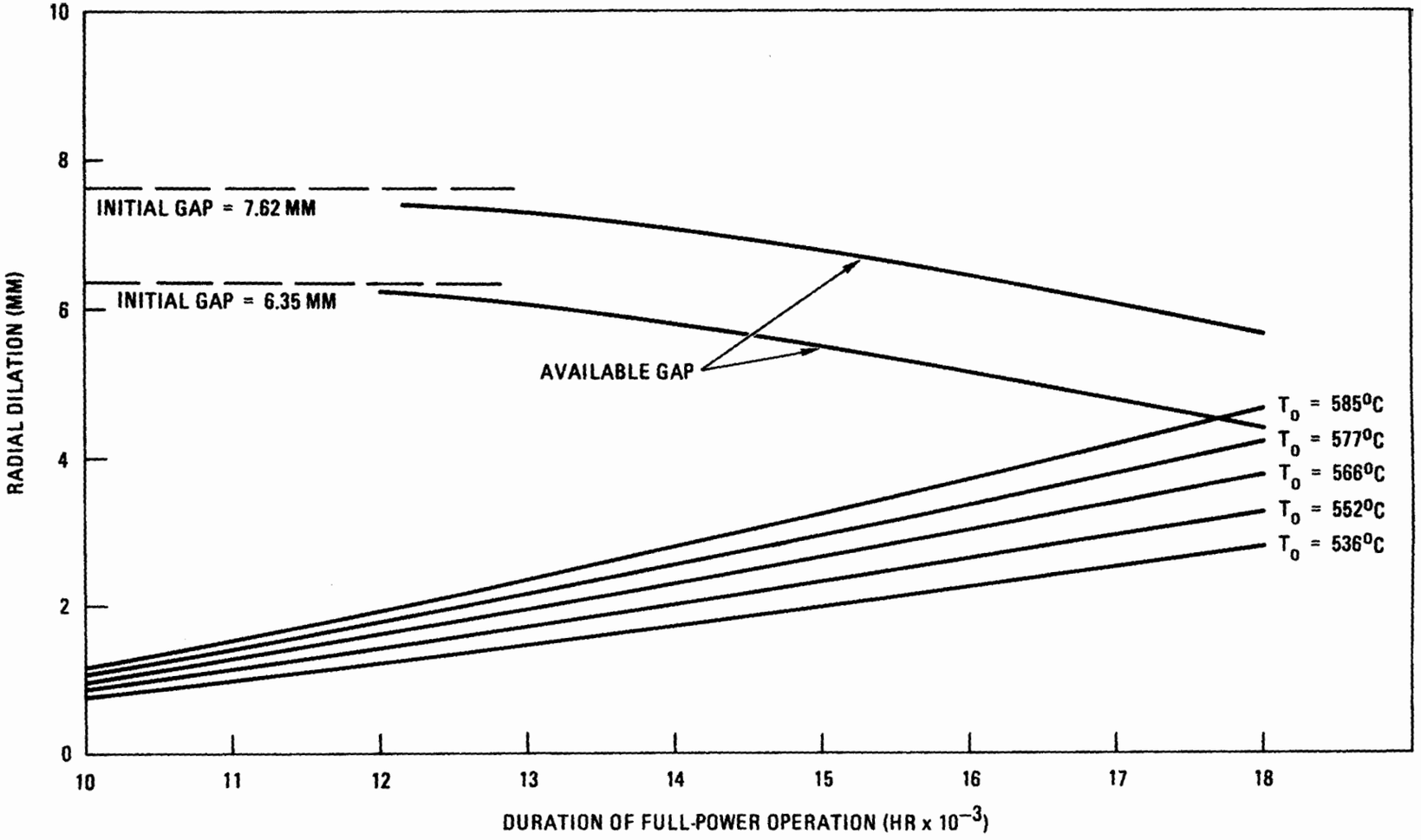

Fig. 2-15. Parametric study of duct wall dilation for a wall thickness of 5.08 mm

2. The present design parameters for duct wall thickness, inter-assembly gap, maximum outlet temperature, and desired burnup are not compatible with a noninterfering core. Although any of these parameters could individually be adjusted to solve the problem, the optimum solution in terms of impact on the rest of the core design will result from a suitable combination of adjustments to all these parameters. This study assumed that assembly interference from duct dilation is the overriding structural problem. However, this is probably not the case, since rod bowing and flow channel size variation from duct dilation will have at least as large an effect on the design. Consequently, the design modifications will have to be determined by future studies which account for an optimum combination of changes in terms of system performance, rod bowing phenomena, and duct dilation requirements.

2.2.2. Flow-Induced Vibration of Core Components

Flow-induced vibration of core components is one of the areas of major concern in the design of any reactor and is of particular concern in the design of gas-cooled reactors because of their high coolant velocities. Certain aspects of flow-induced vibration phenomena are fairly well understood, whereas others, such as the so-called "subcritical" vibration of fuel rods cooled by parallel flow, are hardly understood at all, despite over twenty years of study.

An extensive program of flow testing of major GCFR core components has been planned. However, in view of the complex nature of flow-induced vibration phenomena and present calculational uncertainties, it is imperative that these flow tests be properly designed with regard to similitude requirements so that they can provide usable information about component in-reactor vibration performance. During this quarter the scaling laws and similitude principles which apply to flow-induced vibration testing

of GCFR core components were examined, and on the basis of these laws, various flow test scenarios were evaluated.

2.2.2.1. Analysis. It is useful to divide flow-induced vibration phenomena into three categories: vibrations due to cross flow, vibrations due to axial flow, and vibrations due to acoustic excitation. Vibrations due to cross flow generally arise when the frequency of a periodic fluid force acting on a component happens to coincide with one of the component's natural frequencies. Because core components have relatively small damping, such an occurrence could result in large-amplitude vibrations, which have the potential for doing significant damage in very short periods of time. It is important to note that the amplitude of the vibration is strongly dependent on the degree of coincidence between the exciting frequency and the structure's natural frequency.

The vibrations associated with fuel rods are generally of the parallel flow type. These vibrations are typically of relatively low amplitude, but since they occur for long periods of time, they may result in wear of the cladding which could lead to breaching.* Various mechanisms have been postulated for this type of vibration, but it appears most likely that the vibration is a forced vibration resulting from the turbulent pressure fluctuations around the rod. The pressure fluctuations are of a broadband nature; the rod acts as a small-bandwidth filter, obtaining energy from the portions of the turbulence spectrum at or near the natural frequencies of the rod. Thus, the amplitude of this type of vibration is not strongly frequency dependent.

The third category of flow-induced vibration phenomena, acoustic excitation, is somewhat different than the first two in that the fluid flow is an indirect rather than a direct cause of structural vibration. Acoustic excitation can take on two forms: that due to near-field noise

*The GCFR is designed with a PES for removing gaseous fission products from the fuel rod. The PES is designed to accommodate a large number of leaking rods, so that breaching of the cladding, although undesirable, does not in itself imply rod failure.

and that due to far-field noise. Far-field noise arising from, for example, the circulators is not expected to contribute significantly to the response of GCFR core components, although it may be significant for other components or structures such as the thermal insulation. Furthermore, it is impossible to simulate the GCFR acoustic environment in a test rig; such testing must wait until the preoperational reactor commissioning tests are performed. On the other hand, near-field noise is caused if the fluid flow excites one or more acoustic resonances in the region of the core assemblies. These acoustic resonances can lead to emission of intense acoustic tones, which, owing to the large fluctuating pressures that are generated, can lead to fatigue failures of structural components if a structural resonance is also present. It is clear that the occurrence of these vibrations strongly depends on whether or not an acoustic resonance can be exicted.

The flow-induced vibration tests will be conducted using out-of-pile isothermal test rigs. This precludes duplication of several of the effects which occur in the reactor, among the most important of which are variation of fluid and structural properties with axial location in the assembly and many of the effects of irradiation. It is anticipated that these differences will cause only secondary effects, with the primary effects being adequately simulated if sufficient care is taken in modeling.

The parameters which affect flow-induced vibration and can be controlled for the flow tests are listed in Table 2-4. Fluid density, viscosity, pressure drop, and sound speed are important fluid parameters in addition to flow velocity. Characteristic dimension (which reflects the model scale), density, elastic modulus, frequency of vibration, and damping are important for the structure. This list is by no means all-inclusive (for example, relative roughness has not been included), but is meant to reflect parameters which would have a major effect on the vibration.

Dimensional analysis can be applied to these parameters. Table 2-5 lists the five dimensionless variables normally associated with flow-induced vibration testing. A sixth, independent, dimensionless variable

TABLE 2-4
PARAMETERS AFFECTING FLOW-INDUCED VIBRATIONS

Fluid parameters	
Velocity	V
Density	ρ_f
Viscosity	μ
Pressure drop	ΔP
Sound speed	a
Structural parameters	
Vibration amplitude	δ
Characteristic dimension	d
Average density	ρ_r
Young's modulus	E
Frequency of vibation	ω
Damping/ratio	η

TABLE 2-5
DIMENSIONLESS VARIABLES NORMALLY ASSOCIATED
WITH FLOW-INDUCED VIBRATION TESTING

Reynolds number	$Re = \frac{\rho_f V d}{\mu}$	=	ratio of fluid inertia force to fluid viscosity force
Strouhal number	$S = \frac{\omega d}{v}$	=	ratio of fluid inertia force to force associated with frequency ω
Euler number	$E = \frac{\Delta P}{\rho_f V^2}$	=	ratio of pressure force to fluid inertia force
Mach number	$Ma = \frac{V}{a}$	=	ratio indicating importance of compressibility effects
Cauchy number	$C = \frac{\omega^2 L^2 \rho_r}{E}$	=	ratio of rod inertia force to rod elastic force

is needed for completeness; this can be the ratio of the fluid density to the structural density. The first item to consider is the scale of the models to be tested. It is quite common in structural dynamics to test partial scale models of large or expensive items. This approach is feasible for forced-vibration problems such as earthquake excitation of equipment where the forcing function can be deterministically defined, independent of equipment response. The requirement for Cauchy number similitude requires that, for example, for a 1/5-scale model, the frequency of the input motion be increased by a factor of five and the amplitude decreased by a similar factor. This is readily accomplished in shake table tests. However, flow-induced vibrations involve more complex forcing items, some of which are not very well understood. An analogous modification of the forcing terms in flow-induced vibration tests would be difficult to accomplish correctly, and harder yet to defend. Therefore, only full-scale tests of core components should be considered. Use of partial-section core assembly models (assembly models containing a reduced number of full-scale rods) may be permissible in some cases. If full-scale models are used, the test rig fluid parameters should be chosen to reproduce as accurately as possible the fluid forces expected in the reactor. This choice can most easily be made by separate consideration of the three aforementioned flow-induced vibration categories.

2.2.2.2. Cross Flow Excitation. As noted earlier, cross flow problems often occur if the frequency of a periodic fluid force coincides with one of the structure's natural frequencies. Neglecting for the moment the effects of temperature on structural frequencies, the use of full-scale models provides model natural frequencies very near those of the actual assembly. Therefore, the frequencies of the fluid forces in the test should be the same as those expected in the reactor. These frequencies are characterized by the Strouhal number $S = \omega d/v$, which, for a given system and flow regime, is typically constant at a value of about 0.2. Hence, it is easy to see that to get the same frequency with full-scale models, the fluid velocity in the tests must equal the velocity in the actual assembly. Since the fluid velocity in the actual assembly is highest at

the core outlet, it is this velocity that governs the test rig design. If the effect of temperature on structural frequency is considered, there is only a moderate (<15%) change in the structural frequency between reactor conditions and room temperature. However, if a resonant condition existed only at operating conditions, then this increase in structural frequency could conceivably push the system out of resonance unless compensating steps were taken. The simplest and most direct method of compensation is to increase the maximum test flow velocity in proportion to the maximum anticipated increase of the structural frequencies. Then, since tests at reduced flow will be run in addition to tests at 1.15 times full flow, all possible resonance conditions will be included. To cover for possible future design changes, an additional 15% margin in flow velocity is suggested. It is therefore recommended that the test rig be designed to achieve a flow velocity equal to 1.3 times the maximum velocity expected to be experienced by the component. The amplitude of the fluctuating fluid forces is also important, although precise matching of experimental and reactor levels is not as critical as it is for the frequency.

The Euler number relationship can be rewritten as

$$\Delta P = C_L * (1/2\rho V^2) \quad ,$$

where

$$C_L = C_L(Re,Ma) \quad .$$

Provided that the Reynolds number and Mach number of the model are reasonably close to those for the prototype, C_L will also be similar. Since force is proportional to ΔP and the flow velocity has been chosen to be the same in the test as in the prototype, Euler number similarity requires that the fluid density in the test equal the density of the fluid in the prototype. To be most conservative, the highest density present in the prototype should be simulated, but as mentioned earlier, this is not a

parameter requiring precise matching. Therefore, to ease loop pressure requirements, it is sufficient to simulate the average reactor density.

Vibrations induced by parallel flow arise primarily as a result of pressure fluctuations caused by flow turbulence. The intensity of the turbulence in the fluid is a function of Reynolds number, although above a Reynolds number of about 5×10^4, it becomes a relatively weak function. Therefore, if the test Reynolds number is near or above the Reynolds number of the prototype, vibrations induced by parallel flow should be adequately modeled.

Acoustic excitations will be properly modeled if the frequencies of the acoustic resonances in the model are the same as those for the prototype. If full-size, full-scale models are used, this requirement is reduced to the requirement that the sound speed in the fluid of the test rig equal that of the fluid in the prototype. It is currently planned that some of the initial flow tests will test full-length assembly models with a reduced cross section holding a reduced number of full-size rods. It is important to note that it will not be possible to duplicate the actual acoustic environment with such a model. This can only be done with full-size undistorted models.

2.2.2.3. Comparison of Alternate Test Rigs. Flow parameters for a 300-MW(e) demonstration plant GCFR and four test rig configurations for flow-induced vibration testing are listed in Table 2-6. Test rig 1 is a rig which is most representative of GCFR operating conditions. It is designed to operate with helium at nominal core midplane conditions with "stretch" capability to operate at higher temperatures and flow velocities. The full range of GCFR operating conditions could be simulated. Because the test rig is isothermal, there is no film drop in temperature between cladding and coolant, which means that the fuel rod cladding in the test operates at a lower temperature than in the reactor. This raises the natural frequency of the rods about 7% (Table 2-4), which is probably not

TABLE 2-6
FLOW PARAMETERS FOR A 300-MW(e) DEMONSTRATION PLANT AND FOUR TEST RIG CONFIGURATIONS

	P (MPa)	T (°C)	V (m/s)	$\dot{m}$ (kg/s)	ρ[at T(°C)] (kg/m^3)	μ x 10^5 [(N-s)/m^2]	E (GPa)	C_{gas} (m/s)	Reynolds Number	Mach Number	ω/ω_{nom} (rods)
300-MW(e) GCFR core											
Inlet	9.0	316	53.6	5.37	7.36	3.16	∿177	1428	98,000	0.04	1.07
Outlet	8.71	552	74.4	5.37	5.08	3.99	∿154	1690	74,500	0.04	1.00
Average	8.86	434	64.0	5.37	6.22	3.58	∿166	1562	87,400	0.04	1.04
Test rig 1 (helium, full pressure, full temperature)											
Nominal	8.86	434	64.0	5.37	6.22 (at 434)	3.58	∿166	1562	87,000	0.04	1.04
Design	9.0	550	100	7.16	7.36 (at 316)			1690			1.00
Test rig 2 (helium, reduced pressure, reduced temperature)											
Nominal	7.37	425	75	5.37	5.08 (at 425)	3.55	∿166	1554	84,400	0.05	1.04
Design	7.37	425	100	7.16	6.22 (at 300)						
Test rig 3 (helium, reduced pressure, low temperature)											
Nominal	5.79	175	64.0	5.37	6.22 (at 175)	2.62	∿185	1245	119,400	0.05	1.10
Design	5.79		100								
Test rig 4 (air, low pressure, low temperature)											
Nominal Inlet	0.66	40	54	5.37	7.37	1.96	193	355	159,000	0.15	1.12
Nominal Outlet	0.44	∿30	75	5.37	5.06	1.90	192	350	168,000	0.21	
Design Outlet	0.4		100	7.16						0.29	

very detrimental since the rods vibrate as a result of parallel flow; therefore, precise frequency matching is not required. This test rig is capable of simulating all important parameters (structural, flow, acoustic, and tribological) and is the ideal prototype test rig.

Test rig 2 represents an attempt at a compromise test. The design temperature has been reduced from 550° to 425°C, and the design pressure from 9.0 to 7.37 MPa. At this temperature and pressure, the coolant density just equals the GCFR outlet density, although higher densities could be achieved at lower temperatures. The advantage of this rig over rig 1 is the cost savings resulting from the lower design requirements. The rig still does an adequate job of modeling nominal conditions, although extremes of temperature could not be reached. For vibration testing (as opposed to prototype testing), this would have little deleterious effects, except that the ratio of structural frequencies to acoustic frequencies would not be quite correctly matched at the higher frequencies.

Test rig 3 is a still further simplified test rig which employs helium at 5.8 MPa and 175°C, conditions which should be more compatible with available gas circulators than those of rig 2. Because of the lower gas temperature, the Reynolds number in the test is about 30% higher than that at the core midplane in the reactor, but this should have only a small, conservative effect. In addition, the sound speed is only 80% of the nominal value, which is significant only for full bundle tests. For these tests, potential concurrence between structural resonances and acoustic resonances is properly simulated, although concurrence between fluctuating fluid forces and acoustic resonances is only simulated at reduced flow velocities.

Test rig 4 is designed to use air at relatively low pressure and temperature as the flow medium. Air enters at 0.66 MPa and 40°C and leaves at 0.44 MPa and about 30°C (expansion of the gas causes it to

cool). Because this rig uses relatively low-pressure, low-temperature air, it is presumably much cheaper to build and operate than any of the helium rigs. The rig does an adequate job of simulating parallel flow and cross flow effects, although acoustic effects are not properly simulated, and no compensating steps can be taken to avoid this. An interesting side effect of the use of relatively low-pressure air is that the ΔP through the assembly causes a density variation with axial position in the assembly which resembles that of the actual assembly. In addition to the lack of correct acoustic simulation, the Reynolds number is about a factor of two too high, which, although probably having a conservative effect, is a greater mismatch than is ideally desirable.

2.2.2.4. Conclusions and Recommendations. The following conclusions and recommendations are made:

1. Because of the complexity of flow-induced vibration phenomena, only testing of full-size components should be attempted. The exception to this is that the use of partial (e.g., 19-rod, 37-rod) fuel or blanket rod bundles is permitted to obtain interim information on the rod vibration response, provided that testing of full-size bundles is ultimately done to verify the adequacy of the interim results.

2. Irrespective of the type of fluid used in the test, the test rig should be designed to achieve a fluid velocity at least as great as the maximum coolant velocity expected to be experienced by the component during its service lifetime. If the temperature of the test fluid is substantially below the expected operational temperature, then additional margin in flow velocity is required to compensate for the resulting increase in structural frequencies. Further additional margin should be provided to allow for possible design changes. In the case of testing of fuel or blanket assemblies, it is desirable that the test rig be designed to

provide a total margin on flow velocity of about 30%, although pumping power limitations may dictate a lower margin for the full bundle tests.

3. The combination of test fluid pressure and temperature must be selected to achieve a fluid density equal to the density of the reactor coolant at the location of the component. In the case of the fuel assemblies, where the reactor coolant density varies considerably from inlet to outlet, the average density should be matched. Higher test densities can always be achieved by lower temperatures, and lower densities can be achieved with reduced pressures. Low-pressure air tests may be able to simulate the density variation quite accurately.

4. Acoustic effects will not be properly simulated if air is used as the test medium or partial fuel assembly bundles are used in helium flow tests. Reduced temperature in helium tests will also affect the acoustics somewhat, although not so severely that analysis and modification of the flow velocity cannot be done to obtain useful data from the test results.

5. Choosing the flow parameters as outlined above will cause moderate mismatches of the Reynolds number if helium is used in the test. This is judged to be relatively insignificant, with the error believed to lie on the conservative side. The Reynolds number mismatch is considerably greater if air is used, although again it is believed that any error will be on the conservative side.

6. Mach numbers with helium are relatively low and adequately modeled irrespective of test pressure or temperature. If air is used as the test medium, there is a Mach number mismatch by a factor of 4 to 5. Although the Mach number in this latter case is still fairly low, it is close to the region where sonic effects would need to be considered and thus represents an undesirable distortion.

7. An air test rig could likely provide usable information on flow-induced vibration of fuel rods at a substantial cost savings over a helium rig. However, additional uncertainty in the results would be incurred, and owing to the significant difference in the sound speeds of air and helium, it is possible that spurious acoustic resonances would be introduced, which would further complicate interpretation of the test results. Such spurious acoustic resonances have already been observed in an air flow test of a model of the inlet portion of a GCFR fuel assembly. Thus, an air flow test is a much less desirable alternative than a helium flow test, although it is an option which, in the interest of getting much needed data at the earliest possible time, could be exercised in the event that budget restrictions do not permit a helium test rig.

8. Of the various helium test rigs considered, the best compromise between cost and accuracy of simulation appears to be rig 3. This test rig employs helium at a pressure somewhat lower than the reactor pressure and operates at a temperature range low enough to be compatible with commercial circulator temperature limits. This flow test rig would do a good job of simulating axial flow-induced vibrations of the fuel rods and cross flow effects; when testing full-size bundles, acoustic effects would be reasonably well simulated. Information obtained with such a rig would be quite representative of the results expected from the actual assembly during actual operation and should reveal any major problems in sufficient time to effect and retest corrective design changes. Although this rig would provide good data for vibration purposes, it would not constitute a proof test of the assembly because of the reduced temperature. It may be possible, however, to add on components (such as a recuperator) to upgrade the rig to full pressure and temperature, which would then make it suitable for prototype testing. This could most likely be done at a relatively modest incremental cost.

2.3. CORE ASSEMBLY STRUCTURAL DESIGN CRITERIA

Work continued on the second phase of the trial application program. To make effective use of analyses from other work efforts, rod-spacer interaction was chosen as the phenomenon for consideration. This is a design area which requires analytic feedback and provides an opportunity to study short-term transient effects such as thermal creep and fatigue damage, unstable crack propagation, and buckling instability. To adequately study the phenomenon, a three-dimensional model of a 180-deg segment of ribbed cladding and a 180-deg segment of spacer was chosen. This model has been successfully generated and contains a sufficient number of elements to assure an accurate solution without overtaxing the computer capabilities. The remaining obstacle is the treatment of the gap. Investigation of the gap element used in some general purpose finite-element codes and new approaches from the literature are under way.

2.4. CORE ASSEMBLY MECHANICAL TESTING

The objective of this task is to conduct mechanical tests of core assembly components and subassemblies to simulate the mechanical loads expected during normal and abnormal reactor operating conditions. The current phase of the assembly mechanical testing program involves testing of fuel assembly components. The preliminary fuel rod-spacer interaction test using single spacer cells and rods was conducted during FY-76. Reproducibility testing of the hexagonal spacer cells was completed, and testing of a new modified hex design continued during FY-77. The design and procurement of blanket assembly components for testing was initiated. Further mechanical tests on grid spacers are being planned and designed, and flow-induced vibration test planning is in progress.

2.4.1. Rod-Spacer Interaction Tests

The purpose of previous rod-spacer interaction tests was to evaluate the effect of interacting forces between the fuel rod and the spacers under

the mechanical and environmental operating conditions expected in the GCFR. The simulated forces are primarily caused by bowing induced by temperature gradients and irradiation-induced swelling. Reactor operational transients cause relative motion of the rod and spacer, resulting in frictional forces. The frictional forces and relative motion cause wear of the rod and spacer pad surfaces. The interadtion force is simulated by a deadweight load on a spacer cell resting on a fuel rod. The calculated loads due to rod bowing have always been predicted to be of the order of 5 N. The results of the reproducibility tests using a reference design hexagonal rod spacer indicate that there is no problem due to these loads.

Fabrication of parts for the second phase of rod-spacer interaction testing has resumed and is 80% complete. In this test phase the rod and spacer are misaligned by a definite amount, resulting in interference and friction forces. The magnitude of the friction or interaction force will be continuously measured, and the wear will be measured after each test is complete.

2.4.2. Spacer Grid Structural Tests

The test fixture designs for the modified hex spacer structural tests have been completed. The tests will be conducted on the static Instron test machine, which is capable of testing to a force of about 4000 N. The static tests will be conducted in two loading directions, namely, (1) in the axial direction to simulate thermal expansion of fuel rods which are stuck onto spacer cells and (2) in the horizontal direction to simulate bowing interaction loading of spacer cells.

2.5. HEAT TRANSFER AND FLUID FLOW TESTING

The test assembly for the inlet nozzle flow pressure drop test has been assembled and is awaiting preparation for testing. The testing phase has been indefinitely postponed until additional funding becomes available.

The parts for the blanket flow control device have been received and are being assembled. Testing of this device will take place at an air flow test facility following the fuel assembly inlet nozzle flow tests.

REFERENCES

2-1. Rowe, D. S., "COBRA-IIC: A Digital Computer Program for Steady State and Transient Thermal-Hydraulic Analysis of Rod Bundle Nuclear Fuel Elements," Battelle Northwest Laboratory Report BNWL 1695, March 1973.

2-2. "Gas-Cooled Fast Breeder Reactor Quarterly Progress Report for the Period August 1, 1977 Through October 31, 1977," DOE Report GA-A14613, General Atomic, November 1977.

2-3. Martelli, A., et al., "Comparison Between Measured and Calculated Pressure and Temperature Distributions in a Roughened Rod Bundle of 19 Rods," Paper presented at Fourth Specialist Meeting on GCFR Heat Transfer, Karlsruhe, West Germany, October 18-20, 1977, Nuclear Energy Agency.

2-4. Huggenberger, M., "SCRIMP, A Subchannel Analysis Computer Code," Swiss Federal Institute for Reactor Research Report TM-IN-635, September 1976.

2-5. Martelli, A., "SAGAPO, A Computer Code for the Thermo-Fluid Dynamic Analysis of Gas-Cooled Fuel Element Bundles," Institut für Neutronenphysik und Reaktortechnik Report KFK 2483 (EUR 5510), August 1977.

2-6. Dalle Donne, M., et al., "BR-2 Bundle Mockup Heat Transfer Experiments," Nucl. Eng. Design 40, 143-156 (1977).

2-7. Rohsenow, W. M., and J. P. Hartnett, Handbook of Heat Transfer, McGraw-Hill, New York, 1973.

2-8. "Gas-Cooled Fast Breeder Reactor Quarterly Progress Report for the Period November 1, 1976 Through January 31, 1977," ERDA Report GA-A14240, General Atomic, February 1977.

2-9. Arwikar, K. J., "Thermal and Hydraulic Performance Study of Closely Spaced Wire-Wrapped Tube Bundles with Internal Heat Generation," M.S. Thesis, University of California, Santa Barbara, November 1977.

2-10. "Gas-Cooled Fast Breeder Reactor Quarterly Progress Report for the Period November 1, 1975 Through January 31, 1976," ERDA Report GA-A13815, March 22, 1976.

2-11. Wheeler, C. L., et al., "COBRA-IV-I: An Interim Version of COBRA for Thermal-Hydraulic Analysis of Rod Bundle Nuclear Fuel Elements and Cores," Battelle Northwest Laboratory Report BNWL-1962, March 1976.

2-12. Thompson, W. I., "CALIOP - A Multichannel Design Code for Gas-Cooled Fast Reactors," General Atomic, unpublished data.

2-13. Rucker, R., "GCFR Demo Axial Power and Fast Flux Distributions," General Atomic, unpublished data.

2-14. Nuclear Systems Materials Handbook, Hanford Engineering Development Laboratory (TID-26666).

2-15. Heisser, D. J., "300 MW(e) Fuel Assembly Duct Dilation, Hexagonal vs Cylindrical," General Atomic, unpublished data.

3. PRESSURE EQUALIZATION SYSTEM FOR FUEL (189a No. 00582)

3.1. CORE ASSEMBLY AND PES SEALS

The GCFR core assemblies are hexagonally shaped components except for the upper cylindrically shaped inlet nozzle. The inlet nozzle is the means by which the assemblies are located and retained within the GCFR core during operation. The nozzle is inserted from below and is securely clamped at the conical transition region to mating surfaces on the core support grid plate. A seal must be provided in this inlet nozzle region to limit the amount of coolant which can bypass the core by means of the annulus between the inlet nozzle and the grid plate penetration. This seal must be capable of operating within prescribed leakage limits at the pressure differential between the inlet and outlet coolant plenums. The effectiveness of the seals over the life of the core is uncertain, not only because each assembly may be rotated several times over its life, but also because the seals must be effective in a high-purity, high-temperature helium environment while subject to mechanical, vibrational, and thermal effects. Most of the uncertainties are expected to be resolved in a two-part program: (1) a materials screening test program for the study of static adhesion of simulated fuel assembly and grid plate parts clamped together and (2) leakage tests of fuel assembly and vent connection seals to the grid plate. Current progress in these activities is described below.

3.1.1. Static Adhesion Tests

The first set of static adhesion tests was conducted in FY-75 on 316 and 304 stainless steel at various matching cone angles, contact loadings, and surface finishes. This was followed in FY-76 by a second set of tests using materials including couples of Inconel 718 - 316 stainless steel, Inconel 718 - 304 stainless steel, and 304-316 stainless steel.

The third test set includes adhesion tests of metal samples coated with hardened surface materials. The simulated grid plate materials are 316 or 304 stainless steel and Stellite-6B tested against simulated fuel assembly samples of 316 stainless steel, Stellite-6B, and coatings of chromium carbide, chromium oxide, aluminum oxide, and Stellite-6. The conical surface angle is limited to a 60-deg included angle (30-deg half-cone angle), and the static load is 1,333 N (simulating a 13,330-N clamping load for a full-size assembly). The test furnace and gas system are being set up in the mechanical test laboratory. All the coated test samples have been received and identified and are ready for assembling on the sample holders.

3.1.2. Fuel Assembly Ring Seal Leakage Tests

An alternative to the conical metal-to-metal core assembly seal design being developed uses piston rings as static sealing members. The test equipment, test grid parts, and core subassembly parts from the conical seal test have been modified, and ring seal tests are in progress. These tests include two ring designs provided by two US vendors (Stein and Dover) and one German design [Kraftwerk Union (KWU)]. The KWU design is being fabricated by KWU and two US vendors for performance test comparisons. The rings manufactured by KWU were from Inconel 718 and were chrome plated on the sealing surfaces. Leakage measurements of the KWU piston ring seal design were completed, and the test results are given in Ref. 3-1.

The KWU design piston rings manufactured by Dover and Stein were tested at room temperature; the test results are shown in Figs. 3-1 and 3-2. The performance of the Dover rings was unsatisfactory, and the rings exceeded the specified leakage limit of 48 liters/min helium bypass leakage at all pressure differentials. The Stein rings performed well within the leakage specification limit for all pressure differentials. This is typical of the consistently good performance of the Stein seal rings (Ref. 3-2).

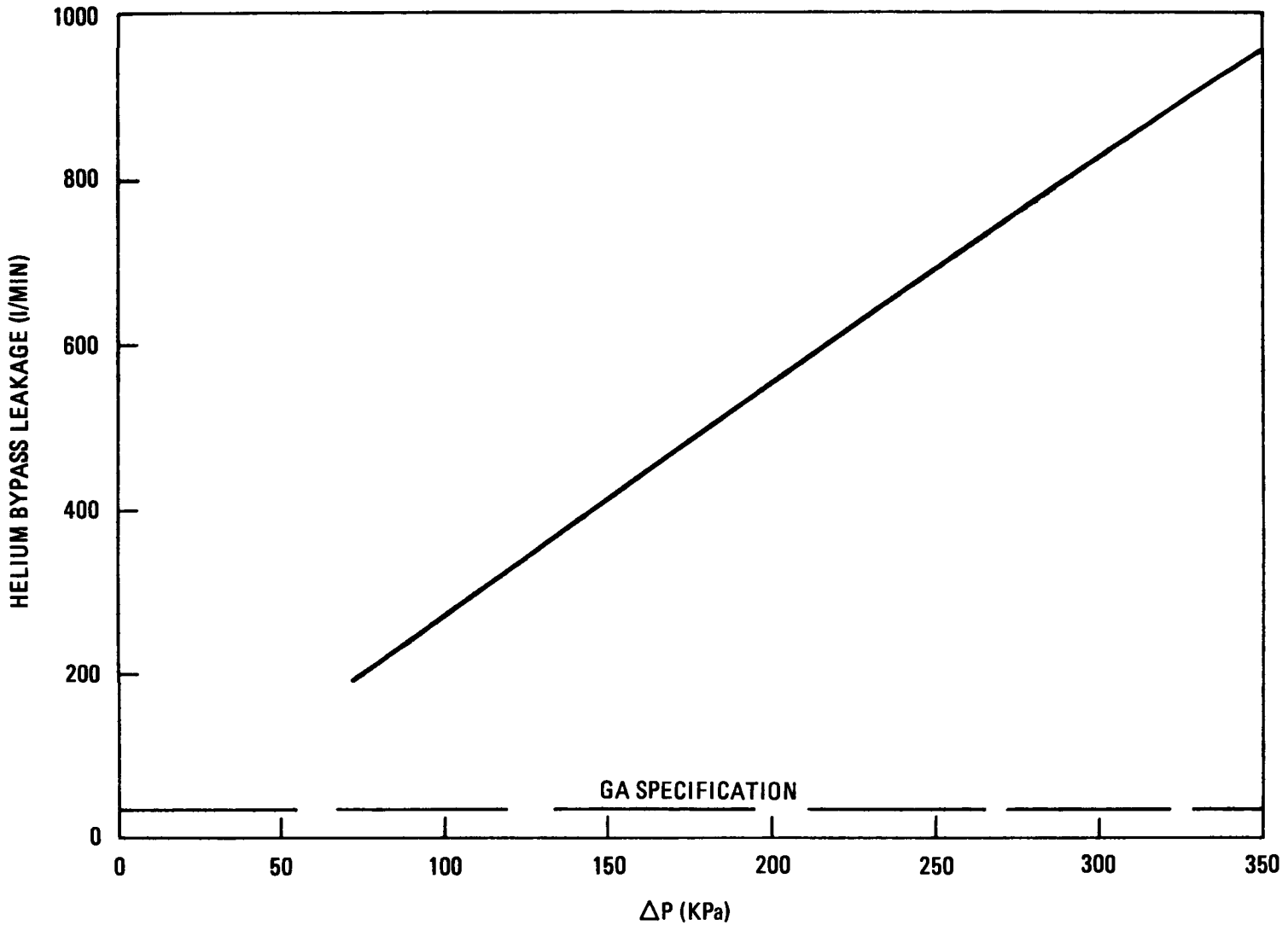

Fig. 3-1. Pressure differential at room temperature for KWU ring design manufactured by Dover

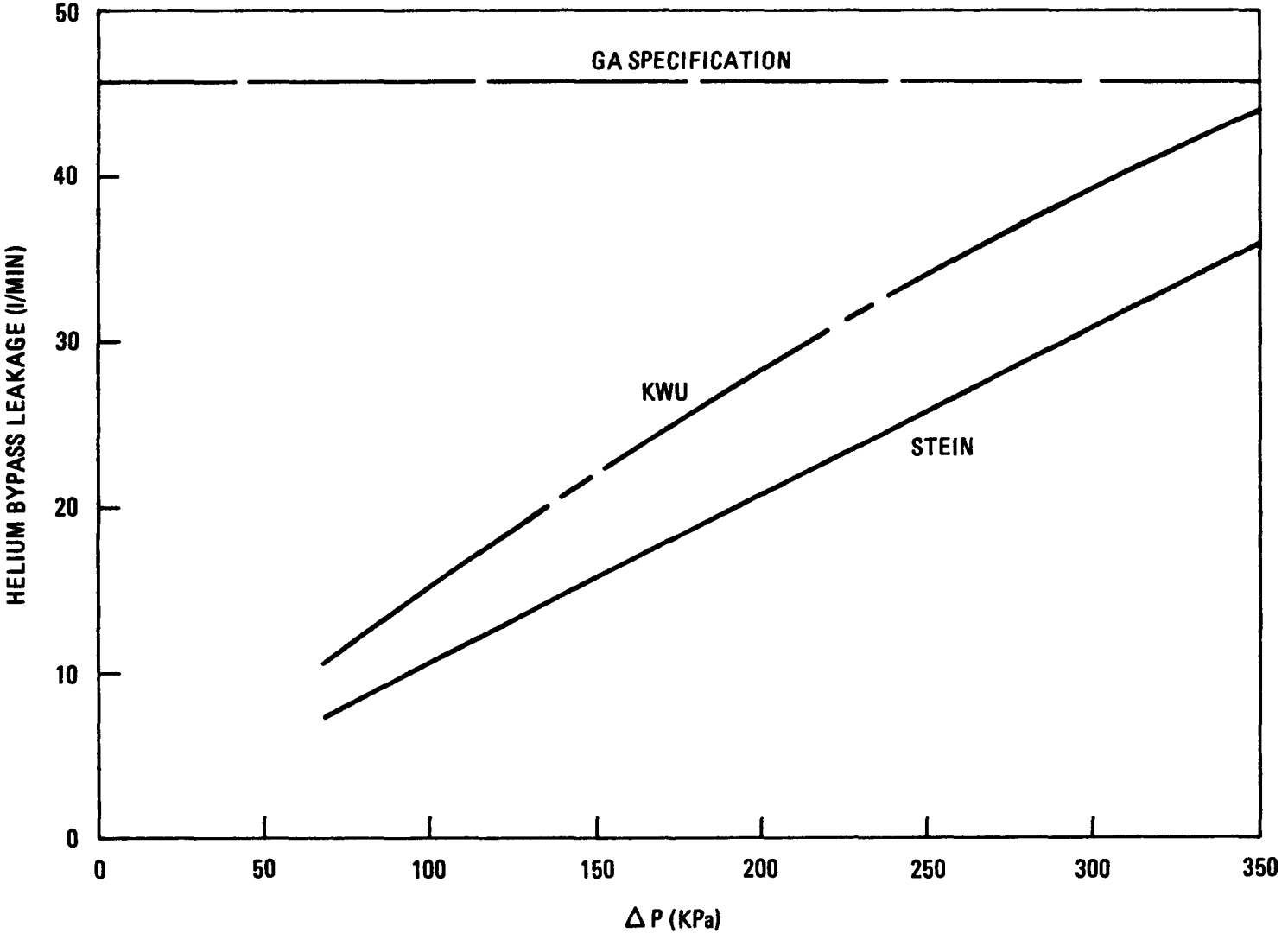

Fig. 3-2. Pressure differential at room temperature for KWU ring design manufactured by Stein

One feature of the KWU seal ring design is that a high spring force is created when the ring is forced into the inlet nozzle. It is the resulting small annular clearance which limits the helium bypass leakage. However, this feature results in high friction force, and very high axial forces have to be applied to remove the assembly from the core. By contrast, the simple single-piece ring design by Stein is easily removed, because its sealing is accomplished by the core ΔP and it has a very low radial spring force.

In summary, the simple low-cost single-piece Stein seal ring design has shown superior overall performance and has the following advantages:

1. The single-piece design should result in lower manufacturing costs as compared with the five-piece design of Dover and KWU.

2. The leakage rate was consistently lower than the specification by a factor of five or more (Ref. 3-2). By contrast, the Dover and KWU designs sometimes exceeded the specification.

3. The cost of the Stein ring is a factor of 30 lower than the KWU manufactured cost.

4. The Stein ring permits easier removal of the core assemblies from the grid plate.

The only deviation of the Stein ring from the GCFR design criteria is that it does not have the retainer ring for holding a broken seal ring in the nozzle assembly. It is recommended that further design work be conducted to resolve the following question: is the retainer ring really necessary for the Stein seal ring design? In the KWU design, the ring has a necessary dual function (broken ring retention and precompression of the ring to permit installation in the nozzle) which is not required in the Stein design. If the retainer ring is necessary, then Stein should be requested to redesign its ring.

3.2. ANALYSIS, MODELS, AND CODE DEVELOPMENT

During the last quarter (Ref. 3-2) it was shown that the thermal network code SINDA (Ref. 3-3) is applicable to transient PES flow analysis. During this quarter the modified code SINDA/PES was used in a transient analysis of the GCFR fuel rod, and the development of this code was continued.

The SINDA/PES model of the GCFR fuel rod is shown in Fig. 3-3. The open circles are so-called diffusion nodes which represent the volumes of the gas shown opposite, and the solid circles are so-called arithmetic nodes which represent junctions without volumes. The arrows denote flow lines, and node 13 is a boundary node. One intent with this model is to determine the equivalent volume and resistance of a lumped parameter representation of the fuel rod. To this end, a step depressurization of node 13 from 9 to 0,18 MPa was used as a boundary condition. The pressure response of several nodes in the model is shown in Fig. 3-4. It can be seen that the pressures near the bottom of the fuel rod respond much more slowly than those near the top. The reason for this difference in response is the high flow resistance of the blanket region of the rod. By comparing the pressure response in Fig. 3-4 and a similar flow response with a simplified model, the equivalent volume and resistance of the rod can be obtained. These dynamic characteristics will then be used in a model of the whole fuel assembly. Further analysis is required to evaluate the response of the fuel rod to GCFR accident transients.

The development of the SINDA/PES code continued with programming of the compressible flow equation derived in Eq. 3-6 of Ref. 3-1. A subroutine GF was written to compute the mass velocity in each line, given the end conditions of the line. Figure 3-5 shows the mass velocity G (relative to the line outlet sonic mass velocity) as a function of the relative line length L, with the end point pressure ratio P_a as a parameter. At a pressure ratio of two, the flow is choked at the outlet for a relative line length of one or less (G = 1). At a pressure ratio of

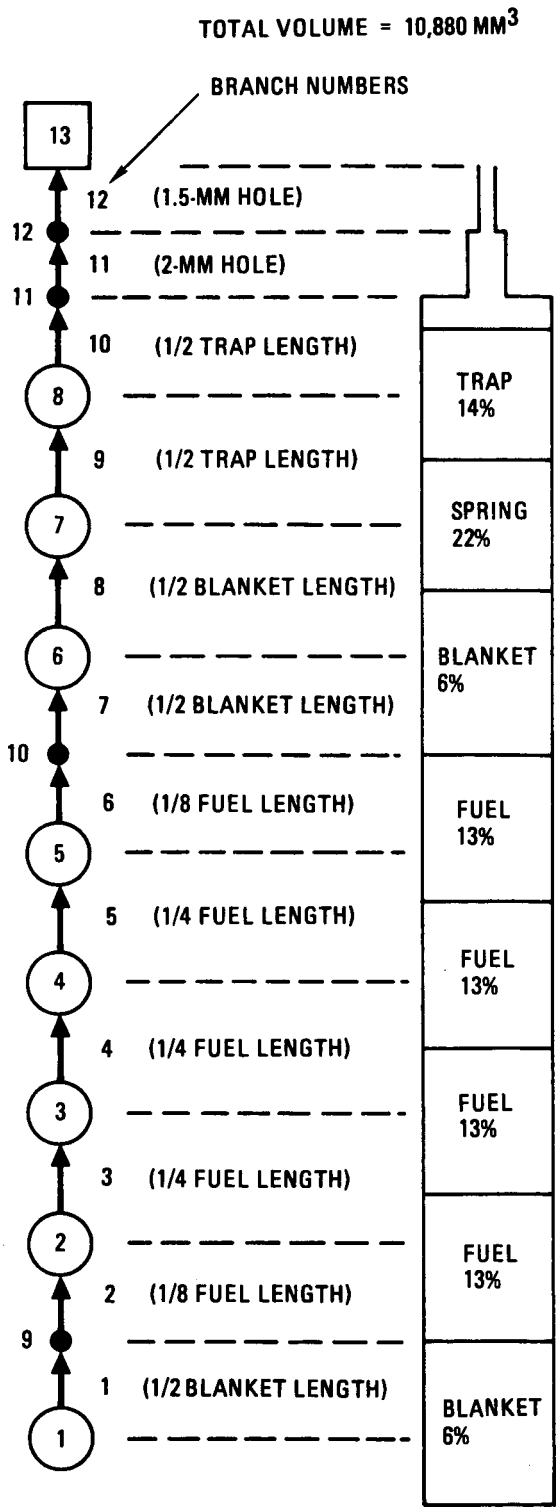

Fig. 3-3. 13-node SINDA model of GCFR fuel rod

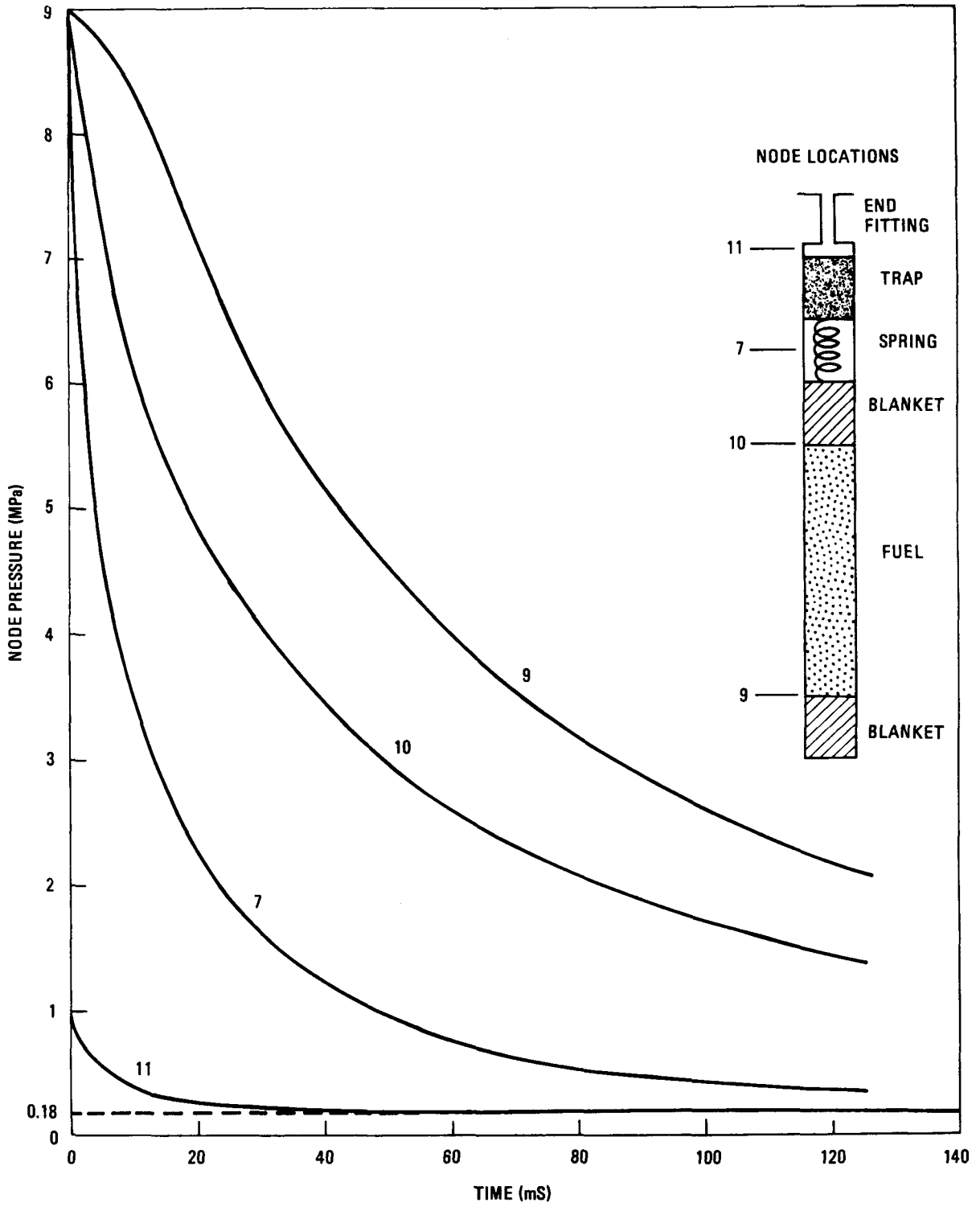

Fig. 3-4. Rod pressure response to step depressurization of boundary

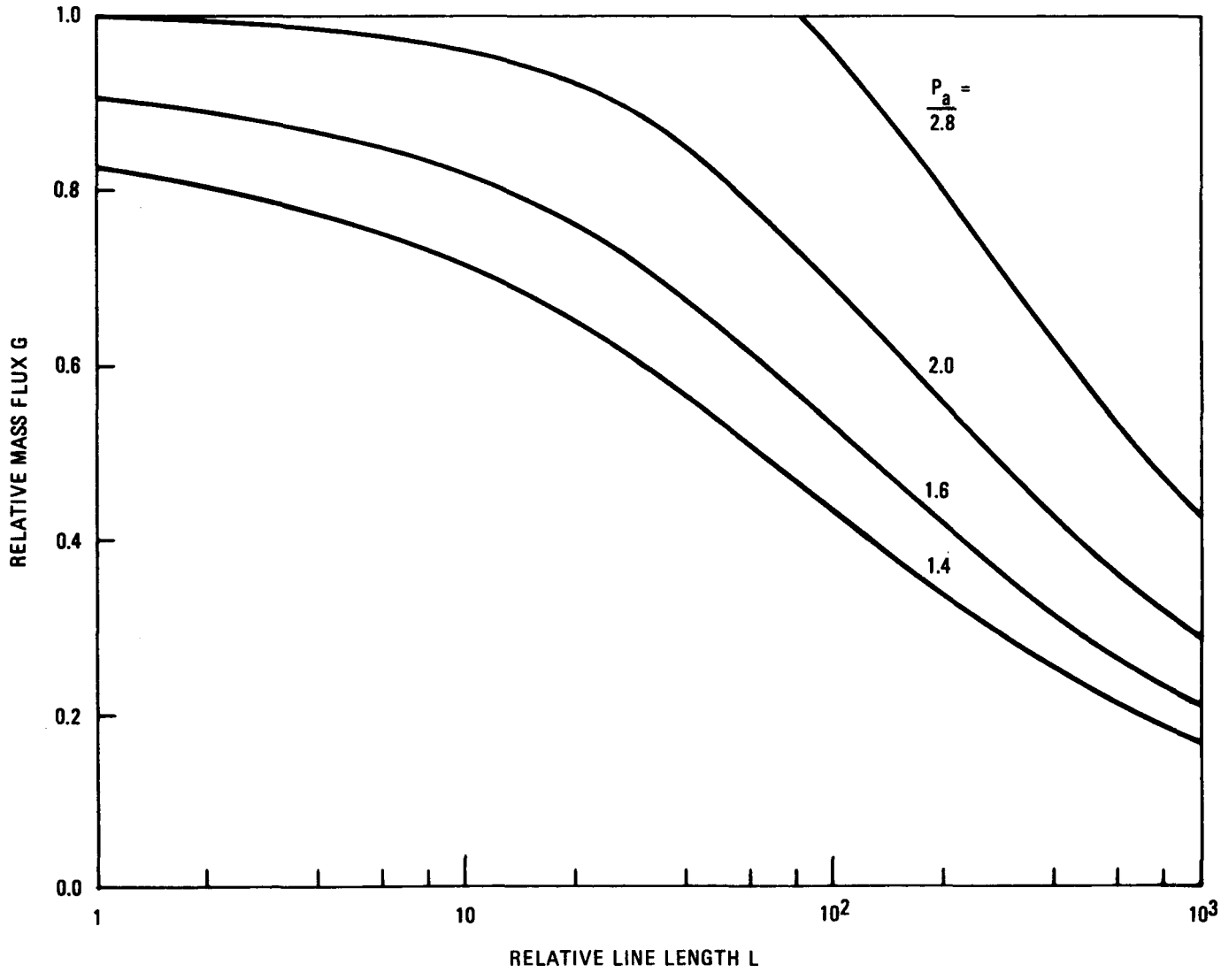

Fig. 3-5. Variation of mass flux with branch length

2.8, the flow remains choked until $L \geq 100$. The subroutine GF, which includes choked flow calculation, is currently being included in the SINDA/PES code.

3.3. PLATEOUT AND PLUGGING

Volatile fission products, particularly cesium and iodine, vented from the core assemblies and produced by gaseous precursor decay of fission products vented from the core assemblies, may plate out on the walls of the monitor lines. These fission products are swept through the monitor lines into the helium purification system (HPS) traps by helium entering at the core subassembly vent connections. Accumulation of deposited material may constrict the sweep gas flow passages and could potentially lead to plugging of the lines. The conditions under which plateout and plugging could occur in the GCFR, the means of minimizing or eliminating them, and the methods for removing deposits are being investigated. A small high-pressure loop has been built and is being used for this purpose. Development of components for injection, control, and measurement of impurities in the helium (i.e., H_2 and H_2O) and sources for simulating venting of the volatile fission products and their compounds is being examined.

Equipment failures (leaking valves, malfunction of two cryogenic baths) impeded experimental progress on the high-pressure loop during this quarter. The necessary repairs have been made, and the system has once again been readied for introduction of cesium vapor into the test segment.

3.4. FISSION PRODUCT RELEASE AND TRANSPORT

The purpose of this subtask is to obtain experimental data on the interdiffusion and gas phase and the surface back diffusion of gaseous and volatile fission products. The diffusion coefficient data will be used to validate or improve the SLIDER code (Ref. 3-4), a one-dimensional model for fission gas diffusion transport (including radioactivity decay).

Surface transport and back diffusion data will be used to establish a model for predicting the importance of these mechanisms to contamination of the reactor coolant system.

Figure 3-6 illustrates the temperature dependence of the diffusion coefficient for Kr-85 obtained experimentally in the open tube diffusion apparatus at high helium total pressure (8.7 MPa). The slope of the line gives a temperature exponential coefficient of 1.588, i.e., $D = D_o(T/T_o)^{1.588}$. This should not be compared with the theoretically predicted exponent 3/2, or 1.5 (Ref. 3-5), since it is known that for diffusing gas couples (with one gas being helium), the measured exponents fall between 1.5 and 2.0. After some study of the literature (Ref. 3-6), a value of 1.6 was selected for GCFR calculations. The measured value compares well with the selected value.

Diffusion experiments carried out in an apparatus containing a precision-ground stainless steel rod insert (to simulate the annular diffusion path in the blanket region of a GCFR fuel rod) have been successfully performed at helium pressures of 0.45 to 0.48 MPa. Problems with rod movement were eliminated by addition of a tab to the rod support shaft, as described in Ref. 3-1.

Figure 3-7 illustrates the Kr-85 diffusion coefficient temperature dependence for the rod insert case. The slope of the line is 1.580, which is in excellent agreement with the value obtained for the open diffusion tube experiments discussed above. Further experimentation and a careful error analysis of the observed temperature exponent will enable the assessment of the confidence level for these values. Problems arose with the application of the SLIDER code to simulate the diffusion behavior for the rod insert experiments. However, the source of the problem appears to have been found, and the requisite calculations to verify the solution are being performed.

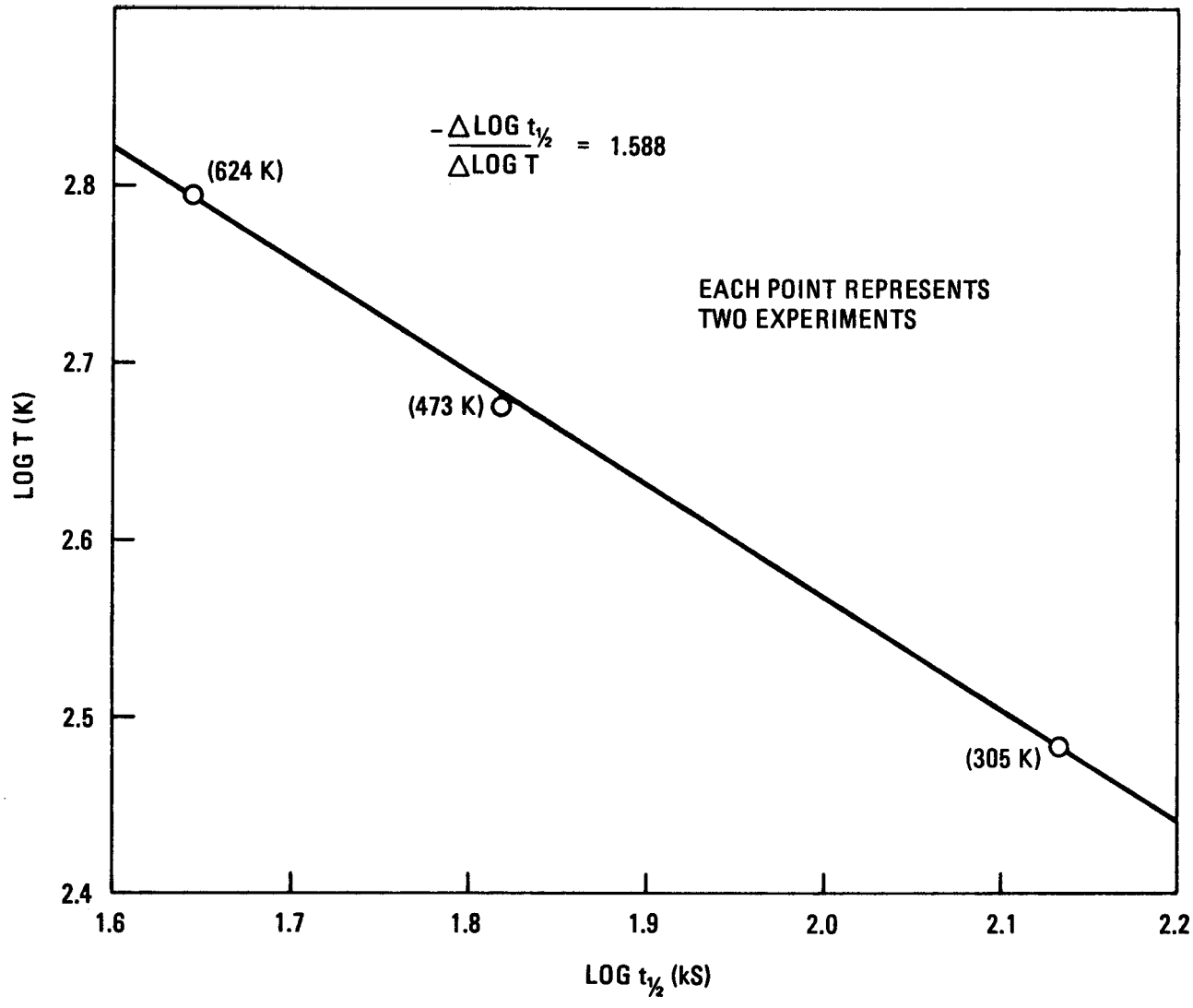

Fig. 3-6. Temperature dependence of diffusion coefficient for Kr-85 open diffusion tube (helium pressure = 8.7 MPa, $t_{1/2} \propto 1/D$)

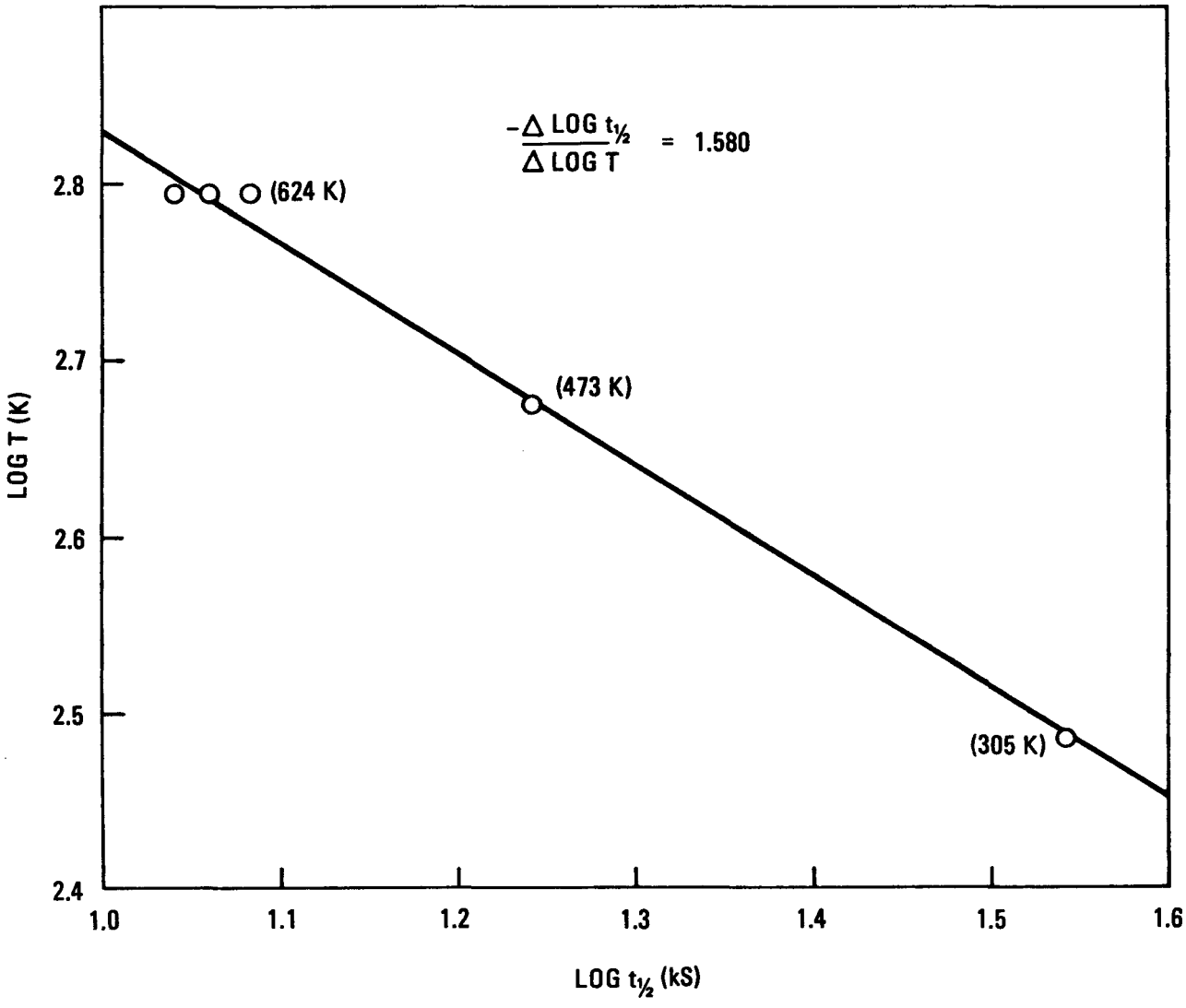

Fig. 3-7. Temperature dependence of diffusion coefficient for Kr-85 rod-loaded tube (diametral gap = 1.27 μm, helium pressure = 0.45 to 0.47 MPa, $t_{1/2} \propto 1/D$

3.5. MONITOR STATION AND INSTRUMENTATION

3.5.1. GCFR Power Plant Monitor Stations

Research and development work on the monitor stations for the proposed GCFR demonstration plant and subsequent commercial GCFR power plants is being conducted. Design studies done in FY-77 (Refs. 3-1, 3-2, 3-7) have indicated that the complexity of the monitor stations can be greatly reduced and design and equipment supply problems greatly simplified if it is possible to use a small gamma photon detector with a large dynamic range ($>10^5$) and a capability to resolve photo peaks comparable to that of an NaI(Tl) detector in the energy range between 80 and 500 keV.

CdTe(In) and CdTe(Cl) semiconductor detectors are also being evaluated. A CdTe(In) detector was evaluated and found to be unacceptable (Ref. 3-1). During this quarter a CdTe(Cl) detector was experimentally evaluated. A 2-mm cube detector supplied by Radiation Measuring Devices, Incorporated, was bench tested, and initial tests with the detector and preamplifier between 273 and 333 K showed marked temperature sensitivity. In subsequent tests it was shown that the preamplifier, which was not temperature compensated, was responsible for this sensitivity. The temperature of the detector was shown to affect the count rate at about 20% kHz by 1% to 2% over the temperature range 273 to 328 K. There was no shift in the photo peak energies and only slight peak broadening over the temperature range. In general, the detector behaved according to the published data provided by the vendor. Thus the CdTe(Cl) semiconductor appears to be suitable for the GCFR monitor station application.

3.5.2. Monitors for Irradiation Tests

A monitor station is being designed for use on the helium loop at Mol (HELM), where GCFR pressure-equalized and vented 12-rod fuel bundles are being irradiated and the proposed GB-11 sweep gas irradiation experiment, will be run. Complementary and more prototypical data will be added to that

previously obtained using a Ge(Li) monitor station on the sweep gas line of irradiation capsule GB-10 at the Oak Ridge Reactor (ORR).

During this quarter it was decided to provide separate monitors for the HELM tests and the GB-11 experiments. The HELM tests are already in progress, which limits the equipment that can be installed to monitors which do not require breaching of the secondary containment or the monitor line carrying the vented radioactive gases from the fuel bundles to the liquid-nitrogen-cooled charcoal traps.

A CdTe(Cl) detector has been selected to provide on-line measurement of the fission gas isotopes and further qualification data on its application to GCFR monitor stations. A 2 x 2 x 7 mm CdTe(Cl) detector has been received and will undergo testing prior to incorporation into the HELM monitor station. Pressure, temperature, flow rate, and reactor and test fuel bundle power will be provided to the monitor station by existing HELM instrumentation. A location has been selected at HELM for the monitor station detector, electronic supplies, and data reduction electronics. Final approval will be required from the Belgian safety authorities before the monitor station is accepted for installation. Drawings, circuit diagrams, and equipment descriptions are in preparation for this purpose. This work will continue for the next two quarters, and delivery of the HELM monitor station is scheduled for mid-1978. The monitor station for monitoring the simulated leaks in the fuel rods of the GB-11 sweep gas irradiation experiment will be designed and planned along with GB-11 experiment planning. The conceptual design of the experiment has just begun and it is expected that the increased understanding of fuel and monitor station performance in the HELM tests will contribute to better designs for the GB-11 experiment and monitor station.

3.6. PES PROGRAM PLANNING

There was no activity on this subtask during this quarter.

REFERENCES

3-1. "Gas-Cooled Fast Breeder Reactor Quarterly Progress Report for the Period August 1, 1977 Through October 31, 1977," DOE Report GA-A14613, General Atomic, November 1977.

3-2. "Gas-Cooled Fast Breeder Reactor Quarterly Progress Report for the Period May 1, 1977 Through July 31, 1977," ERDA Report GA-A14492, General Atomic, August 1977.

3-3. Smith, J. P., "SINDA User's Manual," TRW Systems Group Report 14690-H001-R0-00, April 1971.

3-4. Jadhov, K. B., and B. W. Roos, "SLIDER, A Fortran-V Program for the Computation of Release of Fission Products from One-Dimensional Multi-Layered Fuel Configurations," USAEC Report GA-8566, Gulf General Atomic, August 1969.

3-5. Hirschfelder, J. O., C. F. Curtiss, and R. B. Bird, Molecular Theory of Gases, Wiley, New York, 1964, p. 539.

3-6. Lindgren, J. R., et al., "Planned Thermal Irradiation of Manifolded-Vented $(U,Pu)O_2$-Fueled Rod in ORR Capsule P-9," USAEC Report GA-9896, Gulf General Atomic, March 15, 1970, p. 86.

3-7. "Gas-Cooled Fast Breeder Reactor Quarterly Progress Report for the Period February 1, 1977 Through April 30, 1977," ERDA Report GA-A14358, General Atomic, May 1977.

4. CORE ASSEMBLY DESIGN VERIFICATION (189a No. 00582)

4.1. CORE FLOW TEST LOOP PROGRAM

A series of out-of-pile tests will be performed to (1) demonstrate the ability of the GCFR fuel, control, and blanket assembly designs to meet design goals and (2) verify predictions of analytical models which describe design operation and accident behavior. The emphasis of the tests will be on obtaining thermal-structural data for steady-state, transient, and marginal conditions using electrically heated rod bundles in a dynamic helium loop. Final margin tests will be progressively extended to the highest possible temperature until the heater elements fail. The core flow test loop (CFTL) program plan (Ref. 4-1) describes the requirements for the test program to be conducted in the CFTL, which will be constructed and operated by Oak Ridge National Laboratory (ORNL). The principal work accomplished during this quarter was as follows:

1. An updated draft of the CFTL management plan was reviewed. This plan officially creates the CFTL coordinating committee, which has the responsibility for determining and resolving CFTL issues. The committee members represent GA, Helium Breeder Associates (HBA), and ORNL.

2. The computerized task document index was expanded to over 130 entries during its trial period. Its usefulness has been demonstrated, and it is now entering the implementation phase.

3. The general format and form of the data to be sent to GA for each CFTL test run were identified and transmitted to ORNL.

4. The design for the initial model of the fuel control assembly was completed.

5. GA has continued to maintain close liaison with ORNL by reviewing its draft issue of the CFTL system design description, supporting its efforts to produce heater rods without swagging, and planning review-coordination meetings.

4.1.1. Program Planning

4.1.1.1. Utility Committee Review. One of the results of the GCFR commercialization study (Ref. 4-2) was the development of an updated GCFR demonstration plant schedule which included the identification of "high technical risk" (i.e., high priority) research and development activities. The CFTL program has been designated a high technical risk activity, indicating that results from the CFTL are required as early as possible for the timely verification and/or modification of the core assembly designs.

4.1.1.2. Program Management Planning. The CFTL management plan and ORNL budgeting and scheduling of the CFTL were reviewed by representatives of DOE, HBA, ORNL, and GA. It was agreed to include HBA as a member of the CFTL coordinating committee. A review will be made by GA of the 1974 CFTL program objectives to determine their applicability and/or whether they need redefinition. GA will also review the latest version of the management plan submitted by ORNL, and DOE agreed to specify HBA's role in the GCFR program.

4.1.1.3. Task Document Index. As the CFTL program has expanded, the communication between ORNL and GA has expanded and the documentation has greatly increased. To systematically organize and recall documentation on a particular activity, a computerized task document index has been created. This index includes the following document information: index number,

report number, author, title, source type, status, approval level, cross references, activity area key words, specific activities key words, and brief comment. An important feature is the identification of obsolete documentation. The index has now completed an initial definition and trial period with the entry of over 130 documents and is now in the implementation phase, during which all new documentation will be recorded.

4.1.1.4. ORNL Work Effort. The wide range of research and development activities and the many subtasks generic to several tests at ORNL have tended to obscure the specific activities needed as a minimum to support CFTL testing. Work effort descriptions were requested from ORNL by DOE and are in review. It will be recommended that ORNL keep these work effort descriptions current and expand them to include objectives, milestones, priorities, and operating budgets. Corresponding GA information is contained in subtask work plans and task summaries.

4.1.1.5. Quality Assurance Program. Coordination of quality assurance planning by GA and ORNL is part of a continuing program. GA requested that ORNL ensure that design verification testing is accomplished in accordance with the requirements of 10CFR50, Appendix B. ORNL stated that its formal quality assurance program, which is applied to all GCFR research and development work, is fully responsive to the intent of 10CFR50, Appendix B.

The use of CFTL data to support GCFR licensing submittals was discussed, and to ensure that the quality assurance program associated with this data is acceptable to the Nuclear Regulatory Commission (NRC), ORNL agreed to consult with NRC regarding the adequacy of the CFTL quality assurance plan. Although no official generic approval has been received, ORNL believes that by precedent, national laboratory data are acceptable to NRC.

4.1.2. Test Analysis and Prediction

4.1.2.1. Data Format. The general format and form of data to be sent to GA by ORNL for each CFTL test were identified and transmitted to ORNL. GA is requesting the following:

1. Type of data. The data sent to GA should be in corrected or reduced (not raw) form and should be in the International System of Units (SI). ORNL should supply one complete data set for each steady-state condition and will define steady-state conditions for a given test, i.e., data drift limits. ORNL should supply one complete data set for each transient test condition and will determine the total time span, i.e., initial steady-state, transient, and terminal conditions, for a given run.

2. Data form. Experimental data sent to GA should be on magnetic tape and should be self-contained and identified so as to be of direct use to the reader. GA will produce a hard copy of the tape and will use the data for computer analysis and comparison.

3. Data format. The format will include the experimental data and general information which makes it easy to identify the test loop, test section, and other pertinent design features. The format should consist of general information and test identification as follows.

   a. General information.

      (1) Program title.
      (2) Test procedure number.
      (3) Test specification number.

(4) Test loop drawing number.
(5) Test bundle assembly drawing number.
(6) Test instrumentation drawing numbers (loop and bundle).
(7) Fuel rod simulator drawing number.

b. Test identification.

(1) Date.
(2) Test title.
(3) Test objective.
(4) Test number.
(5) Test conditions desired.
(6) Fuel rod simulator power distribution.
(7) Bundle power distribution.
(8) Bundle description.
(9) Thermocouple location.

c. Experimental data. Detailing of the specific experimental data will be accomplished after specification of the test instrumentation for each test model.

d. Auxiliary data.

(1) Calibration data.
(2) Drift data for steady state.
(3) Instrument failure.

4.1.2.2. Application of COBRA Code. To firmly establish the design of the 37-rod CFTL test bundle, detailed thermal-hydraulic analysis has been initiated using the COBRA (Ref. 4-3) code. In preparing the required geometric input to the code, emphasis has been placed on the design of the corner hanger rod and adjacent fuel rods. As an initial attempt to

obtain nearly uniform helium temperatures in the corner region, a circular hanger rod diameter has been chosen such that the gaps between the hanger rod and adjacent fuel rods are equal and virtually identical to the fuel rod to duct wall gap. If, after utilizing several hanger rod diameters, the required degree of uniformity is not obtained, a shaped (other than circular) hanger rod will be investigated.

4.1.2.3. Test Prediction and Instrumentation. Instrumentation requirements, accuracy, and calibration procedures for the CFTL experiment are being evaluated. Various methods are being investigated for calibrating the fuel rod simulator thermocouples to obtain the maximum quantity of experimental data for comparison with predictions of the COBRA code, including (1) isothermal in-place temperature calibration of rod thermocouples (without heat generation) and (2) in-place calibration of rod thermocouples with heat generation to obtain heat flux as a function of the temperature difference between the internal thermocouple and the cladding wall (outside).

4.1.3. Test Specifications

The scope of the total CFTL test specifications, which covers the entire CFTL program, was issued and contains the following:

1. CFTL priority one test verification matrix.

2. CFTL priority one test series summary; type and number of tests.

3. Quantity of fuel and blanket rod simulators required for CFTL test bundles.

4. Tables 1 through 17 of the preliminary series (F1) test specification (37-rod bundle); tabulated test conditions.

5. Tables of test conditions for the F-2 series (61-rod fuel bundle).

6. Tables of test conditions for the F-3 series (91-rod fuel bundle).

7. Tables of test conditions for the C-2 series (90-rod control bundle).

8. Tables of test conditions for the B-1 series (61-rod control bundle).

The purpose of this information is to assist in continued program planning by GA and ORNL.

4.1.4. Test Bundle Design and Fabrication

Drawings of the control bundle assembly and components have been issued and sent to ORNL. Figure 4-1 shows the assembly drawing. Six pieces of GCFR quality fuel rod tubing were sent to ORNL for the purpose of producing prototype fuel rod simulators by a new method which does not involve a swagging operation, as is the current practice in fabricating fuel rod simulators. The potential advantages of this method include fewer rejects, shorter fabrication time, less handling, and greater reliability.

4.1.5. Liaison

The following major topics were reviewed:

1. Work plans.

    a. Tentative ORNL schedule.
    b. GA work status and major milestones.
    c. European information to ORNL via GA.

2. Structural analysis and measurements.

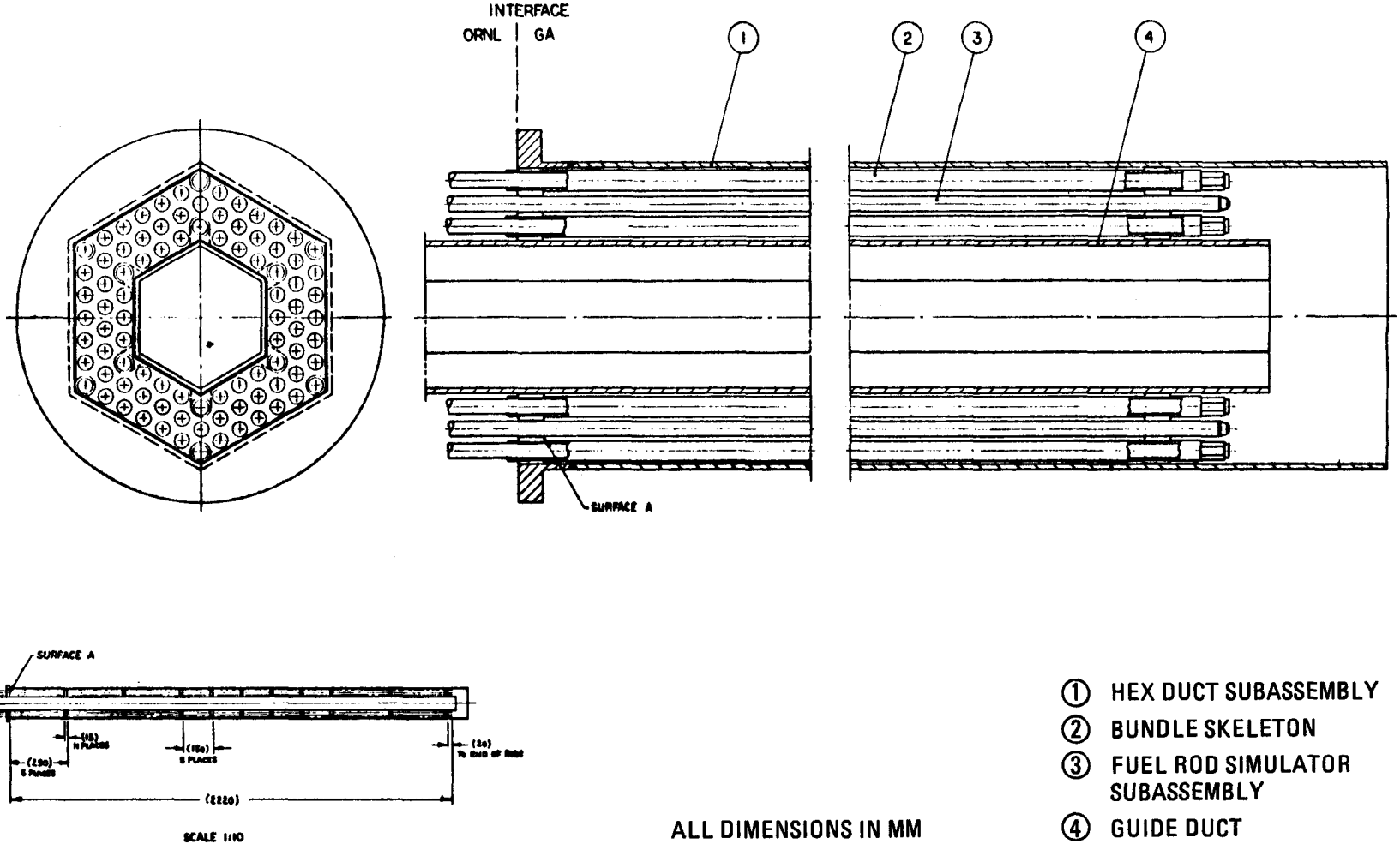

Fig. 4-1. 90-rod control bundle test assembly

3. Areas of concern (ORNL).

   a. Current reference test model designs versus GCFR alternative designs.

   b. Flow entrance region.

   c. Proposed use of less chemically active gas to simulate containment air in gas during depressurization.

   d. Inlet and outlet gas temperature measurements.

   e. Fuel rod simulator (heater rod) fabrication.

   f. Sizing of helium purification system.

   g. Thermocouple measurements.

4. Conceptual design. The reference heater element material is Nichrome-V, and the reference thermocouples are type K in an Inconel sheath.

Drafts of the CFTL management plan and the system design description were reviewed by GA, and proposed changes and comments have been sent to ORNL. In addition, GA responded to ORNL comments on the test specification for a 37-rod bundle of the fuel assembly model (Ref. 4-4).

4.2. GCFR PROTOTYPE ASSEMBLY TEST PROGRAM

Program planning for testing of the prototype core assemblies is continuing. The tests will be conducted on full-size core assemblies to ensure that they meet design qualification requirements prior to fabrication of the demonstration plant initial core. The prototype assemblies

will be the same as the GCFR demonstration plant core assemblies except that the PuO_2-UO_2 fuel in the GCFR fuel rods will be simulated by depleted UO_2. The assemblies will be subjected to maximum GCFR helium flow conditions to closely simulate the reactor core environment; however, there will be no radiation. One assembly of each type (fuel, control, and blanket) will be subjected to the equivalent of approximately one year each of reactor operation in a hot helium test loop. The helium test loop temperature will be maintained external to the test section, since fuel rod heating will not be simulated in these tests.

Review of the test loop facility options for the ptototype tests is continuing. These options include upgrading of the proposed GCFR core assembly helium flow test rig; a modification of the EBOR loop at Idaho Nuclear Engineering Laboratory (INEL); use of the CARMEN-2 loop at Saclay, France; and development of a new facility which most likely will be situated in Germany. EG&G has completed a preliminary proposal based on Ref. 4-5 for conducting the prototype tests in the modified EBOR loop. Recent information indicates that some of the EBOR loop components have been removed from the EBOR facility and have been either disposed of or placed in storage. This action necessitates a reappraisal of the EG&G proposal for using the EBOR facility for the prototype tests. One of the items removed from the facility is the main helium circulator/electric motor combination. The EG&G proposal included the suggestion that this blower, which failed during the last operation of the loop in 1966, be inspected, refurbished, and checked out by the blower manufacturer. Lack of funding has prevented this effort.

Discussions pertaining to the economic and technical feasibility of conducting the prototype tests in the CARMEN-2 loop have continued with representatives of the Commissariat à l'Energie Atomique (CEA). GA requested that the French (1) provide feasibility and cost information for testing of the prototype assemblies in the CARMEN-2 loop with minimal changes to the loop and (2) determine if the possibility of upgrading the

loop to provide the higher pressure desired for the prototype tests. The French indicate that with minimal loop changes, the CARMEN-2 loop can provide a helium flow of 8 kg/s with a test assembly ΔP of 290 kPa at 75 bars and 550°C. With additional changes, particularly upgrading of the recuperator/reheater and test vessel, the loop would meet the desired prototype test condition requirements of 8 kg/s with a ΔP of 290 kPa at 90 bars and 450°C.

A feasibility study on upgrading of the proposed GCFR core assembly helium flow test rig to permit prototype testing has been initiated. The proposed helium flow test rig (which will be located in the US) will be capable of relatively low pressure and temperature test conditions and will be used for design evaluation testing of full-size core assemblies. The design evaluation studies will include vibration, acoustic, and pressure drop testing. Upgrading to meet prototype test requirements would include raising the system pressure from approximately 6 to 9 MPa and raising the test assembly temperature from approximately 200° to 450° or 550°C. This could be accomplished using the same circulator used for the helium flow tests, but would require the addition of a helium heater and a regenerator/recuperator to the system.

It was agreed that Germany should complete an engineering design assessment of the prototype test facility by mid-1978 to establish the funding and schedule requirements necessary for the program. The outline plan for the GCFR prototype core assembly test program has been rewritten. The prototype test Resource Evaluation and Control System (RECS) cost management plan schedule has been completed, and the resource and cost projection reports have been issued (Ref. 4-6). The schedule is currently being interfaced with other GCFR program schedules to assure compatibility with the overall GCFR schedule.

REFERENCES

4-1. Hopkins, H. C., Jr., "Program Plan for GCFR Core Flow Test Loop," USAEC Report GA-A13080, General Atomic, August 9, 1974.

4-2. "Gas-Cooled Fast Breeder Reactor Commercialization Study for U. S. Energy Research and Development Administration," Helium Breeder Associates, October 31, 1977.

4-3. Rowe, D. S., "COBRA-IIIC: A Digital Computer Program for Steady State and Transient Thermal-Hydraulic Analysis of Rod Bundle Nuclear Fuel Elements," Battelle Northwest Laboratory Report BNWL-1695, March 1973.

4-4. "Test Specification for GCFR-CFTL Priority One Preliminary Series P-1 and P-2," General Atomic, unpublished data.

4-5. Strong, W. R., "Outline Plan for GCFR Prototype Core-Element Test Program," General Atomic, unpublished data.

4-6. Rao, S. B., "Status of the Transient Thermal Hydraulic Analysis Methods for the GCFR and CFTL," General Atomic, unpublished data.

5. FUELS AND MATERIAL ENGINEERING (189a No. 00582)

5.1. OXIDE FUEL AND BLANKET TECHNOLOGY

This subtask is concerned with oxide fuel and blanket technology. As a result of the decision to replace ThO_2 with UO_2 as a candidate radial blanket material, differentiation of the axial and radial blanket material has been suspended.

During the present quarter a study of possible GCFR irradiations in the fast flux test facility (FFTF) was carried out. The genesis of this study was comments on the GCFR Core Element Development Program Plan (Ref. 5-1) submitted by reviewers. The substance of these comments was that additional irradiations in the Fast Test Reactor should be considered. The experiments which are prime candidates have been identified, and their conceptual design, technical feasibility, and approximate cost are being discussed with the Irradiation Test Management Activity (ITMA) group at Hanford Engineering Development Laboratory (HEDL). The two irradiation experiments identified as prime candidates (out of six potential experiments initially identified) are

1. Irradiation of a 13-rod* helium-cooled, vented, and pressure-equalized bundle using ribbed cladding and grid spacers in a closed-loop in reactor assembly (CLIRA) position. The fuel rods would be subjected to prototypical fast breeder reactor axial and radial power profiles. The fuel length and blanket column length would be about 80% and 100%, respectively, of those of the GCFR demonstration plant design. The helium environment would also be prototypical of the demonstration plant.

---

*19-rod subassembly.

2. Irradiation of a 121-rod* sealed, sodium-cooled bundle using ribbed cladding and grid spacers. Such an irradiation would provide statistical performance data on a large number of rods, but the coolant environment would not be prototypical of the demonstration plant. In fact, it is clear that many of the objectives of the vented experiment would be lost, and most of the objectives will have been attained by other liquid metal fast breeder reactor (LMFBR) irradiations.

HEDL has estimated that the cost of the first experiment would be $40 to $50 million, and the second experiment could be completed for $2 to $3 million. GA is continuing its investigation of Fast Test Reactor experiments and has forwarded some CLIRA design requirements to ITMA. HEDL will attempt to refine the original cost estimates.

5.2. CLADDING TECHNOLOGY

5.2.1. Mechanical Testing Program

The objective of the ANL test program is to determine the effects of the following factors on the behavior and properties of GCFR ribbed and smooth cladding:

1. Ribs, rib geometry, fabrication technique, and stress state.

2. Helium impurity levels typical of the environment expected in the GCFR demonstration plant.

These tests are biaxial creep rupture tests with a hoop to axial tensile stress ratio of 2. Tests at a hoop to axial tensile stress ratio of unity and pure tensile tests are planned in support of the irradiated cladding test program.

---

*127-rod subassembly.

Two tests at 650°C and a hoop stress of ∿238 MPa in a purified helium atmosphere (i.e., 0_2 partial pressure of $<10^{-1}$ Pa) have been completed. In general, ribs increased rupture life and did not affect strain at failure. The third biaxial creep rupture test (ANL-III) in helium containing 300 Pa of H_2 and 30 Pa of H_2O is in progress. This test includes specimens fabricated by various techniques and smooth as-received specimens. Hoop stress levels of 238 and 262 MPa are being used at a test temperature of 650°C. Fifty-one out of a total of 81 test specimens have ruptured. Initial analysis indicates that the ribs strengthen the cladding, but the rupture lives are low and the minimum creep rate high in comparison with HEDL data on developmental cladding (Ref. 5-2). Other HEDL data on FFTF cladding (Ref. 5-2) also show low rupture life and high creep rate compared with developmental cladding. This type of behavior is attributed to melt stock variation and corresponding chemistry variation. HEDL data also indicate that the low-rupture-life melt stocks exhibit cold work instability.

The GCFR cladding in test ANL-III was fabricated from heat 90216. This particular heat had marginal mechanical properties at 538°C. The low rupture lives may very well be characteristic of this melt stock. Data from test ANL-III as currently designed will not distinguish between effects due to the GCFR environment being used and those due to heat-to-heat variations. To separate the effect of environment, if any, it is essential to include at least one more heat of material in the test program. Therefore, a test matrix for test ANL-IV has been designed and is given in Table 5-1. The new heat of material (90400) in this test matrix was purchased for the F-5 irradiation test program. A few specimens of this heat will also be added to test ANL-III at high stress levels. The number of specimens will be determined by material availability, and the environment will contain 30 Pa of H_2 and 300 Pa of H_2O. This is a new environment and may be modified prior to the start of the test.

TABLE 5-1
TEST MATRIX FOR TEST ANL-IV

Heat No.	Specimen Type				
90400	Mechanically ground, ribbed	--	Chemically etched, ribbed	Mechanically ground, smooth	As-received, smooth
90216	Mechanically ground, ribbed	Electro-chemically ground, ribbed	Chemically etched, ribbed	Mechanically ground, smooth	As-received, smooth

5.2.2. Helium Loop Test Program

The primary objective of the helium loop test program is to compare the mechanical properties in recirculating helium determined at Pacific Northwest Laboratory (PNL) with those in quasi-static helium determined at ANL. The loop has been modified to include moisture sensing instrumentation, and the first test has been initiated. The first 100 hr of the test indicated many significant problems, one of which is calibration of the equipment. A calibration setup for the impurity monitoring instrumentation has been assembled. Efforts to calibrate the EG&G dew point meter and the Thermox oxygen analyzer have been plagued with problems of equipment failure; the EG&G dew point meter has been repaired and installed. An effort was made to repair the gas chromatograph, but there is only a slim chance that this very old gas chromatograph can be repaired.

5.3. F-1 (X094) FAST FLUX IRRADIATION EXPERIMENT

The encapsulated fuel rods in the F-1 (X094) experiment received burnup exposures up to ∿13.0 at. % (121 MWd/kg, 8 x 10^{26} n/m^2) total fluence and 6.1 x 10^{26} n/m^2 (E > 0.1 MeV). Postirradiation examination of the seven fuel rods removed at the termination of the experiment is continuing at ANL and GA. At ANL, three of the seven rods (G-4, G-8, and G-9) have been sectioned, and samples have been distributed for burnup analyses, fission product isotopic profile determinations near the fuel-blanket interface, and metallographic examination. The analyses of the fission gases collected from the G-4, G-8, and G-9 fuel rods (Table 5-2) appear to be consistent with previously observed composition values.

ANL has prepared the various F-1 rod components for shipment to GA for postirradiation examination. These include charcoal traps from the G-4, G-9, G-10, and G-11 fuel rods and miscellaneous dosimetry assemblies. Components from all remaining F-1 rods are expected to be received at GA early in 1978 so that they can be processed through the GA hot cell prior to its closing for refurbishment.

TABLE 5-2
FISSION GAS ANALYSES OF FUEL RODS G-4 AND G-9

Elemental Analysis in Atom Percent

Rod	H_2	He	N_2	O_2	Ar	CO_2	Kr	Xe
G-4[a]	0.1	7.7	0.3	0.02	0.04	<0.05	12.1	79.8
G-8	0.1	8.5	0.2	<0.01	0.03	0.06	12.6	78.5
G-9[a]	0.1	6.6	0.1	<0.02	0.08	<0.05	12.4	80.7

[a]Tritium content was found to be less than 5×10^{-4} μCi.

Isotopic Analyses

Rod	Kr-82	Kr-83	Kr-84	Kr-85	Kr-86
G-4	0.06	14.7	27.8	6.2	51.3
G-8	0.04	15.0	28.0	6.2	50.8
G-9	0.04	14.8	27.6	6.4	51.2

Rod	Xe-128	Xe-130	Xe-131	Xe-132	Xe-134	Xe-136
G-4	0.02	0.06	13.5	22.8	34.8	29.0
G-8	0.014	0.044	13.7	22.8	34.7	28.7
G-9	0.01	0.04	13.9	22.6	34.7	28.8

5.4. F-3 (X206) FAST FLUX IRRADIATION EXPERIMENT

The F-3 experiment was irradiated in location 4B3 in EBR-II to an exposure of 4.9 at. % (∿46 MWd/kg); the burnup goal was 100 MWd/kg. The experiment reached an exposure of 46 MWd/kg in February 1976, at which time it was removed. Nine of the ten rods had failed owing to inadequate capsule sodium bonds.

During this quarter gamma ray spectral scans of the F-3 charcoal trap dosimetry assemblies received from ANL were examined. These scans confirm the early observation of intrusion of Cs-137 and Cs-134 into the lower charcoal traps. The G-18 rod contained a sealed charcoal trap which showed a minimum, but detectable, quantity of Cs-137 and Cs-134, indicating possible breaching of the charcoal trap can. Neutron radiography showed a bulge of the fuel rod cladding slightly above the midplane, but there was no evidence of sodium intrusion. The trap contents will have to be examined for fission products to ascertain whether the integrity of the sealed trap was affected. Neutron radiography and gamma spectrometry confirmed breaching of the sealed charcoal trap in rod G-16. The radiograph indicated sodium intrusion into the trap. Fission gas analysis of the plenum gas indicated a normal xenon-drypton isotopic distribution. No T_2, H_2O, or HTO were detected in the plenum gas.

Because of budgetary restrictions in FY-78, postirradiation examination of rods from the F-3 experiment will be severely curtailed so that available resources can be focused on the successfully irradiated rods from the F-1 experiment.

5.5. F-5 PROTOTYPE FUEL ROD GRID-SPACED BUNDLE FAST FLUX IRRADIATION EXPERIMENT

Design and fabrication of the components for the F-5 grid-spaced fuel rod bundle experiment and related quality data packages were completed. The components are at the EBR-II site awaiting EBR-II project review,

and the safety analysis portion of the F-5 experiment data package [submitted by ANL Material Sciences Division (ANL-MSD)] is waiting for approval. As reported previously (Ref. 5-3), the F-5 experiment was designed to study the performance of fuel rods irradiated under simulated GCFR conditions to determine (1) the reliability of the GCFR design and (2) the effect of a step power increase which simulates a 180-deg rotation of a subassembly at the core blanket interface in the proposed GCFR demonstration plant.

The grid-spaced bundle for the F-5 fast flux irradiation experiment was successfully assembled by GA. The assembly was loaded with dummy ribbed rods for flow testing prior to final loading with the $(Pu,U)O_2$ fueled rods. The assembly operation went very smoothly and was recorded on film (Figs. 5-1 through 5-10). Motion pictures (in color) were also obtained. The bundle hardware (and dosimeters) was shipped to the EBR-II site; inspection of the hardware upon receipt at EBR-II showed that all of it was in good condition.

It was necessary to qualify a shipping container for the F-5 grid-spaced bundle hardware to DOT 7A requirements.* The box required for F-5 was 1980 mm long, whereas the longest DOT 7A qualified box was 1575 mm long. Consequently, a duplicate box was subjected to a compression test, a series of drop tests, and a penetration test. As-built quality assurance documentation for the F-5 grid-spaced bundle, dosimeters, and fuel rod hardware components supplied by GA have been shipped to the EBR-II project.

Air flow testing of the F-5 grid-spaced bundle at the EBR-II site produced inexplicable results. The testing was done in a flow rate region where data on the friction factor for ribbed rods are not known. Consequently, the air flow test results were set aside, and flow testing in 66°C water was conducted to measure bundle and bypass flow. The water flow test is a good representation of the sodium flow during actual operation because the viscosity of the 66°C water at 0.5 MPa back pressure is the same as that of the hot sodium in EBR-II.

*Department of Transportation.

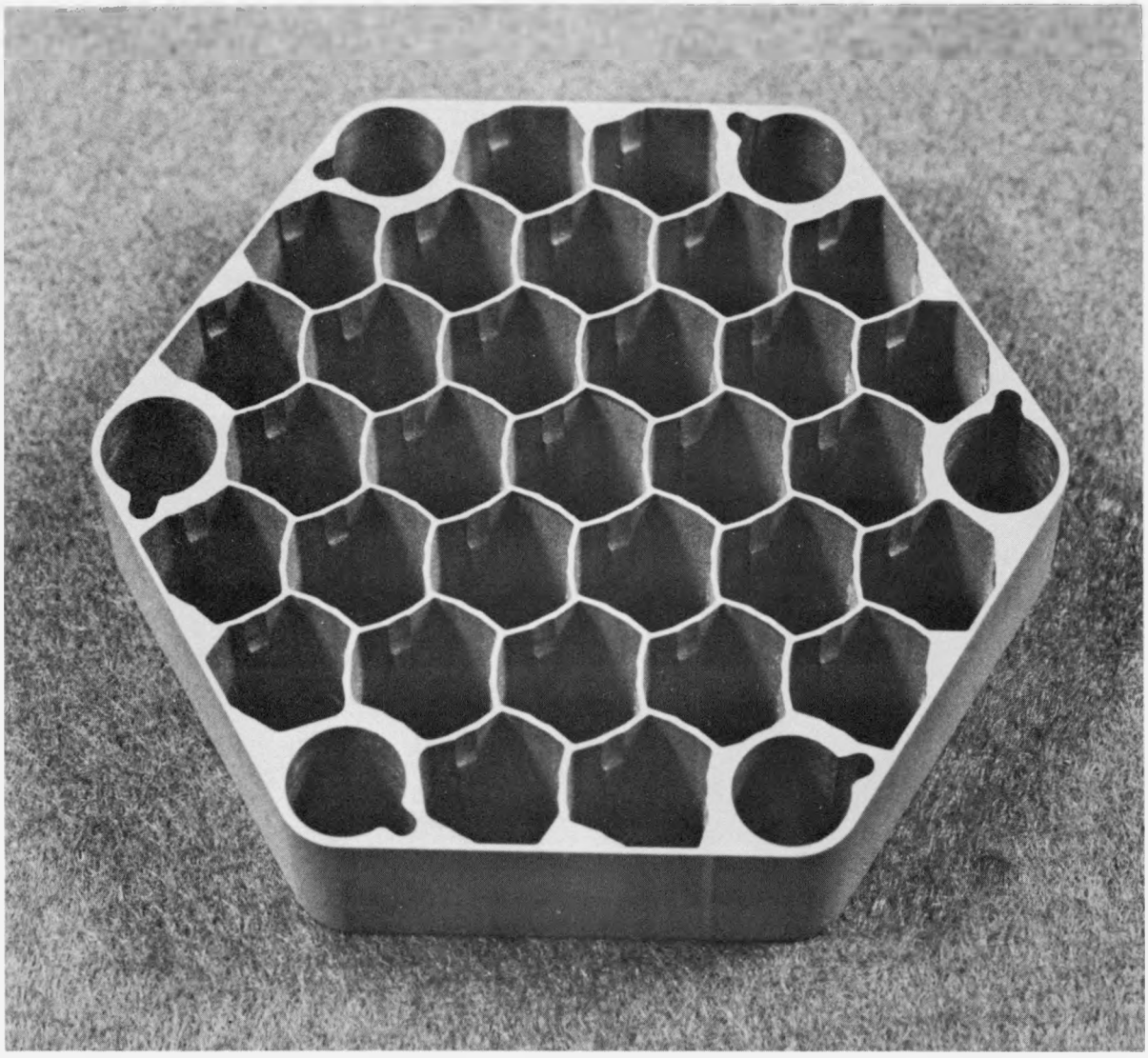

Fig. 5-1. F-5 grid spacer fabricated from 20% cold-worked 316 stainless steel by wire electrodischarge machining

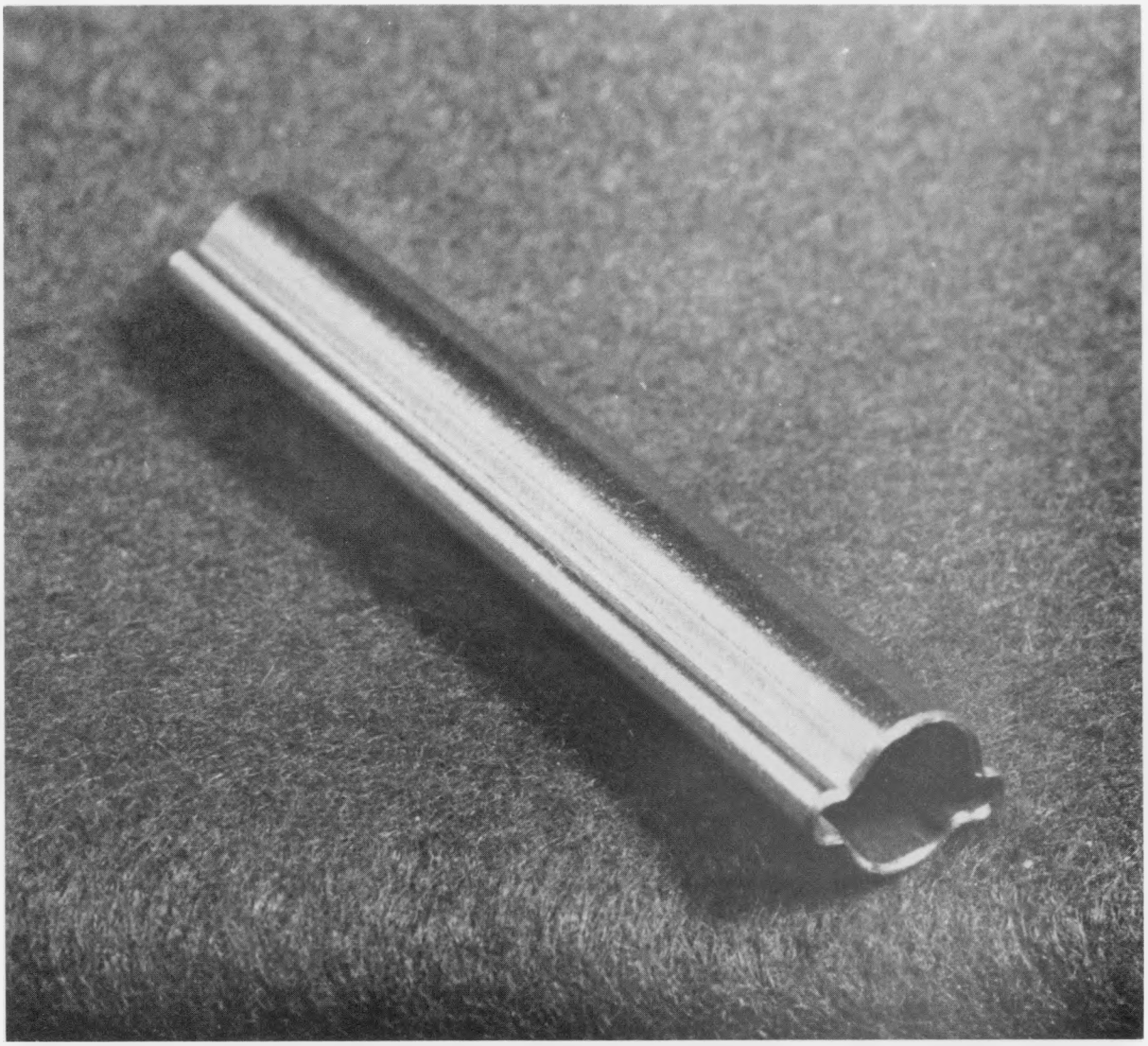

Fig. 5-2. F-5 spacer tube fabricated from 304 stainless steel by (1) forming to obtain shape and (2) chemical etching to thin wall locally on one side

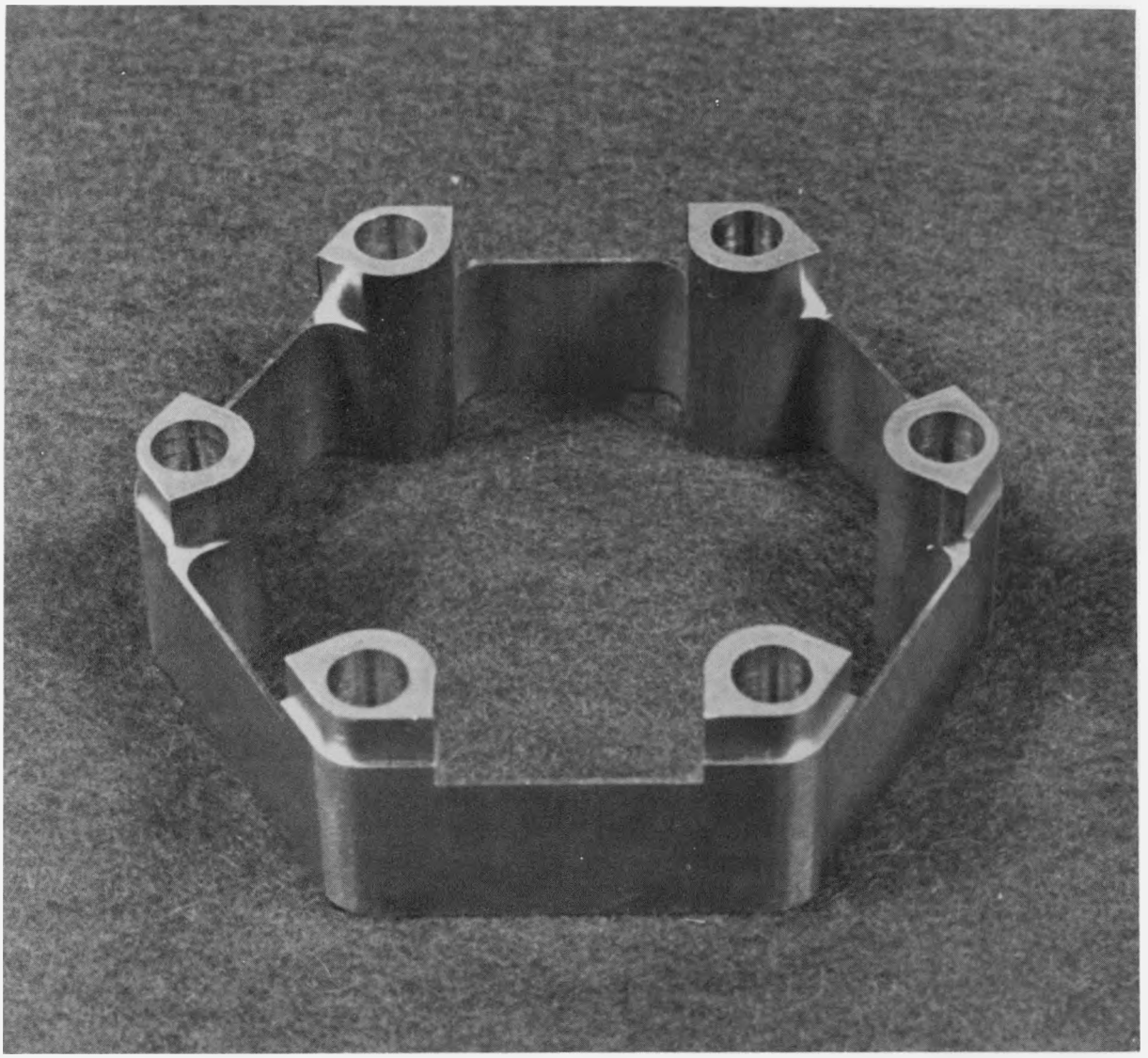

Fig. 5-3. F-5 adapter ring (adapts insulated corner rods to slotted hex tube at bottom) fabricated from 20% cold-worked 316 stainless steel by wire electrodischarge machining; threaded holes made by conventional means

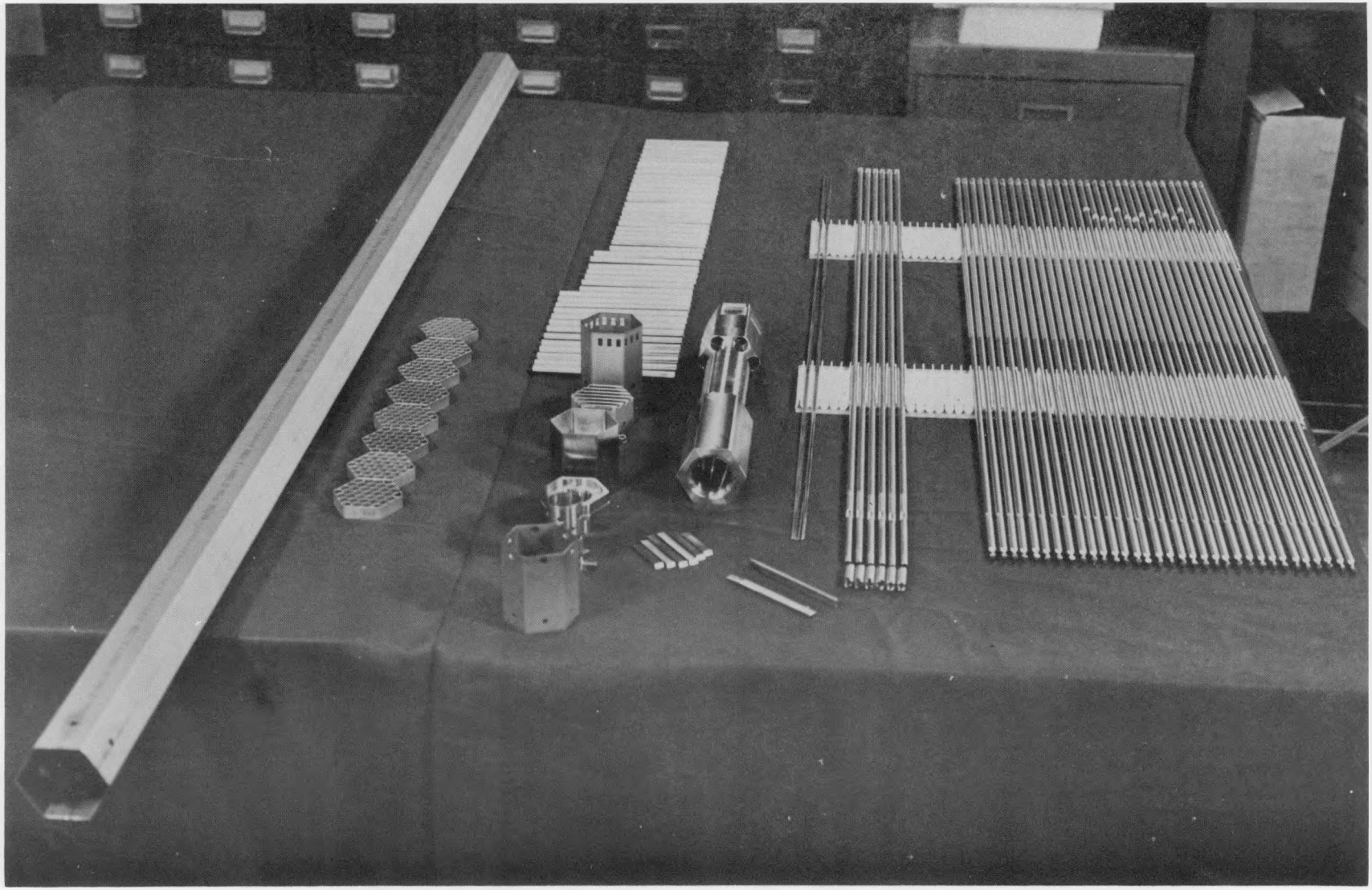

Fig. 5-4. F-5 grid-spaced bundle components prior to assembly

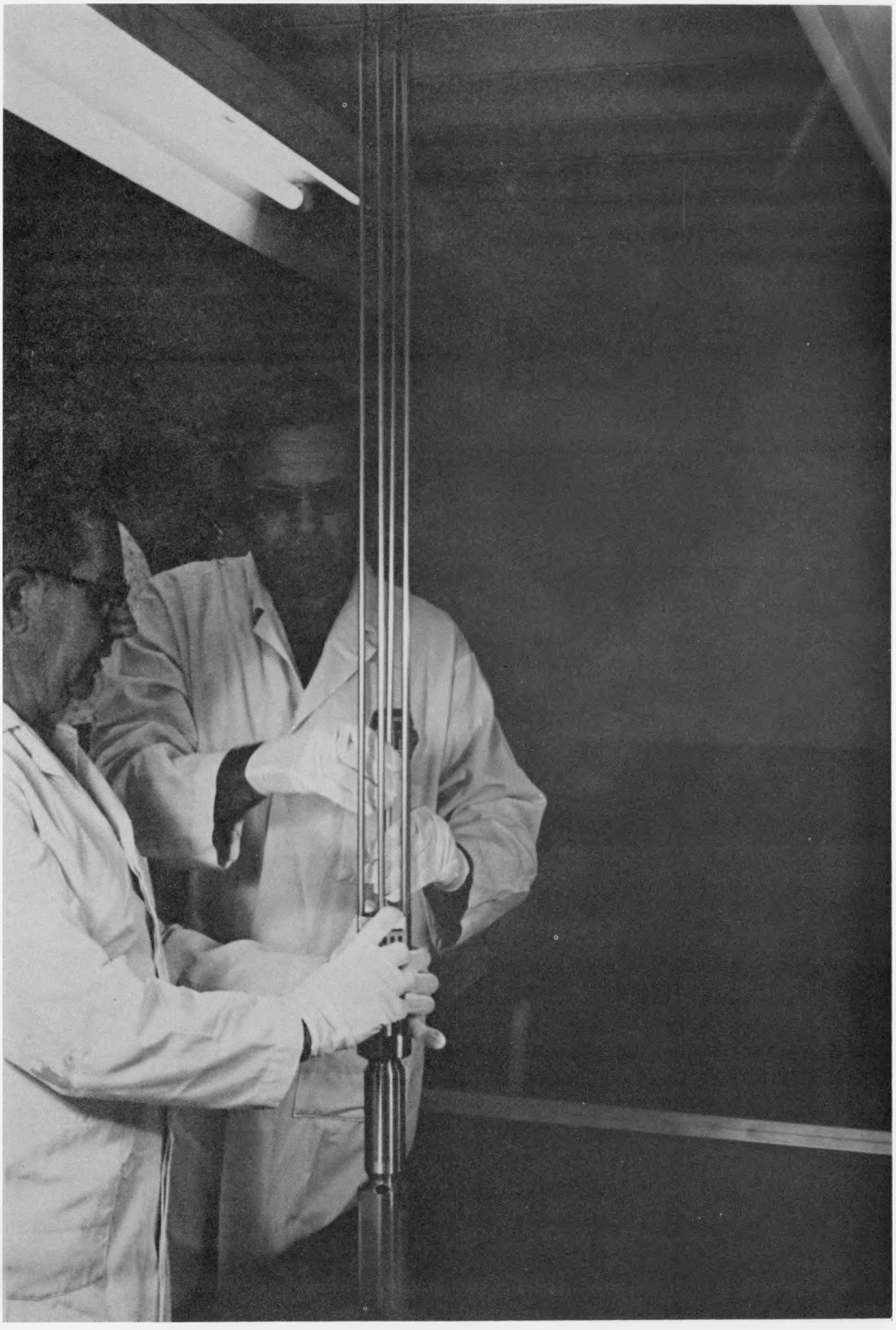

Fig. 5-5. Installation of insulated corner bypass flow tubes into bottom adapter for F-5 grid-spaced bundle skeleton

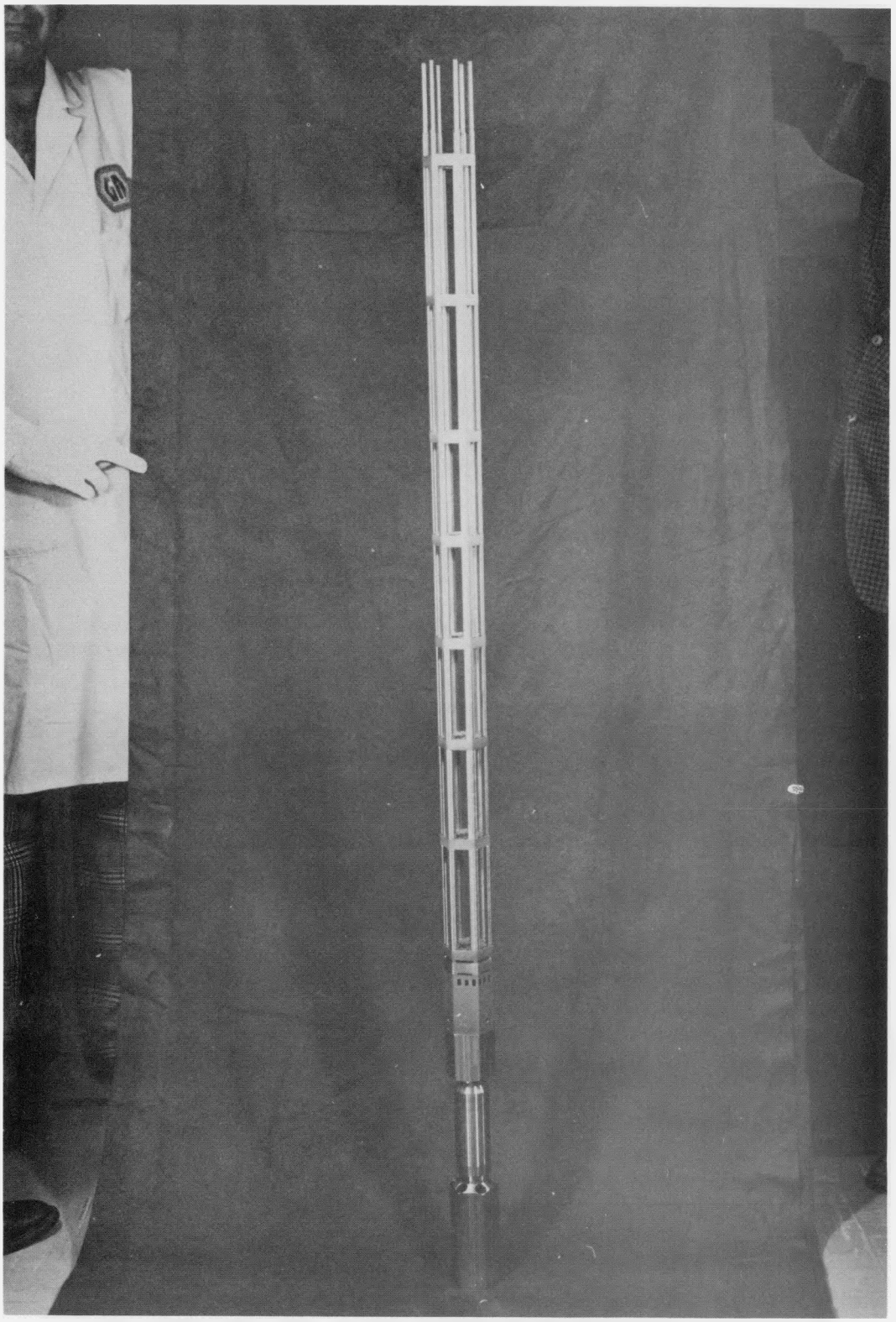

Fig. 5-6. F-5 grid-spaced bundle skeleton after assembly

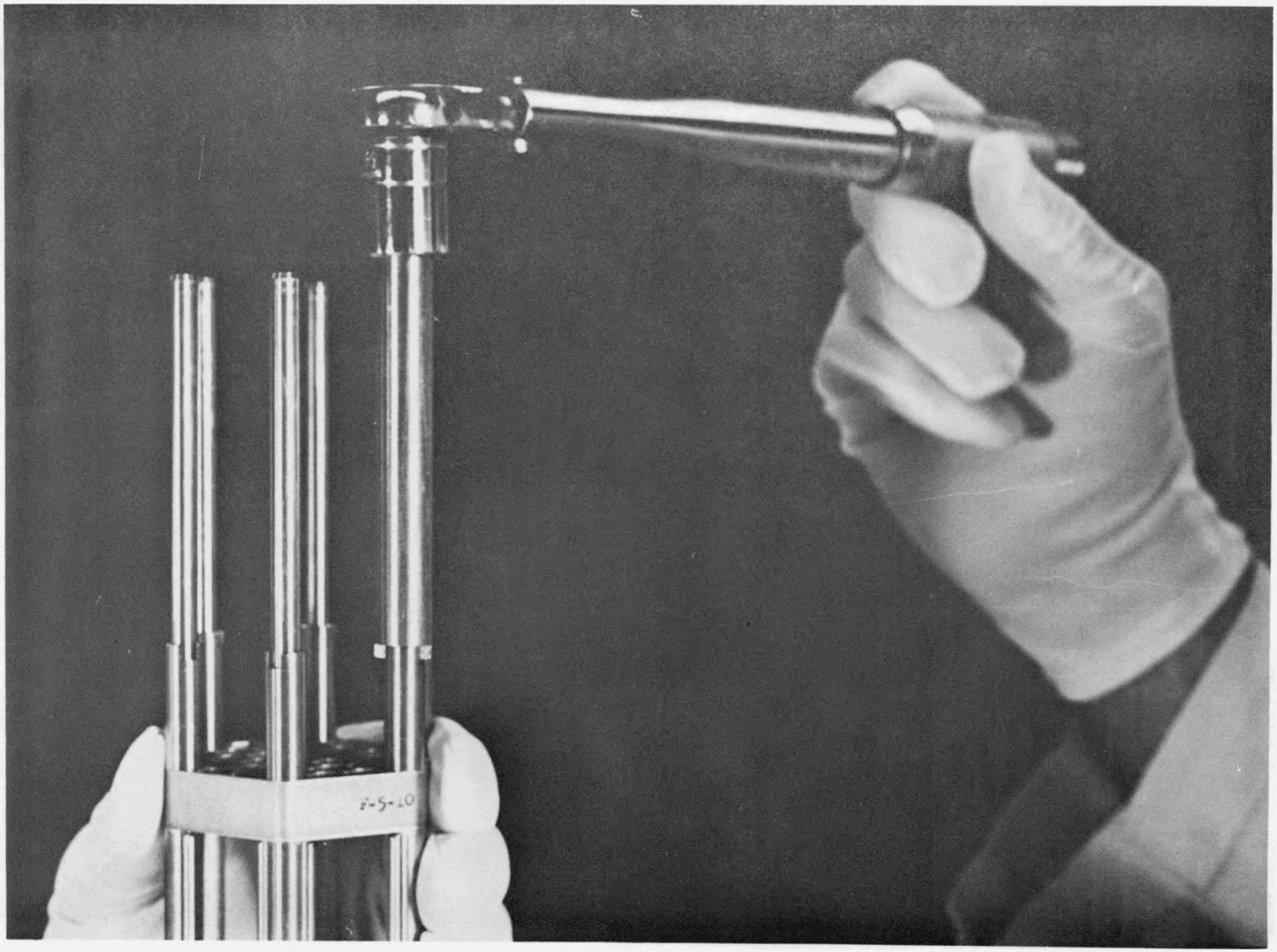

Fig. 5-7. Tensioning of spacer hold-down until after assembly of F-5 grid-spaced bundle skeleton

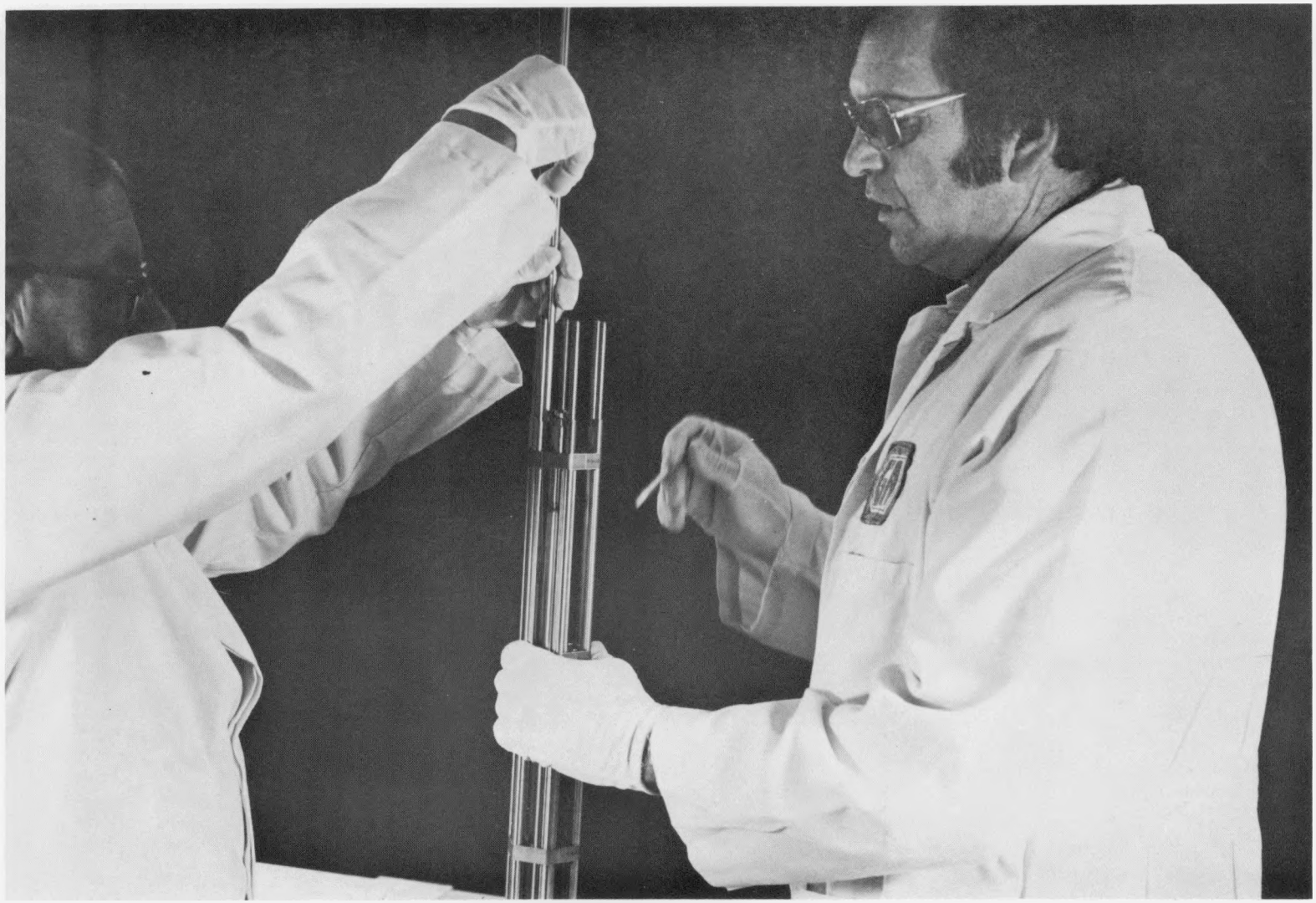

Fig. 5-8. Insertion of ribbed rod into F-5 grid-spaced bundle skeleton

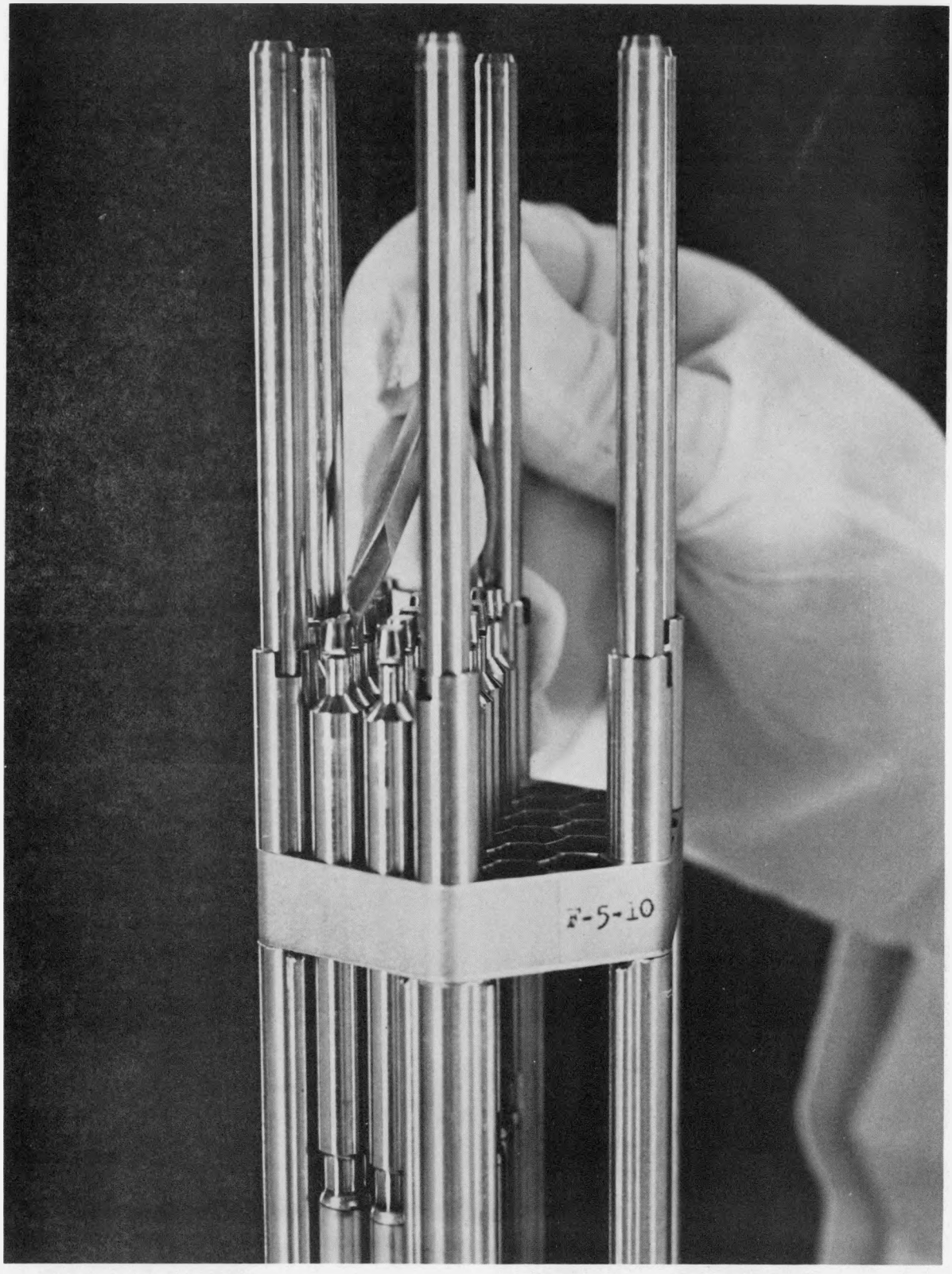

Fig. 5-9. Top end of F-5 grid-spaced bundle after partial loading with ribbed rods

Fig. 5-10. Bottom end upon insertion of rod locking keys after insertion of ribbed rods into F-5 grid-spaced bundle

Water flow testing of the F-5 bundle subassembly has been completed (a GA representative witnessed both the preliminary air and the water tests). An adjustment of the bundle orifice was required to obtain the necessary split of bundle and bypass flow. The water flow tests showed that there was insufficient flow through the bundle and excessive flow through the bypass flow tubes. Subsequently, the bundle orifice was removed, and the flow area of the holes in the orifice was increased by a factor of two to obtain the required flow split.

Quality control inspection of the 50 fuel rods assembled by HEDL showed 47 to be completely acceptable, but three rods showed some porosity in a weld. Although the weld porosity is minor, the three rods have been classified as two spares and one archive.

The F-5 fuel rods were shipped from HEDL to the EBR-II site for loading into the grid-spaced bundle assembly. The rods arrived at EBR-II and underwent receiving inspection. The final assembly of the F-5 bundle with the $(Pu-U)O_2$ fueled rods is now complete.

The results of thermal-hydraulic analyses of the F-5 bundle performed with the COBRA-IV and THI-3D (Ref. 5-5) subchannel analysis computer codes were compared. Since the THI-3D model of the bundle includes flow areas in the corners, the output was extrapolated to obtain predictions for the as-built configuration. The Nusselt number correlation previously used by GA produced values which were approximately 20% higher than those calculated by THI-3D using a correlation developed by Kazimi (Ref. 5-6); the more conservative lower values were adopted for subsequent COBRA runs. Both codes predicted that the maximum nominal (as opposed to hot spot) cladding midwall temperature could be held to 700°C with a total bundle flow rate of 0.96 kg/s. The resulting sodium temperature profile at the core outlet axial location is shown in Fig. 5-11 along with the total heat flow rates through the six faces of the duct wall over the full length of the bundle (based on the assumption that the F-5 assembly is located at the 5N2 core position). These values total nearly 18% of the power generated in the bundle (376 kW).

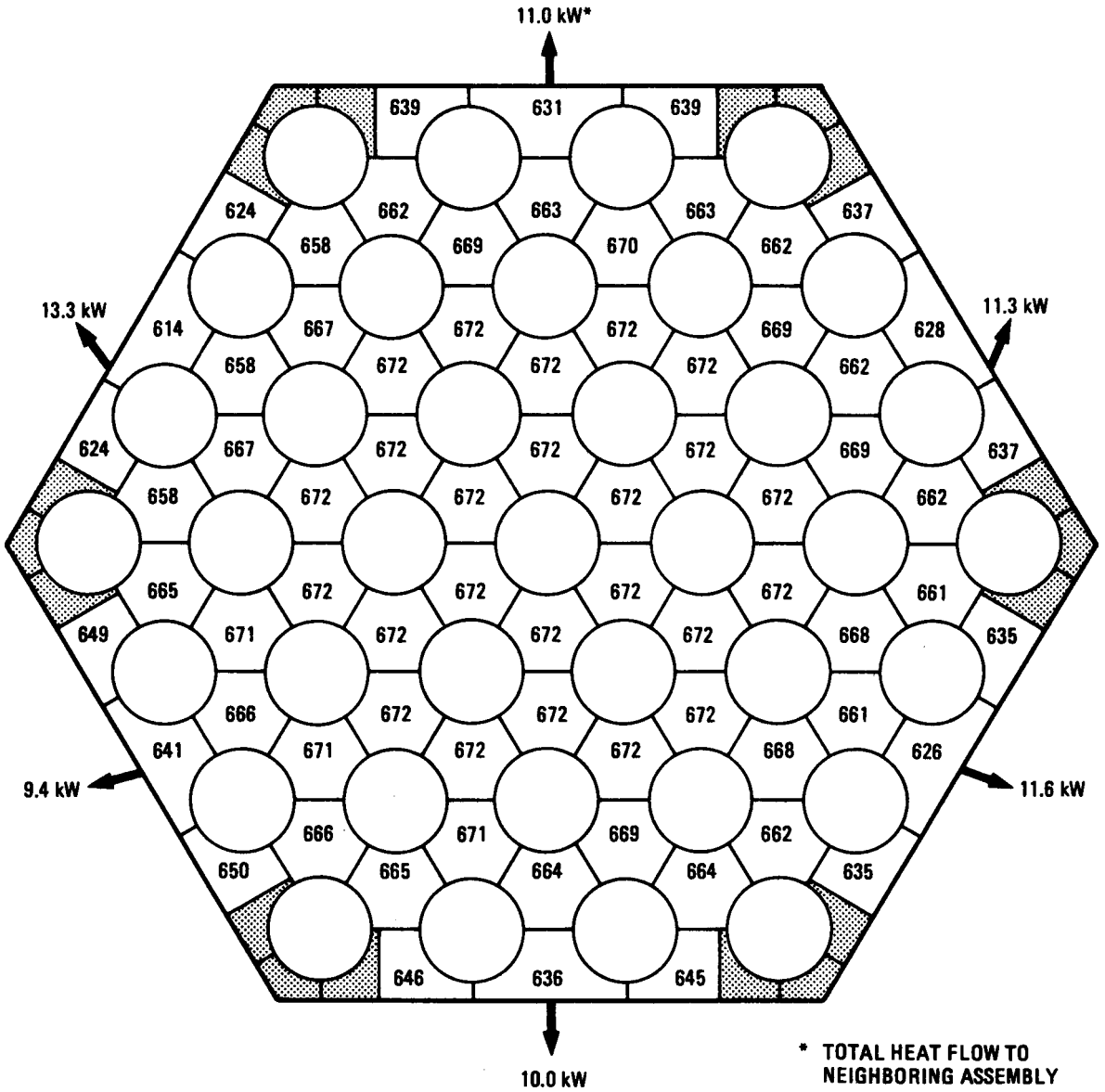

Fig. 5-11. Sodium temperatures at core outlet location

5.6. GB-10 VENTED FUEL ROD EXPERIMENT

During this quarter destructive examination of GB-10 vented fuel rod GA-21, which achieved an exposure of ∿112 MWd/kg in the ORR, continued at ANL. Examination of the upper fuel blanket interface metallographic section shows a dark region beyond the fuel which may contain cesium and other fission products. An election microprobe investigation will be conducted on this sample to characterize the darkened region.

5.7. HEDL CLADDING IRRADIATIONS

The objectives of the GCFR cladding irradiation and postirradiation test program are as follows:

1. To determine if the mechanical behavior of irradiated ribbed cladding is different from that of irradiated smooth cladding under biaxial loading conditions.

2. To determine the effect of stress state on rupture life and creep ductility.

3. Using a statistically designed test program, to determine the quantitative effect of ribs and stress state on creep rupture behavior.

Some ribbed cladding specimens have already been irradiated and are at ANL-MSD for postirradiation testing. Others are being irradiated, and a Request for Approval in Principle for additional irradiation has been submitted to DOE by ANL.

REFERENCES

5-1. "Core-Element Development Plan for the Gas-Cooled Fast Breeder Reactor Demonstration Plant," ERDA Report GA-A13312, General Atomic, May 6, 1975.

5-2. Nuclear Systems Materials Handbook, Hanford Engineering Development Laboratory (TID-26666).

5-3. "GCFR Quarterly Progress Report for the Period August 1, 1976 Through October 31, 1976," ERDA Report GA-A14112, General Atomic, November 1976.

5-4. Wheeler, C. L., et al., "COBRA-IV-I: An Interim Version of COBRA for Thermal-Hydraulic Analysis of Rod Bundle Nuclear Fuel Elements and Cores," Battelle Northwest Laboratory Report BNWL-1962, March 1976.

5-5. Sha, W. T., and R. C. Schmidt, "THI-30 - A Computer Program for Steady-State Thermal-Hydraulic Multichannel Analysis," Argonne National Laboratory Report ANL-8112, December 1975.

5-6. Kazimi, M. S., "Heat Transfer Correlation for Analysis of CRBRP Assemblies," Westinghouse Electric Report WARD-D-0034, April 1974.

6. FUEL ROD ENGINEERING (189a No. 00583)

The objective of this task is to evaluate the steady-state and transient performance of the fuel, blanket, and control rods for the determination of the performance characteristics, operating limits, and design criteria. To this end, analytical tools [such as the LIFE-III code (Ref. 6-1)] are being adapted and/or developed and applied to the analysis of GCFR prototypical rods and experimental rods. In addition, continuous surveillance of the LMFBR fuels and materials development program and technology is maintained to maximize the use of development technology and material properties. Support is also given to planning and designing of irradiation experiments.

6.1. FUEL, BLANKET, AND CONTROL ROD ANALYTICAL METHODS

6.1.1. Isotopic Fission Gas Release Subroutine

A radioactive isotopic fission gas release subroutine called GAREL has been written and successfully incorporated in the integral thermo-mechanical fuel rod performance code (LIFE). The theory employed in GAREL is based on the Booth spherical diffusional model (Ref. 6-2). GAREL is set up to calculate the release-to-birth ratio of isotopic fission gases for given radioactive decay constants and diffusivities in the fuel. When applied to sweep gas fuel rod irradiation tests, GAREL is able to determine the diffusivity. Because GAREL does not take into account trapping effects due to material defects, the diffusion coefficient used should embrace the effects of the unaccounted physical processes and is therefore called an "apparent diffusivity."

6.1.2. Fission Gas Release with Trapping and Resolution

The fission gas release model developed in the preceding section is based solely on classical diffusion theory, which includes variables and physical mechanisms such as material structural defects in the effective diffusivity. As a result, the fission gas release calculation in the GAREL subroutine depends only on the fuel temperature and oversimplifies the fission gas release phenomenon. Among the important physical processes which have been neglected in the GAREL model are trapping and resolution. To improve the theory, these two phenomena have been included in the present formulation. In addition, the effect of the precursors has been included. This problem has been solved for rectangular plate geometry (Ref. 6-3). However, the solution for spherical geometry used in Booth's diffusion model has not been found in the literature. The solution of this problem has consequently been prepared and is now ready for inclusion in the GAREL subroutine.

6.2. ANALYSIS OF IRRADIATION TESTS

6.2.1. F-1 Experiment Postirradiation Analysis

Irradiation analysis of the 13 fuel rods from the F-1 experiment has been undertaken. The run-by-run peak linear powers of each rod have been calculated from the fission rate data and reactor operating powers of the EBR-II reactor as shown in Tables 6-1 through 6-3. The rod axial power profile has been derived from the actual Zr-95 postirradiation gamma ray scan of the fuel rods and idealized to be suitable for the LIFE code input, as shown in Fig. 6-1. The thermal analysis model for the cladding o.d. calculation has been set up to reflect the most up-to-date material properties, and calculation is in progress.

6.3. ROD ANALYSIS AND PERFORMANCE

There was no activity on this subtask during this quarter.

TABLE 6-1
F-1 ROD PEAK LINEAR POWER

Run	MWd	Linear Power (W/cm)						
		G-1	G-2	G-3	G-4	G-5	G-6	G-7
47B	479.8	366.7	389.9	398.3	400.4	422.3	418.9	435.1
48	75.1	341.0	363.9	369.3	372.6	390.0	393.1	405.1
49B	621.3	373.2	374.1	403.5	404.7	425.8	422.1	437.4
49C	277.4	367.6	390.1	398.9	400.4	423.2	417.1	434.2
50F	817.0	360.9	384.0	393.3	395.8	418.0	415.1	431.8
50H	518.7	343.2	373.9	368.9	379.9	409.9	393.1	417.6
51A	613.7	375.2	401.3	408.2	412.4	438.6	430.8	450.9
51C	862.6	371.0	396.4	402.0	406.1	432.3	422.1	442.4
52A	395.2	353.5	376.2	382.5	385.0	409.2	398.9	417.6
52C	1077.3	355.5	378.5	385.0	387.6	412.6	401.4	420.9
53A	197.6	356.3	382.9	385.5	391.5	417.7	407.5	427.9
53D	345.8	339.9	364.0	370.2	374.6	398.0	392.6	410.5
53E	930.0	334.6	358.3	364.6	369.0	391.8	386.8	404.3
54	1445.9	340.9	360.8	371.4	371.7	392.6	388.0	403.5

TABLE 6-2
F-1 ROD PEAK LINEAR POWER

Run	MWd	Linear Power (W/cm)						
		G-1	G-2	G-4	G-5	G-6	G-7	G-8
56	1475.3	431.5	437.3	408.9	415.2	388.7	388.2	442.9
57	1354.7	415.3	421.7	394.5	399.9	374.0	374.2	425.8
58	1475.3	433.9	440.8	413.6	418.3	390.7	391.9	445.1
59	1473.4	425.1	434.3	408.8	410.9	382.4	386.1	434.8
60	1472.5	425.1	433.9	407.7	410.8	383.3	385.9	435.0
61	1472.5	428.3	435.1	408.4	413.7	388.1	388.6	440.4

TABLE 6-3
F-1 ROD PEAK LINEAR POWER

Run	MWd	Linear Power (W/cm)						
		G-4	G-8	G-9	G-10	G-11	G-12	G-13
67A	614.6	407.0	447.8	432.8	450.2	469.9	428.2	473.6
67B	696.3	409.4	448.4	433.2	451.9	473.0	429.5	475.6
68	1450.6	430.7	466.9	449.6	473.1	499.6	448.1	499.6
69	1472.5	420.4	430.5	436.3	454.4	486.4	442.2	468.1
70	1700.5	432.0	468.1	451.7	474.2	499.1	450.4	499.4
71	1559.9	408.8	435.0	421.5	444.9	470.9	424.2	466.9
72	1399.7	417.3	438.1	428.3	450.8	475.4	434.4	468.6
73	1994.1	406.2	426.1	416.8	438.9	463.6	422.6	456.6
74	2588.7	370.6	407.4	397.2	411.5	431.2	391.5	432.6
75	2567.9	369.4	410.5	400.5	412.0	428.3	392.9	432.4
76	1593.1	383.9	428.2	415.5	429.2	448.1	406.6	452.9
77	3732.5	369.2	410.1	397.8	411.6	430.2	390.3	434.1
78	2671.4	360.4	400.8	388.3	402.0	420.2	380.7	424.4
79	2668.5	370.7	413.1	402.2	413.8	429.8	394.1	434.6
80B	2454.8	329.1	371.8	357.8	369.8	385.4	348.1	392.4
81	2762.6	347.4	393.9	379.2	391.1	406.8	368.2	414.9

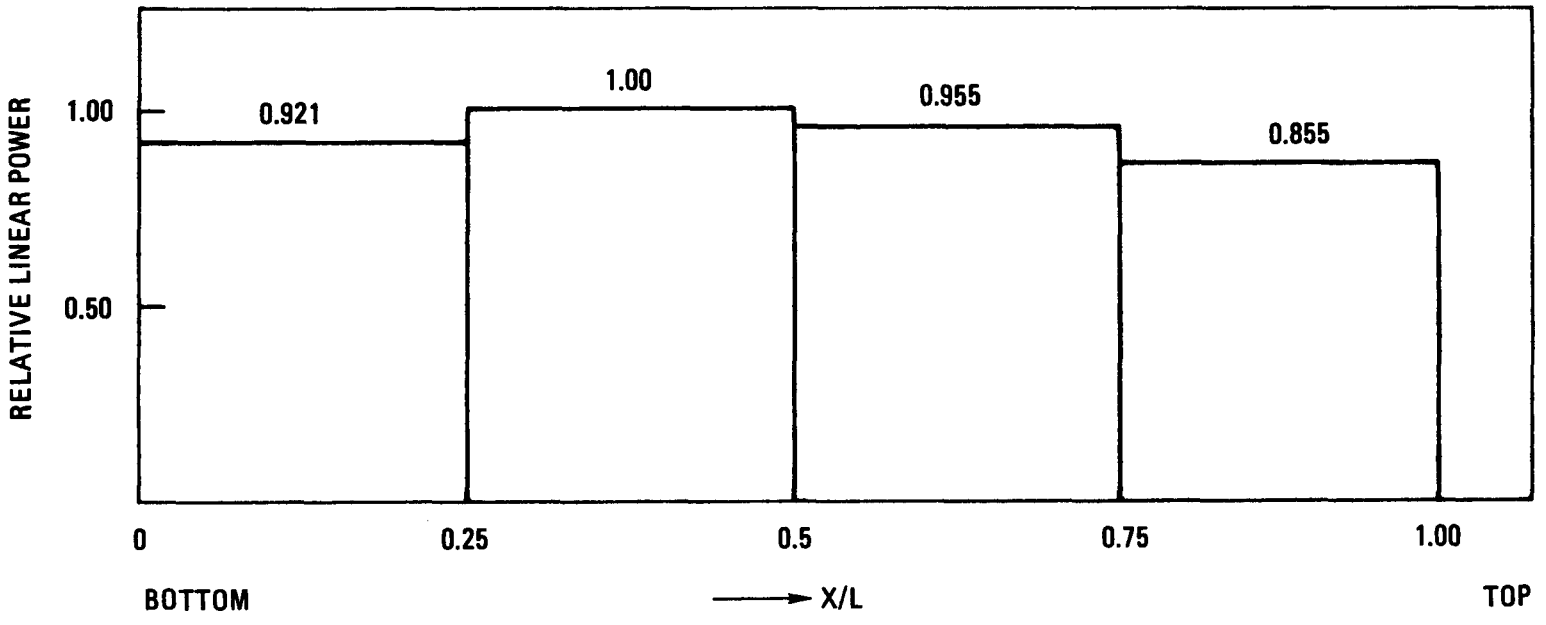

Fig. 6-1. F-1 rod axial power profile

6.4. FUEL ROD MECHANICAL TESTS

The initial mechanical testing of fuel rods includes the following three phases:

1. Tensile testing.
2. Compression testing (column loading).
3. Flexure testing (beam loading).

Each phase includes tests on smooth and ribbed fuel rods to evaluate the effect of ribbing on structural performance. Tensile testing was initiated in FY-77, and further tensile tests at room temperature and elevated temperature are planned. A furnace for tensile testing in the Instron mechanical test machine has been procured.

The design of a test fixture for column loading tests of a fuel rod on the Instron test machine has been completed, and the test fixture parts are being fabricated by an outside vendor. The design of test fixtures for flexure, or beam loading, tests of a fuel rod has also been completed. The flexure test will be done on the Instron test machine at various beam lengths up to 30 cm. The test fixture parts are being machined. The dynamic test machine for fatigue testing is being installed.

A flexure test of a CFTL-type heater rod and an empty cladding tube was conducted to estimate and compare the effective modulus and elastic limits of the two. The effective modulus of the heater rod was about 20% higher than that of the cladding tube. This difference is attributed to the heater wire and compacted insulation inside the heater tube.

REFERENCES

6-1. Billone, M. C., et al., "The LIFE-III Fuel-Element Performance Code User's Manual," Argonne National Laboratory Revised Draft, September 1976.

6-2. "Gas-Cooled Fast Breeder Reactor Quarterly Progress Report for the Period May 1, 1977 Through July 31, 1977," ERDA Report GA-A14492, General Atomic, August 1977.

6-3. Carroll, R. M., R. B. Derek, and O. Sisman, "Release of Fission Gas During Fissioning of UO_2," J. Am. Ceram. Soc. 48, 55-59 (1965).

7. NUCLEAR ANALYSIS AND REACTOR PHYSICS (189a No. 00584)

The scope of activities planned under this subtask encompasses the validation and verification of the nuclear design methods which will be applied to the GCFR core design. This will primarily be done by evaluating the methods using a critical assembly experimental program specifically directed toward GCFR development. Program planning and coordination activities, critical assembly design and analysis, and the necessary methods development will be carried out.

During the previous quarter, evaluation of the steam worth at low densities (8.8 g/l CH_2) was continued with improved modeling of the experimental configuration. Several topical reports have been written and reviewed. These reports cover nuclear data testing (Ref. 7-1); phase I steam entry scoping studies (Ref. 7-2); and phase II whole-core steam ingress (Ref. 7-3). Methods development continued with formulation of algorithms for an improved spectrum code and participation in Code Evaluation Working Group (CEWG) benchmark calculations.

During the present quarter, calculations of the phase II GCFR critical assembly experiments neared completion. Included in the current efforts are two-dimensional diffusion theory calculations in XY geometry with detailed modeling of the as-built Phase II configurations on ZPR-9. Using these models, power profiles have been derived for appropriate comparison with fission rate measurements using foil irradiations. Testing of the ENDF/B-4 data for U-233 has been carried out using discrete ordinates calculations for the U-233 bare-sphere benchmark.

7.1. PHASE II GCFR CRITICAL ASSEMBLY ANALYSIS

7.1.1. Diffusion Theory Calculations in XY Geometry for As-Built Critical Configurations

A series of two-dimensional diffusion theory calculations were carried out with the 2DB code (Ref. 7-4) using 10-group cross sections and XY geometry models of the phase II reference configurations with and without steel reflectors around the blankets. These XY models, representing the midplane views of the ZPR-9 matrix with stepped regional outlines, are deemed essential for accurately treating the influence of various asymmetries of reactor construction, including zone-stepped boundaries, vertical alignment of fuel plates and void channels (with preferential leakage in the y direction), and massive reactor table and matrix support knees. Details of the reference configuration geometries were obtained from Ref. 7-5.

The procedure for the XY analyses involves detailed geometric modeling of the as-built core and blanket regions, with several concentric subregions in both material zones to provide for varying transverse (axial) leakage parameters as a function of radius from the reactor axis. Also included is the full extent of empty matrix beyond the blankets and the table and knees in the rectangular model of ZPR-9. A 2DB model in RZ geometry which corresponded to each of the XY models was established, with concentric cylindrical subregions in the core and radial blanket to match the concentric regions of the XY model in the midplane area; cylindrical approximations were also used to represent the square outer ZPR-9 steel regions. 2DB calculations with the RZ models were then carried out, and neutron balance edits with the PERT code (Ref. 7-6) using the RZ fluxes yielded the groupwise midplane axial leakage terms for use in the XY subregions. The leakage parameters, entered as pseudoabsorber (DB^2) cross sections, were also checked using one-dimensional cylindrical calculations with the 2DB code.

Table 7-1 summarizes the results of the various 2DB calculations run to date, comparing eigenvalues from using RZ, one-dimensional, and XY geometry models. In essence, the procedure of combining RZ and XY results artificially yielded a three-dimensional solution for the flux distribution at the midplane of the assembly. The asymmetries and noncylindrical outlines of the XY cases thus provide lower eigenvalues than the smooth RZ cylindrical representations by 0.128% and 0.058% $\Delta k/k$ for the bare and reflected configurations, respectively. The three-dimensional results from the 10-group analysis are 1% lower than the measured eigenvalues, which is very similar to ANL experience with the Clinch River breeder reactor (CRBR) clean-core mock-ups.

7.1.2. Radial Reaction Rate Profiles at Midplane of Unreflected Phase II Critical Configuration

The aforementioned XY calculations yielded midplane flux distributions from which power and reaction rate distributions can be derived for more appropriate comparisons with measured rates than previously available from RZ results. Figures 7-1 through 7-4 plot these comparisons for profiles in the horizontal direction of fission in U-235, U-238, and plutonium and captures in U-238. With core center normalization of measurements and calculations, the figures show that the calculated profiles for all four reactions increasingly undershoot the experimental rates going out toward the core boundary and into the blanket. In general, the calculated fluxes provide for a core edge-to-center power ratio which is 4% to 5% lower than that indicated by the measured fission profiles in the unreflected configuration. Although considerable uncertainty exists in Fig. 7-4 for normalization of the measured capture rates in U-238, it appears that relative to the core center rate, the capture rates in the blanket are underpredicted by about 10%.

TABLE 7-1
RESULTS OF 10-GROUP 2DB CALCULATIONS IN ONE- AND TWO-DIMENSIONAL GEOMETRIES FOR THE PHASE II GCFR ASSEMBLY

	Phase II GCFR Assembly Reference Loading	
	Without Steel Reflectors	With Steel Reflectors
Average core radius (cm)	58.39	56.88
Experimental k	1.00116	1.00068
RZ geometry 2DB k_{eff}	0.99183	0.99217
One-dimensional cylinder 2DB k_{eff}	0.99192	0.99220
XY geometry 2DB k_{eff}	0.99066	0.00163
Three-dimensional synthesis calculated/experimental	0.9895	0.9910

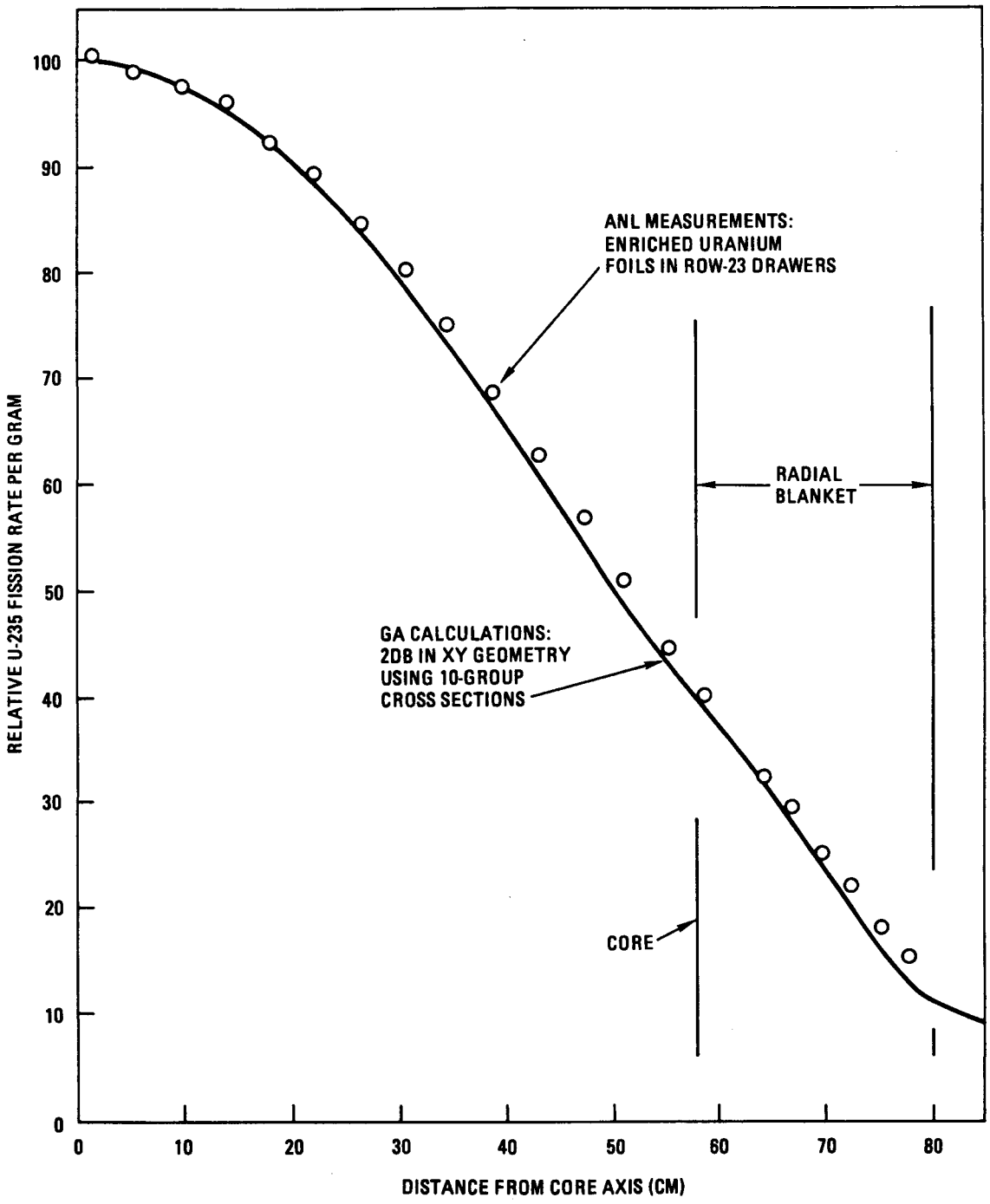

Fig. 7-1. Comparison of calculated and experimental U-235 radial fission rate profiles at the midplane in the unreflected phase II assembly

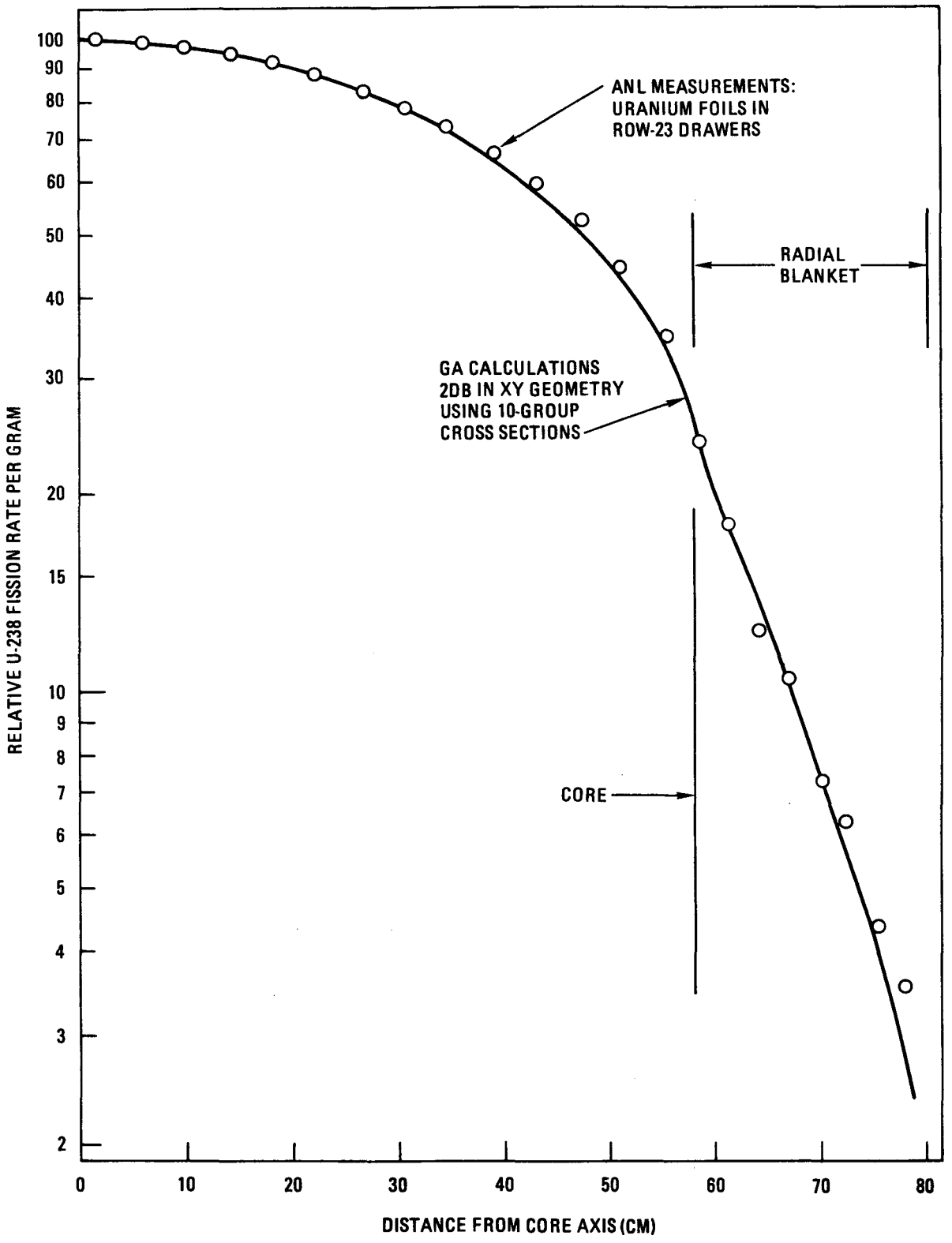

Fig. 7-2. Comparison of calculated and experimental U-238 radial fission rate profiles at the midplane in the unreflected phase II assembly

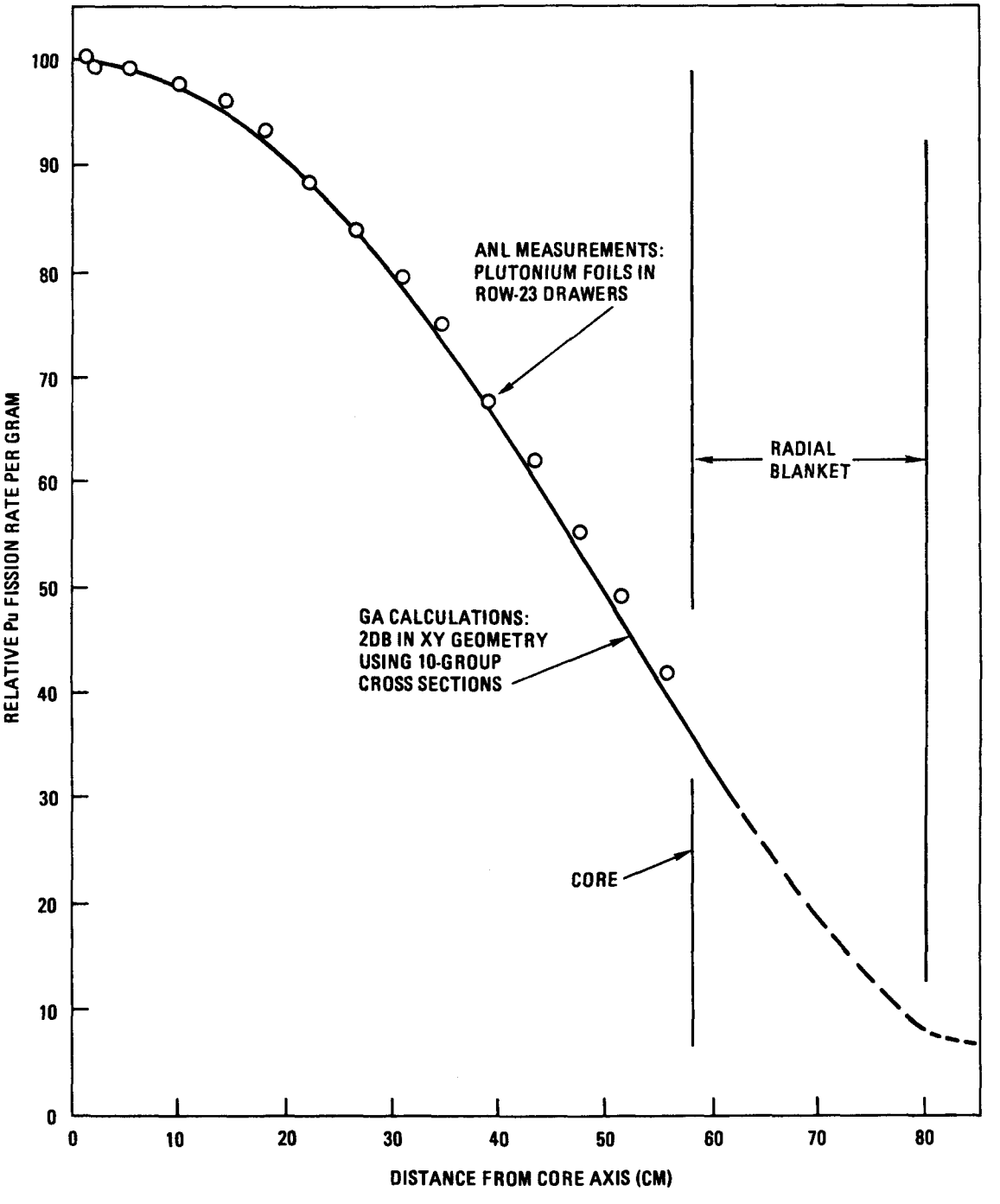

Fig. 7-3. Comparison of calculated and experimental plutonium radial fission rate profiles at the midplane in the unreflected phase II assembly

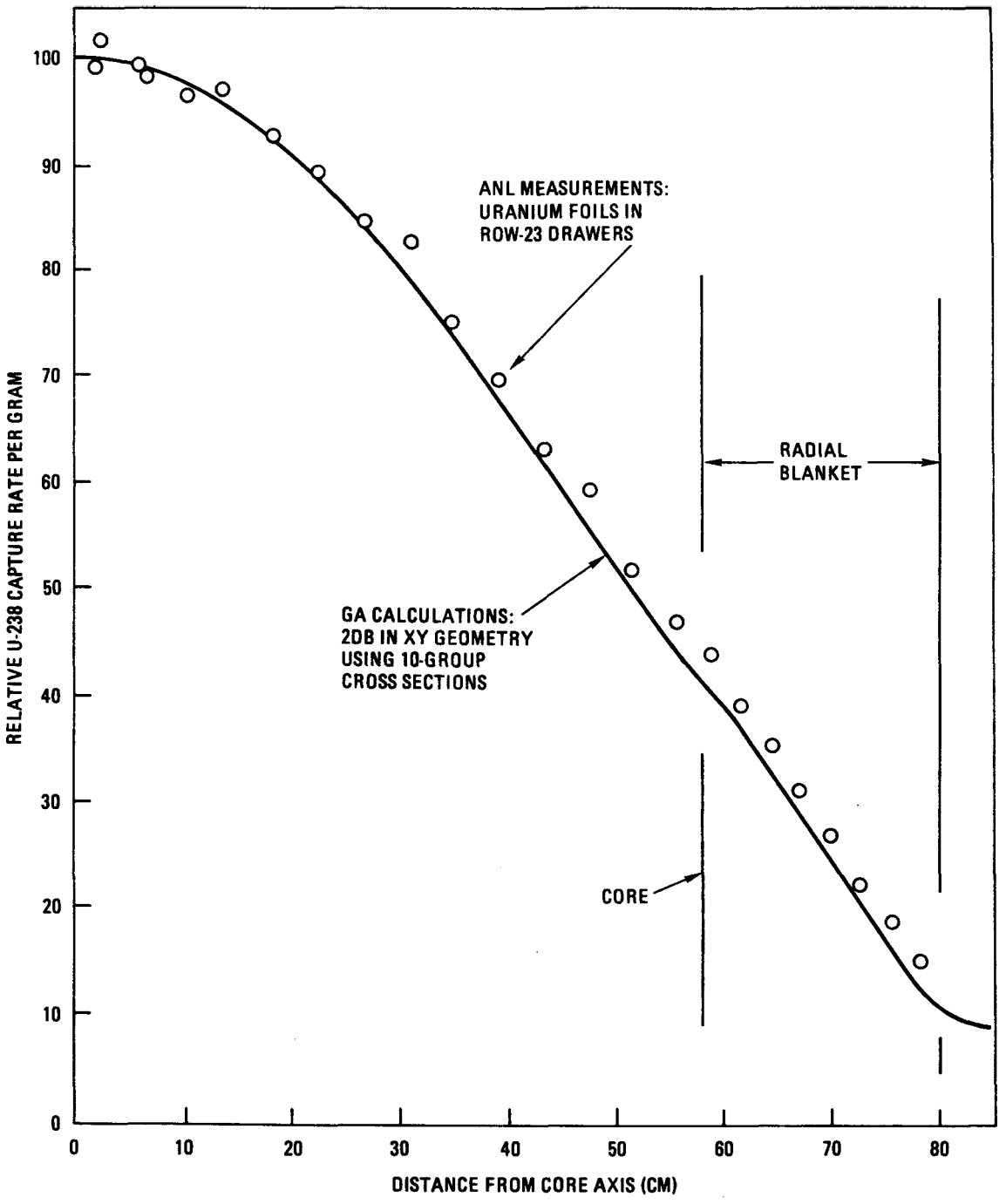

Fig. 7-4. Comparison of calculated and experimental U-238 radial capture rate profiles at the midplane in the unreflected phase II assembly

7.2. METHODS DEVELOPMENT

7.2.1. Benchmark Test of ENDF/B-IV Data for U-233

Discrete ordinates transport theory criticality calculations have been performed using ENDF/B data for a homogeneous sphere of U-233 metal (the so-called "233-Jezebel" critical assembly). This assembly is a bare sphere of nearly pure U-233 metal. The spherical homogeneous model has a core radius of 5.9832 cm and the following composition (Ref. 7-7):

Isotope	Density (10^{24} atoms/cm^3)
U-233	0.046719
U-234	0.000590
U-235	0.000014
U-238	0.000286

The GGC-5 code (Ref. 7-8) was used to generate 27 broad group cross sections for the above composition. A buckling of 0.1452 cm^{-2} yielded an eigenvalue of 0.995 in a GGC-5 B_3 calculation. The 27 broad group energy structure was chosen for approximately equal fluxes in the high-energy groups (see Table 7-2), and a check calculation using the standard GCFR one-half lethargy 28 broad group structure gave essentially identical results. A check calculation using a U-235 fission spectrum instead of a U-233 fission spectrum also yielded essentially identical results (an incident neutron energy of 1.35 MeV was used to prepare the fission spectra).

The discrete ordinates calculations were done with the DTFX code (Ref. 7-9) using P_3 scatter and S_{16} double P_n angular quadrature. Using 40 space intervals for the radial model, an eigenvalue of 0.9616 was obtained with the ENDF/B-IV data base. This result is comparable to a previous result of 0.966 reported in Ref. 7-10. The S_{16} quadrature should give an eigenvalue about 0.0008 higher than a hypothetical S-infinity calculation (Ref. 7-11). A P_2 instead of P_3 scattering calculation changed

TABLE 7-2
CROSS SECTION GROUP STRUCTURE FOR U-233 BENCHMARK
ANALYSIS AND FLUXES FROM DTFX CALCULATION

Group	Lower Energy (eV)	Lower Lethargy	Flux (n/cm^2-s)	Leakage (n/cm^2-S)
	1.49+7[a,b]	-0.4[a]		
1	1.00+7	0.0	4.988-3	4.236-4
2	6.06+6	0.5	7.937-2	1.284-2
3	4.49+6	0.8	1.751-1	2.807-2
4	3.68+6	1.0	1.844-1	2.863-2
5	3.01+6	1.2	2.338-1	3.563-2
6	2.47+6	1.4	2.741-1	4.147-2
7	2.02+6	1.6	3.043-1	4.626-2
8	1.65+6	1.8	3.198-1	4.932-2
9	1.35+6	2.0	3.182-1	4.988-2
10	1.11+6	2.2	3.045-1	4.796-2
11	9.07+5	2.4	2.890-1	4.567-2
12	7.43+5	2.6	2.718-1	4.297-2
13	6.08+5	2.8	2.433-1	3.777-2
14	4.98+5	3.0	2.155-1	3.255-2
15	3.69+5	3.3	2.680-1	3.918-2
16	2.73+5	3.6	2.019-1	2.840-2
17	1.83+5	4.0	1.837-1	2.477-2
18	1.11+5	4.5	1.314-1	1.672-2
19	6.74+4	5.0	6.517-2	7.762-3
20	4.09+4	5.5	3.051-2	3.384-3
21	2.48+4	6.0	1.315-2	1.387-3
22	1.50+4	6.5	5.377-3	5.447-4
23	9.12+3	7.0	2.200-3	2.137-4
24	3.35+3	8.0	1.231-3	1.156-4
25	1.23+3	9.0	1.893-4	1.718-5
26	2.26+1	13.0	2.713-5	2.272-6
27	4.14-1	17.0	3.783-10	2.316-11

[a] Upper bound for group 1.

[b] 1.49+7 = 1.49×10^7.

the calculated eigenvalue by less than 0.0001, indicating that P_2 is sufficient (P_1 is not sufficient; a P_1 scattering calculation yielded a 0.0057 lower eigenvalue). The GGC-5 and DTFX broad group fluxes agreed well (for a further internal consistency check).

7.2.2. Reevaluation of U-233 Data for Version Five of ENDF/B

Reevaluation of U-233 cross sections for version five of ENDF/B includes changes which should provide better agreement between calculations and experiment on the 233-Jezebel benchmark test. Because the proposed changes include substantially increased U-233 elastic scattering cross sections, additional DTFX calculations were run with the self-scatter and adjacent-group downscatter increased by 20% and 40%. The results were

Case	Eigenvalue
Reference	0.9616
$\sigma^s_{g,g}$ and $\sigma^s_{g,g+1}$ x 1.20	0.9776
$\sigma^s_{g,g}$ and $\sigma^s_{g,g+1}$ x 1.40	0.9933

Thus, it appears that extremely large changes in the U-233 elastic scattering cross sections would be required to provide agreement of calculations and experiment for this test case.

It appears that the ENDF/B-V U-233 cross section evaluation will indeed have about 20% larger elastic scattering cross sections as well as larger fission cross sections and mean number of neutrons per fission in the energy range of interest in the 233-Jezebel system (Ref. 7-12). All these changes should improve the agreement between calculations and experiment for this small hard-spectrum U-233 system (62% leakage and 38% absorption). These calculations were supplied to CSEWG as an aid to the U-233 cross section evaluation process for ENDF/B-V.

REFERENCES

7-1. Hess, A. L., R. A. Moore, and D. R. Mathews, "Testing of ENDF/B-IV With GCFR Design Codes," ERDA Report GA-A14084, General Atomic, September 1977.

7-2. Hess, A. L., R. A. Rucker, and R. A. Moore, "Analysis of Steam Entry Experiments in the Phase I Critical Assembly," DOE Report GA-A14798, General Atomic, to be published.

7-3. Hess, A. L., and R. A. Rucker, "Analysis of Full-Core Steam Flooding Experiments in the Phase II GCFR Critical Assembly," DOE Report, General Atomic, to be published.

7-4. Little, W. W., Jr., and R. W. Hardie, "2DB, A Two-Dimensional Diffusion-Burnup Code for Fast Reactor Analysis," USAEC Report BNWL-640, Battelle Northwest Laboratory, January 1968.

7-5. Pond, R. B. (ed.), "Reactor Physics Studies in the GCFR Phase II Critical Assembly," ERDA Report ANL-76-108, Argonne National Laboratory, September 1976, Figs. 1-9, 1-10.

7-6. Hardie, R. W., and W. W. Little, Jr., "PERT-IV, A Two-Dimensional Perturbation Code in Fortran-IV," USAEC Report BNWL-409, Battelle Northwest Laboratory, 1967.

7-7. Hansen, G. E., and H. C. Paxton, "Reevaluated Critical Specifications of Some Los Alamos Fast-Neutron Systems," Los Alamos Scientific Laboratory Report LA-4208, September 1969.

7-8. Mathews, D. R., et al., "GGC-5, A Computer Program for Calculating Neutron Spectra and Group Constants," Gulf General Atomic Report GA-8871, September 27, 1971.

7-9. Archibald, R. K., K. D. Lathrop, and D. Mathews, "1DFX - A Revised Version of the 1DF (DTF-IV) SN Transport Theory Code," Gulf General Atomic Report Gulf-GA-B10820, September 27, 1971.

7-10. McNeany, S. R., and J. D. Jenkins, "Comparison of Hansen-Roach and ENDF/B-IV Cross Sections for ^{233}U Criticality Calculations," Oak Ridge National Laboratory Report ORNL-TM-5313, January 1976.

7-11. Argonne Code Center, "Numerical Determination of Space, Time, Angle and Energy Distribution of Particles in an Assembly," Argonne National Laboratory Report ANL-7416, 1968.

7-12. Stewart, L., Los Alamos Scientific Laboratory, private communication.

8. SHIELDING REQUIREMENTS (189a No. 00584)

The purposes of the shielding task are to verify the adequacy of the methods and data (physics and engineering) for the design of GCFR shields and to evaluate the effectiveness of various shield configurations. This task also coordinates and provides liaison with the analytical and experimental GCFR shielding activities at ORNL.

During the last quarter the shielding aspects of the two alternate 300-MW(e) GCFR designs were analyzed, and a response to ORNL specifications for the grid plate shield design confirmation experiment was prepared. In addition, shutdown gamma ray, beta ray, and neutron source terms were evaluated for use in fuel handling equipment shielding studies, and an investigation of the sensitivity of radial shielding response to radial source distribution and radial zoning was completed. During this quarter the results of two-dimensional calculations of the upper axial shield assembly were received from ORNL and evaluated. In addition, improved calculations of the shutdown Cr-51 activation were performed.

8.1. 300-MW(e) GCFR REVISED UPPER AXIAL SHIELD ASSEMBLY

The new configuration for the revised 300-MW(e) GCFR upper axial shield assembly is described in Refs. 8-1 and 8-2. The calculational model reported in Ref. 8-2 was transmitted to ORNL for two-dimensional DOT-IV (Ref. 8-3) transport calculations. During this quarter the results of the ORNL calculations were reviewed.

Reference 8-1 indicates that the basic transport calculations require a three-dimensional transport code. Even if the instrument tree penetrations are ignored, the six inlet ducts complicate the two-dimensional

modeling. Since the "open" area of the six ducts is about equal to the "closed" area on the circumference of the PCRV cavity liner above the upper annular shield, two sets of two-dimensional calculations in RZ geometry are necessary to approximate the fluxes in this region. The two, two-dimensional calculational models are shown in Figs. 8-1 and 8-2. Figure 8-1 approximates a vertical section between the inlet ducts, and Fig. 8-2 approximates a vertical section through the ducts. Both figures show a proposed 4-cm stainless steel liner shield above the upper annular shield.

The results of ORNL transport calculations for the upper axial shield assembly (Fig. 8-1) are shown in Figs. 8-3 through 8-10. The calculations were performed with the DOT-IV code using 51 neutron and 25 gamma groups with S_6 angular quadrature and P_3 anisotropic scattering. The grid plate source for the results given in Figs. 8-3 through 8-8 is for EOC. The source for the results in Figs. 8-9 and 8-10 is for BOC. The flux output from the BOC calculations was used as the initial guess for the EOC calculations.

Figure 8-3 presents isoflux plots for EOC total neutron flux; Fig. 8-4, thermal neutron flux ($E < 2.38$ eV); Fig. 8-5, neutron flux with $E > 1.0$ MeV; and Fig. 8-6, neutron flux with $E > 0.1$ MeV. Figure 8-7 presents the EOC concrete gamma heating rates; the traced isoheating contours are stopped at the concrete boundary because the gamma production terms apply only to concrete. Figure 8-8 presents the EOC gamma dose rates during operation, and Figs. 8-9 and 8-10 present the BOC total neutron flux and thermal flux, respectively.

Comparison of the EOC solutions in Figs. 8-3 and 8-4 for the total flux and thermal flux, respectively, with the corresponding BOC solutions, Figs. 8-9 and 8-10, shows that at the height of the inlet ducts, the EOC fluxes are about twice the BOC fluxes. This very significant difference must be considered in future shielding analysis. Figure 8-7 indicates

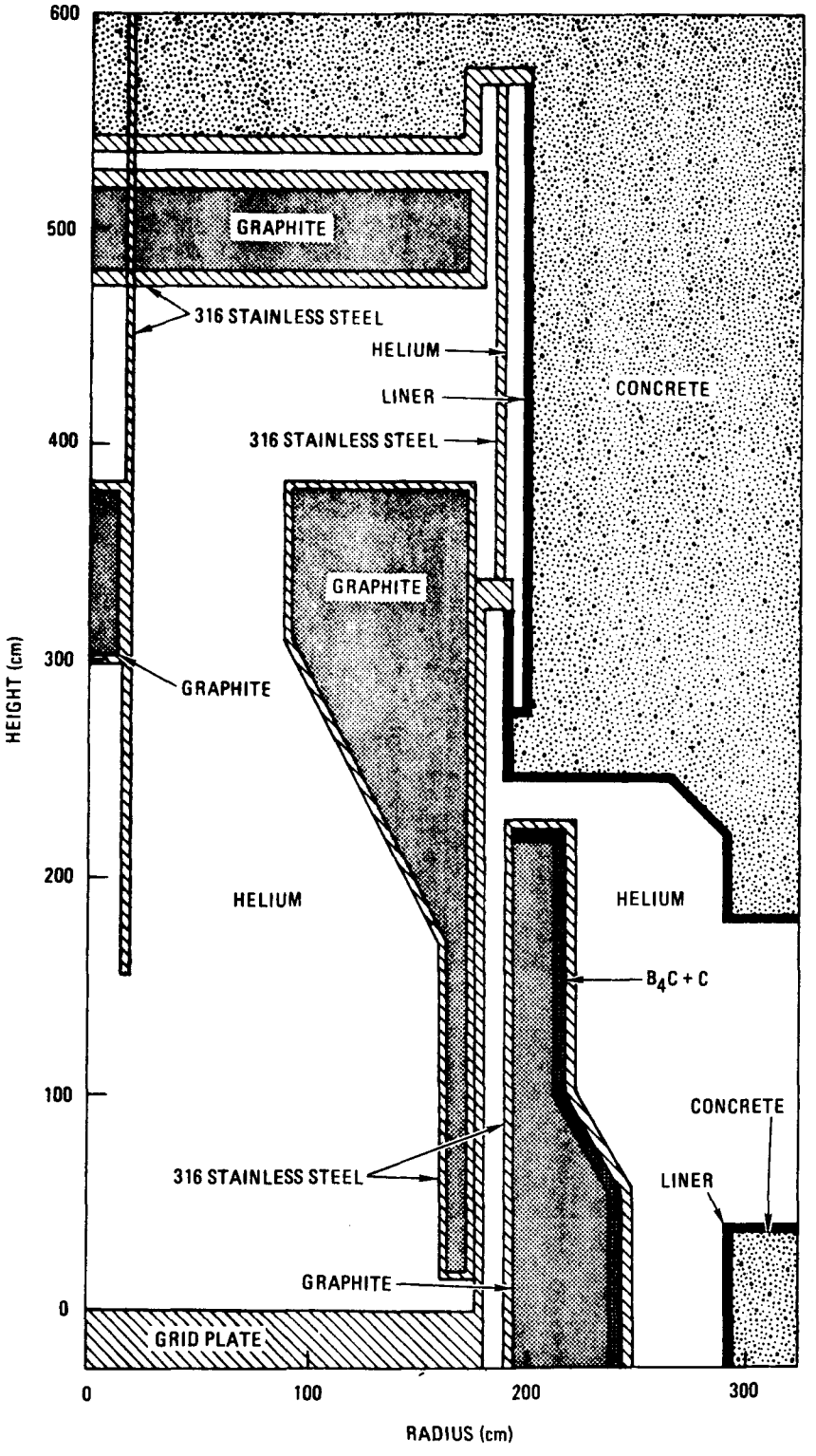

Fig. 8-1. Calculational model for upper axial shield assembly (vertical section between coolant inlet ducts)

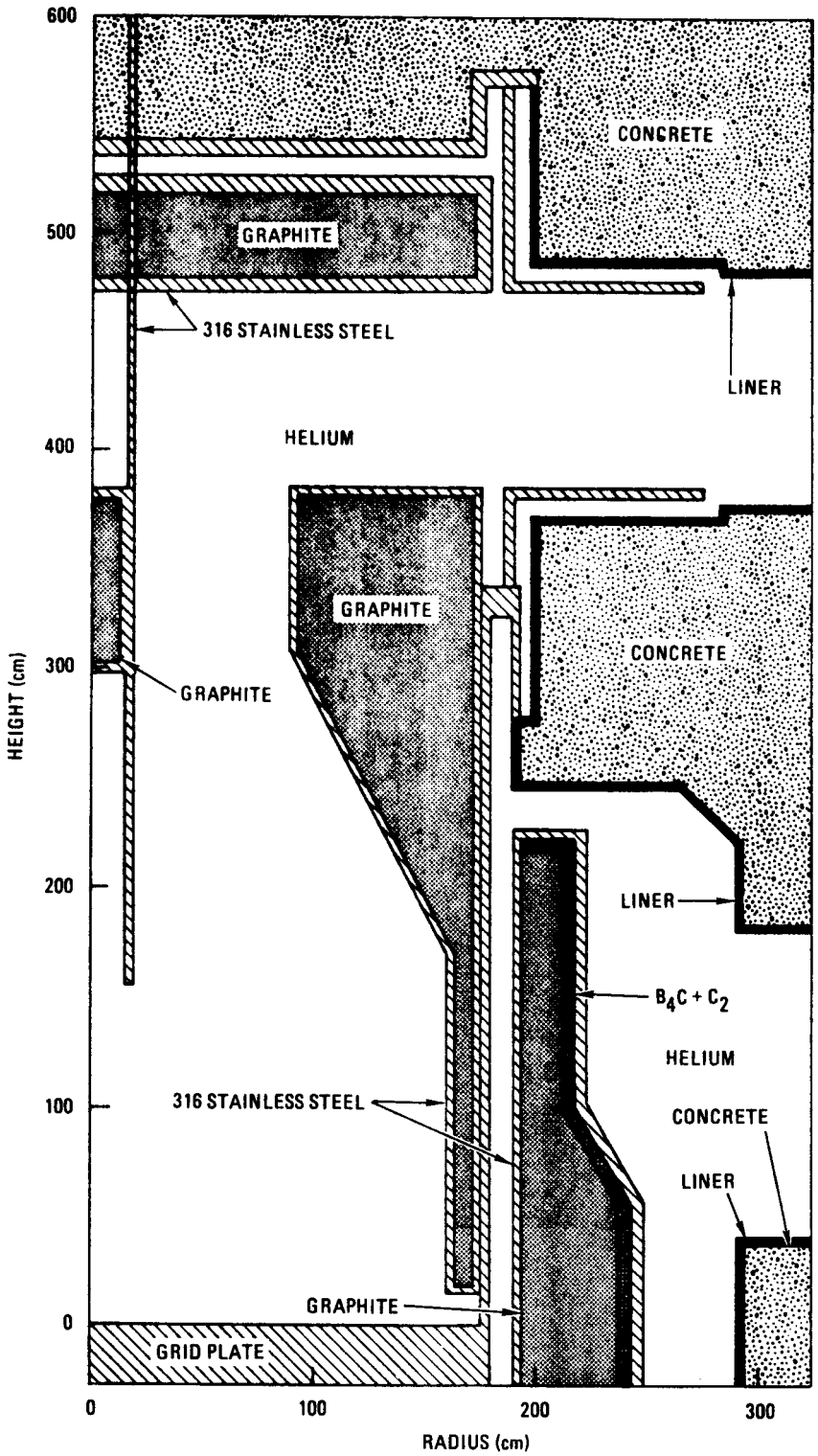

Fig. 8-2. Calculational model for upper axial shield assembly (vertical section through a coolant inlet duct)

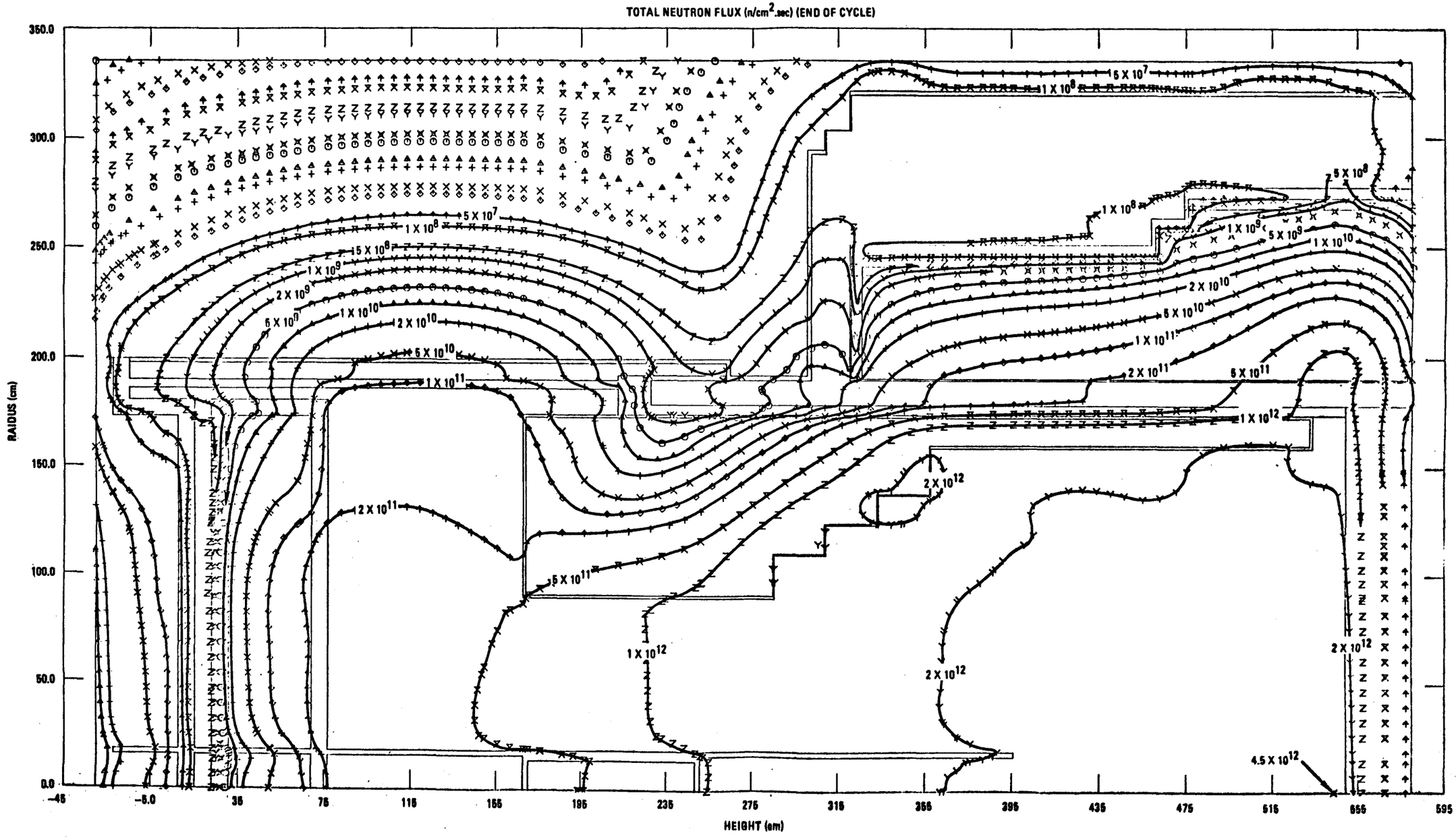

Fig. 8-3. Upper axial shield assembly isoflux contours for total neutron flux at EOC

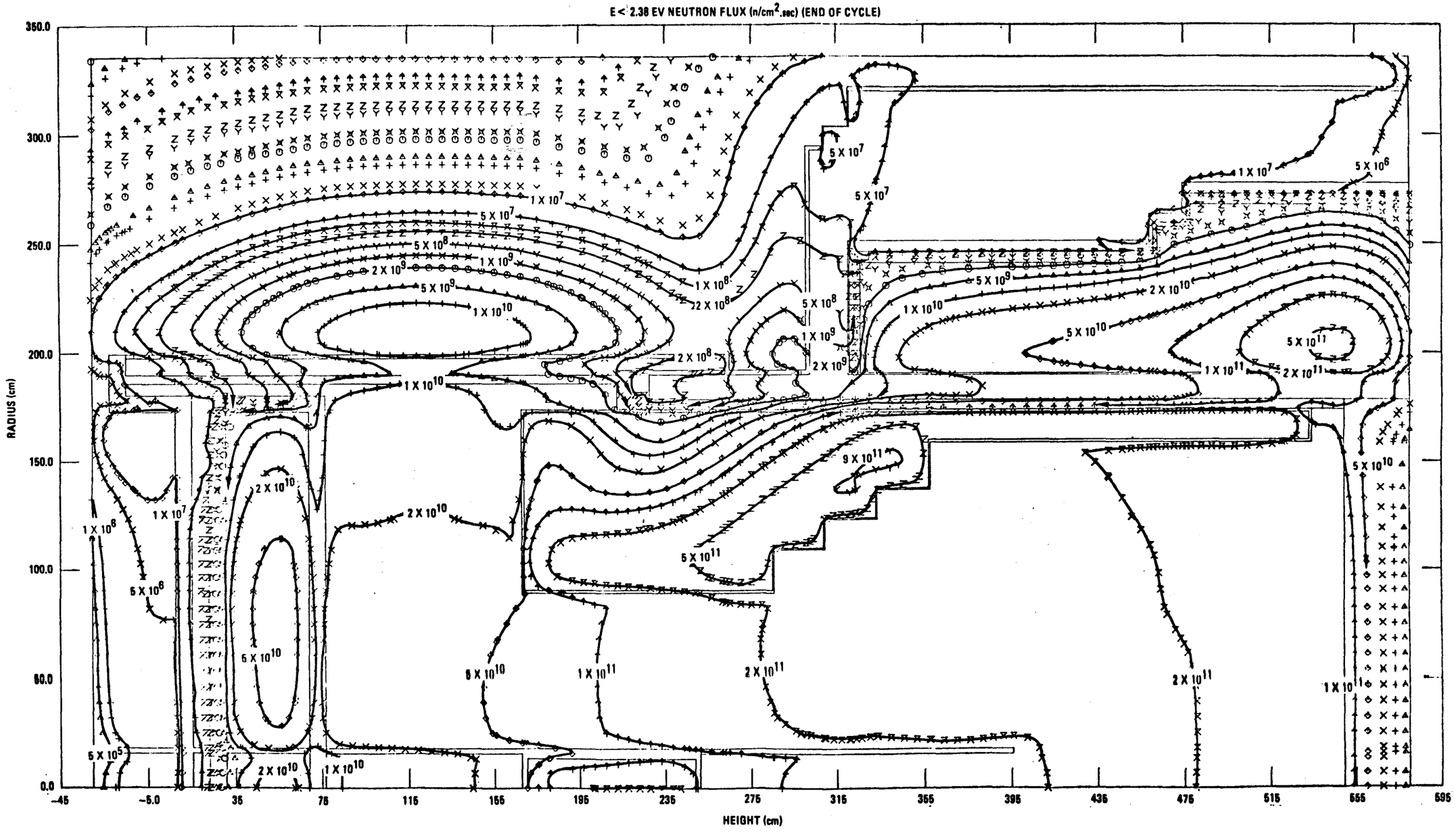

Fig. 8-4. Upper axial shield assembly isoflux contours for thermal neutron flux (E < 2.38 eV) at EOC

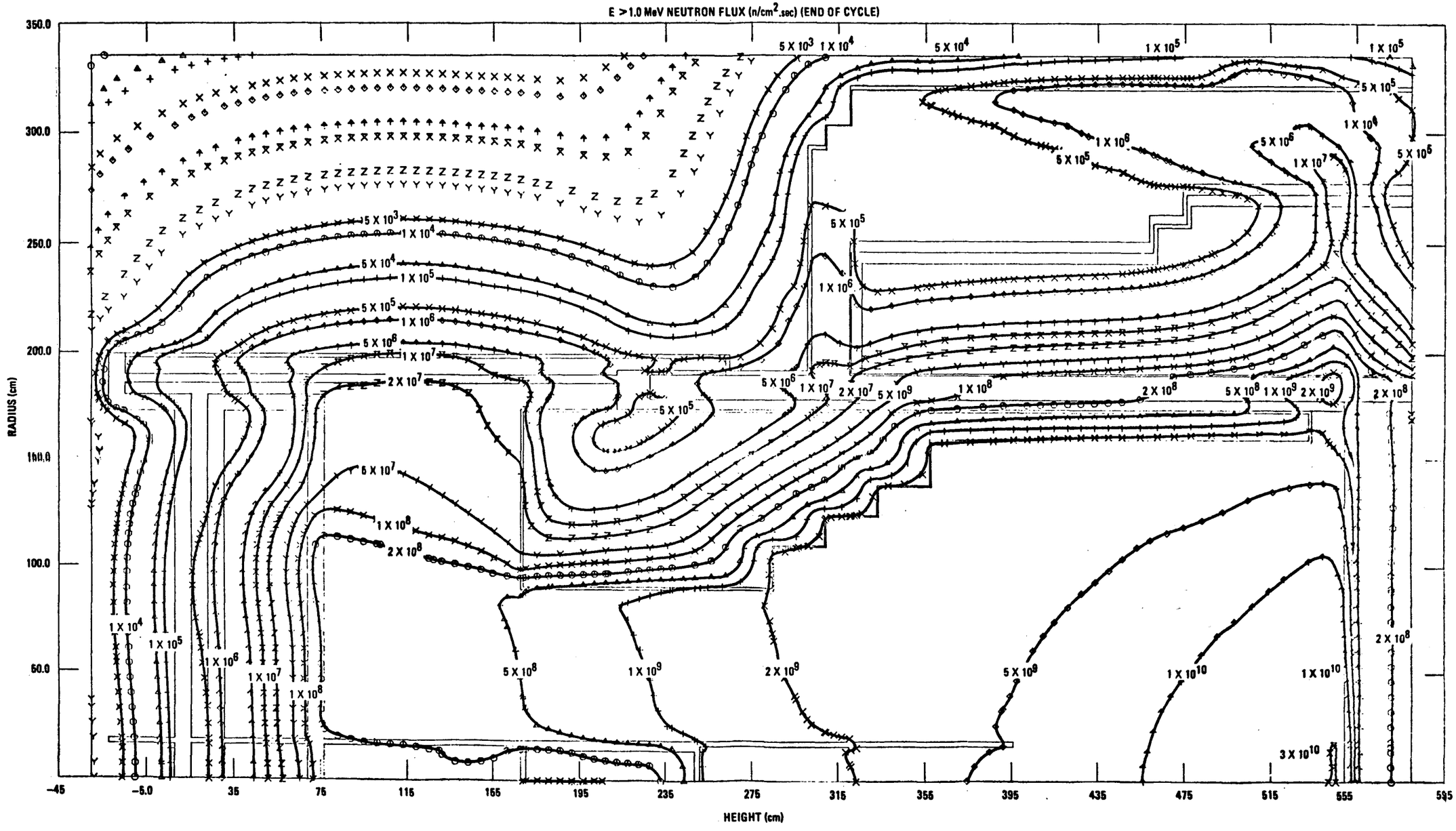

Fig. 8-5. Upper axial shield assembly isoflux contours for fast neutron flux with E > 1.0 MeV at EOC

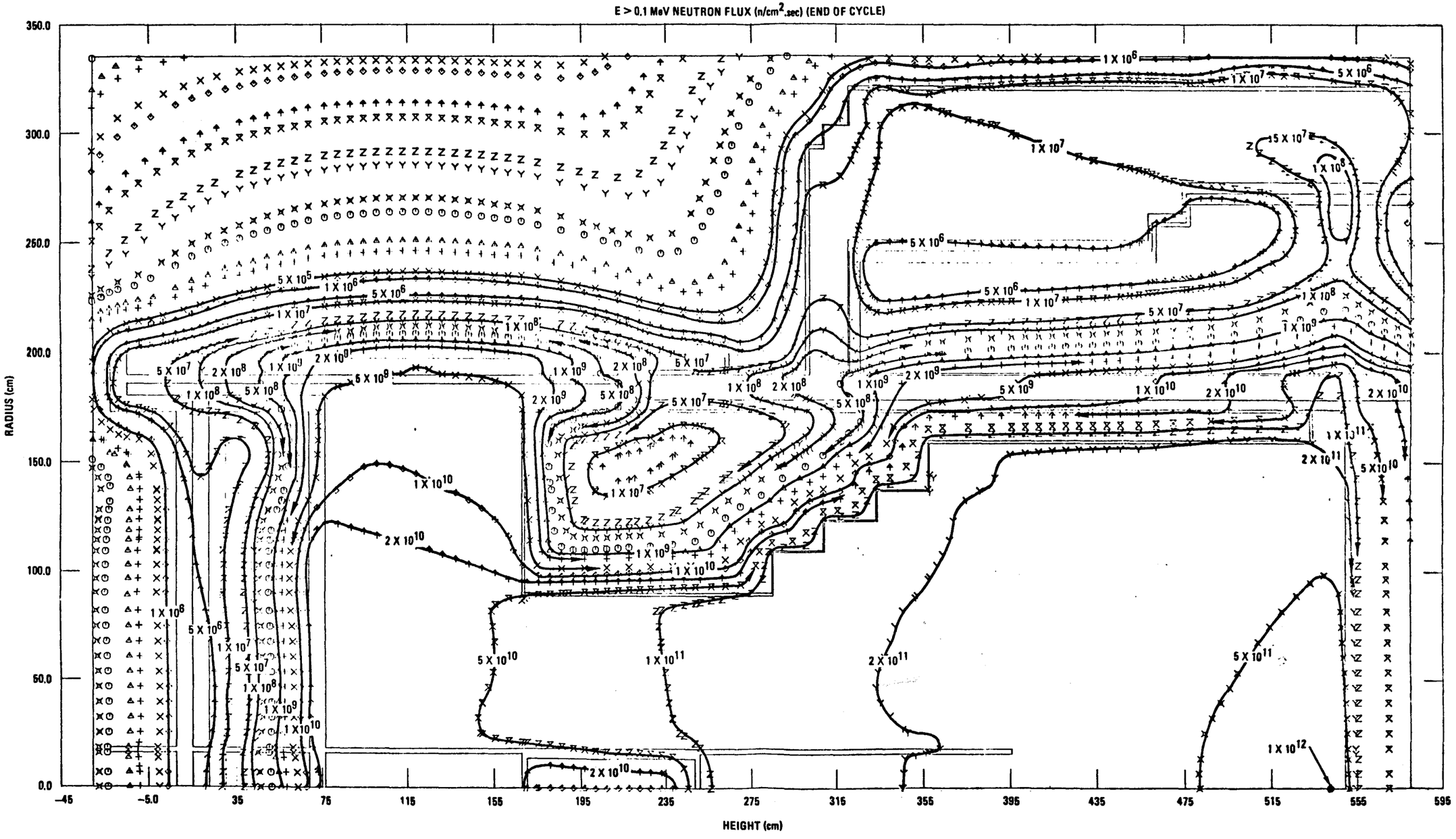

Fig. 8-6. Upper axial shield assembly isoflux contours for fast neutron flux with E > 0.1 MeV at EOC

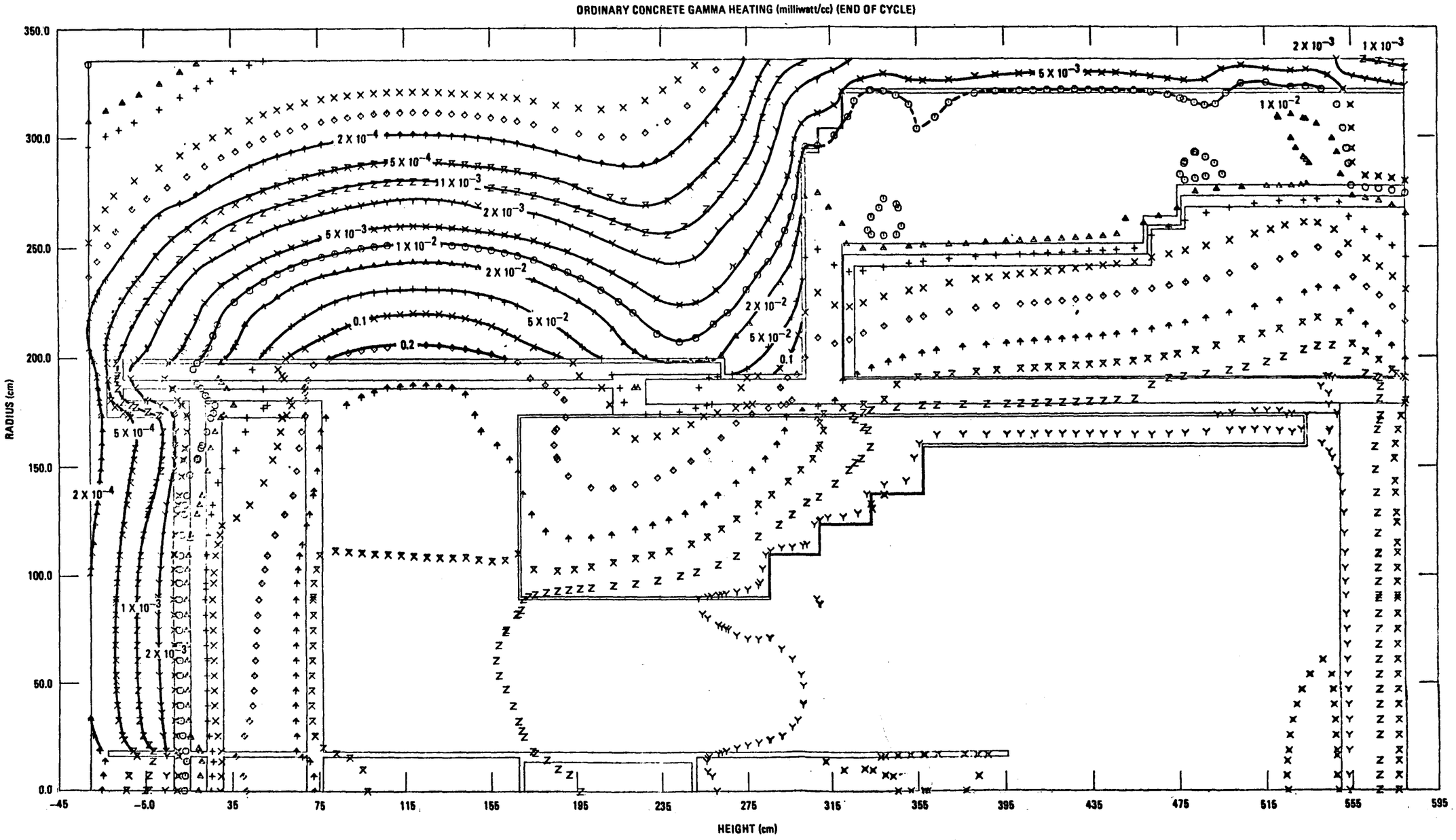

Fig. 8-7. Upper axial shield assembly isoheating contours for gamma heating in ordinary concrete at EOC

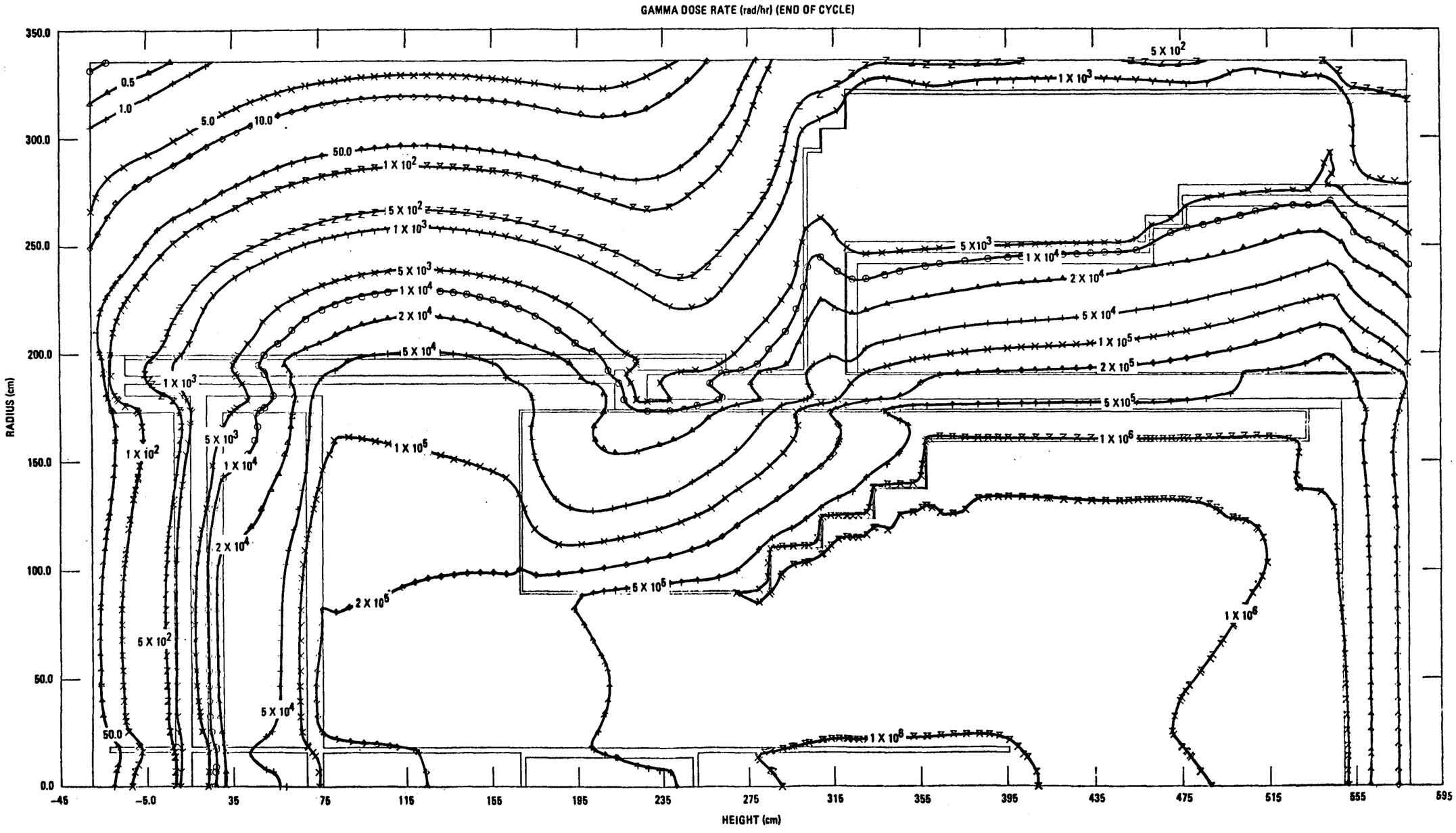

Fig. 8-8. Upper axial shield assembly isodose contours for gamma rays at EOC

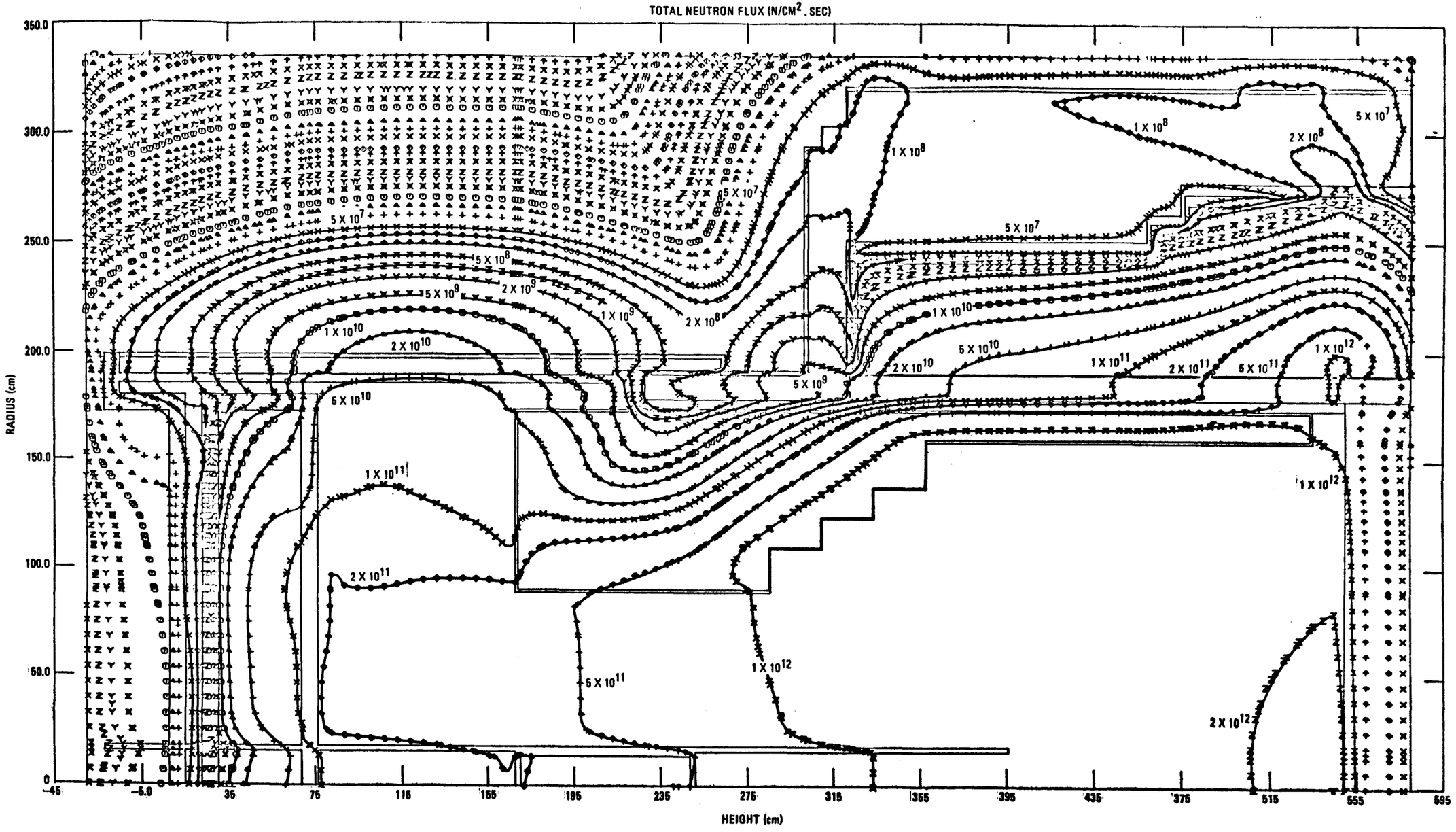

Fig. 8-9. Upper axial shield assembly isoflux contours for total neutron flux at BOC

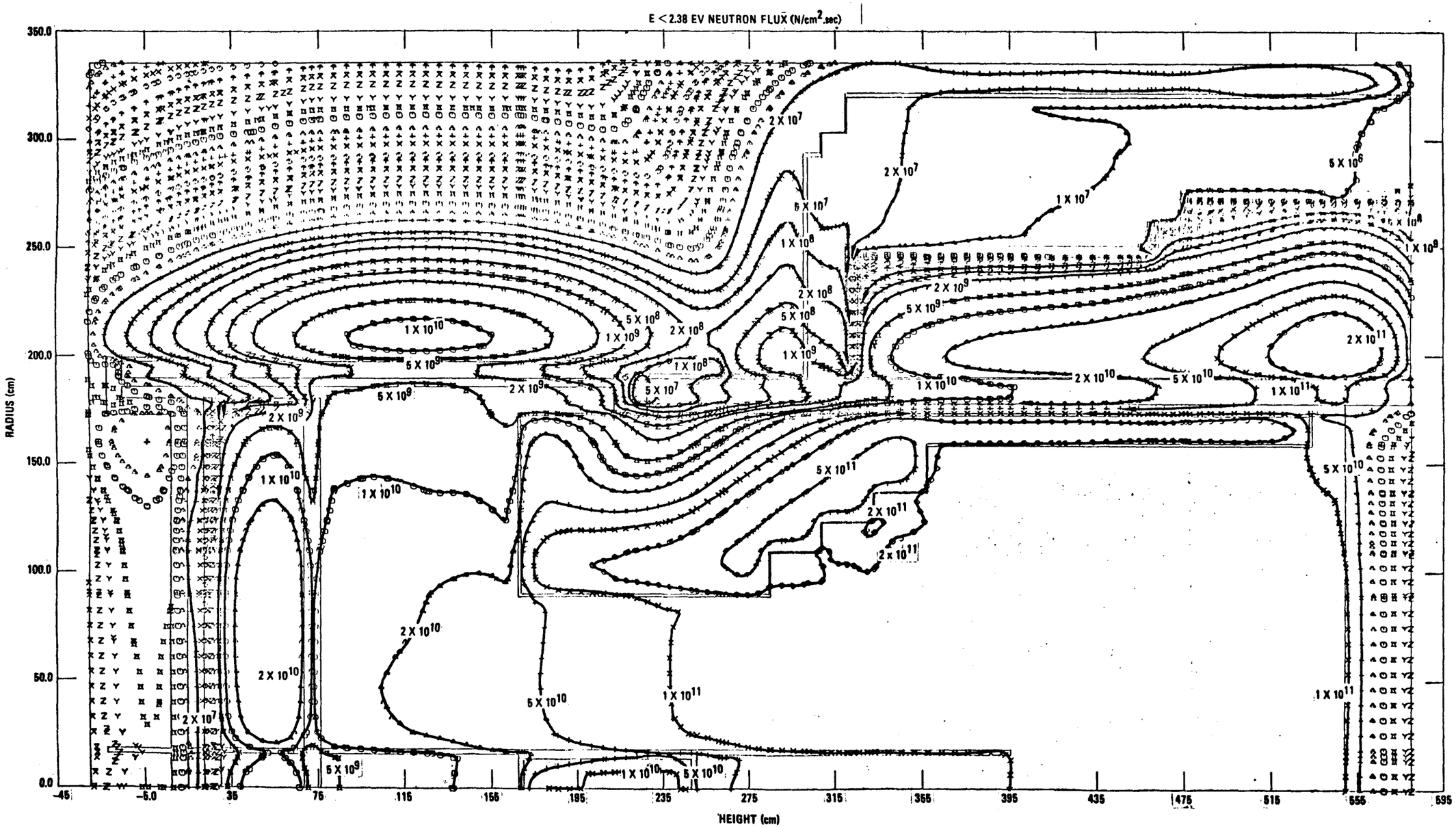

Fig. 8-10. Upper axial shield assembly isoflux contours for thermal neutrons (E < 2.38 eV) at BOC

that the maximum EOC concrete gamma heating rate of about 0.3 mW/cm^3 at the height of the inlet ducts is about a factor of 7 below the allowable rate of 2.0 mW/cm^3. Figure 8-8 shows that the gamma dose rate at the radius of the tendons at about r = 332 cm is well within the allowable dose rate. In the upper axial shield region the only damage mechanism that is near the design criteria limit is the 47°C nil ductility temperature shifts (NDTS). A preliminary assessment at the height of the inlet duct indicates a PCRV liner 47°C NDTS margin of about a factor of 2, but a factor of 2 allowance for calculational cross section uncertainties nullifies the calculated 30-yr fluence margin. Consequently, additional shielding must be considered in the next revision of the upper axial shield assembly.

8.2. IMPROVED CR-51 SHUTDOWN GAMMA DOSE RATES

The shutdown Cr-51 gamma dose rates approximated at various points in the 300-MW(e) reference design reported in Ref. 8-4 were improved by allowing for the fact that in Cr-51 decay, a 0.32-MeV gamma ray is emitted in only 9% of the nuclide disintegrations; Tables 8-1 and 8-2 correct the results in Tables 8-1 and 8-2 of Ref. 8-4. An additional change shown in Table 8-2 is that the Co-60 gamma dose rate for stainless steel is increased by an order of magnitude to explicitly reflect the 2000-ppm Co-59 expected in stainless steel. With these changes, the total gamma dose rates for stainless steel are increased by about 30%. Therefore, the conclusion that <u>in situ</u> human inspection and repair of the GCFR liner and shields is not possible has not changed.

REFERENCES

8-1. "Gas-Cooled Fast Breeder Reactor Quarterly Progress Report for the Period May 1, 1976 Through July 31, 1976," ERDA Report GA-A13975, General Atomic, August 31, 1976.

8-2. "Gas-Cooled Fast Breeder Reactor Quarterly Progress Report for the Period November 1, 1976 Through January 31, 1977," ERDA Report GA-A14240, General Atomic, February 1977.

TABLE 8-1
ACTIVATION OF A-537-B PLATE STEEL AND 304 STAINLESS STEEL IN A THERMAL NEUTRON FLUX $\phi = 10^{10}$ N/CM^2-S

Parent Nuclide				Radioactive Nuclide			Source[b] for $\phi_{th} = 10^{10}$ (n/cm^2-s)	A-537-B Plate Steel		304 Stainless Steel	
Identity	Density n_i (atoms/b-cm)	Activation Cross Section σ_{th}[a]	Reaction	Identity	Half-Life	Radiation (MeV)		Dose on Surface at t = 0 (rad/hr)	Dose on Surface at t = 72 hr (rad/hr)	Identity	t = 72 hr (rad/hr)
Fe (97.87%)											
Fe-58 (0.31%)[b]	2.57-4[c]	1.14	(n,γ)	Fe-59	45 days	γ (1.30;1.10)	2.9+6	5.3	5.1	Fe (69%)	3.6
Mn (1.17%)											
Mn-55 (100%)[b]	1.01-3	13.3	(n,γ)	Mn-56	2.6 hr	γ (0.82;1.77;2.06)	1.3+8	2.4+2	4.6-9		
Cr (0.16%)											
Cr-50 (4.35%)[b]	6.34-6	16	(n,γ)	Cr-51	27.7 days	γ (0.32) (9%)	1.0+6	0.061	0.056	Cr (19%)	6.7
Ni (0.11%)											
Ni-64 (0.9%)[b]	7.99-7	1.49	(n,γ)	Ni-65	2.52 hr	γ (1.49;1.12;0.37)	1.2+4	0.022		Ni (9%)	
Co (200 ppm)											
Co-59 (0.02%)[d]	1.7-5	37	(n,γ)	Co-60	5.3 yr	γ (1.33;1.17)	6.3+6	11.0	11.0	Co (200 ppm)	11.0

[a] Wt % of nuclide.
[b] $n_i \sigma_{th} \phi_{th}$.
[c] 2.54-4 = 2.54×10^{-4}.
[d] Wt % of steel.

TABLE 8-2

SUMMARY OF NEUTRON FLUXES AND GAMMA DOSES IN THE REFERENCE 300-MW(e) VESSEL AND INTERNALS

Point[a]	Flux		Total Fluence[b] (n/cm^2)	Material[c]	Dose (rad/hr)[d] 3 Days After Shutdown			
	Total (n/cm^2-s)	Thermal (n/cm^2-s)			Fe-59[e]	Cr-51[e]	Co-60[f]	Total[g]
A	2.5+14[h]	6.1+12	1.9+23	CS	3.1+3	3.5+1	6.4+3	9.5+3
				SS	2.2+3	4.1+3	6.4+4	7.0+4
B	1.5+13	1.2+12	1.1+22	CS	6.1+2	6.7+0	1.3+3	1.9+3
				SS	4.3+2	8.0+2	1.3+4	1.4+4
C	4.0+10	2.1+9	3.1+19	CS	1.1+0	1.2+2	2.3+0	3.4+0
				SS	7.6-1	1.4+0	2.3+1	2.5+1
D	3.6+13	3.6+12	2.7+22	CS	1.8+3	2.0+1	4.0+3	5.8+3
				SS	1.3+3	2.4+3	4.0+4	4.4+4
E	2.0+11	2.0+10	1.5+20	CS	1.0+1	1.1-1	2.2+1	3.2+1
				SS	7.0+0	1.3+1	2.2+2	2.4+2
F	1.6+13	1.0+12	1.2+22	CS	5.1+2	5.6+0	1.1+3	1.6+3
				SS	3.6+2	6.7+2	1.1+4	1.2+4
G	4.7+11	7.2+10	3.6+20	CS	3.7+1	4.1-1	7.9+1	1.2+2
				SS	2.6+1	4.9+1	7.9+2	8.65+2
H	6.9+10	1.2+10	5.2+19	CS	6.1+0	6.7-2	1.3+1	1.9+1
				SS	4.3+0	8.0+0	1.3+2	1.4+2
I	2.6+12	3.1+11	2.0+21	CS	1.6+2	1.7-1	3.4+2	5.0+2
				SS	1.1+2	2.1+2	3.4+3	3.7+3

TABLE 8-2 (continued)

Point[a]	Flux		Total Fluence[b] (n/cm^2)	Material[c]	Dose (rad/hr)[d] 3 Days After Shutdown			
	Total (n/cm^2-s)	Thermal (n/cm^2-s)			Fe-59[e]	Cr-51[e]	Co-60[f]	Total[g]
J	1.9+12	1.1+11	1.4+21	CS	5.6+1	6.2-1	1.2+2	1.8+2
				SS	3.9+1	7.4+1	1.2+3	1.3+3
K	5.3+12	1.7+11	4.0+21	CS	8.7+1	9.5-1	1.9+2	2.8+2
				SS	6.1+1	1.1+2	1.9+3	2.1+3
L	7.1+13	3.6+12	5.4+22	CS	1.8+3	2.0+1	4.0+3	5.8+3
				SS	1.3+3	2.4+3	4.0+4	4.4+4

[a] See Fig. 8-1 for location of positions in 300-MW(e) GCFR reference design.

[b] Fluence based upon 24-full power years, which equals 7.57×10^8 s.

[c] CS = carbon steel, e.g., A-537-B; SS = stainless steel, e.g., SS-304 or SS-316.

[d] Approximate gamma doses 3 days after shutdown.

[e] Saturation activity reached in about 1 yr of irradiation.

[f] Saturation activity for cobalt is based upon assumed abundances of 200 ppm in CS and 2000 ppm in SS and is reached after about 25 yr of irradiation. Fraction of saturation activity for Co-60 varies as 1-exp(-0.693 * t/5.3), where t is in yr. Fraction of saturation activity after 1 yr is about 0.123; 10 yr, about 0.73; and 20 yr, 0.93.

[g] Total doses based upon saturation activities.

[h] $2.5+14 = 2.5 \times 10^{14}$.

8-3. Mynatt, F. R., "DOT Two-Dimensional Discrete Ordinates Transport Code," Oak Ridge National Laboratory Report ORNL-CCC-89, K1694, October 1969.

8-4. "Gas-Cooled Fast Breeder Reactor Quarterly Progress Report for the Period August 1, 1977 Through October 31, 1977," ERDA Report GA-A14613, General Atomic, November 1977.

9. SYSTEMS ENGINEERING (189a No. 00585)

9.1. SYSTEMS DESIGN

Preliminary overall plant performance at full and part load was established for a plant with steam-driven main circulators (Table 9-1). Full-load plant performance was also established for a plant with electric-motor-driven main circulators (Table 9-2).

9.2. SYSTEMS INTEGRATION

A draft of the baseline data book was completed and is being reviewed. The first issue of this document is expected by the end of the second quarter of FY-78.

TABLE 9-1
GCFR DEMONSTRATION PLANT OPERATING CONDITIONS WITH STEAM-DRIVEN MAIN CIRCULATORS

	Electrical Power (%)			
	100	75	50	25
Plant performance				
Net electrical power [MW(e)]	304.3	225.0	150.0	75.0
Net plant efficiency (%)	34.98	35.27	34.35	30.67
Net heat rate (Btu/kW-hr)	9756	9675	9936	11,128
Auxiliary electric power [MW(e)]	9.0	7.0	5.2	3.4
Primary coolant system				
General reactor				
Number of loops operating	3	3	3	3
Reactor thermal power [MW(t)]	870	637.9	436.7	244.6
NSSS efficiency (%)	99.65	99.40	99.0	98.0
NSSS thermal power [MW(t)]	866.7	634.1	432.3	239.7
Total helium flow rate [kg/s (lb/s)]	709.3 (1563.9)	533.7 (1176.5)	355.8 (784.4)	194.8 (429.5)
System pressure [MPa (psia)]	8.96 (1300)	8.83 (1281)	8.69 (1260)	8.62 (1250)
System pressure drop [MPa (psi)]	0.37 (54.0)	0.21 (31.0)	0.097 (14.1)	0.03 (4.3)
Reactor pressure drop [MPa (psi)]	0.29 (42.0)	0.17 (24.2)	0.075 (10.9)	0.023 (3.4)
Reactor inlet temperature [°C (°F)]	315.6 (600)	302.8 (577)	287.2 (549)	275.6 (528)
Reactor outlet temperature [°C (°F)]	551.7 (1025)	531.1 (988)	520.6 (969)	511.7 (953)
Main helium circulators (1 of 3)				
Power [MW (hp)]	15.9 (21,250)	7.2 (9607)	2.5 (3352)	0.8 (1092)
Helium inlet temperature [°C (°F)]	302.8 (577)	295.0 (563)	283.3 (542)	273.3 (524)
Steam inlet pressure [MPa (psia)]	16.4 (2380)	12.84 (1863)	10.64 (1543)	9.79 (1420)
Steam inlet temperature [°C (°F)]	506.7 (944)	490.0 (914)	479.4 (895)	475.0 (887)
Steam outlet pressure [MPa (psia)]	9.24 (1340)	8.91 (1293)	8.78 (1273)	8.71 (1263)
Steam outlet temperature [°C (°F)]	425.0 (797)	438.9 (822)	452.2 (846)	458.3 (857)
Steam generators (1 of 3)				
Heat duty [MW(t)]	304.8	218.5	146.6	80.7
Helium pressure drop [MPa (psi)]	0.04 (6.0)	0.023 (3.4)	0.0 0 (1.5)	0.003 (0.4)
Water/steam flow rate [kg/s (lb/s)]	126.6 (277.3)	87.8 (193.5)	56.9 (125.5)	30.0 (66.1)
Feedwater pressure [MPa (psia)]	19.65 (2850)	18.60 (2697)	17.84 (2588)	17.39 (2522)
Feedwater temperature [°C (°F)]	210.0 (410)	192.2 (378)	171.7 (341)	145.6 (294)
Superheated steam pressure [MPa (psi)]	17.24 (2500)	17.24 (2500)	17.24 (2500)	17.24 (2500)
Superheated steam temperature [°C (°F)]	510.0 (950)	510.0 (950)	510.0 (950)	510.0 (950)
Secondary system				
Throttle steam pressure [MPa (psia)]	8.68 (1259)	8.68 (1259)	8.68 (1259)	8.68 (1259)
Throttle steam temperature [°C (°F)]	421.7 (791)	437.8 (820)	452.2 (846)	458.3 (857)
Exhaust moisture (% at expansion line end point)	13.4	11.7	10.2	8.0

TABLE 9-2
300-MW(e) GCFR DEMONSTRATION PLANT 100% POWER OPERATING CONDITIONS
WITH ELECTRIC-MOTOR-DRIVEN CIRCULATORS

	100% Electrical Power
Plant	
Electric power [MW(e)]	303.6
Net cycle efficiency (%)	34.90
Core	
Thermal power [MW(t)]	870
Helium pressure drop [MPa (psi)]	0.29 (42.0)
Helium flow rate [kg/s (lb/s)]	709.3 (1563.9)
Inlet temperature [°C (°F)]	315.6 (600)
Outlet temperature [°C (°F)]	551.7 (1025)
Circulator (1 of 3)	
Motor power [MW(e) (hp)]	17.6 (23,600)
Helium flow rate [kg/s (lb/s)]	236.5 (521.3)
Helium inlet pressure [MPa (psia)]	8.59 (1246)
Helium pressure rise [MPa (psi)]	0.37 (54.0)
Helium inlet temperature [°C (°F)]	302.8 (577)
Steam generator (1 of 3)	
Heat duty [MW(t)]	304.8
Helium flow rate [kg/s (lb/s)]	236.5 (521.4)
Helium pressure drop [MPa (psi)]	0.04 (6.0)
Helium inlet temperature [°C (°F)]	551.7 (1025)
Water/steam flow rate [kg/s (lb/s)]	126.6 (277.3)
Feedwater pressure [MPa (psia)]	19.65 (2850)
Feedwater temperature [°C (°F)]	210.0 (410)
Superheated steam pressure [MPa (psia)]	17.24 (2500)
Superheated steam temperature [°C (°F)]	510 (950)
Secondary	
Throttle steam flow rate [kg/s (lb/s)]	377.3 (831.9)
Throttle steam pressure [MPa (psia)]	16.55 (2400)
Throttle steam temperature [°C (°F)]	507.8 (946)
Exhaust moisture (% at expansion line end point)	13.7

10. COMPONENT DEVELOPMENT (189a No. 00586)

10.1. REACTOR VESSEL

The scope of this subtask is to ensure that the design of the PCRV and related components which contribute to the integrity of the pressure boundary is satisfactory and to test critical component configurations to make certain that they attain the design objectives. This subtask will demonstrate by analyses and tests that the PCRV and its penetrations and closures meet the design criteria, and it will also ensure that (1) the design of the thermal barrier satisfactorily protects the liner and PCRV from the effects of high temperatures and (2) the flow restrictors for the large penetrations can be developed to limit the flow of helium from the primary coolant systems to acceptable levels in the event of structural failure of a penetration or closure component.

During the last quarter the advantages and disadvantages of the two PCRV configurations with bottom-mounted helium circulators were reviewed. The PCRV configuration (D-1) with the horizontally mounted helium circulator in the bottom head is shown in Figs. 10-1 through 10-3. The PCRV configuration (D-2) with a vertically mounted helium circulator in the bottom head is shown in Figs. 10-4 and 10-5. Both configurations have the major components in separate cavities, which allows easier maintenance and servicing. The vertically mounted helium circulator does not affect the circumferential prestress system (CPS), and the arrangement with the horizontally mounted helium circulator prevents the use of wire winding in the area of the circulator penetration. Circumferential prestressing is achieved by a combination of horizontal tendons and increased number of wire layers in the channels above and below the penetrations. Proposed component changes were incorporated into the PCRV configuration (E-1), as

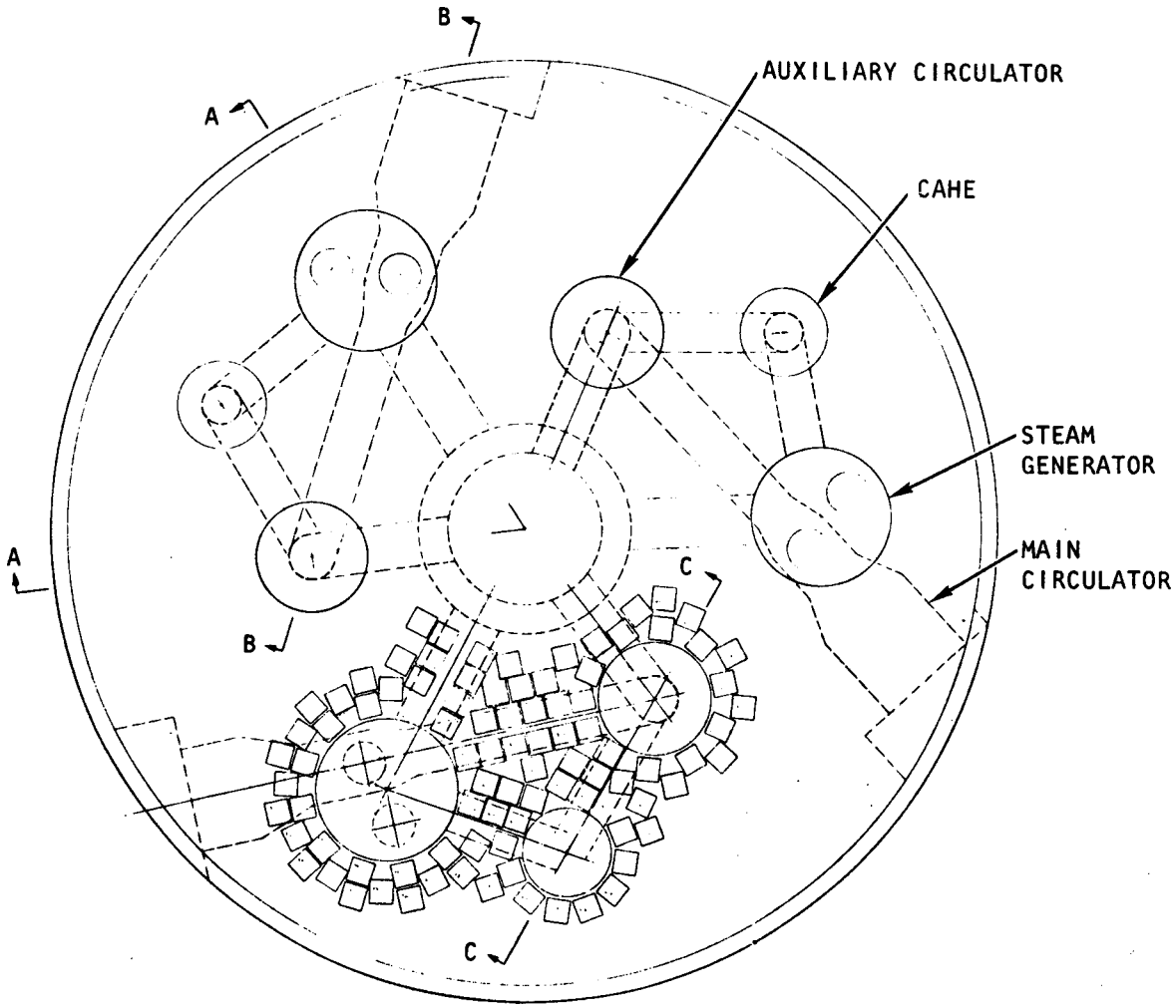

Fig. 10-1. Plan view of PCRV showing horizontal circulator mounted in bottom head (D-1)

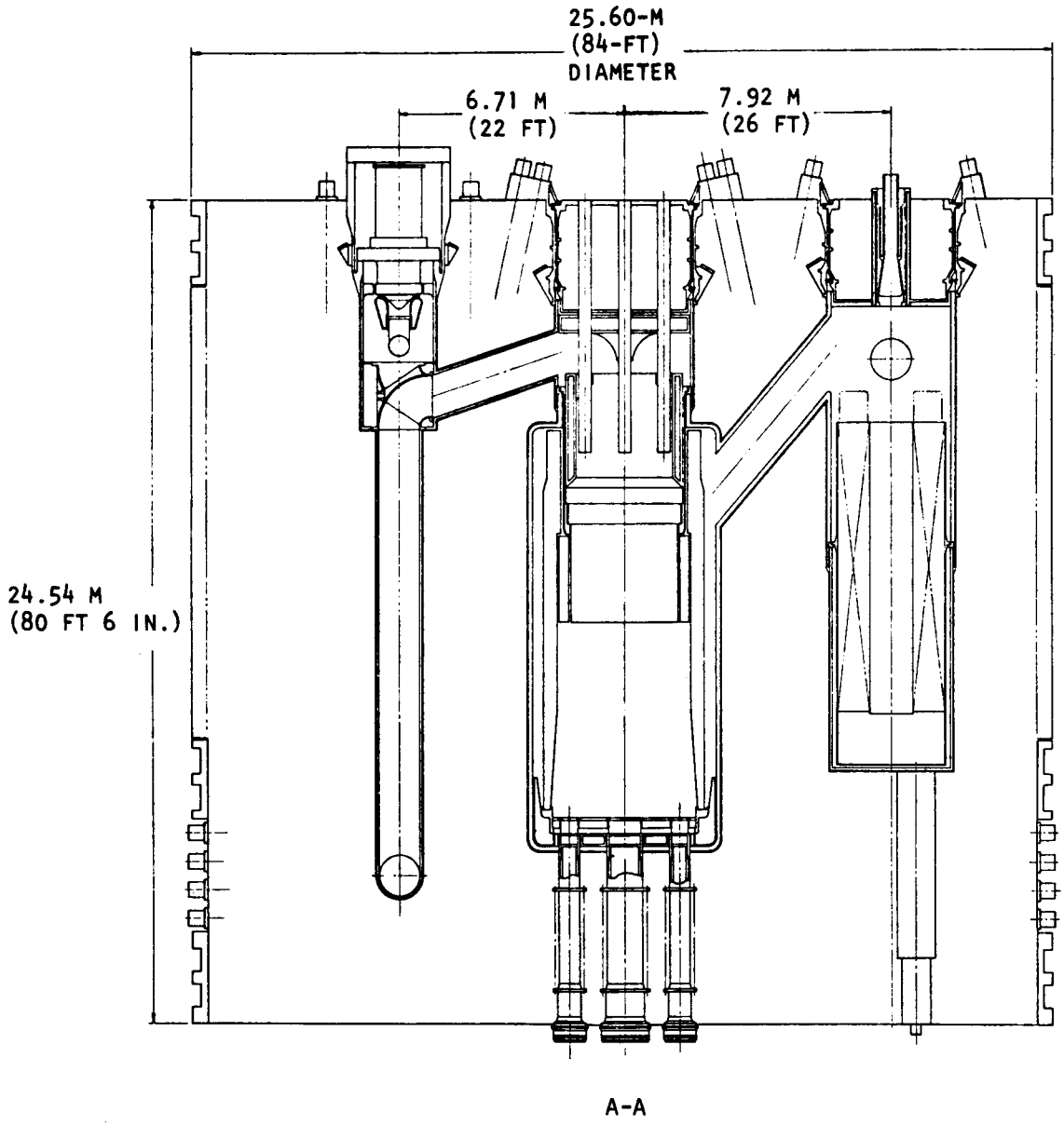

Fig. 10-2. Elevation view of PCRV showing horizontal circulator mounted in bottom head (D-1)

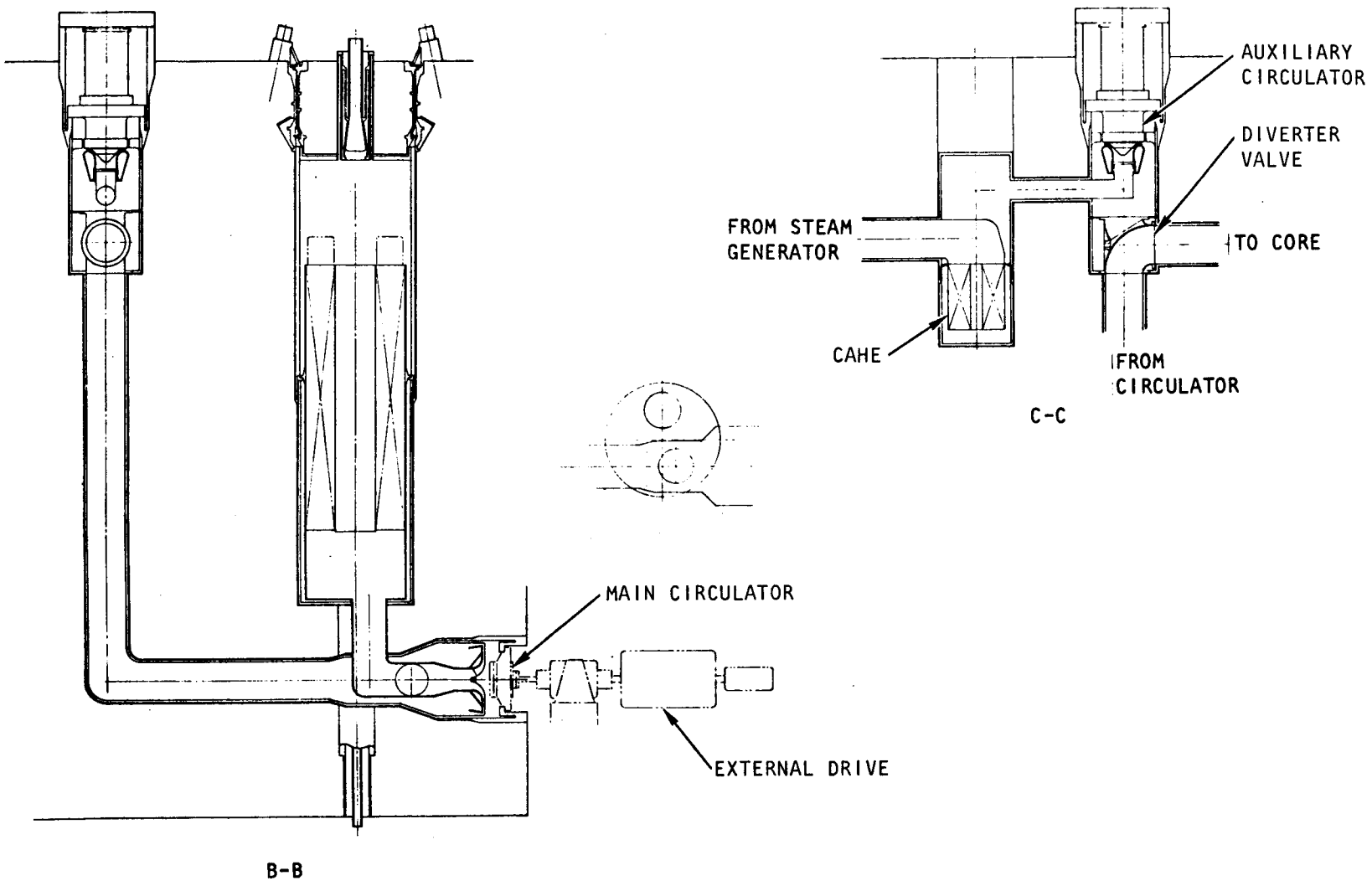

Fig. 10-3. Elevation sectional view of PCRV showing horizontal circulator mounted in bottom head (D-1)

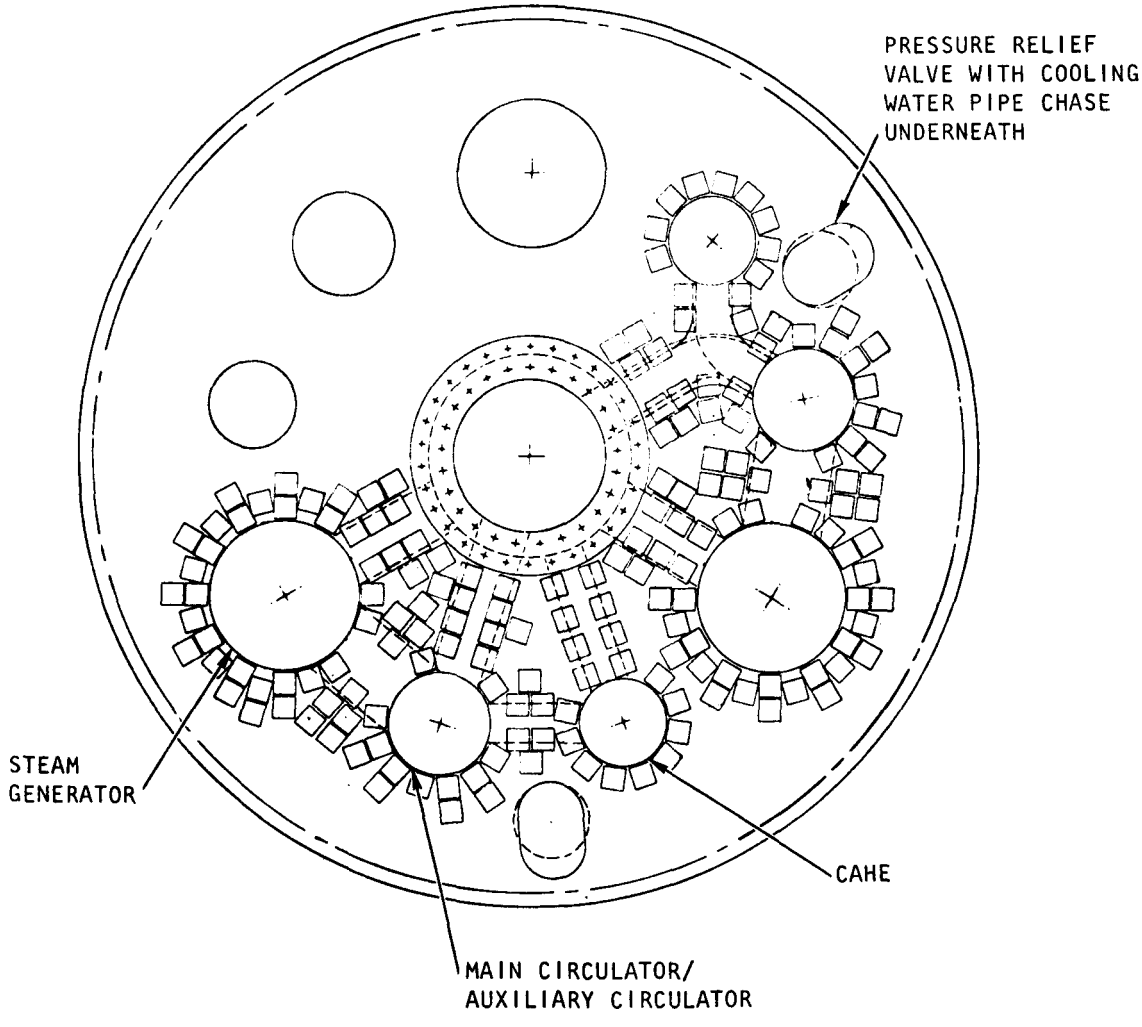

Fig. 10-4. Plan view of PCRV showing vertical circulator mounted in bottom head (D-2)

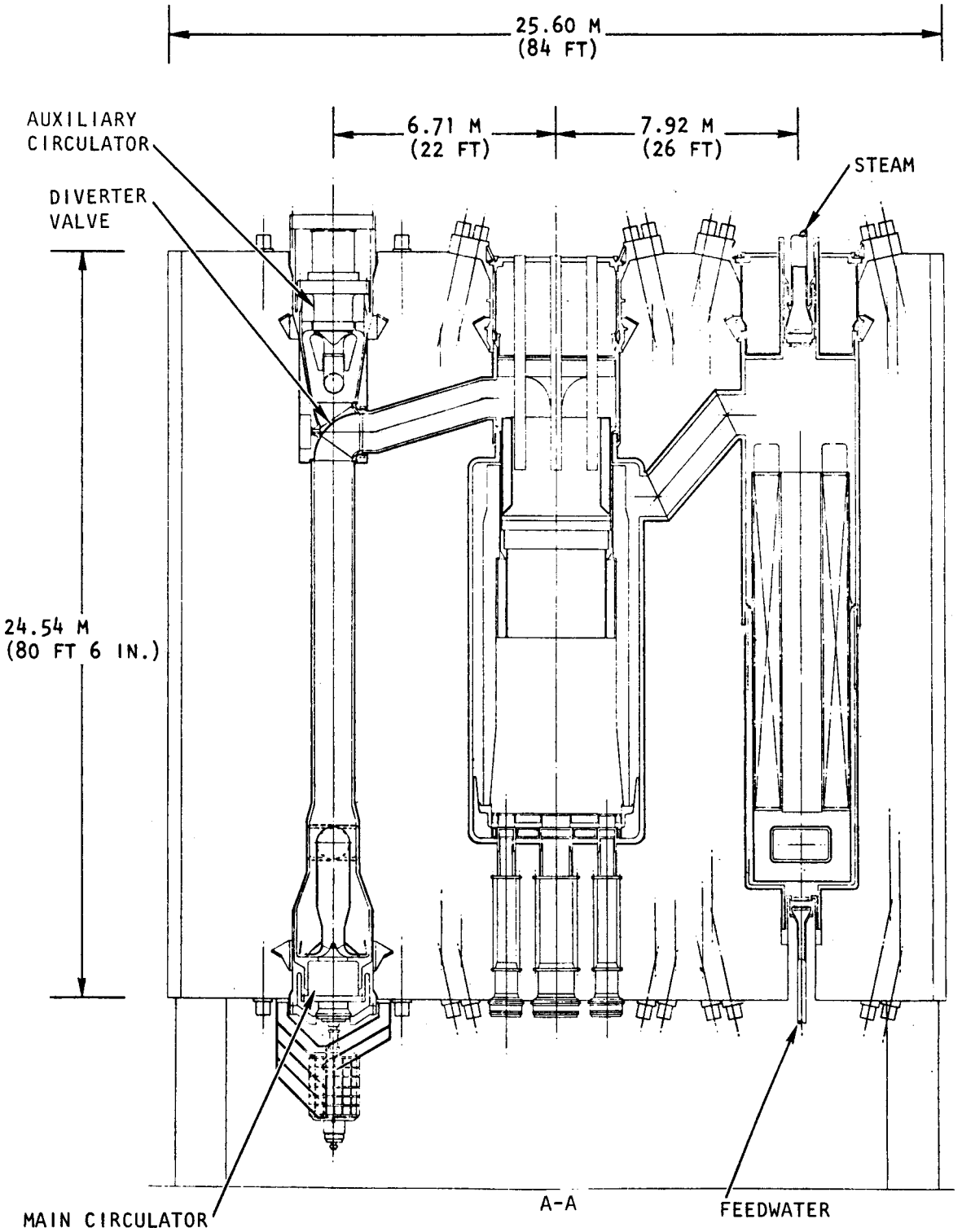

Fig. 10-5. Elevation view of PCRV showing vertical circulator mounted in bottom head (D-2)

shown in Fig. 10-6. This configuration includes the proposed PAFC crucible with a single refueling penetration in the bottom head. To avoid any potential problems involved with the use of a diverter valve, the secondary coolant loop is separated from the primary coolant loop as shown in Figs. 10-7 and 10-8 (PCRV configuration E-2).

To determine whether there would be structural or component limitations on raising the coolant pressure, an investigation was conducted on a 1200-MW(e), 8.88-MPa (1288-psia) commercial plant design for normal working pressures (NWPs) of 10.34, 12.07, and 13.79 MPa (1500, 1750, and 2000 psia). Preliminary PCRV dimensions are given in Table 10-1. No major problems were found in the PCRV structure, but the increased pressure caused the central cavity penetration ring to have to accommodate three rows of tendons, which in turn presents the problem of manufacturing such a large forging. From an engineering point of view, the PCRV designs for higher pressure are feasible.

During this quarter, work continued on configuration E-2 (Fig. 10-7) with a vertical circulator mounted in the bottom head. A plan view of the bottom head (Fig. 10-9) was prepared to determine the feasibility of tendon placement. In coordination with the design development of the helium circulators, a PCRV configuration (F-1) was generated to incorporate the radial flow helium circulator, as shown in Figs. 10-10 and 10-11. This configuration is basically that of Fig. 10-6 except that it incorporates a radial flow helium circulator.

A test on the 1/15-scale half-depth model of the steam generator cavity closure was performed at ORNL. This model is identical to the one tested in January 1977 except that the depth was halved and the shear console inside the closure removed. The model went through 10 cycles of pressurization to 10.08 MPa [(1462 psi = 1 maximum cavity pressure (MCP)] without any sign of inelastic behavior. This was followed by an ultimate capacity test in which the pressure was increased at 3.45-MPa (500-psi) increments.

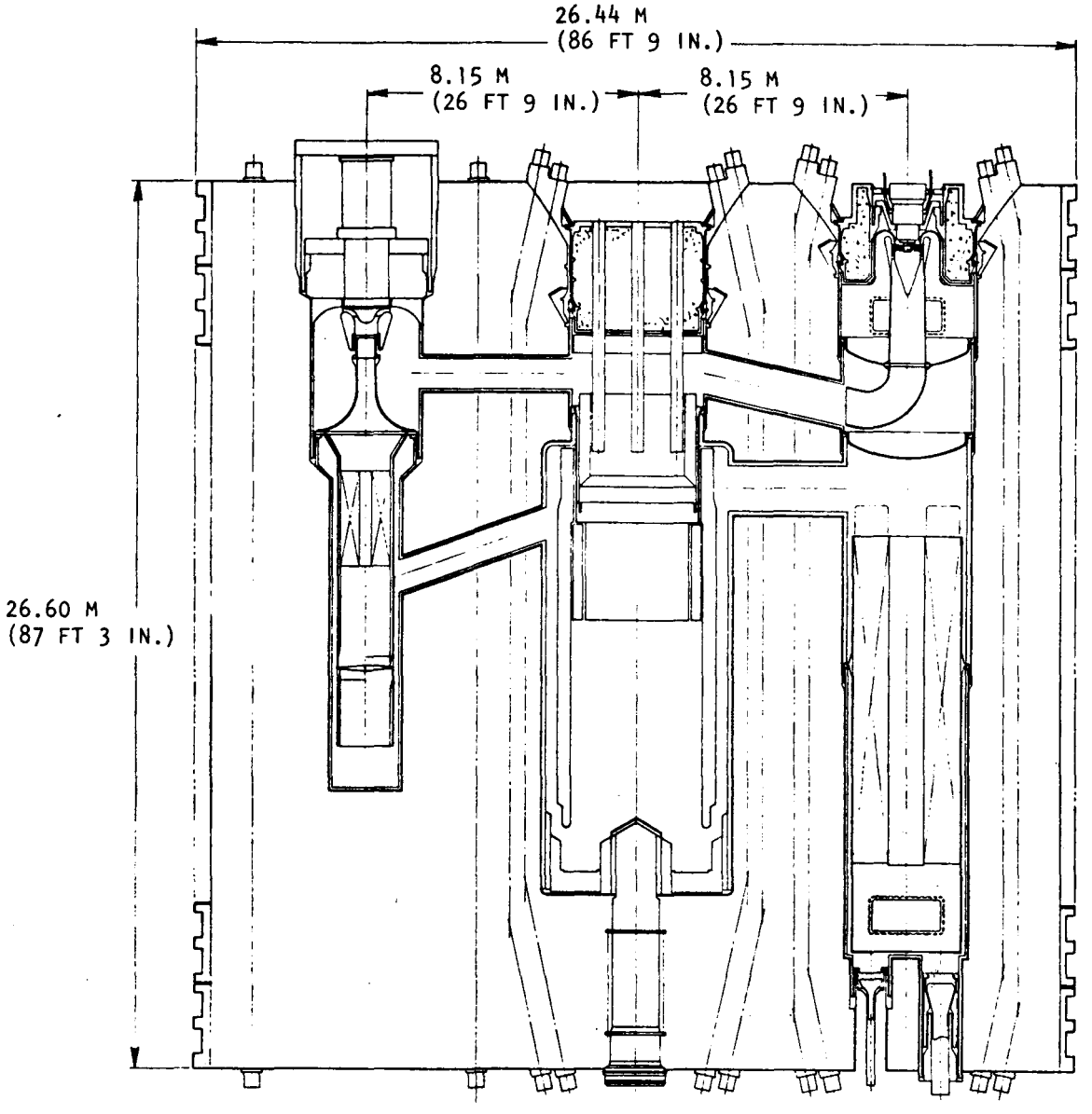

Fig. 10-6. Elevation view of PCRV showing PAFC crucible and single cavity penetration (E-1)

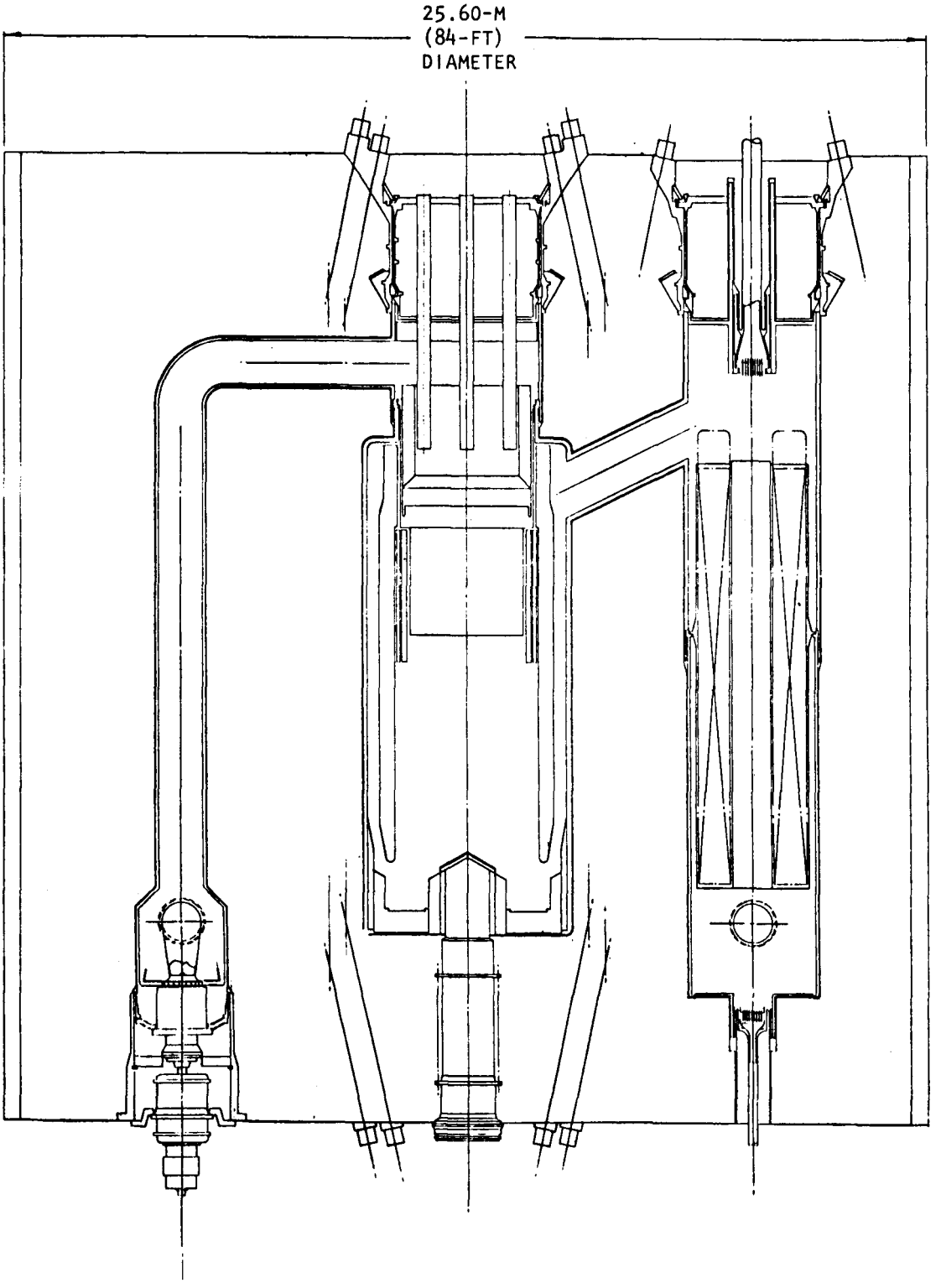

Fig. 10-7. Elevation view of PCRV with vertical circulator mounted in bottom head (E-2)

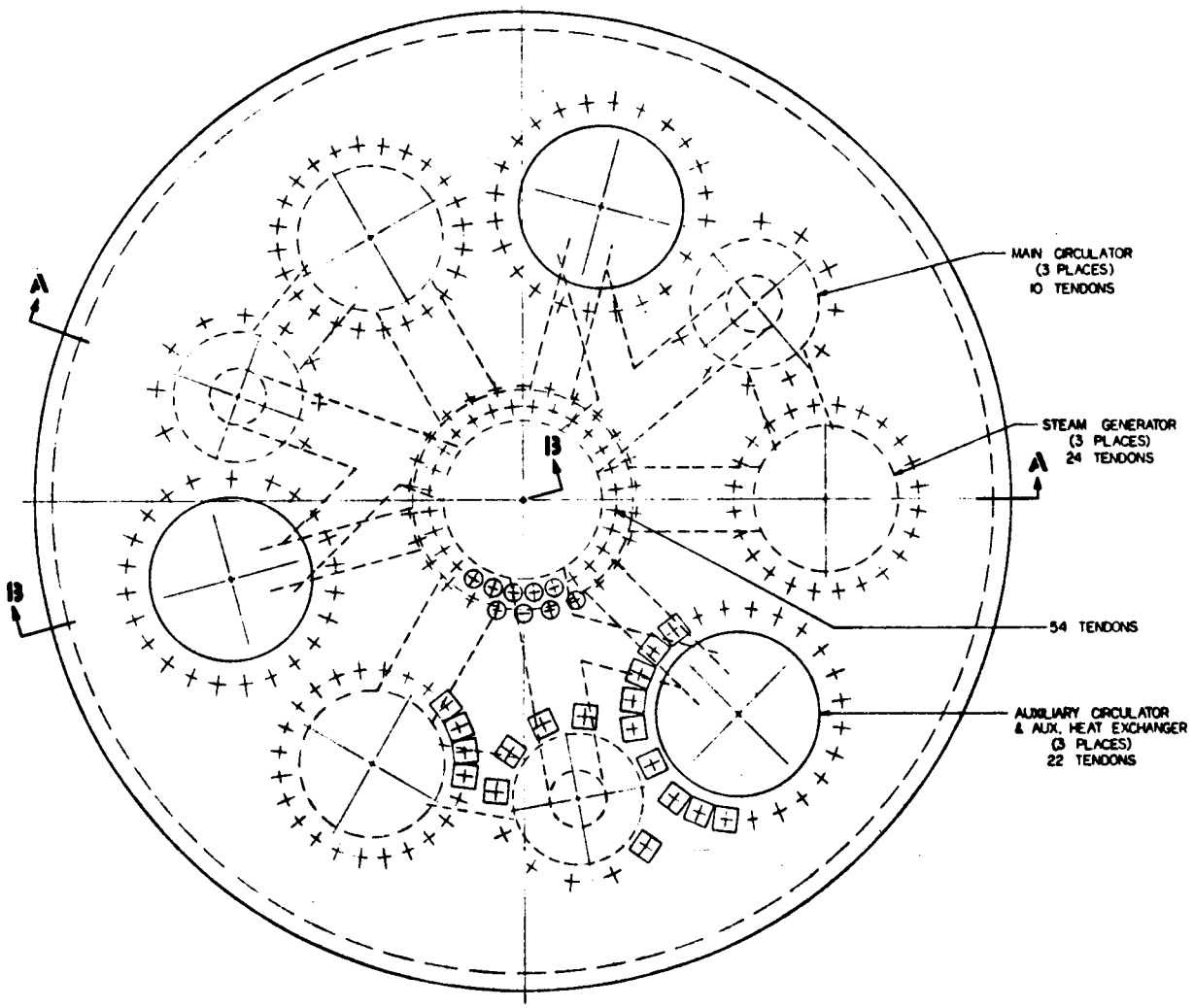

Fig. 10-8. Plan view of PCRV with vertical circulator mounted in bottom head (E-2)

TABLE 10-1
PCRV GEOMETRIES FOR INCREASED PRESSURE: 1200-MW(e) GCFR
HIGH-PRESSURE STUDY

Design Parameter	Normal Working Pressure			
	8.88 MPa (1288 psi)	10.34 MPa (1500 psi)	12.07 MPa (1750 psi)	13.79 MPa (2000 psi)
Design pressure [MPa (psi)]	9.77 (1417)	11.38 (1650)	13.27 (1925)	15.17 (2200)
Maximum cavity pressure [MPa (psi)]	10.07 (1460)	11.72 (1700)	13.67 (1983)	15.62 (2266)
PCRV diameter [m (ft-in.)]	31.70 (104-0)	33.98 (111-6)	36.72 (120-6)	39.54 (129-9)
PCRV height [m (ft-in.)]	31.70 (104-0)	33.52 (110-0)	35.68 (117-1)	37.84 (124-2)
Core cavity diameter [m (ft-in.)]	8.13 (26-8)	8.13 (26-8)	8.13 (26-8)	8.13 (26-8)
Steam generator diameter [m (ft-in.)]	4.22 (13-10)	4.22 (13-10)	4.22 (13-10)	4.22 (13-10)
Reactor head [m (ft-in.)]	7.42 (24-4)	8.63 (28-4)	10.05 (33-0)	11.50 (37-9)
Steam generator head [m (ft-in.)]	3.86 (12-8)	4.50 (14-9)	5.23 (17-2)	5.97 (19-7)
Tendons (linear prestress system)	522	660	780	932
Wire wrap (circumferential prestress system)	16 layers	18 layers	21 layers	24 layers
PCRV volume [m^3 (yd^3)]	24,865 (32,721)	30,233 (39,780)	37,558 (49,418)	46,213 (60,806)

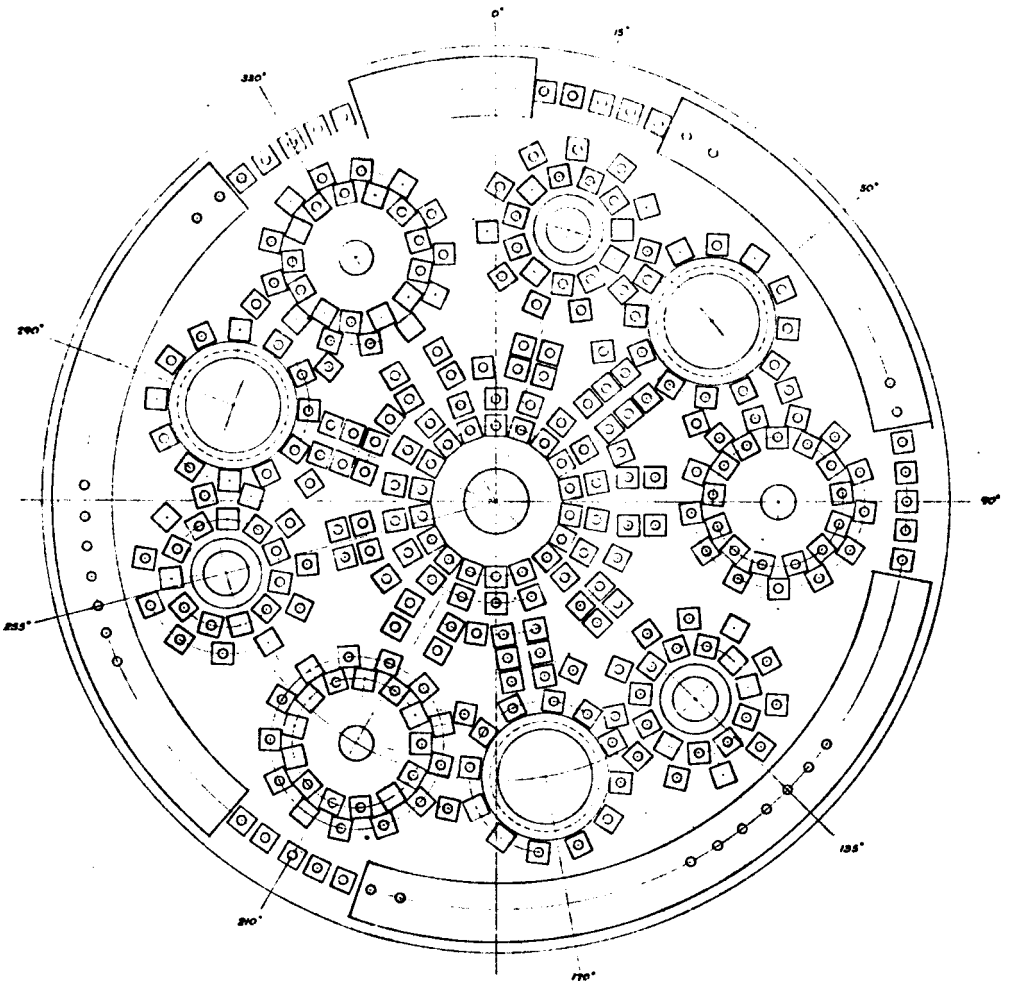

Fig. 10-9. Plan view of bottom head of PCRV with vertically mounted helium circulator (E-2)

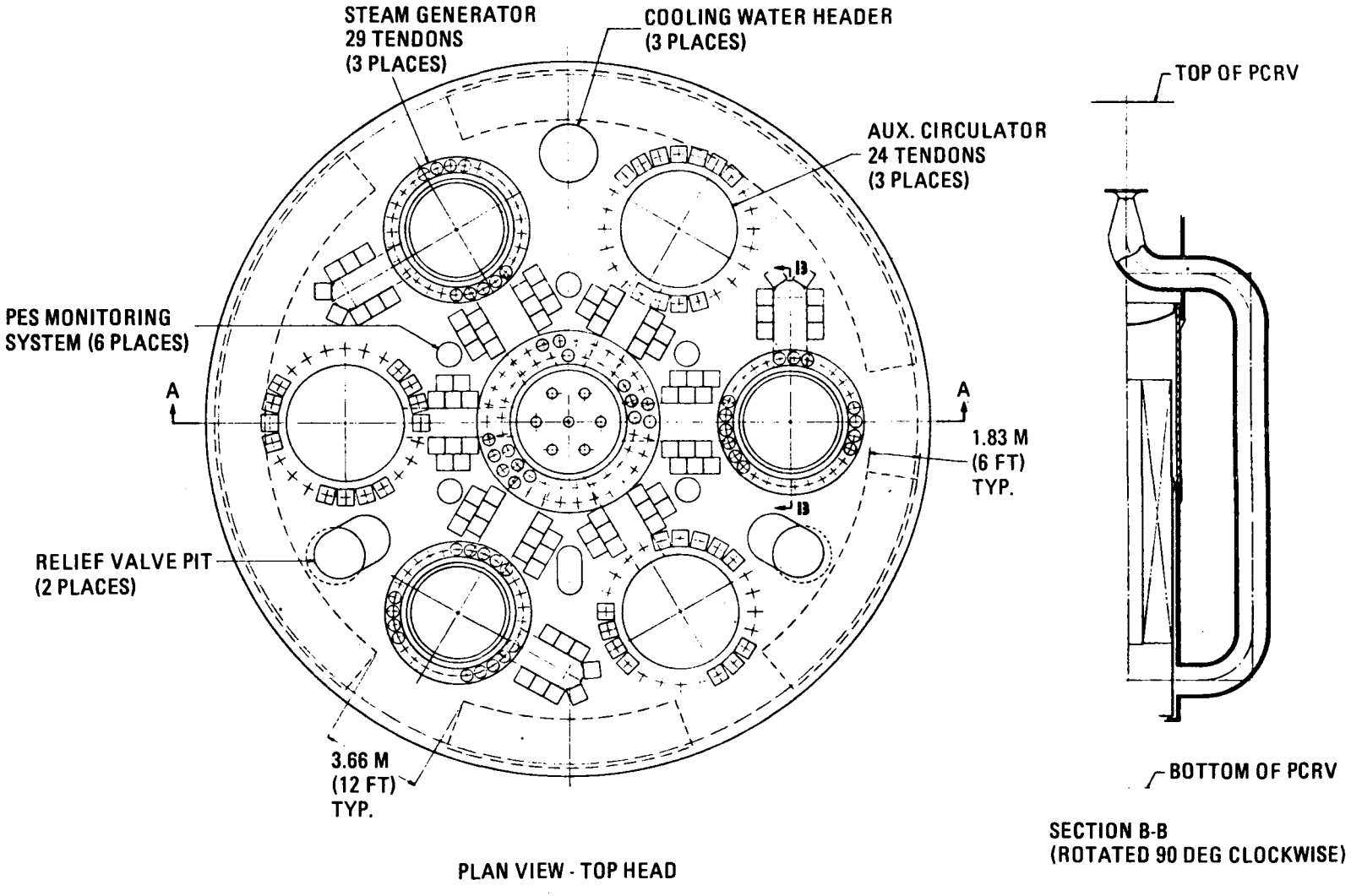

Fig. 10-10. Plan view of PCRV with radial flow circulator in top head (F-1)

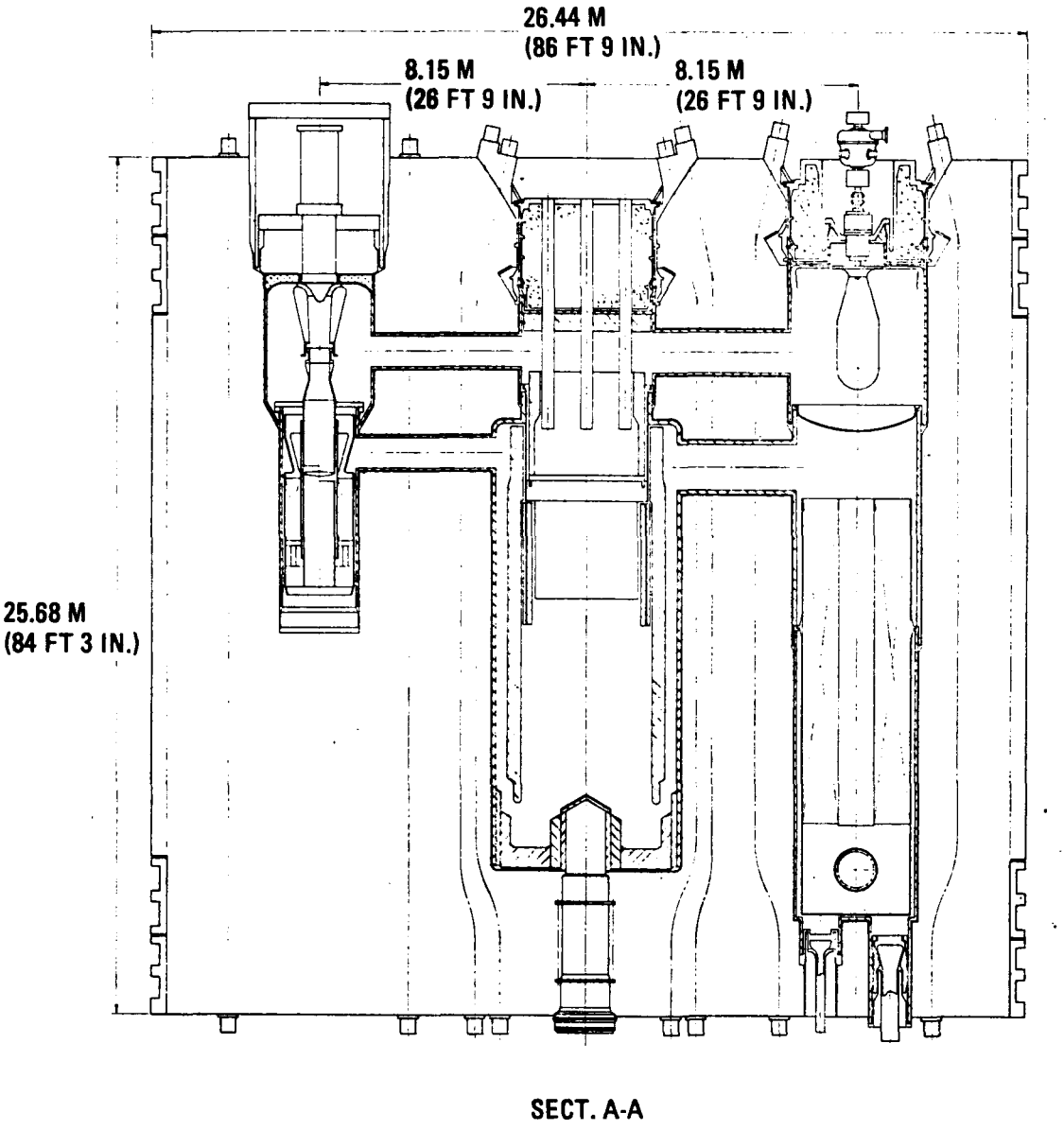

Fig. 10-11. Elevation view of PCRV with radial flow helium circulator in top head (F-1)

The model failed in shear at 98.3 MPa (14,250 psi = 9.75 MCP), demonstrating a substantial overpressure capacity. Significant nonlinearity was recorded for a number of strain and displacement gages prior to the failure, although no crack was visible.

The overall closure test program was reviewed by GA and ORNL. In accordance with an agreement resulting from this review, GA completed a review of the proposed 1/15-scale core cavity closure test model and recommended testing of a revised model which would simulate a 4.57-m (15-ft) diameter closure with 37 penetrations having 0.36-m (14-in.) diameters. GA also agreed to review the overall test program in three months. Preliminary design and analysis for various types of hold-down systems for the cavity closures are in progress. In addition to use of a toggle system, concrete and steel containment rings are being considered as possible alternatives.

Conceptual design studies for a molten core retention and cooling system continued. The high-temperature crucible (HTC) concept utilizes a buildup of ceramic materials to form an annular crucible that will contain the molten debris and maintain liner temperatures below 177°C (350°F) during the PAFC period. Magnesia was chosen for the outer layers because of its high melting point, resistance to thermal shock and thermochemical erosion, machinability, and shielding effectiveness. The graphite layers were introduced to form a refractory bed and shielding layer which will tend to distribute heat more uniformly to the liner cooling system. Thermal barrier materials were used against the liner to provide protection during normal operation.

The heavy metal bath (HMB) design consists of an annular crucible with a large mass of depleted uranium at the bottom and magnesia plates around the periphery. The core debris decay heat will melt the depleted uranium to the point where only a solid crust remains at the liner, and the higher-temperature and less dense core materials will remain on top. Decay heat

is removed by internal convection, conduction, and radiation to the reactor cooling system. The depleted uranium was chosen for its low melting point, high boiling point, shielding effectiveness, and high density.

The envelope for an HTC core catcher which interfaces with a single refueling penetration has been defined. The core catcher envelope and its effect on the PCRV core cavity are largely controlled by the estimated molten oxide fuel pool depth limit. A pool depth in excess of 0.46 m (18 in.) is required.

Several design concepts for replaceable thermal barriers (RTBs) which were developed in conjunction with the high-temperature gas-cooled reactor (HTGR) (Ref. 10-1) were reviewed and evaluated in relation to GCFR design characteristics and operational requirements. The general applicability of these concepts to the GCFR was tentatively confirmed, and it was concluded that the two RTB concepts considered to be most favorable for the HTGR should be equally viable for the GCFR.

10.2. CONTROL AND LOCKING MECHANISMS

The reactivity control and core locking concept described in Ref. 10-2 is continuing to be pursued on a design detail level which would allow fabrication of a proof-of-principle model of the locking mechanism. Design activity is also being applied to developing the control rod drive mechanism configuration in more detail so that it is compatible with the core locking principle. The impact of this new concept on areas such as PCRV design, core design, and safety are being evaluated. The results of this ongoing effort are required to provide an adequate technical base for establishing a new baseline reference design for the core locking and reactivity control system.

10.3. FUEL HANDLING DEVELOPMENT

Under contract to GA, Aerojet Manufacturing Company (AMCO) formally presented the results and recommendations of its three-month study on the

conceptual design of GCFR ex-vessel fuel transfer equipment; namely, the fuel transfer cask (FTC), lifting transfer cask (LTC), and cask transfer car (CTC). The studies included system operations, facility interfacing and requirements, cask shielding designs, spent fuel cooling, and ex-vessel fuel handling.

The fuel handling system requirements for the nuclear island and their impact on the facility was identified. Preliminary RECS input on schedule, manpower, and budget was completed for the fuel handling ex-vessel machines and the in-vessel machines. In addition, the RECS planning and scheduling input effort for the fuel storage and shipping equipment was reinitiated.

A preliminary report (Ref. 10-3) was submitted to ERDA which summarizes the conceptual design status of a fuel handling machine which utilizes a single-bottom PCRV penetration for refueling. The primary advantage of this system is that it reduces the number of PCRV bottom penetrations from three to one, which simplifies the core catcher design and could lessen machine installation and refueling time. Its primary disadvantage is that a more complex fuel handling machine is required.

Conceptual design layouts of top and bottom grapples showing the required fuel assembly interfaces have been prepared, and a preliminary analysis for cooling the fuel assembly in the fuel handling machine has been completed. Studies on simplification and packaging of the fuel handling machine drive mechanisms within the single PCRV penetration envelope diameter of 1219 mm (48 in.) are continuing.

10.4. CORE SUPPORT STRUCTURE

The purpose of this subtask is to assure the availability of the structural analysis methods and materials mechanical behavior required to assess the structural integrity of the GCFR core support structure under all anticipated operational and safety-related loading conditions in the GCFR environment.

Work accomplished during last quarter included a finite-element thermal stress analysis of the grid plate, a study on shortening the length of the core support cylinder, and a grid plate parametric study. Seismic analysis of the core support structure was continued.

During this quarter a draft of the section on the core support for the GCFR baseline data book was completed, and an effort to establish preliminary routing of the PES was initiated. The seismic and thermal stress analyses were continued.

10.4.1. Seismic Analysis of GCFR Core Support Structure With Effects of Core Assemblies

Most of the seismic analysis of the core support structure with attached core assemblies has been completed. The analysis consists of the following parts:

1. Theoretical derivation.

    a. Axisymmetric free and forced vibrations of grid plate with attached core assemblies.

    b. Asymmetric free vibration of grid plate with attached core assemblies.

    c. Axisymmetric and asymmetric free vibration of core support cylinder and grid plate.

2. Finite-element analysis.

    a. Axisymmetric free and forced vibrations of grid plate with attached core assemblies.

    b. Asymmetric free and forced vibrations of grid plate with attached core assemblies.

10.4.2. Thermal Stress Analysis of Grid Plate

A simplified model was used in the theoretical derivation, and it is assumed that (1) elastic thin plate theory is applicable, (2) the grid plate is perforated throughout the whole plate (the in-plane force generated by the solid rim is added later using the compatibility condition), and (3) the temperature distribution is axisymmetric but varies linearly in the axial direction. The finite-element thermal stress analysis of the grid plate was accomplished using a two-dimensional axisymmetric solid element. The orthotropic material behavior in the perforated region was simulated, and the solid rim was modeled using real material properties. Discrete temperature loading was assigned to each node of the model. The results show that the deflections due to the thermal load are small, and the corresponding change in reactivity is well within the acceptable limits. The stresses were found to satisfy the requirements of the ASME Code. Reasonably good agreement was found between the two different methods.

10.5. REACTOR SHIELDING ASSEMBLIES

The purpose of this task is to design and develop analytical methods and experimental programs to evaluate the reference design of the reactor shields. This evaluation is expected to cover nonuniform temperature distribution, material behavior, seismic effects, hydrodynamic tests, and structural analysis. This design study also includes alternate shield configurations so that a satisfactory and optimized shield design can be developed.

During the previous quarter two separate thermal analyses were performed. One analysis concerned shielding criteria for maximum allowable gamma ray heating of the PCRV concrete, and the other was performed to evaluate the feasibility and predict the temperatures of an alternate shielding configuration in which the outer radial shield is positioned against the thermal barrier. A decision on placement has not been made. During this quarter the major emphasis was placed on two items: (1) alternate inner shield design and (2) design criteria.

10.5.1. Alternate Inner Shield Design

A quantitative assessment of potential radiation damage problem areas indicated that the radiation levels in the support structures for the replaceable inner shields would exceed allowable levels over the 30-yr plant life. Accordingly, alternate design concepts were developed to make the inner radial shield support structures, as well as the shield assemblies themselves, replaceable at refueling intervals.

10.5.2. Design Criteria

The design criterion for the residual total elongation (RTE) of the stainless steel components of the inner radial shield was examined. This investigation suggests that the RTE requirement should be lowered to 1%, the value used for the fuel assembly duct material, since the inner radial shield is being designed for replacement at refueling intervals.

10.6. MAIN HELIUM CIRCULATOR, VALVE AND SERVICE SYSTEM

The purpose of this subtask is to develop the helium circulator and its service system and main loop isolation valve to demonstrate performance and reliability by testing under anticipated operating conditions. The overall objective for FY-78 is to continue first-of-a-kind conceptual design and performance analysis of the circulator reference design configuration (external steam drive), the service system, the loop isolation valve, and the alternate electric drive selected from studies made in FY-77. Preliminary layouts of the circulator components will be made and requirements established for bearings, shaft critical speeds, seal flow rates, helium and nitrogen buffer systems, drains, jet pumps, inlet, diffusor, shaft coupling, rotor dynamics, and aerodynamic performance. The work outlined will provide input to the circulator pretest analysis task.

The results of alternate main circulator studies and selection of a new reference design have been presented to DOE, HBA, and the Program Review Committee (PRC). The new reference design is a radial compressor with

water-lubricated bearings and an external series flow steam turbine drive; an alternate electric motor drive will be developed. It was agreed that circulator test facility schedule 44 needs to be accelerated to meet the circulator development plan schedule. Since the test facility contains critical components which need to be developed, additional funding through construction, planning, and design resources has been requested to develop a steam compressor and an alternate vertical electric motor drive. These items are critical for selecting options for the test facility development program.

10.6.1. Main Helium Circulator

A summary report (Ref. 10-4) was completed on the past reference design, which consisted of a two-stage axial flow helium compressor driven by a two-stage series flow steam turbine. Integral designs and external drive configurations were included. A summary report (Ref. 10-5) covering the alternate design studies and reference design selection for the GCFR main helium circulator was also completed.

A preliminary layout, Fig. 10-12, was completed for a radial compressor using water-lubricated bearings. A single-stage design operating at 3600 rpm will satisfy the GCFR flow and installation requirements and is within normal design practice for radial flow compressors. The circulator operating requirements are listed in Table 10-2.

A study of main loop cooling during the design basis depressurization accident (DBDA) has shown that overspeed is required for an extended period of cooling. It is possible to make the DBDA the design condition and accept the resulting efficiency penalty for pressurized operation. Table 10-2 shows the GCFR main helium circulator reference design parameters for the two conditions, and Table 10-3 shows the main dimensions and design parameters when designed for pressurized operation at 3600 rpm and a DBDA

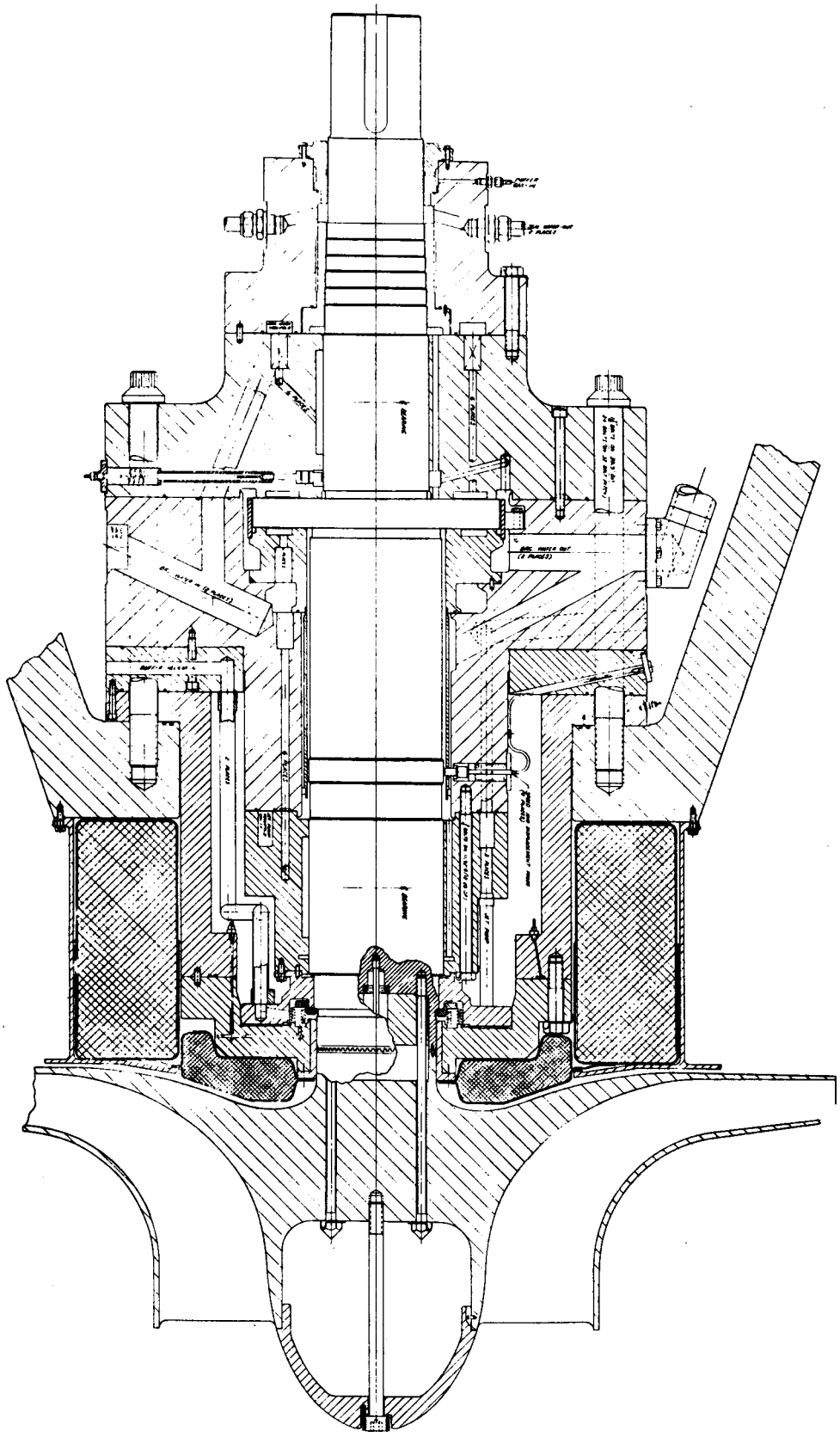

Fig. 10-12. Single-stage radial helium compressor

TABLE 10-2
GCFR MAIN CIRCULATOR REQUIREMENTS

	DBDA	Pressurized Operation
Mass flow rate [kg/s (lbm/s)]	4.536 (10.0)	245.85 (542.0)
Inlet pressure [kPa (psi)]	158.5 (23.0)	8618.5 (1250.0)
Outlet pressure [kPa (psi)]	171.2 (24.83)	9032.0 (1310.0)
Pressure rise ratio	0.079565	0.048
Volumetric flow rate [m^3/s (ft^3/s)]	33.64 (1188.1)	33.33 (1176.98)
Inlet temperature [K (°R)]	303 (577)	303 (577)

TABLE 10-3
GCFR MAIN HELIUM CIRCULATOR DESIGN PARAMETERS

	DBDA	Pressurized Operation
Type	Radial	Radial
Drive	Electric	Electric
Fluid	Helium	Helium
Speed (rpm)	4500	3600
Estimated efficiency (%)	80	75
Tip diameter [m (in.)]	1.549 (61)	1.549 (61)
Tip width [mm (in.)]	65.3 (2.57)	65.3 (2.57)
Eye diameter [m (in.)]	0.734 (28.9)	0.734 (28.9)
Hub diameter [m (in.)]	0.367 (14.45)	0.367 (14.45)
Adiabatic head [kJ/kg (Btu/lbm)]	93.1 (40)	57.9 (24.9)
Volumetric flow [m^3/s (ft^3/s)]	33.64 (1188.1)	33.33 (1176.98)
Specific speed	66.2	75.2

speed of 4500 rpm. The main disadvantage of this design is the large diameter of the impellers, as shown in Figs. 10-13 and 10-14.

To reduce the overall dimensions of the electric motor and the compressor, an alternate version of the main helium circulator was studied for design point operation at 4500 rpm with no overspeed capability for DBDA conditions. The specific speed under these conditions is still in the range for which the centrifugal compressor is optimum. For minimum impeller diameter, a design with radially oriented impeller blades was chosen, and a slip factor of 0.9 was assumed. The resulting design has an impeller tip diameter of 1219 mm (48 in.), and satisfactory blade channel proportions are obtained with a constant meridional velocity of 111 m/s (363 ft/s). With this meridional velocity and an inlet radius ratio of 0.333, the inlet dimensions for minimum relative Mach number are

Inlet tip (eye) diameter	660 mm (26.000 in.)
Inlet hub diameter	220 mm (8.667 in.)
Inlet tip vane angle (measured from plane of rotation)	35.4 deg

The exit tip width is 79.4 mm (3.125 in.), and the rotor has 28 vanes.

A conventional diffuser with a single row of circular arc vanes was designed for the compressor. The tentative design, which is subject to further optimization, has 23 vanes with an inlet angle of 24.4 deg, an inner diameter of 1383 mm (54.45 in.), and an exit diameter of 2282 mm (89.85 in.). The vaned diffuser is preceded by a vaneless space with a radial length of 164 mm (3.2 in.) and a geometric area ratio of 2.5.

A preliminary layout, Fig. 10-15, was completed for a separate multistage steam turbine drive unit for powering the radial flow compressor through an external coupling. The turbine has eight stages to obtain reasonable blade characteristics and sufficient power to operate the

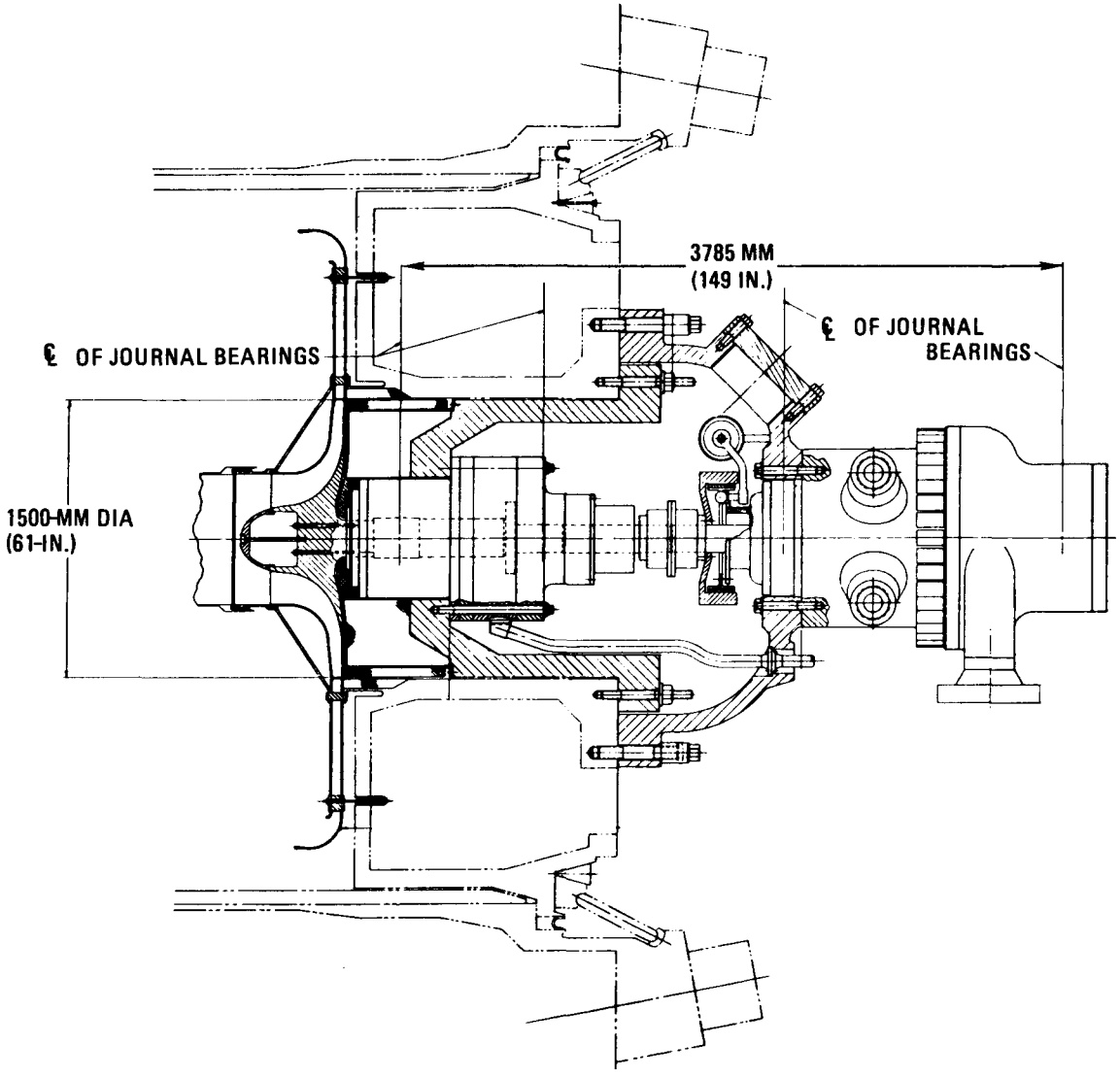

Fig. 10-13. Installation of radial flow circulator with external steam turbine drive

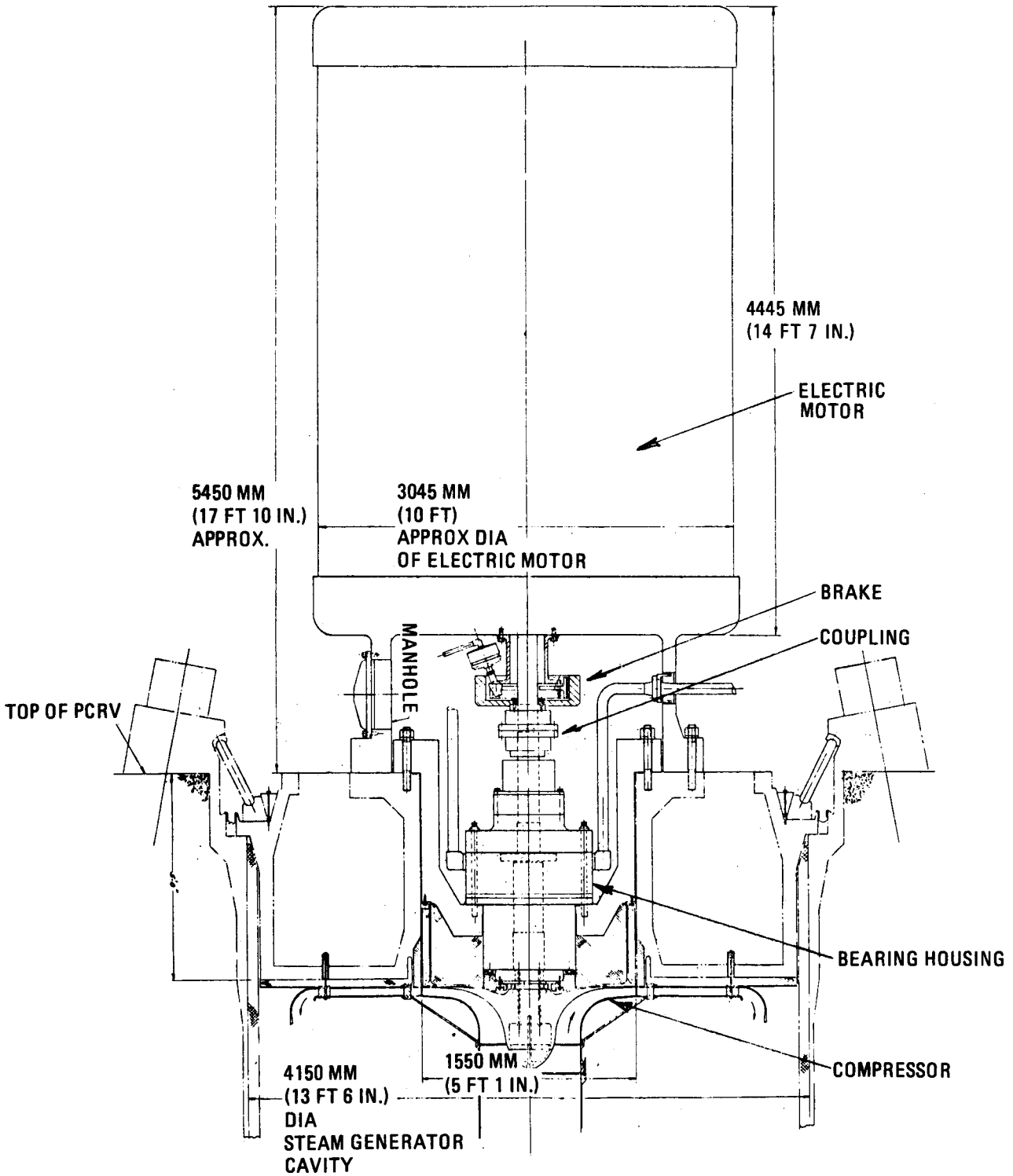

Fig. 10-14. Installation of radial flow circulator with external electric motor drive

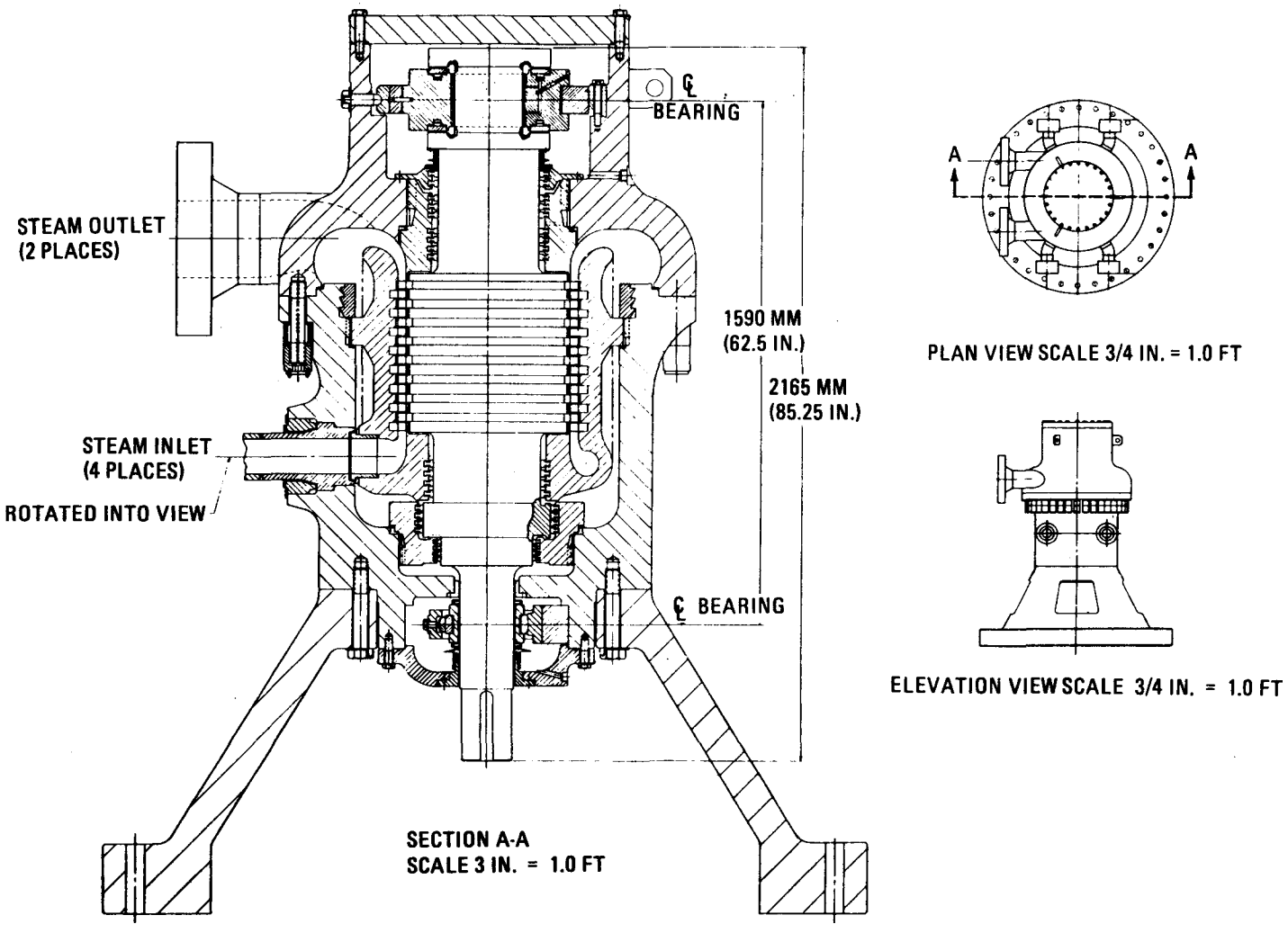

Fig. 10-15. External steam turbine drive for radial flow circulator

compressor at 3600 rpm. A barrel-type design similar to the Fort St. Vrain main plant high-pressure turbine was adopted because of its compact design, advantageous seal arrangements, and ease of support and alignment in a vertical installation compared with a turbine design with a split housing. The turbine is vertically installed on top of the steam generator cavity plug (Fig. 10-13). The design point characteristics for the turbine are given in Table 10-4.

10.6.2. Electric Motor Drives

The reference design evaluation has specified the electric motor circulator drive as a viable alternative to the series steam turbine, and as a result, an electric-motor-driven circulator test facility concept must be developed. A major component of this facility is the vertically mounted circulator compressor drive motor. This motor is sized at 18 MW (24,000 hp) and will rotate at 3600 rpm. Vertical motors in this size range have not been built before, and areas of technical concern are bearings, rotor integrity, cooling, motor controls, and the rotating shaft seal between the test vessel helium and the atmosphere. Construction, planning, and design funds have been requested from DOE to support an electric motor and controls technical feasibility and cost study by a generator manufacturer. The present electric motor configuration, shown in Fig. 10-14, has the following features:

1. A vertically mounted 18-MW synchronous electric motor. The motor operates in the containment building atmosphere, but is totally enclosed and water cooled. A solid-state, variable-frequency power supply is used to control motor speed; the maximum motor speed is 470 rad/s at full power. The motor uses conventional oil bearings.

2. A mechanical brake which can be applied at 260 rad/s to stop the circulator rapidly in case of failure of the compressor bearing water supplies.

TABLE 10-4
TURBINE FULL-POWER OPERATING CHARACTERISTICS FOR AN EXTERNAL EIGHT-STAGE TURBINE DRIVE

Inlet pressure	16.4 MPa (2380 psi)
Inlet temperature	512°C (943°F)
Outlet pressure	9.13 MPa (1325 psi)
Outlet temperature	419°C (785°F)
Flow rate	127 kg/s (278 lb/s)
Tip diameter	550 mm (21.4 in.)
Hub diameter	496 mm (19.6 in.)
Tip velocity	104 m/s (340 ft/s)
Rotating speed	3600 rpm
Efficiency	82%
Power	17.4 MW (23,900 hp)

3. Shaft coupling. Studies are currently being conducted to determine if this should be a rigid or a flexible coupling.

4. The compressor assembly utilizes water bearings similar to those of previous GCFR circulator designs and a radial flow impeller. A high-pressure shaft seal at the coupling end of the bearing housing uses controlled leakage of water and jet pump scavenging to seal the 9-MPa (1310-psi) PCRV pressure. Bellows-actuated face seals are used when the circulator is shut down.

10.6.3. Loop Isolation Valves

A layout of an alternate loop isolation valve which utilizes a rolling ball to shut off the primary coolant loop when the flow reverses has been completed (Fig. 10-16). This valve would be located in the cross duct entrance. Another design, Fig. 10-17, is for a valve on the exit of a radial flow compressor diffuser. This valve utilizes a hexfurcated diffuser discharge and six movable, flow-actuated cover plates. The purpose of these studies is to develop viable alternatives for the main and auxiliary loop isolation valve for the GCFR.

A split butterfly concept and a pneumatically actuated concept have also been developed. The butterfly concept consists of a Fort St. Vrain design flapper valve located in the compressor inlet. It is equipped with linkages and an overriding valve actuator mechanism. The valve is normally self-actuating, and the override mechanism is manually initiated. Valve position indication is accomplished through dual fluidic devices, one for each valve blade. The pneumatically actuated valve is also a Fort St. Vrain design flapper valve and is located in the compressor inlet. It is equipped with dual gas turbine (Terry turbine type) actuators, one for each valve blade. There are no moving parts in the actuator and no physical contact between actuator and valve blades. Valve position indication is accomplished from dual fluidic devices, one for each valve blade.

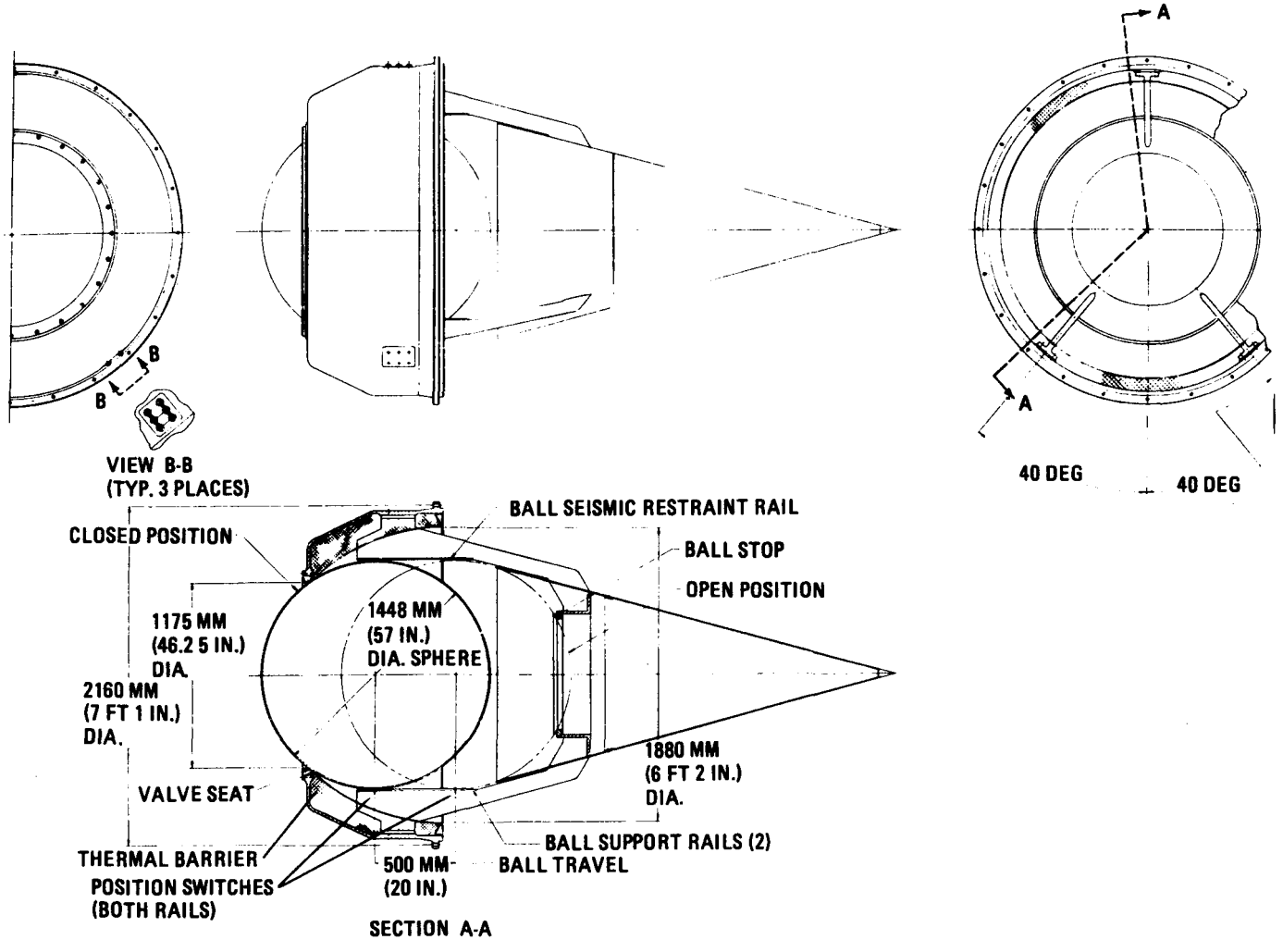

Fig. 10-16. Rolling ball valve concept

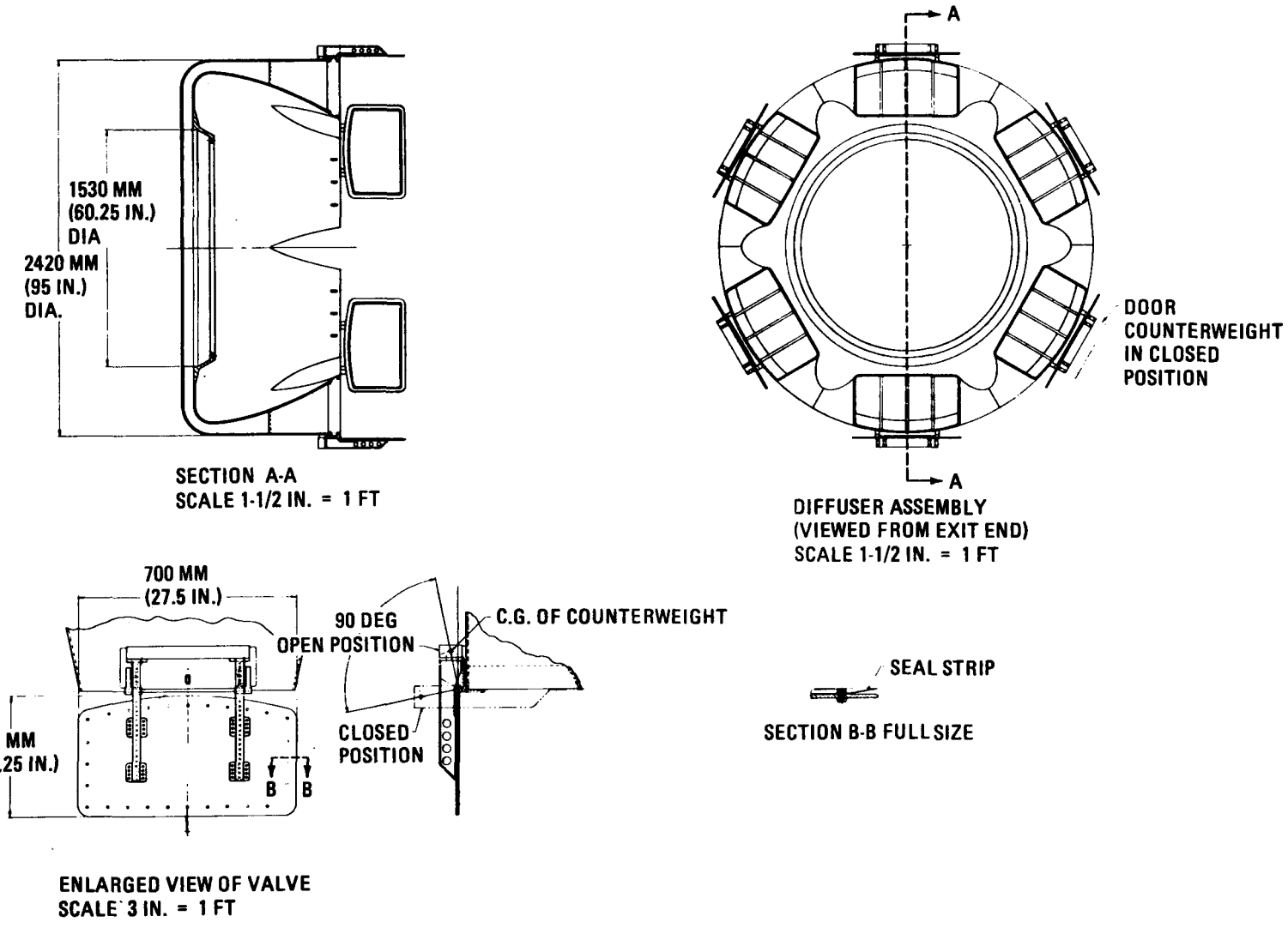

Fig. 10-17. Hexfurcated diffuser with flow-actuated valve

10.7. STEAM GENERATOR

The objective of this task is to design and develop a steam generator which meets the operational, performance, and safety requirements of the GCFR. The conceptual design of a steam generator without a resuperheater was established as the basis for further development. Because of the transfer of the design responsibility, a substantial amount of effort was made to ensure that continuity in design evolution is preserved. As part of this effort, an in-depth review of the GCFR steam generator conceptual design (Fig. 10-18) was made, and recommendations primarily based on HTGR steam generator design and manufacturing experience are being incorporated into a revised configuration to be sized and analyzed. Sizing will be based on the expected system conditions provided in the GCFR baseline data book. The uncertainties associated with the methods and data used for sizing will be identified for use in calculating GCFR system design conditions.

Proposed steam generator reference material for each component of the assembly is being reviewed. In particular, the superheater tube sheet, identified as the critical component for material selection, is being subjected to thermal and stress analyses for normal and transient conditions. A complete transient from initiation of reactor trip to steady steam generator flood-out conditions will be used for thermal and stress analyses.

The requirement that the steam generator produce steam at 2% flow to drive the steam-driven circulator during a normal shutdown transient leads to the necessity for a low-flow boiling stability test. A preliminary flow map analysis indicates that at 2% flow, the boiling is in a stratified region in which little thermal and hydraulic information is available for use in assessing the boiling stability characteristics. Testing will therefore be the only source of design data, and the completion of testing may turn out to be a critical path item for steam generator development. Test planning is being studied, with consideration being given to the technical aspects of the testing as well as the scheduling impact on the overall steam generator program.

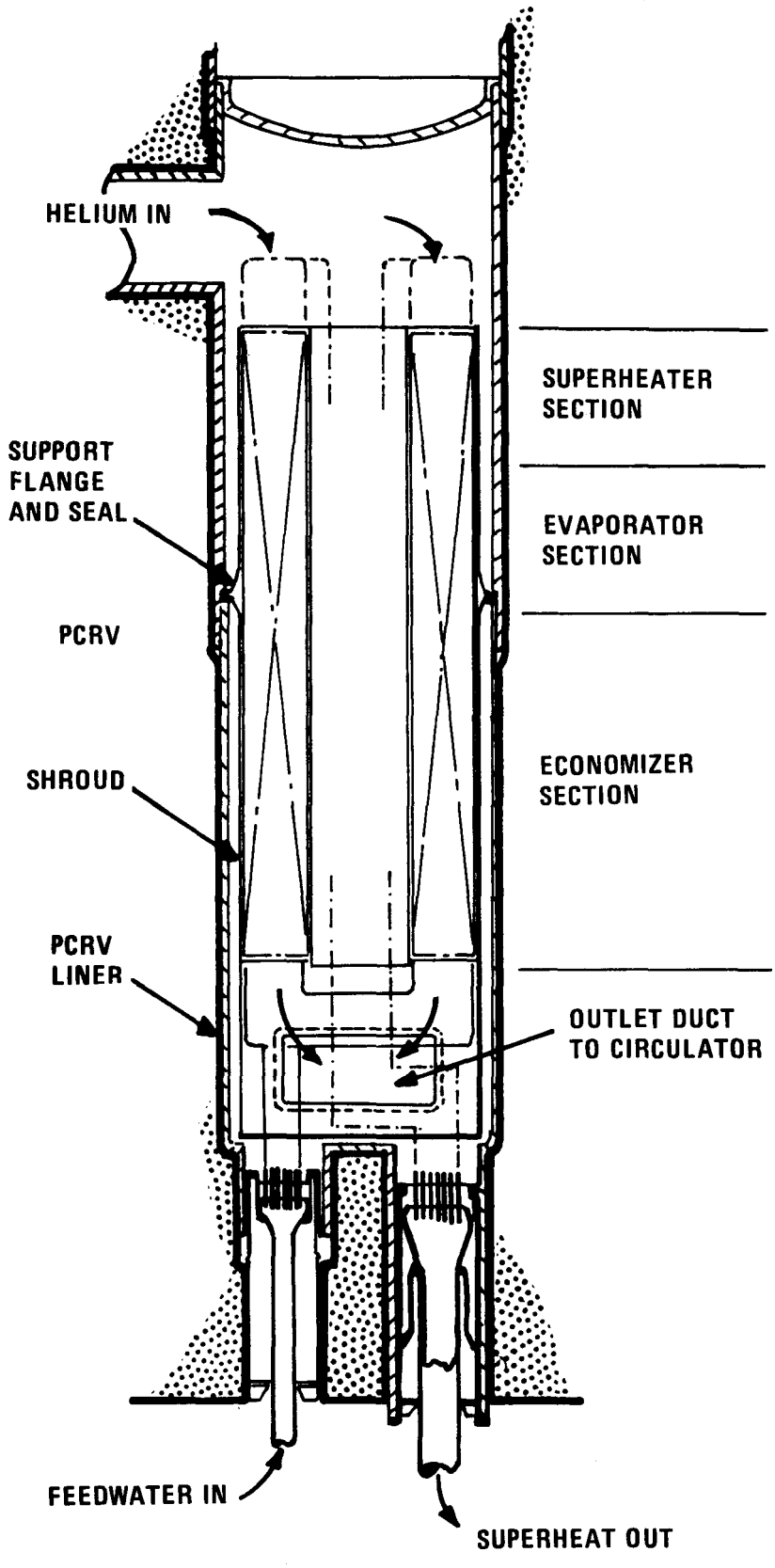

Fig. 10-18. Steam generator section

RECS is being developed to provide scheduling and manpower information for steam generator development. The major components and subassemblies of the steam generator will first be identified, and then estimates will be made for the manpower and time span required to achieve milestones such as completion of preliminary design, completion of final design, manufacturing drawing release, tooling fabrication, material procurement, and so on. The information will be input to RECS, which will generate a complete Program Evaluation and Review Technique (PERT) chart together with manpower requirement for the entire steam generator development program.

10.8. AUXILIARY CIRCULATOR, VALVE AND SERVICE SYSTEM

The general objectives of this task are (1) to develop components for the core auxiliary cooling system (CACS), namely, the auxiliary loop circulator (ALC) and the auxiliary loop isolation valve (ALIV); (2) to meet reliability and safety criteria; and (3) to demonstrate the performance and reliability of critical components by testing under anticipated operating conditions. Specific objectives for FY-78 are

1. Complete auxiliary circulator valve and service system (ACVS) conceptual design initiated in FY-77 for critical components.

2. Initiate preliminary design of ACVS critical components.

3. Update and revise the RECS schedule for the ACVS.

4. Initiate work on the test specifications required by the development plan schedule.

10.8.1. Design Requirements of the Auxiliary Circulator

The auxiliary circulator is part of an engineered safety system which provides core cooling when main loop circulator cooling is not available, e.g., during pressurized cooldown of the reactor when the main circulators

stop functioning. This is referred to as a pressurized cooldown accident and is expected to occur a few times during the lifetime of the plant. The other accident under consideration is a DBDA. During a DBDA, the main circulators are shut down, and the auxiliary circulators must be started and begin circulating helium within 85 s. The DBDA is not an anticipated event, although the auxiliary circulator is designed for its occurrence.

The power requirements of the auxiliary circulator drive are determined by DBDA conditions. Two cases have to be considered when determining the speed and torque requirements of the circulator blower and its drive, respectively. One is a DBDA in pure helium, and the other results from considerations of air ingress due to a potential leak area of 0.0164 m^2 (75 $in.^2$). It can be shown that the pure helium case results in the high volumetric flow and head requirement, whereas the air ingress case demands a higher torque at a lower volumetric flow. In summary, the following conclusions are valid:

1. The maximum speed of operation is determined by the DBDA, assuming the gas is pure helium.

2. The maximum horesepower and torque are determined by air ingress conditions.

3. The head and flow requirements on the compressor reach a maximum at the same time.

10.8.2. Design Point Sizing of Impeller

Table 10-5 shows the design data of the auxiliary circulator for the following design basis events:

1. DBDA in pure helium.
2. DBDA with air ingress [0.0164 m^2 (75-$in.^2$) leak area].
3. Pressurized cooldown.

TABLE 10-5
AUXILIARY CIRCULATOR REFERENCE DESIGN PARAMETERS

Parameter (One Loop)	Pressurized Operation	DBDA	
		Helium	Air Ingress
Mass flow rate [kg/s (lbm/s)]	14.74 (32.5)	6.59 (14.53)	9.81 (21.63)
Molecular weight (kg/mol)	4	4	6.17
Total inlet temperature [K (°R)]	614 (1105)	494.4 (890)	494.4 (890)
Inlet pressure [MPa (psi)]	8.8253 (1280)	0.174 (25.3)	0.174 (25.3)
Discharge pressure [MPa (psi)]	8.8264 (1280.16)	0.186 (27.0)	0.191 (27.74)
Ratio of specific heats	5/3	5/3	1.63

Since condition 1 determines the maximum speed of operation, the impeller has been sized for this condition, assuming a rotational speed of 3600 rpm. To decide on the type of impeller (radial or axial) required, it is instructive to examine the specific speed (N_s) and specific diameter (D_s) of the impeller for the given conditions. The specific speed concept ignores compressibility effects, but they are not appreciable in helium, and even with air ingress, the Mach numbers can be shown to be relatively low. The design point is indicated in a typical Balje (Ref. 10-6), or N_s-D_s, diagram with isoefficiency curves superimposed on Fig. 10-19. It can be seen from this figure that the design point lies in the high-efficiency island of 80%. The figure also indicates that the preferred type of impeller for this range of operation is a radial impeller.

Table 10-6 shows some of the more important design parameters of the radial impeller. It is important to note that the auxiliary circulator operates approximately in the same range of volumetric flow and adiabatic head as the main helium circulator. The main disadvantage of this concept is that the large diameter of the impeller, when coupled with a diffuser, tends to make the circulator assembly large. Although this problem is not insurmountable, it does place a premium on increasing the speed of rotation and thereby decreasing the size of the compressor driven possibly by a nonelectric source.

10.8.3. Core Auxiliary Heat Exchanger

The purpose of this task is to develop a core auxiliary heat exchanger (CAHE) for the CACS which meets performance, safety, and reliability criteria. The existing CAHE conceptual design (Fig. 10-20) using a top-fed helical bundle suspended from a top flange in the CAHE cavity was reviewed as part of the effort of transferring the CAHE design responsibility. The review identified the following requirements: (1) elimination of subheadering to relieve the difficulty of performing in-service inspection (facilitation of in-service inspection is considered a mandatory requirement); (2) provision of good drainage of the CAHE, required during

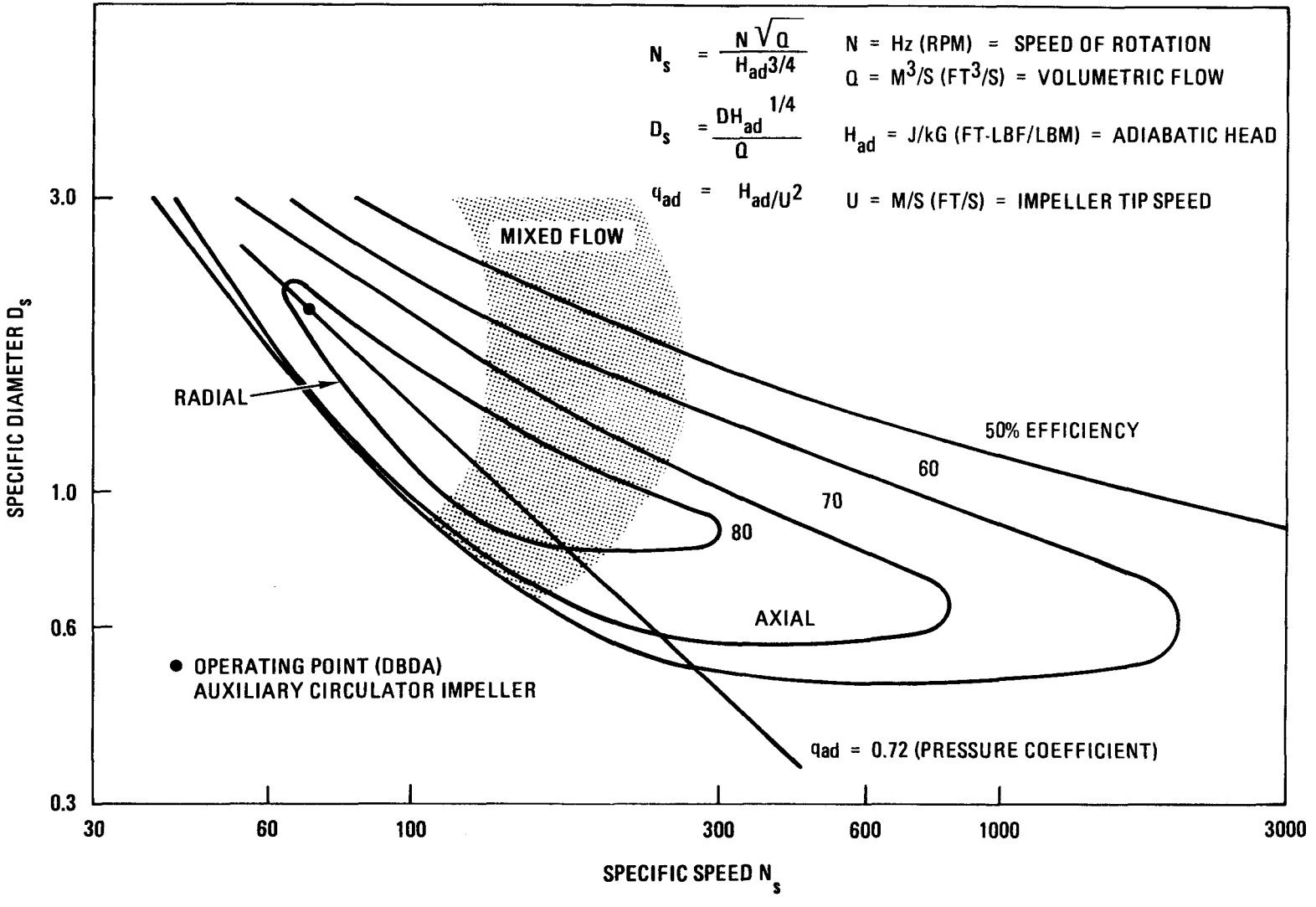

Fig. 10-19. Approximate N_s-D_s diagram for low-pressure-ratio compressors (from Ref. 10-6)

TABLE 10-6
AUXILIARY LOOP CIRCULATOR DESIGN DATA

Type	Radial
Drive	Electric
Design condition	DBDA (helium)
Speed (rpm)	3600
Estimated efficiency (%)	80
Tip diameter d_2 [m (in.)]	1.624 (63.94)
Tip width b_2 [mm (in.)]	77 (3.03)
Eye diameter d_{is} [m (in.)]	0.830 (32.66)
Hub diameter d_{ih} [m (in.)]	0.415 (16.33)
Adiabatic head H_{ad} [kJ/kg (Btu/lbm)]	67.4 (28.98)
Volumetric flow Q [m^3/s (ft^3/s)]	38.8 (1371.4)
Specific speed N_s $\left(\text{ft}\cdot\text{lbm}^{\frac{3}{4}}/\text{min}\cdot\text{s}^{\frac{1}{2}}\cdot\text{lbf}^{\frac{3}{4}}\right)$	72.44
Specific diameter D_s $\left(\text{s}^{\frac{1}{2}}\cdot\text{lbf}^{\frac{1}{4}}/\text{ft}^{\frac{1}{4}}\cdot\text{lbm}^{\frac{1}{4}}\right)$	1.76

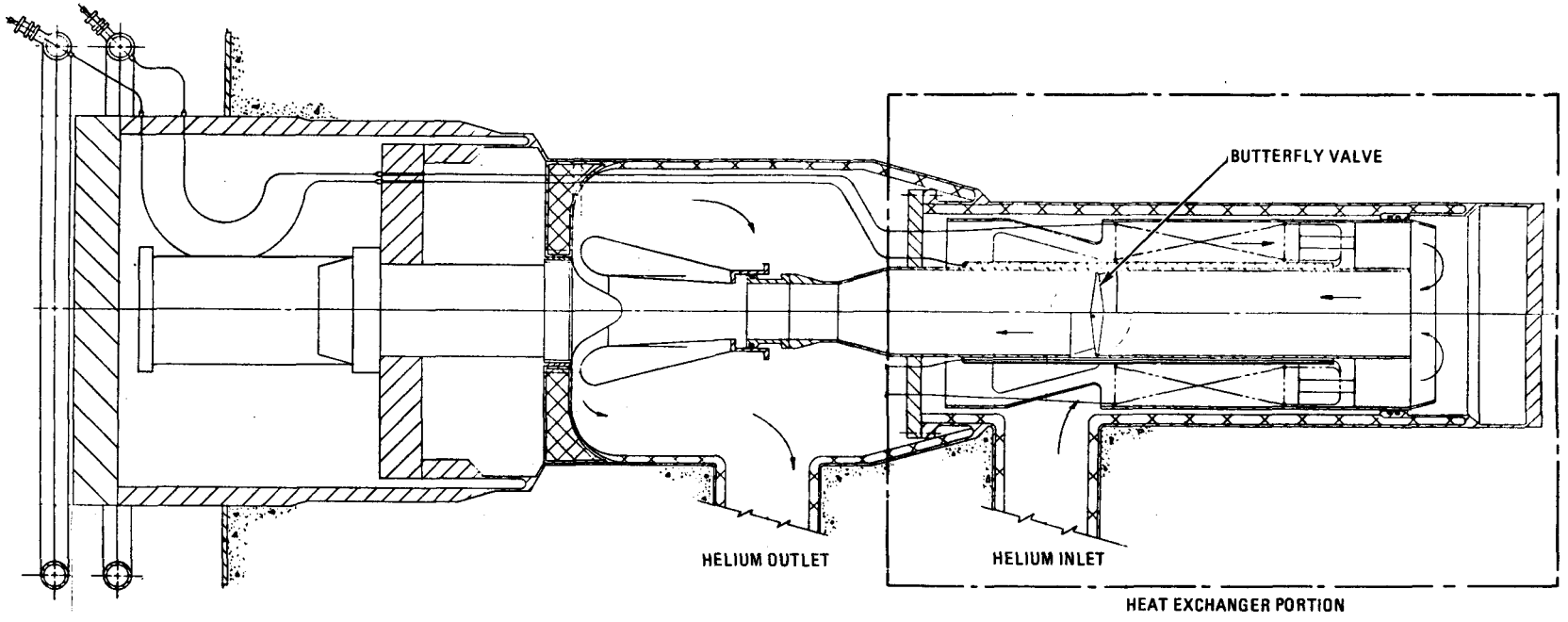

Fig. 10-20. Section view of auxiliary loop heat exchanger

in-service inspection or other nondestructive examination (NDE) techniques; and (3) improvement of ease of shipping of the CAHE assembly. A bottom-fed bayonet configuration (Fig. 10-21) satisfies these requirements and has been adopted for the HTGR CAHE design. The study of a GCFR bayonet CAHE has been expanded and the computer sizing code modified to incorporate methods applicable for bayonet design under air ingress transient conditions after initiation of a DBDA. RECS is being developed for the overall CAHE program and in support of alternate heat removal studies, since RECS is capable of producing scheduling and manpower requirements for various CAHE configurations corresponding to various heat removal concepts.

10.9. HELIUM PROCESSING COMPONENTS

A review of the design basis and process selection for the HPS has been completed, and based on this review the following changes are being implemented:

1. The amount of purified helium being produced for purge and buffer requirements is being increased from 0.202 kg/s (1600 lb/hr) to 0.328 kg/s (2600 lb/hr) based on current user needs.

2. The steam cycle HTGR (lead plant) helium purification processing scheme will be adopted by the GCFR purification system. This change includes an oxidizer module in the regeneration section.

3. With the change to the steam cycle HTGR helium purification processing scheme, the radioactive gas recovery system is no longer required and will be deleted from the GCFR scope of supply.

REFERENCES

10-1. Hucknall, A., "Component and Systems Development Program Final Report: Replaceable Thermal Burners for High-Temperature Gas-Cooled Reactors," DOE Report GA-A14710, General Atomic, to be published.

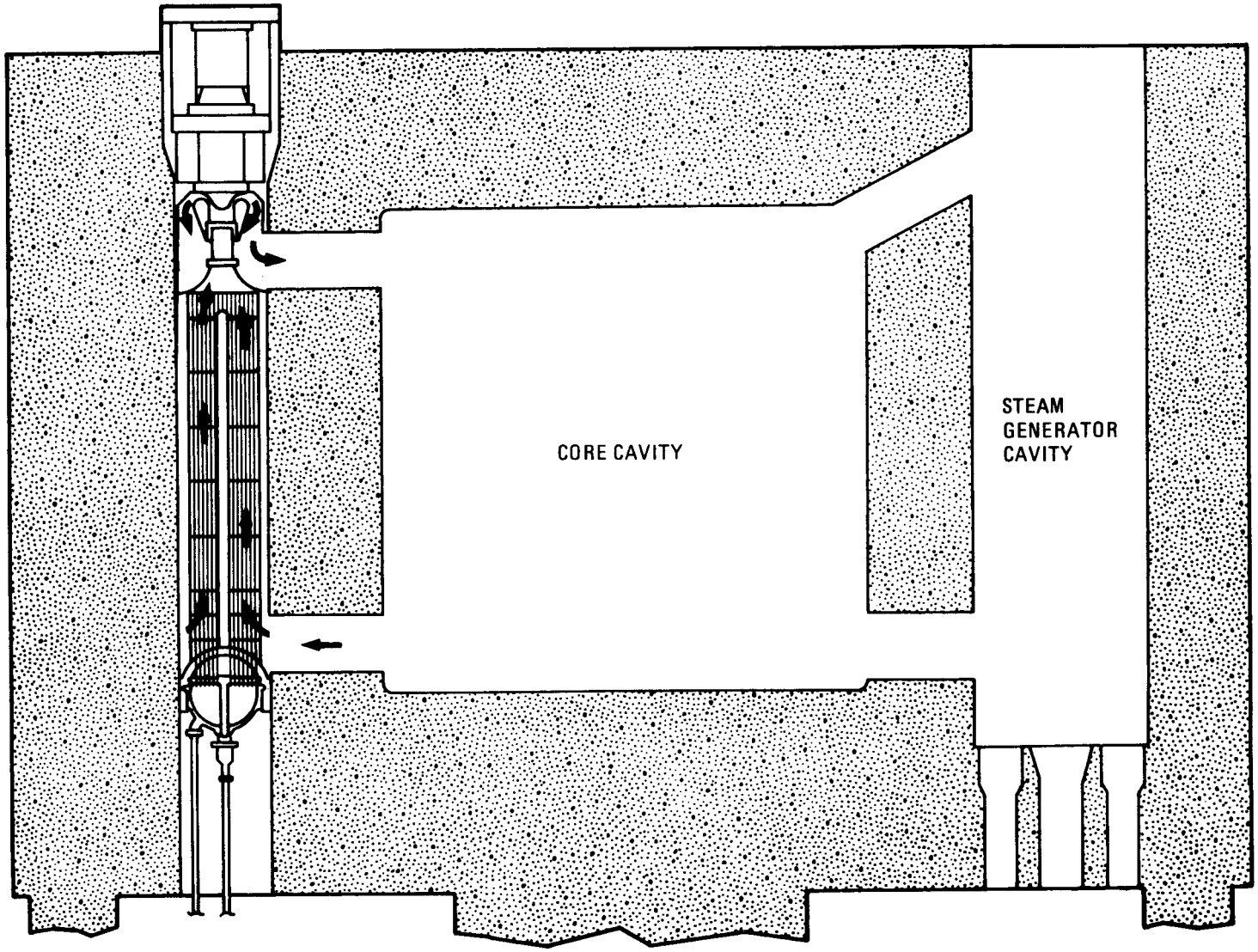

Fig. 10-21. Bottom-fed bayonet core auxiliary heat exchanger

10-2. "Gas-Cooled Fast Breeder Reactor Quarterly Progress Report for the Period August 1, 1977 Through October 31, 1977," DOE Report GA-A14613, General Atomic, November 1977.

10-3. Lockett, G., and S. Keaney, "GCFR Refueling - Single Center Bottom PCRV Penetration Study," General Atomic, unpublished data.

10-4. Mouritzen, G., "Alternate Circulator Design Concept No. 1 for a 300-MW(e) GCFR Demonstration Plant - Two Stage Axial Flow Helium Circulator and Two Stage Steam Turbine Drive," DOE Report GA-A14530, General Atomic, December 1977.

10-5. Mouritzen, G., "Alternate Design Studies and Reference Design Selection for GCFR Main Helium Circulator," DOE Report GA-A14754, General Atomic, January 1978.

10-6. Balje, O. E., "A Study on Design Criteria and Matching of Turbomachines," J. Eng. Power 84, 103 (1962).

11. CIRCULATOR TEST FACILITY (189a No. 00586)

The objective of this task is to develop a facility for qualification testing of the GCFR main helium circulator. The scope of this task involves (1) evaluation of alternative test facility concepts in terms of technical feasibility and cost, (2) identification of the most promising test facility concept, (3) an architect/engineer conceptual design, and (4) final design, construction, and checkout of the facility. The available FY-78 funding does not permit the conceptual design of separate steam and electric test facility concepts. Consequently, the steam concept has been deleted, and the test facility will be designed for an electric-motor-driven circulator. In the event that the alternate main circulator concept studies being conducted retain the steam-driven circulator, a steam loop can be added later.

The electric circulator test facility concept consists of an electrical supply and distribution system connected to a helium loop. Electrical power is taken from a local utility grid via a transformer and furnished to the circulator drive motor controller and hence to the motor. The circulator compressor is mounted in a large, heavy-walled pressure vessel which provides a helium flow loop. Valves are provided for restricting the helium flow generated by the compressor. A heat exchanger is also included to reject the heat generated by the compressor.

A task summary and short-term schedule describing the conceptual design project have been prepared, and appropriate interfaces have been provided for the electric motor and controller study. A comprehensive schedule for the entire GCFR circulator test facility task with associated funding distributions of operating and construction money has also been prepared. A statement of work has been formulated, and architect/engineering firms have been requested to submit proposals for the conceptual

design of the electric-motor-driven circulator test facility. A final selection will be made very shortly.

Prior to deletion of steam test facility concepts, a statement of work describing a steam compressor technical feasibility and cost study was distributed to eight domestic manufacturers (the steam compressor circulates steam to and from the circulator drive turbine). All the manufacturers declined to bid. Package boilers or utility steam must be used if the steam concept is reinstated.

12. PLANT DYNAMICS (189a No. 00638)

12.1. CONTROL SYSTEMS

An analysis of the plant dynamic characteristics for normal transients and an investigation of plant control configurations were started; this work will be continued through the remainder of FY-78. Before proceeding with these analyses, several modifications were made to the plant dynamic simulation (Ref. 12-1). First, the feed pump turbine was added (Fig. 12-1). Early analytical results indicate that this turbine, and its use for control of feedwater flow, could introduce a significant degree of coupling interaction with the other controllers in the steam loop. Therefore, the dynamic properties of this turbine were added to the simulation, including high-pressure turbine extraction to provide the turbine drive. Two other modifications were removal of the resuperheater from the overall plant model (Fig. 12-1) and recalculation of the simulation input data to reflect new steam generator and helium circulator component data and overall plant steady-state heat balances. This was done so that the dynamic analyses would be applicable to the current demonstration plant configuration. The modular construction of the simulation made removal of the resuperheater a very easy modification to implement. Control valve actuator models and general purpose position integral derivative (PID) controller models were also added to the simulation. The open-loop simulation (plant only) now has 53 state variables; with control action added, the number of state variables increases to approximately 66.

12.2. SEISMIC ENGINEERING

There was no activity on this subtask during this quarter.

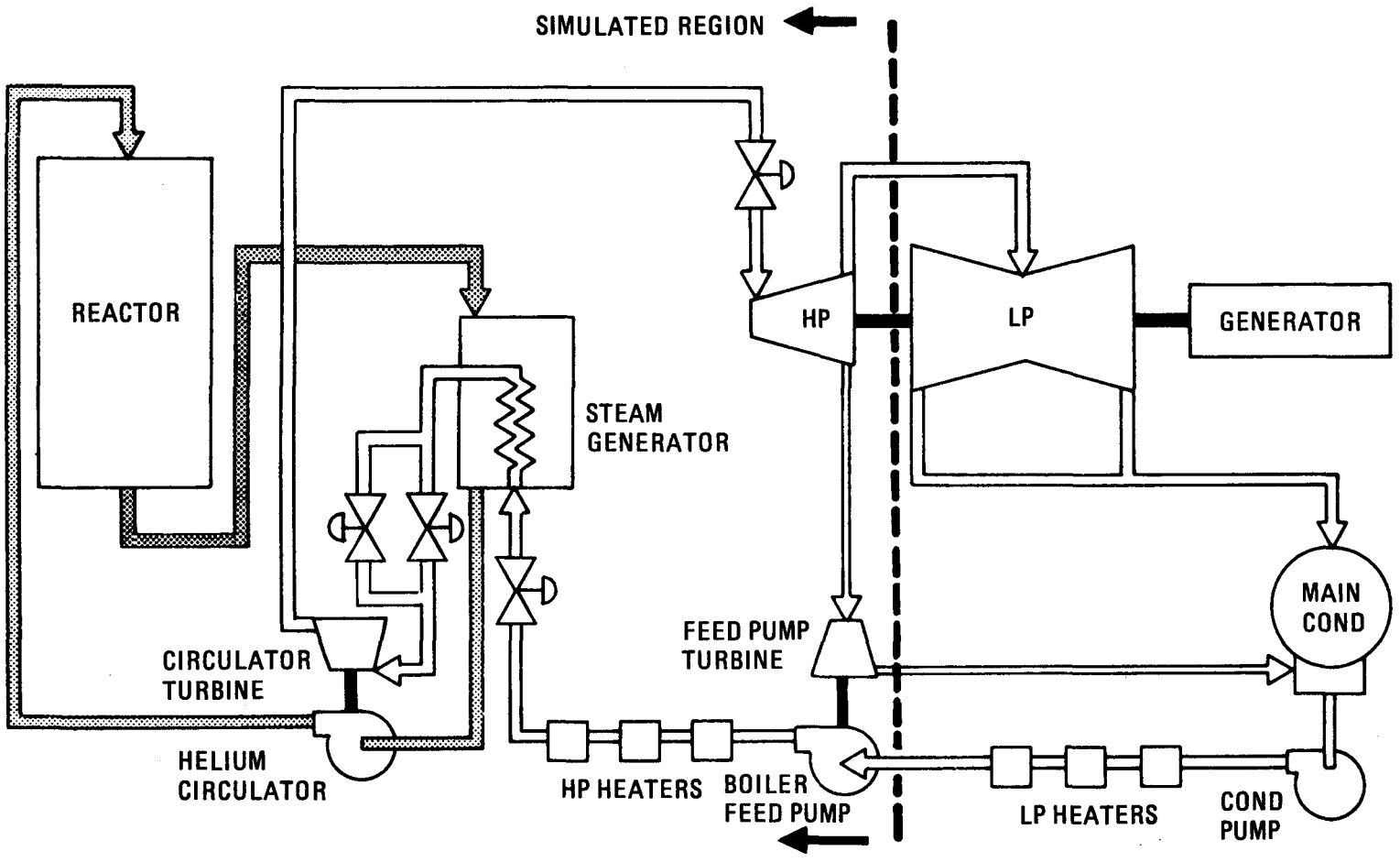

Fig. 12-1. Single-loop plant model (no resuperheat)

12.3. FLOW-INDUCED AND ACOUSTICALLY INDUCED VIBRATIONS

In the past, acoustic design criteria for helium-cooled reactors have had no decisive influence on the design of primary coolant boundary components. The mechanical criteria determined the design, and the acoustic acceptance criteria were always satisfied. This was not the case for the reference design of the 300-MW(e) GCFR demonstration plant with three one-stage axial flow circulators, assuming the power spectral distribution (PSD) given in Ref. 12-2 and reproduced for convenience in Table 12-1 (case 1). As discussed in Section 10.6, radial (centrifugal) circulators are now under study, and a study was carried out to determine the influence of such a design change on the expected acoustic loads for the primary coolant boundary components. The tentative design parameters for the one-stage radial circulators, used for the following calculation, are listed in Table 12-2. Since the Peistrup-Wesler correlation, used in Ref. 12-2 to calculate the overall sound power emission of the axial circulators, was developed on the basis of results for axial as well as radial circulators, it was also used to determine the overall source strength of the radial circulator:

$$\pi_{a,He} = 1.76 \times 10^{-8} N^{-0.27} \pi_{s,He}^{1.77} \left[\frac{\rho_{air} c_{air}^3}{\rho_{He} c_{He}^3} \right]^{0.77} ,$$

where $\pi_{a,He}$ = overall acoustic source strength (W),
$\pi_{s,He}$ = circulator shaft power (W),
N = number of rotor blades,
ρ_{air} = density of air (kg/m^3),
ρ_{He} = density of helium (kg/m^3),
c_{air} = velocity of sound in air (m/s),
c_{He} = velocity of sound in helium (m/s).

Substitution from Table 12-2 gives

$$\pi_{a,radial} = 663 \text{ W } (148 \text{ dB re } 10^{-12} \text{ W})$$

TABLE 12-1
CIRCULATOR OCTAVE BAND SOUND POWER VALUES

Center Frequency of Octave Bands (Hz)	Case 1 Axial Π_1 (W)	Case 2 Axial Π_2 (W)	Case 3 Radial Π_3 (W)	Case 4 Axial Π_4 (W)	Case 5 Radial Π_5 (W)
31.5	0.1	41.2	373.3	46.3	73.7
63	0.3	58.3	166.7	46.3	73.7
125	0.5	65.3	74.0	46.3	73.7
250	1	65.3	29.7	46.3	73.7
500	2.1	65.3	11.8	46.3	73.7
1000	10.9	65.3	4.7	46.3	73.7
2000	52.6	41.2	1.8	46.3	73.7
4000	120	20.7	0.4	46.3	73.7
8000	120	5.2	0.04	46.3	73.7

TABLE 12-2
MAIN HELIUM CIRCULATOR DESIGN PARAMETERS

	Axial Circulator (Reference Design)	One-Stage Radial Compressor[a]
Speed (rpm)	11,700	3,600
Inlet pressure (MPa)	8.63	8.61
Pressure rise (MPa)	0.37	0.41
Shaft power (MW)	15.7	17.4
Mass flow (kg/s)	234	247
Tip diameter (mm)	725	1652
Tip velocity (m/s)	444	317
Number of rotor blades	41	19

[a]Provisional.

compared with

$$\pi_{a,axial} = 428 \text{ W } (146 \text{ dB re } 10^{-12} \text{ W}) \quad .$$

More important, however, than the approximately 50% increase in overall source strength is the expected change in the PSD. There is evidence indicating that an increase in the low-frequency energy content of the spectrum should be anticipated. Results of measurements carried out for small-scale axial and radial circulators indicate a PSD as shown in Fig. 12-2. Using Ref. 12-3 to construct a PSD for both the axial one-stage circulator of the reference design and the radial one-stage circulator results in the octave band PSD listed in Table 12-1 (cases 2 and 3). Case 1 represents the octave band PSD used for the scoping study (Ref. 12-2), which was based on work for the steam cycle HTGR, and cases 4 and 5 refer to the axial and radial circulators, respectively, if the total acoustic energy is equally divided over the nine bands. Figure 12-3 shows the octave band sound power level distributions for these five cases. Note the significant difference between cases 1 and 2. The expected space- and time-averaged sound pressures in the primary coolant volume excluding the core have been calculated with the aid of the PSD values, and the results are listed in Table 12-3. Note that these values represent the base values, and the total space- and time-averaged sound pressures in, for example, the circulator inlet and outlet plena may be higher owing to the direct contribution from the circulators. This table clearly shows that a significant increase in the acoustic design loads for the first three octave bands should be expected if radial circulators are used. A sample calculation for one thermal barrier cover plate mode showed that in this case the acoustic design criteria for this mode are not met with the present design. For all cases, the stress margin, defined as the ratio of the allowable stress and the calculated stress minus one, appear to be negative, which is unacceptable. Follow-up experimental work has been proposed which will lead to a more accurate determination of the acoustic source strength and PSD of radial circulators with shaft powers in the range 15 to 20 MW. These data will be factored into the circulator design decisions.

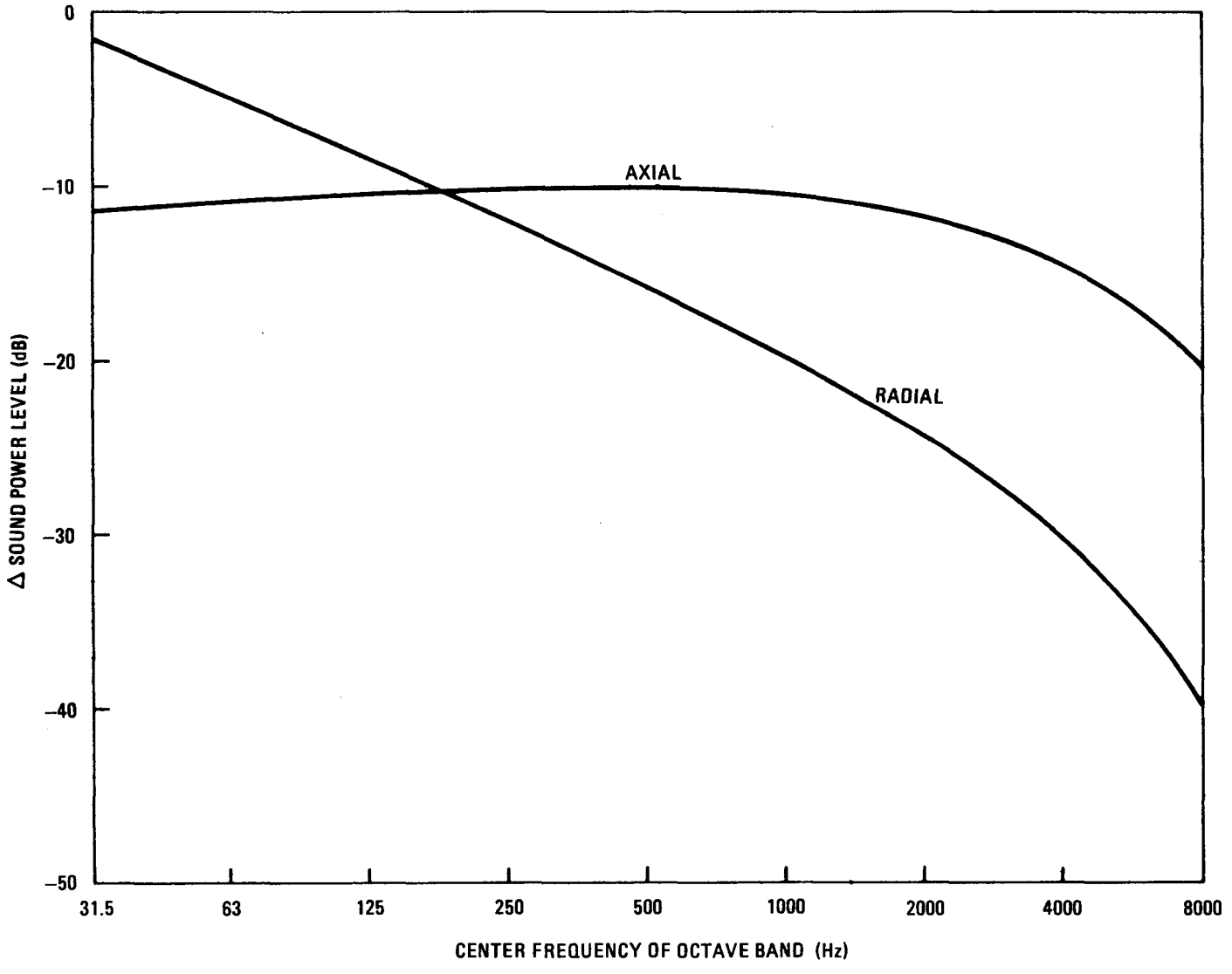

Fig. 12-2. Typical power spectra distributions for small-scale axial and radial circulators

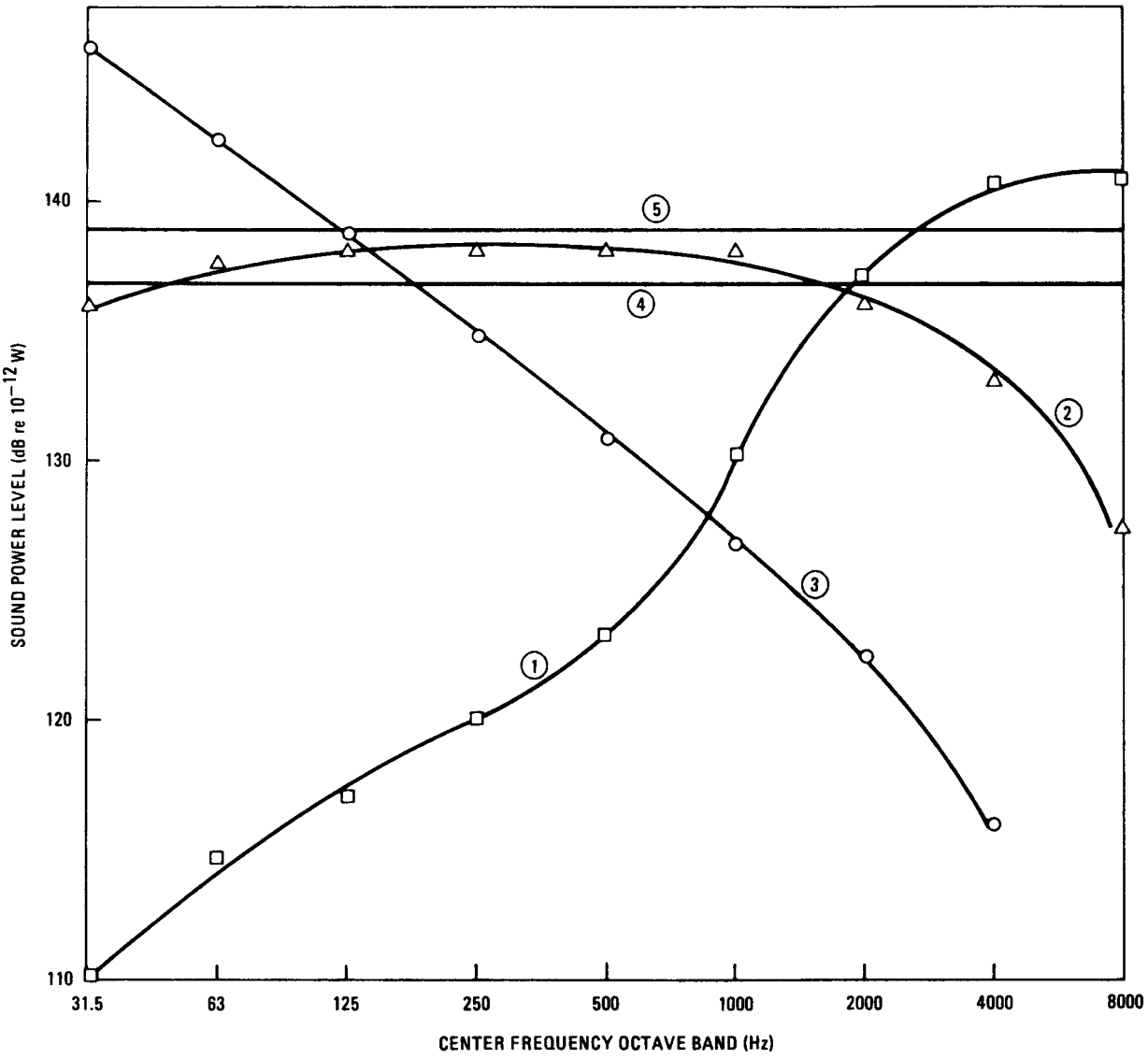

Fig. 12-3. Octave band sound power level distributions for five cases (circled numbers)

TABLE 12-3
EXPECTED SPACE- AND TIME-AVERAGED ACOUSTIC LOADS

Center Frequency of Octave Bands (Hz)	Case 1 Axial (Pa^2)	Case 2 Axial (Pa^2)	Case 3 Radial (Pa^2)	Case 4 Axial (Pa^2)	Case 5 Radial (Pa^2)
31.5	550	226×10^3	2.05×10^6	255×10^3	405×10^3
63	1.6×10^3	315×10^3	0.9×10^6	250×10^3	398×10^3
125	1.3×10^3	172×10^3	0.2×10^6	122×10^6	194×10^3
250	2.5×10^3	166×10^3	76×10^3	118×10^3	188×10^3
500	5.1×10^3	159×10^3	29×10^3	112×10^3	180×10^3
1000	25×10^3	150×10^3	10×10^3	106×10^3	169×10^3
2000	111×10^3	87×10^3	3.9×10^3	98×10^3	156×10^3
4000	229×10^3	39×10^3	0.76×10^3	89×10^3	141×10^3
8000	201×10^3	8.7×10^3	67	78×10^3	124×10^3

REFERENCES

12-1. "Gas-Cooled Fast Breeder Reactor Quarterly Progress Report for the Period August 1, 1977 through October 31, 1977," DOE Report GA-A14613, General Atomic, November 1977.

12-2. Halvers, L. J., "Acoustically Induced Vibrations in the 300-MW(e) GCFR Demonstration Plant," DOE Report GA-A14681, General Atomic, to be published.

12-3. Beranek, L. L., J. L. Reynolds, and K. E. Wilson, "Apparatus and Procedures for Predicting Ventilation System Noise," J. Acoust. Soc. Am. 25, 313-321 (1953).

13. REACTOR SAFETY, ENVIRONMENT, AND RISK ANALYSIS (189a No. 00589)

The purpose of this task is to investigate the safety characteristics of the GCFR. A liaison and coordination subtask integrates the DOE-sponsored GCFR safety work at GA and the national laboratories into a national GCFR safety program which is responsive to the need for GCFR safety research. A GCFR safety program plan is being developed to define the safety research needed for the demonstration plant and the longer-term GCFR commercialization program. Safety research at GA includes probabilistic accident analysis, accident consequence analysis, radiological and environmental analyses, and post accident fuel containment (PAFC) analyses.

Logical probabilistic methods are employed to determine the probabilities associated with various accident initiation and progression sequences and to identify potential design modifications which would help reduce risks. A methodology for integrating reliability considerations into the GCFR engineering effort at the system, subsystem, and component levels is being developed for trial use on a selected system, with the objective of determining the optimal use of reliability engineering methods in the GCFR. The thermal behavior of the fuel assembly under conditions of loss of shutdown heat removal is being analyzed to determine the heat-up and melting sequence of the cladding, duct walls, and fuel, because duct wall melting has been identified as an important phenomenon influencing the accident sequence. Analyses are being performed to assess the PAFC capability of the current design and to identify modifications which could improve the molten fuel containment capability.

13.1. REACTOR SAFETY PROGRAM COORDINATION

The draft of the GCFR Safety Program Plan was rewritten to more closely identify the work tasks with the basic radionuclide release barriers.

13.2. PROBABILISTIC ACCIDENT AND RISK ANALYSIS

Accident initiation and progression analysis (AIPA) techniques developed in FY-74, -75, and -76 (Refs. 13-1 and 13-2) are being applied to the probabilistic analysis of potential accident sequences leading to low-probability, high-consequence outcomes. The consequences of these sequences are also under study at ANL and at GA under other subtasks. The objective of this work is to assess the risks associated with these accident chains.

13.2.1. Expected GCFR Scram Frequency

An assessment of the frequency of scram failures within the GCFR requires an estimate of the expected GCFR scram frequency. GCFR design duty cycles which will serve as the basis for component design have been established, and the duty cycles have been categorized into normal, upset, emergency, and faulted events. To determine the scram system duty cycle, the plant duty cycles have been categorized into events leading to a normal plant shutdown or those which contribute to the scram duty cycle. Events in the latter category have been further analyzed to determine the number of expected scrams over the plant's 30-yr lifetime.

Over the lifetime of the plant, there are assessed to be a total of 551 duty cycle events requiring reactor shutdown, 157 of which could result in a reactor scram and thus define the scram duty cycle. Further elimination of events for which the plant can be controlled without reactor scram establishes the number of expected scrams at 112 over the 30-yr plant lifetime, or an expected scram frequency of 4/yr. It was determined that over 50% of the expected scrams are related to operator training, errors, and regulatory requirements. The reactor safety study (Ref. 13-3) assessed the expected scram frequency for light water reactors (LWRs) to be 7 scrams/yr. The difference in scram frequency is related to differences in the feedwater supply system.

13.2.2. Initiating Events for Loss of Flow Without Scram Accidents

A review was made of GCFR initiating events which could lead to a loss of flow without a scram accident if the reactor scram system and the backup shutdown system failed to respond to the trip signals generated. The objectives of the review were (1) to assure that at least two trip signals would be generated by each initiating event and (2) to make a rough estimate of the time available for manual operator action before the cladding safety limit is exceeded if both the operational protection system (OPS) and the plant protection system (PPS) fail. A total of 15 initiating events were analyzed, and in each case at least two scram signals were generated. The shortest time for operator action was in the range 30 to 60 s for a loss of feed and failure of OPS and PPS action. More detailed analysis of each initiating event would be required to define more accurately the time available for manual operator action.

13.2.3. Reliability Comparison of Alternate Main Circulator Configurations

Comparative reliability analyses for the GCFR main circulator reference design and four alternate circulator drive configurations were completed. No significant differences could be identified for the five systems with respect to main loop residual heat removal (RHR) reliability or plant availability. The analyses considered the main circulator drive system and its control and support systems for the following alternate configurations:

1. Direct steam, high-pressure turbine, noncondensing turbine (reference configuration).

2. Direct steam, separate condenser, condensing turbine.

3. Electric drive with ac pony motor.

4. Electric drive without ac pony motor.

5. Variable-speed electric motor with asynchronous converter.

The availabilities of the basic components utilized during normal operation were compared. Figure 13-1 shows the simplified loop availability models and the failure rates and mean times to restore for the various components. Within the confidence range for the data used, no significant differences could be established in the total system failure rates.

The reliability analysis for main loop RHR is summarized in Table 13-1. The numbers in parentheses are estimates of the failure probability per year of main loop RHR for circulating components only, excluding the peripheral equipment. These numbers do not significantly affect the overall main loop RHR failure probability per year, and thus the peripheral equipment and its configurations and not the circulator configurations are the dominating contributor to main loop RHR failure.

The separate condenser for configuration II, with the cooling water and ultimate heat sink provided from either the circulating water system or the service water system, had the greatest effect on main loop RHR failure probability. This eliminated the single failure point of the main condenser and the circulating water system which was assumed to exist for the reference design and the other configurations. The separate condenser may be required for configuration II, but can also be incorporated into the other configuration, so that it is not unique for this design. Thus, there are no significant inherent reliability advantages for any of the five configurations for main loop RHR.

It is concluded that from the standpoint of main loop reliability, each of the five systems provides acceptable reliability. The choice of circulator drive system must therefore be based on other considerations such as performance, state of the art, functional requirements, and diversity of the core auxiliary cooling systems.

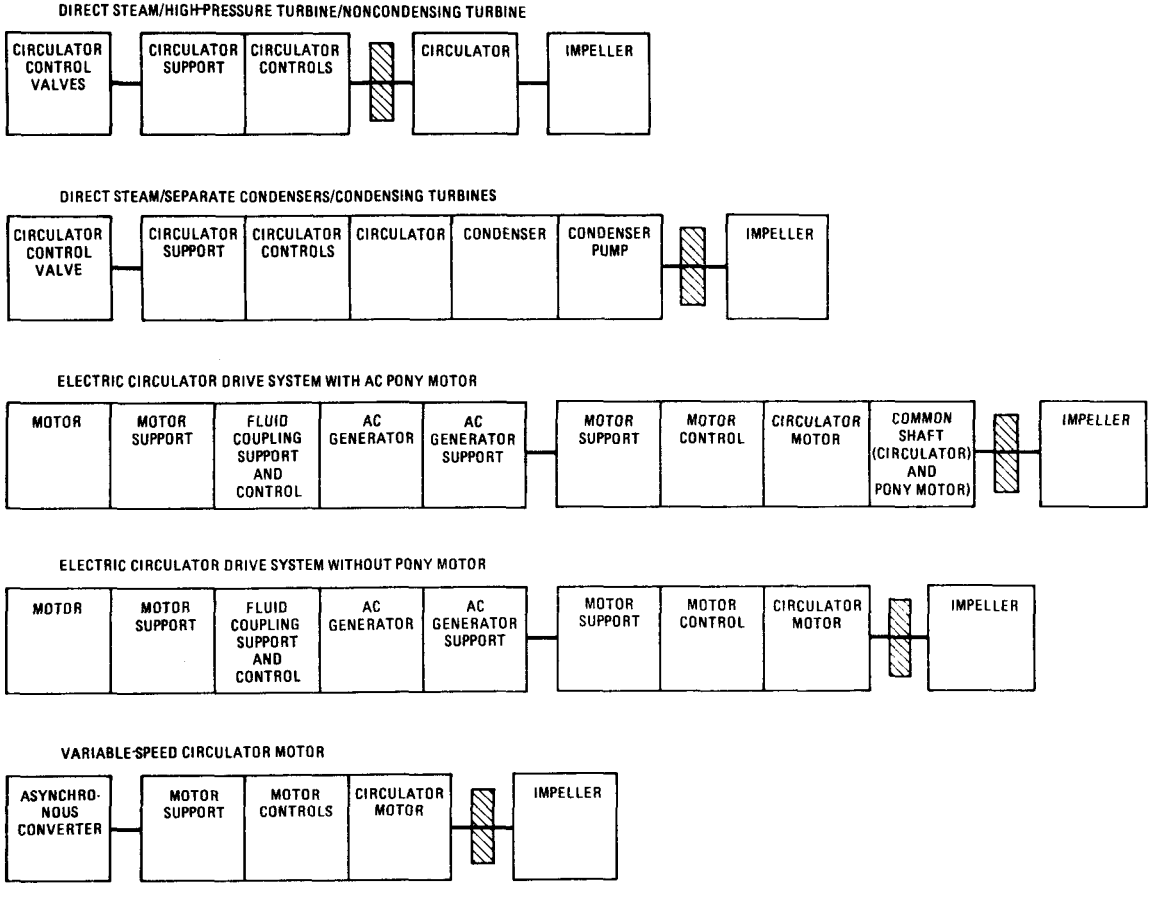

CONFIGURATION	CIRCULATOR ESTIMATES			
	FAILURE RATE (PER HR)	WEIGHTED MEAN TIME TO RESTORE (HR)	ASSUMED: 80% AVAILABILITY ~7000 HR/YR OPERATION	
			EXPECTED NO. OF OUTAGES PER YEAR	EXPECTED OUTAGE DURATION PER YEAR (HR)
I	1.05E-4	68	0.735	50
II	1.95E-4	42	1.965	57
III	1.95E-4	36	1.365	49
IV	1.93E-4	36	1.351	49
V	8.3E-5	30	0.581	17

Fig. 13-1. Loop availability models for circulator configuration

TABLE 13-1
COMPARISON OF GCFR CIRCULATOR CONFIGURATIONS FOR RHR

Configuration	Estimated Probability Per Year of Loss of Main Loops For RHR[a]
Direct steam, high-pressure, noncondensing turbine	3.2E-1 (8.7E-5)
Direct steam, separate condensers, condensing turbine	1.0E-1 (1.9E-4)
Electric drive with ac pony motor	1.7E-1 (4.0E-5)
Electric drive without pony motor	1.7E-1 (4.1E-5)
Variable-speed motor with battery backup	1.7E-1 (4.1E-5)

[a]Numbers in parentheses are for main loops only; assumes all peripheral components function.

13.3. ACCIDENT CONSEQUENCE ANALYSIS

13.3.1. Introduction

The consequence of low-probability accident sequences leading to core damage are being investigated to determine the expected behavior of the GCFR core and the ability of its barriers to mitigate the release of radioactive material from the containment. Particular emphasis is given to analysis of the loss of decay heat removal accident [henceforth referred to as the protected loss of flow (PLOF) accident], which has been shown to be the dominant contributor to the probability of a loss of coolable core geometry. Analyses of unprotected accidents are currently being emphasized at ANL.

During this quarter, results were obtained on two of the PLOF accident sequence analyses. The first analysis indicates that melt-through of steel blockages, if such blockages occur, in lower axial blanket coolant channels is not likely to be an early accident termination mechanism. The second analyses suggests that development of local convection flow patterns in the upper axial blanket subassemblies which are blocked at the lower axial blanket-core interface will not cause early relief valve opening. Both analyses are explained in detail below.

13.3.2. Melting of Steel Blockages in Lower Axial Blanket Coolant Channels

Previous analyses have demonstrated that substantial blockages due to the refreezing of molten cladding are likely to occur in lower axial blanket coolant channels during a PLOF (Ref. 13-4). A preliminary recriticality study at ANL (Ref. 13-5) has shown that criticality may be expected 50 s after the beginning of fuel motion in the absence of duct fallaway. In combination with the results of Ref. 13-6, this suggests that recriticality may occur as soon as 4 min 10 s after accident initiation, or 2 min 20 s after blockage formation in the lower axial blanket. The recriticality configuration is that of molten fuel compaction upon a steel blockage beginning at the lower axial blanket-core interface. Since molten fuel

comes in direct contact with the steel blockages, a competition of thermal and neutronic phenomena arises. Specifically, the relevant question becomes, is molten fuel likely to melt through the lower axial blanket blockage and drain out of the core prior to recriticality?

The TAP code (Ref. 13-7) was used to study molten fuel penetration into a steel-blocked lower axial blanket. A transient sequence of slumped fuel depths are modeled for a subassembly in which all core cladding and duct walls had melted. Part of the molten steel had refrozen and blocked the coolant channels in the lower axial blanket, as indicated by previous analyses. The remaining steel forms a pool on the solid steel blockage. This configuration constitutes the initial setting for fuel slumping initiation.

A procedure developed in Ref. 13-5 was used to estimate molten fuel slumping and layer depth as a function of time after incipient melting. A series of TAP calculations were performed which varied the molten fuel layer depth in a way which approximated the calculated buildup of a molten layer, as illustrated in Fig. 13-2. The one-dimensional axial configuration modeled in the analysis consists of the following (from the top of the subassembly to the PCRV thermal shield):

1. Cladding upper axial blanket rods.

2. Void created by fuel slumping.

3. Molten steel filling the spaces between partially erect, declad fuel columns.

4. Molten fuel filling the spaces between partially erect, declad fuel columns (decay heat source).

5. Solid steel blocking the coolant channels in the lower axial blanket.

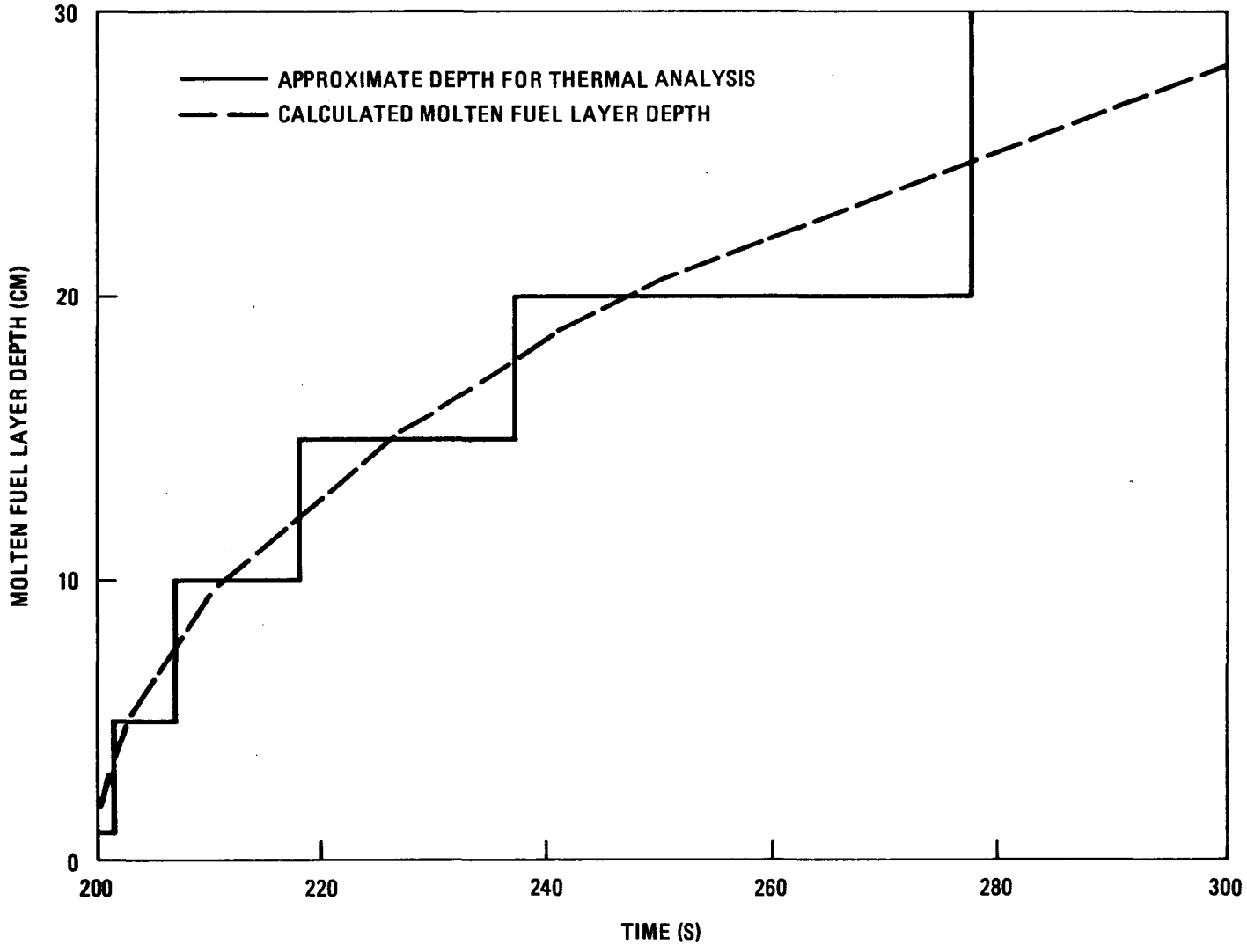

Fig. 13-2. Molten fuel layer depth during fuel slumping

6. Unblocked lower axial blanket rods.

7. Lower thermal shield (constant temperature heat sink).

Figure 13-3 presents the transient penetration depth of the melt front into the lower axial blanket blockage; the penetration depth of temperatures greater than or equal to the solidus is also shown. Under decay heat conditions the steel blockage melts (reaches the liquidus) at an average rate of 0.01 cm/s; at nominal full power this rate is about 20 times higher. The thermal model is limited to conduction heat transfer, and molten steel is not allowed to levitate through the molten fuel. Inclusion of convection would probably enhance upward heat removal at the expense of melting rate.

The existence of a solid fuel crust between the molten fuel and solid steel under simulated decay heat conditions has been experimentally observed (Ref. 13-8), and the results indicate that the fuel crust prevents the molten steel below the crust from levitating. Blockage thicknesses have been calculated to be about 20 cm (Ref. 13-4). Therefore, fuel removal due to blockage melt-through in the lower axial blanket is calculated to occur much later than estimates of fuel-slumping-induced recriticality in the core.

13.3.3. Natural Convection Effects in a Blocked Fuel Assembly During Protected Loss of Flow

During the previous quarter a model was provided for investigating the development of convective heat transfer in the upper axial blanket assuming no flow through the inlet portion of the subassembly (Ref. 13-4). The model attempts to estimate the upward propagation of a natural convection heat and mass transfer front from the core - upper axial blanket interface and has been used to indicate whether local subassembly natural convection phenomena can influence global PCRV heat-up and pressurization during a PLOF.

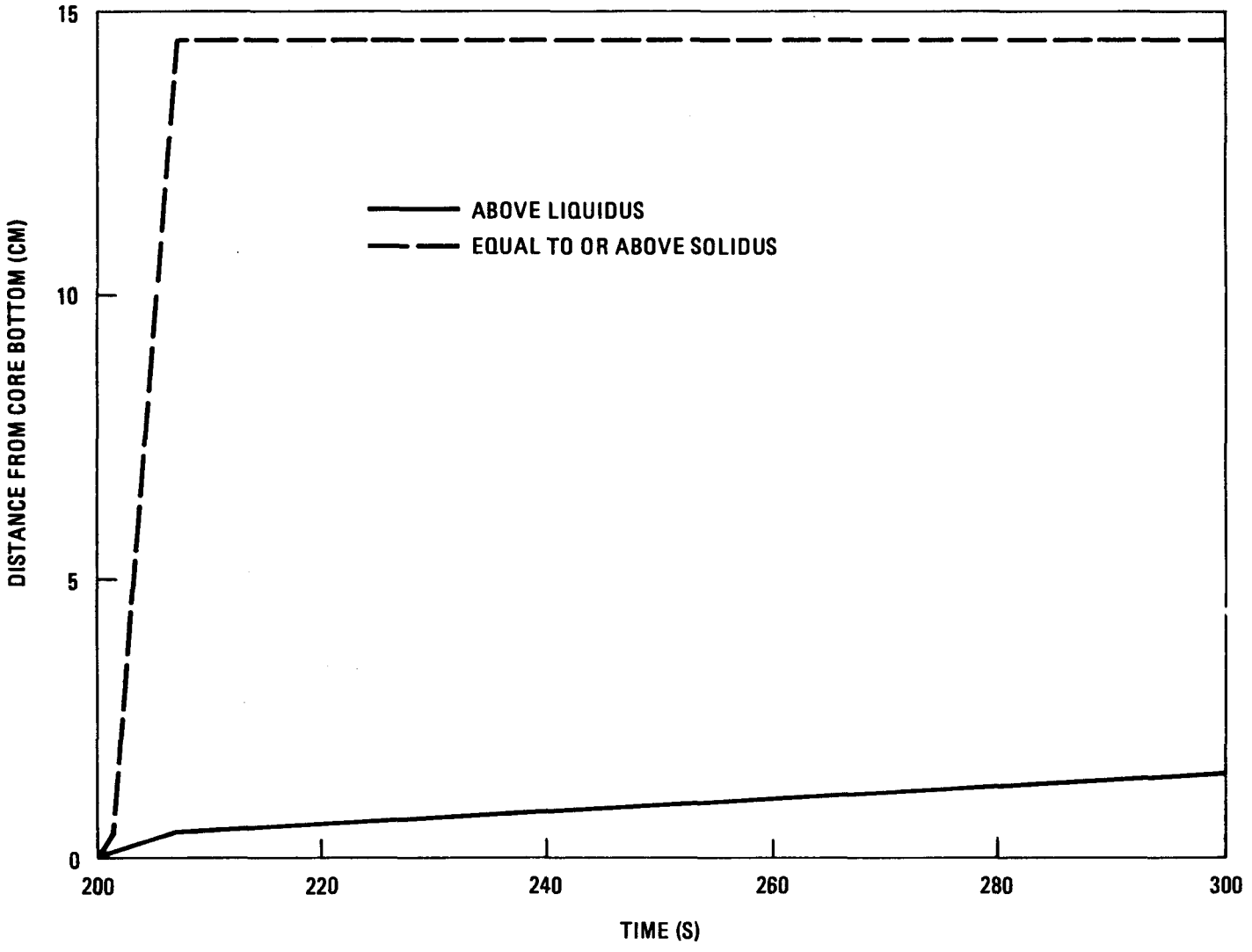

Fig. 13-3. Blockage penetration depth

A case was chosen which is representative of conditions during a PLOF after lower axial blanket blockage. Table 13-2 summarizes the important input parameters, and Fig. 13-4 shows the natural convection mass flow rate 4.5 min after the blockage occurs. The mass flow rate decreases to zero slightly above the upper axial blanket (450 mm) but well before the subassembly grid plate (660 mm). Since a natural convection front has not yet reached the subassembly inlet nozzle, this phenomenon cannot influence global PCRV conditions at this time (4.5 min).

Sensitivity studies of PCRV pressurization have been performed for core meltdown situations to estimate the time to relief valve opening by varying the fraction of decay heat available to heat up the upper plenum helium inventory adiabatically. It was found that only low values of decay heat (less than 10% of the total heat generation rate) produced relief valve opening times longer than 4.5 min from core meltdown. Since a core meltdown is a conservative approach for estimating upper plenum heat-up relative to PLOF conditions after subassembly blockage, it is considered unlikely that internal subassembly natural convection effects will influence PCRV relief valve opening times.

13.4. POSTACCIDENT FUEL CONTAINMENT

A study has been completed on natural convection upward heat removal from a molten core through helium, water, and air loops, and feasibility has been established in principle. Because of the potential drawbacks of the HMB core catcher, some thoughts have been given to a steel bath core catcher.

13.4.1. Upward Heat Removal by Natural Convection

A study of upward heat removal by natural convection through only the auxiliary helium loops has previously been reported (Ref. 13-9). The water and air loops were assumed to have forced circulation under CACS conditions. This study has been extended to a totally natural convection system including all three loops.

TABLE 13-2
INPUT DATA FOR UPPER AXIAL BLANKET
NATURAL CONVECTION STUDY

Rod bundle geometry	
Rod o.d. (mm)	7.46
Rod to rod pitch (mm)	10.18
Distance across flats (mm)	166.0
Pressure and temperature conditions	
Pressure in subassembly (MPa)	8.7
Initial helium temperature (°C)	350
Assumed temperature transient of heat source (core - upper axial blanket interface)	$T = 875 + 4.9t$ when T is in °C (t is in seconds)

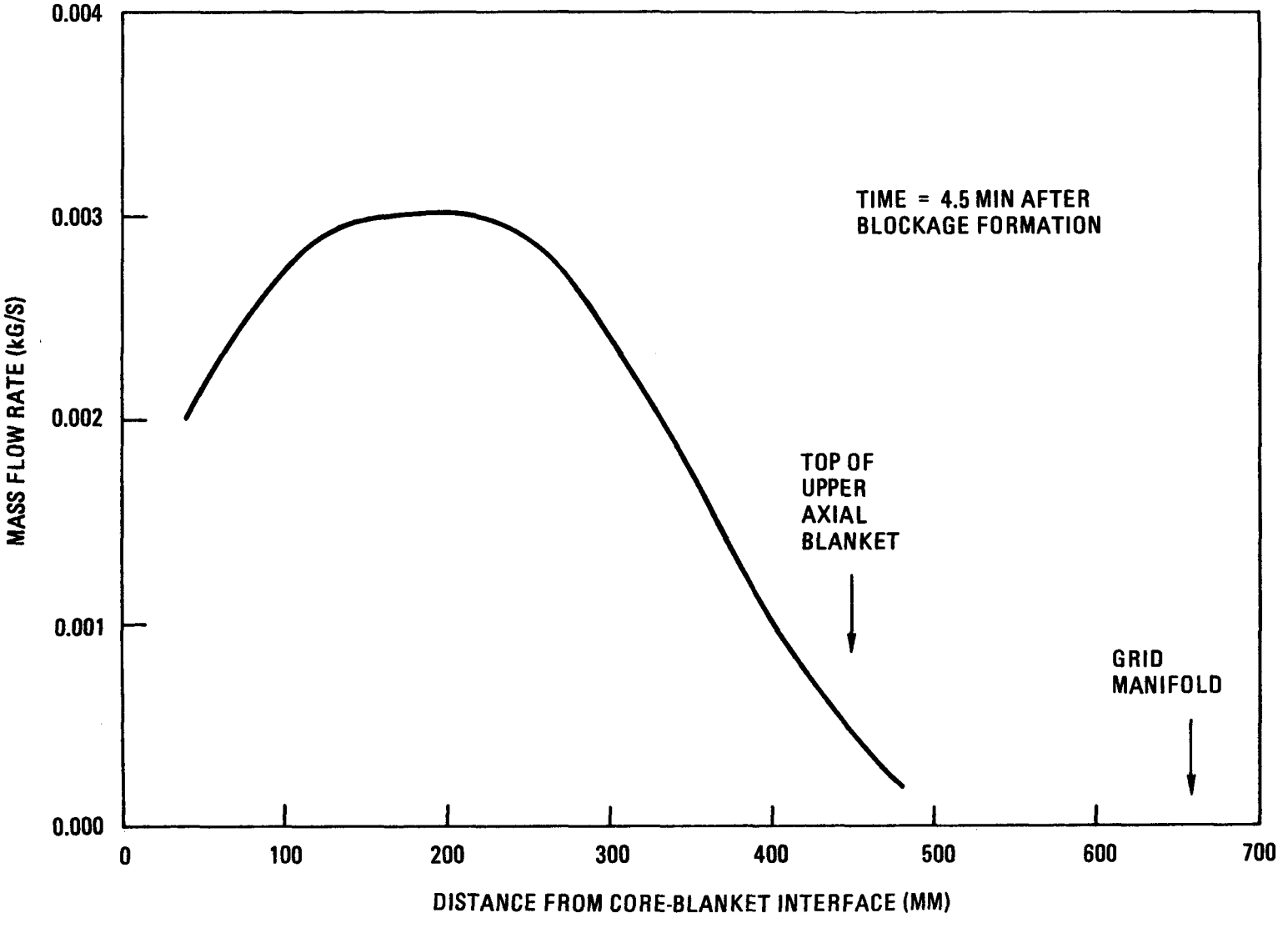

Fig. 13-4. Natural convection mass flow distribution in the upper blanket

The natural convection system for upward heat removal from a molten core is shown in Fig. 13-5. The assumptions specific to the computational model are as follows:

1. Quasi-steady-state calculation starting 0.5 hr (Ref. 13-9) after meltdown.

2. Nonboiling CAHE.

3. All three CACS loops available for natural convection.

4. Partial core meltdown with the radial blanket remaining in place.

5. No contribution to hot leg temperature by volatile fission products.

Based on the current CACS design (Ref. 13-10) and a revised design of the CAHE, the following input information is obtained:

1. Total pressure drop (helium side) through the core and the CACS for a partial core meltdown (Ref. 13-11) is 3.8 kPa at a helium flow of 5.05 kg/s per loop and a system pressure of 179 kPa.

2. Design pressure drop (water side) through the CAHE is 207 kPa at a water flow rate of 76 kg/s and a water pressure of 8.96 MPa.

3. Design pressure drop (water side) through the ALC is 55.2 kPa at a water flow rate of 19.4 kg/s.

4. Design pressure drop (air side) through the ALC is 0.043 kPa at an air flow rate of 333 kg/s.

Using an iterative procedure, a system of eight equations (three heat balance equations and three natural convection equations for the helium,

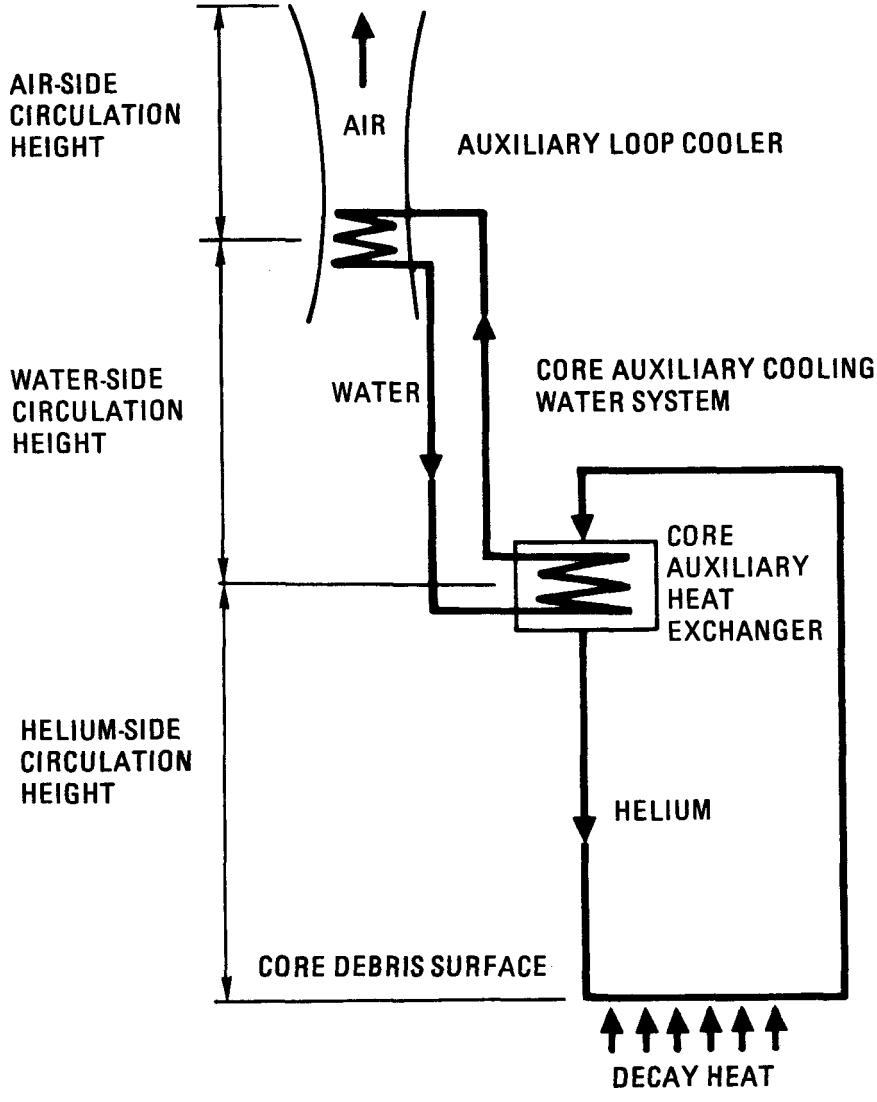

Fig. 13-5. Natural convection PAFC cooling system

water, and air sides and two heat exchanger equations at the helium-water and water-air interfaces) has been solved for the following typical input parameters:

System pressure of helium = 179 kPa (equilibrium system pressure),
Decay heat delivered by helium at 0.5 hr = 5.2 MW (Ref. 13-4),
Decay heat in vapor and gases at 0.5 hr = 4.5 MW (Ref. 13-11),
Air cold-side temperature = 3.8°C,
Water hot-side temperature = 260°C (boiling point = 303°C at 8.96 MPa),
Helium hot-side temperature = 520°C,
Air-side circulation height = 6.1 m.

The following results were obtained:

Air hot-side temperature = 56°C,
Water cold-side temperature = 79°C,
Helium cold-side temperature = 260.3°C,
Mass flow of air = 96.8 kg/s,
Mass flow of water = 2.07 kg/s,
Mass flow of helium = 0.163 kg/s,
Water-side circulation height = 0.49 m,
Helium-side circulation height = 11.4 m.

These results show that for a completely depressurized condition, a large helium-side circulation height is required because of the very low helium density. Since a great portion of the upward-flowing decay heat ($\sim$7.6 MW at 0.5 hr) is absorbed by the internal structures, the small amount of heat delivered to the water requires a water circulation height of only 0.49 m. The helium circulation height can be reduced by allowing a higher helium hot-side temperature. If the allowable helium temperature is set at 816°C, the helium circulation height is reduced to 2.8 m.

For full system helium pressure at 8.9 MPa, the decay heat delivered by helium will be increased to 12.8 MW. With the other input parameters kept the same as those in the first depressurized case, the following results are obtained:

Air hot-side temperature = 71.2°C,
Water cold-side temperature = 180.2°C,
Helium cold-side temperature = 278°C,
Mass flow of air = 127 kg/s,
Mass flow of water = 11.6 kg/s,
Mass flow of helium = 2.06 kg/s,
Water-side circulation height = 19.7 m,
Helium-side circulation height = 0.49 m.

These results show that helium cooling is sufficient under full system pressure, so that only a small helium circulation height is required. However, a large water circulation height is required owing to the increased heat delivered to the cooling system. Allowing the water hot-side temperature to increase to 274°C reduces the water circulation height to 11.3 m, increasing the air circulation to 15.2 m reduces the water circulation height to 6.2 m.

As noted above, the required helium and water circulation heights depend on system helium pressure. For the existing CACS (with revised CAHE) and the chosen input parameters, the resulting temperatures and circulation heights are within reasonable limits. In addition, several means of improving the natural convection cooling system are available. A conclusion of the study is that it appears that totally natural convection PAFC cooling may be feasible.

13.4.2. Steel Bath Core Catcher Concept

Preliminary results of heavy metal bath (HMB) heat transfer studies indicate some drawbacks of the concept, i.e., (1) limited stored heat capacity

and (2) very high cavity liner temperature. These disadvantages led to consideration of the stainless steel bath concept. If sufficient stainless steel is supplied in the lower shield, the fuel debris should, in principle, keep its solid form until at least the stainless steel has melted. If the subsequent upward and downward cooling is efficient, the stainless steel pool temperature is expected to be just slightly higher than its melting point but far below the melting point of the oxide fuel. A configuration of solid fuel debris immersed in a stainless steel pool would then be expected.

It is uncertain whether a molten pool of fuel debris will form before the formation of a stainless steel pool. Therefore, formation of a molten fuel pool has always been assumed in previous analyses to be conservative. However, previous analyses (Ref. 13-11) indicate that for a partial core meltdown the fuel layer never reaches its melting point in the transient process. These analyses also show that a partial core meltdown case is most likely, and even without helium cooling, the radial blanket will remain in place for at least 3.5 hr. At 3.5 hr, a stainless steel pool with the fuel debris submerged should be formed on the cavity floor.

If a full core meltdown should occur, the oncoming radial blanket material could be suddenly quenched by the liquid stainless steel. Depending on the temperature difference of the falling blanket material and the stainless steel pool, the UO_2 content could be fragmented to form particulates which would settle either on top of the fuel debris or in the voids. Heat transfer of a debris bed formed in a sodium pool has been widely studied in the LMFBR program. If sodium dry-out does not occur, the debris bed is capable of being cooled. For the GCFR condition, dry-out of stainless steel is unlikely because of the high boiling point of stainless steel. A debris bed immersed in a stainless steel pool appears to be practical for long-term core retention.

Figure 13-6 shows a suggested configuration for the steel bath core catcher. The expected sequence of events following a core meltdown is as follows:

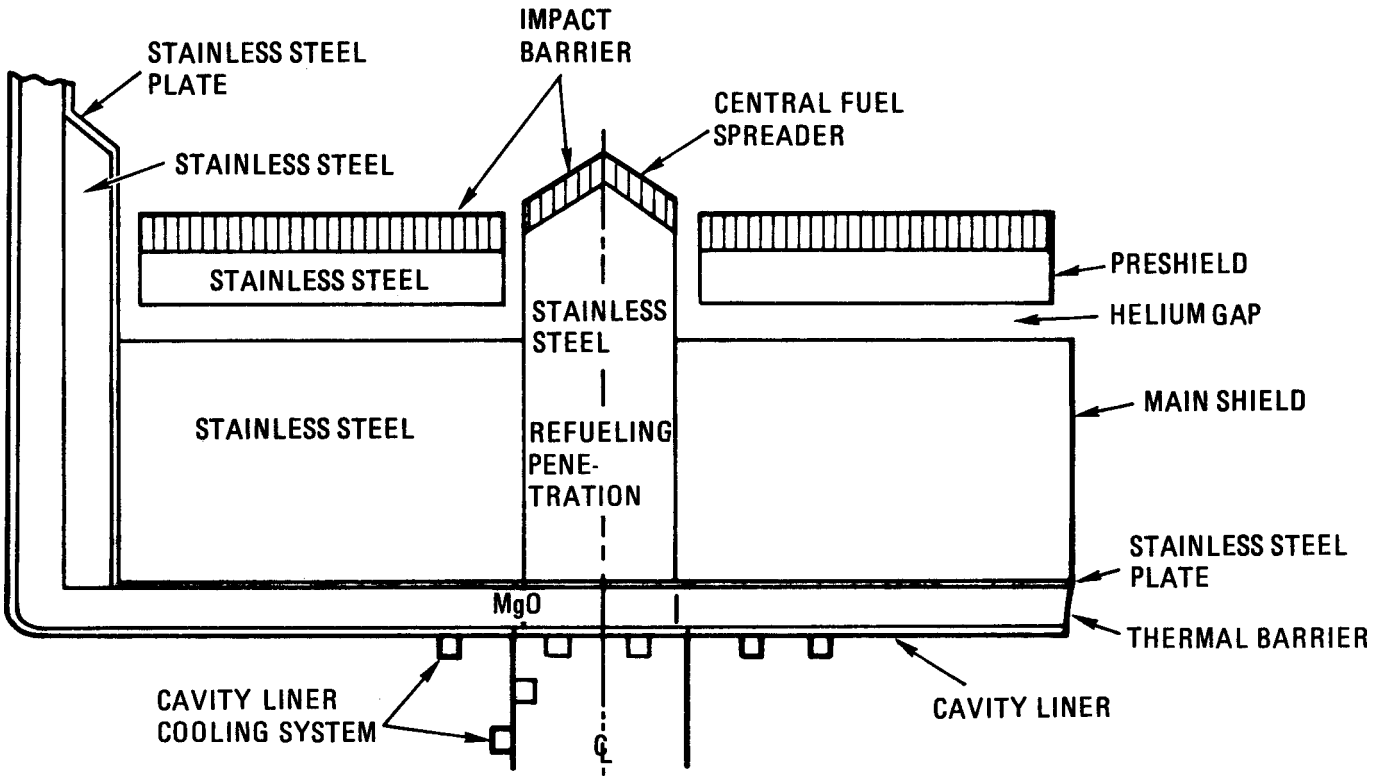

Fig. 13-6. Suggested configuration for a stainless steel bath core catcher

1. Solid fuel debris is relocated from the original core location to the top of the preshield.

2. Solid fuel melts through the preshield and into the main shield, and a stainless steel pool is formed.

3. Solid fuel debris finally comes to rest above the MgO thermal barrier. The shape of the melting front is expected to be irregular. Locally, some fuel debris may arrive on the MgO layer earlier, but any hot spot effects will be smoothed out by the MgO layer.

4. Penetration of molten stainless steel into the gaps of the MgO bricks is possible. The melt is expected to be frozen before it reaches the cavity liner. Flotation of MgO bricks must be prevented, possibly by fastening them to the cavity liner.

The steel bath concept has the following advantages:

1. Greater stored heat effect and lower cavity liner temperature.
2. Materials which are not exotic.
3. Pool temperature can be managed by MgO thickness.
4. Sideward heat removal can be managed.
5. Fuel debris will not be permanently exposed to helium.

It also has the following disadvantages:

1. Lower stainless steel crust may not exist for forming a crucible.

2. Possibilities of local penetration into the steel and flotation of the MgO bricks.

3. Preferably, pool growth is downwards, so that nonuniform melting and some hot spot effects are expected.

In conclusion, the steel bath concept appears to be a modification of and possibly an improvement over the HMB concept. The feasibility of the concept needs to be demonstrated by analysis and possibly some experimentation.

13.4.3. Postaccident Fuel Containment Documentation

A report on the preliminary analysis of PAFC has been completed (Ref. 13-11). This report summarizes investigations of the in-vessel PAFC capability of the 300-MW(e) GCFR demonstration plant following a postulated core meltdown accident. The basic background information for the investigation are given along with an analysis of downward heat removal, analyses of upward heat removal by forced helium circulation and natural helium circulation, and a feasibility study on PAFC for the current design. In the course of this investigation it was found that many areas of uncertainty remain to be resolved, e.g., thermal and chemical processes occurring during core meltdown and thermodynamic properties of the solid and molten materials associated with core debris, reactor internal structures, and products resulting from chemical reactions. To be able to deal with these uncertainties using present knowledge and mathematical tools required the use of conservative assumptions and simplified conceptual models for a feasibility assessment. This investigation was confined to in-vessel fuel containment because it is the first step in the analytical treatment of the problem. Studies of ex-vessel fuel containment are planed; however, the experimental basis to guide analytical development in this area is not extensive.

In general, the results showed that the capability of the reactor cavity to serve as a natural crucible for the molten core debris is adequate. Decay heat removal is feasibly if a moderate amount of extra cavity liner cooling is provided to remove downward-flowing heat and either forced helium with one CACS loop or natural circulation of helium is used to remove the upward flowing heat. A feasibility study for the current design was also performed, and it appears that with minor modifications, the current GCFR design may be feasible for PAFC. Design studies and more detailed analyses are required to support this conclusion.

13.5. ENGINEERING RELIABILITY INTEGRATION

A report has been written on engineering reliability integration methods (Ref. 13-12). Application of the methods identified in the report has been deferred until the third quarter of FY-78.

13.6. GAS-COOLED REACTOR RELIABILITY DATA BANK

The functions of the data bank are to obtain, supply, and store reliability data estimates in support of the probabilistic accident and risk analysis tasks. This function was carried out during this quarter to support the work described in Section 13.2.

REFERENCES

13-1. "GCR Accident Initiation and Progression Analysis Progress Report for the Period February 1 Through June 30, 1974," USAEC Report GA-A13094, General Atomic, October 8, 1974.

13-2. Kelley, A. P., Jr., "Gas-Cooled Fast Breeder Reactor Accident Initiation and Progression Analysis Progress Report for the Period July 1, 1975 Through June 30, 1976," ERDA Report GA-A14079, General Atomic, March 1977.

13-3. "Reactor Safety - An Assessment of Accident Risks in U.S. Commercial Nuclear Power Plants," Nuclear Regulatory Commission Report WASH-1400 (NUREG-75/014), October 1975.

13-4. "Gas-Cooled Fast Breeder Reactor Quarterly Progress Report for the Period August 1, 1977 Through October 31, 1977," DOE Report GA-A14613, General Atomic, November 1977.

13-5. "Gas-Cooled Fast Reactor Core Disruption Accidents," Argonne National Laboratory Report ANL/RAS/GCFR-76-1, November 1976.

13-6. Torri, A., and J. L. Tomkins, "Accident Termination by Element Dropout in the GCFR," in Proceedings of the International Meeting on Fast Reactor Safety and Related Physics, October 1976, Chicago.

13-7. Leach, C. E., and E. L. Kelley, Jr., "TAP-Loop: A Stable Thermal Analyzer Code for Thermal Analysis of Closed Hydraulic Systems," USAEC Report BNWL-1172, Battelle Northwest Laboratory, January 1970.

13-8. "Reactor Development Program Progress Report, July-August 1977," Argonne National Laboratory Report ANL-RDP-62, October 1977, pp. 6.42-6.46.

13-9. Kang, C. S., and A. Torri, "Post-Accident Fuel Containment in the Gas-Cooled Fast Breeder Reactor," in Proceedings of the International Meeting on Fast Reactor Safety and Related Physics, October 1976, Chicago.

13-10. "Gas-Cooled Fast Breeder Reactor Preliminary Safety Information Document, Amendment 7," General Atomic Report GA-A10298, February 23, 1976.

13-11. Kang, C. S., A. Torri, and R. D. Elliott, "Preliminary Analysis of Post-Accident Fuel Containment for a Gas-Cooled Fast Breeder Reactor," DOE Report GA-A14789, General Atomic, to be published.

13-12. Reilly, J. T., "A Review of Methods for the Integration of Reliability and Design Engineering," General Atomic, to be published.

14. GCFR SAFETY TEST PROGRAM (189a No. 00588)

It is the responsibility of GA to coordinate the National GCFR Safety Test Program; GA reviews and directs the program so that it is responsive to safety test needs and identifies new test needs for which test plans must be proposed and implemented on a time scale consistent with GCFR program needs.

14.1. GRIST-2 PROGRAM

The GCFR Safety Program Review Committee has recommended that GCFR fuel tests be undertaken in a transient facility to investigate fuel behavior during unprotected loss of flow and reactivity insertion transients. Therefore, the GRIST program is being developed to complement analytical and experimental programs being conducted under other GCFR and LMFBR programs.

A Program Review meeting was held to review the GRIST test loop and test train designs and to develop the overall program objective and milestones for FY-78. The loop system and its projected costs were also examined. The facility cost projected by EG&G is considered to exceed the funding support currently anticipated by DOE. Therefore, the program to review the estimated cost of conducting alternate design trade studies is being evaluated and the test requirements are being reviewed, both of which could lead to reduced program costs. Expected accomplishments for ANL and GA for FY-78 were defined. The major undertaking at ANL is the conceptual design of the test train; this work is expected to be 90% complete by the end of the fiscal year. In addition to technical coordination of the GRIST-2 program, GA plans to prepare a GRIST-2 program management plan. GA will also initiate work on development of a GRIST-2 test program plan and a survey of preirradiation facilities for fuel rods which will be used in future GRIST tests.

A review of the GRIST-2 and safety research facility (SAREF) programs was made to examine GRIST-2 functional requirements and how the SAREF program can best accommodate the GRIST-2 tests. SAREF personnel indicated that there are no major problems in incorporating the GRIST-2 needs into the program; however, as yet, no guidelines have been given to them by DOE as to how this will be accomplished. SAREF has delineated the LMFBR [advanced loop tests in the transient reactor test facility (TREAT)] and GRIST requirements for the TREAT Upgrade and associated facilities (Ref. 14-1).

14.2. DUCT MELTING AND FALLAWAY TEST PROGRAM

A series of meetings were held at Los Alamos Scientific Laboratory (LASL) to discuss the pretest analyses for the first 37-rod bundle tests and to define the specific objectives and procedures for these tests. An initial review of the conceptual design of the test fixture for the 271-rod bundle test was also conducted. The original objectives of these analyses were (1) to determine the need for a preheat phase of the 271-rod bundle tests and (2) to estimate the power requirements as a function of time and temperature. Although these analyses were for the 271-rod bundle, they have an immediate bearing on the 37-rod tests, since they predict that the alumina (Al_2O_3) insulator sleeve melts about halfway through the tests. A number of assumptions were made in these calculations, and perhaps the most important is that there is no convective heat transfer within the test bundle. The natural convection heat transfer was considered to be significant enough by LASL to justify running the tests. It was agreed by GA and LASL that checking the analytical model predictions with empirical measurements to determine the effect of natural convection should be one of the main objectives of the upcoming test. The objectives for the first 37-rod bundle test are as follows:

1. Establish heater bundle performance under DMFT test conditions, including heater operation following cladding melting.

2. Determine natural convection heat transfer to the upper axial blanket and the duct wall as a function of helium pressure level.

3. Determine degree of alumina insulator tube melting and heater performance with melted alumina tubes.

4. Determine limiting condition for heater operation.

5. Determine molten cladding relocation and freezing behavior from post-test examination. Characterize location of once-molten cladding and infer the blockage thickness and geometry in the lower axial blanket as it existed during the test.

6. Record time-dependent heater power and temperature data for use in post-test analysis and comparison with analytical predictions.

7. If duct melting occurs, characterize molten duct region and relocation of molten duct steel.

Note that the original intent of the 37-rod bundle test series is to establish the performance of the simulated fuel rods prior to proceeding to the full-scale 271-rod bundle tests. These tests will be very valuable in establishing initial verification of the analytical methods used to evaluate these tests.

A firm date for conducting the first test has not been set. LASL is in the final stages of assembling the test fixture and simulated fuel rod bundle. A few remaining components are still being fabricated.

REFERENCE

14-1. Avery, R., Argonne National Laboratory, private communication.

15. GCFR NUCLEAR ISLAND DESIGN (189a No. 00615)

The purpose of this subtask is to provide the general arrangement of the nuclear island so that the feasibility of several nuclear island concepts and the major dimensions of the buildings can be established. A study was conducted to assess the design impacts of various circulator drive options. Four basic concepts were evaluated:

1. The reference case with a steam-driven main circulator mounted vertically near the top of the PCRV.

2. A steam-driven circulator mounted vertically at the bottom of the PCRV.

3. An electrically driven main circulator mounted vertically at the top.

4. An electrically driven main circulator mounted vertically at the bottom.

Layout drawings were prepared to show the feasibility of routing major piping runs within the containment (feedwater and main steam from steam generator to circulator and from circulator to containment penetration), and stress analyses were performed utilizing U.S. Navy Mare Island Computer Code MEL 21 to verify that the induced stresses caused by thermal expansion, internal pressure, and weight deflection do not exceed allowable limits. Calculations were also made to confirm selected line sizes and related pressure drops to satisfy NSSS design criteria. The conclusions of the study are

1. A steam-driven circulator located at the bottom of the PCRV decreases piping runs but increases congestion in the restricted

area below the PCRV. Access for in-service inspection and removal of equipment is more difficult and time consuming compared with the reference design because of potential interference with refueling operations. Furthermore, more sophisticated equipment and complex maneuvers would be necessary to accomplish removal of the circulators.

2. A motor-driven circulator mounted on top of the PCRV is relatively attractive because it removes the high-energy piping and associated restraint structures from this area (PCRV top head), assuming that both feedwater in and steam out of the steam generator are at the bottom.

3. The largest impact on nuclear island structures and services is incurred by the use of motor-driven main circulators. This introduces the requirement of adding variable-frequency inverters to regulate the speed of the main circulator motors. Additional batteries, rectifiers, and inverters are also required to drive the main circulators and to accomplish partial emergency core cooldown upon loss of off-site power. The building space required to accommodate these inverters, rectifiers, and batteries will be considerable. This, in combination with the increased diesel generator capacity, has a significantly greater impact than the equivalent services/structures supporting the reference case.

16. ALTERNATE DESIGN STUDY (189a No. 00759)

The objectives of this task are to investigate, develop, and evaluate alternate design concepts for the GCFR demonstration plant NSSS configuration, components, and related plant facilities and equipment. During this quarter, design and evaluation and safety assessments were completed. Some of the more significant trends and conclusions of the evaluation are not solely related to the nonintegrated NSSS configuration study but will have a general application to the GCFR, including the bare liner, upflow or downflow core, natural convection, and some safety assessments.

16.1. BARE HOT LINER STUDY

Work on the bare hot liner concept analysis concluded that it appears to offer no improvement over the present cold liner and thermal barrier design from the viewpoint of structural and leakage integrity. In the hot liner concepts studied, the core inlet gas in contact with the liner is 315°C (600°F). To reduce the temperature difference between the liner and the thermal concrete, the temperature of the structural concrete is required to be raised to 120°C (248°F). This is not consistent with the requirements of Section III, Division 2, of the ASME code for pressure vessels, which limits the temperature of the stressed concrete to 65.5°C (150°F) for normal operating conditions. To meet these requirements would require reduction of the liner sweep gas to below 315°C (600°F), which represents the lower range of core inlet gas temperature for the GCFR. An alternate concept which considered the use of a stagnant gas barrier adjacent to the liner indicated the possibility of reducing the liner temperature and the concrete temperature. However, such a complex system does not warrant further consideration for the GCFR, since simplicity and improved accessibility to the liner are among the principal objectives of the hot liner concept. Liner penetrations and duct/barrel liner interactions which represent manageable

structural problems for the cold liner design became major feasibility considerations for the hot liner design.

16.2. CONFIGURATION STUDY

The design of a base nonintegrated NSSS configuration for the alternate GCFR design was established and used as a basis for upflow and downflow core designs. Major objections to the nonintegrated design are the structural integrity and safety considerations of the cross ducts. A design consisting of individual prestressed concrete vessels for the reactor and steam generator vessels was examined. These units are attached to each other so that the cross ducts are embedded in the concrete and accordingly are not subject to the objections associated with the nonintegrated design. This design arrangement provides minimum concrete for the PCRV structure compared with the integrated multicavity designs.

16.3. CLOSURE STUDY

A closure study which included four different closures and hold-down systems has been completed. A composite steel and concrete closure with a concrete retainer ring for the PCRV was selected as a viable alternate to the Swedish design primary closure hold-down featured in the reference design.

16.4. REFUELING

Owing to the requirement of no penetration in the bottom head of the PCRV, top refueling methods for the upflow core arrangement were investigated. One scheme uses the center penetration of the 19-control-rod penetration array in the cavity closure for insertion of a fuel handling machine. This machine in combination with a permanently installed and rotating rail system in the core cavity can remove and insert the fuel assemblies through the center hole. A second scheme uses four predetermined control rod penetrations and two additional radial penetrations of the same size in a rotating cavity closure for insertion of a fuel handling machine. By

rotating the closure and radially changing the position of the fuel handling machine, every core assembly can be removed or replaced. Both schemes are still under investigation.

A rotating plug was designed for the alternate design in an attempt to apply the rotating plug method used by the LMFBR for refueling. Because of the geometry of the control rod penetration array, the minimum feasible plug diameter is larger than the cavity diameter. Consequently, this design was not pursued beyond this conceptual stage.

16.5. HEAT REMOVED BY NATURAL CONVECTION

A preliminary study to investigate the feasibility of natural convection circulation to remove post-trip residual heat in the event of total loss of forced cooling under pressurized conditions has been completed. Upon loss of main circulator drive power with failure of the auxiliary circulators to start, the natural convection CACS would be designed to take over from the coast-down of the main circulators and cool the core to prevent cladding melting for an upflow core under pressurized conditions. Forced circulation supplied by the auxiliary circulators (including water pumps and auxiliary loop cooler fans) would still be the primary means of decay heat removal upon loss of main loops at pressurized conditions, with natural convection being a last ditch backup to prevent cladding melting. This scenario is considered because

1. A natural convection CACS may not be licensable for a first-of-a-kind plant without full-scale prelicensing tests of natural convection on the helium side.

2. A second mode of cooling must be available as a backup to the main loops for DBDA under low-pressure cooling conditions and for refueling.

3. Although natural convection does prevent cladding melting, the core outlet, fuel rod cladding, and outlet plenum temperatures

reached would be greater than those currently prescribed for upset and emergency accidents. Therefore, it is desirable to have an auxiliary circulator to meet cladding and outlet plenum component temperature limits.

Based primarily on an idealized steady-state analysis (with some transient analysis of the primary side) under pressurized conditions, the natural convection CACS appears feasible with a circulation height between the heat source and sink of 15.24 m (50 ft) on the air side, 21.33 m (70 ft) on the water side, and 9.14 m (30 ft) on the helium side. Cladding hot spot temperatures reach 1149°C (2100°F), and core outlet and plenum temperatures reach approximately 843°C (1550°F).

The system may experience start-up problems on the water side, where a certain amount of flow must be provided to prevent boiling and reject the desired amount of heat from the primary system. Although the current study was limited to nonboiling CAHE designs, a boiling CAHE will not necessarily eliminate start-up problems on the secondary side. Ways of improving system performance include an increase of ALC and CAHE heat transfer area; design optimization of the ALC, specifically for a natural convection system; cold water storage; use of a battery-powered pump to enhance water-side start-up capabilities; and improved main circulator coast-down characteristics by using an electrically driven circulator or improving the water bearing idle speed characteristics for a steam-driven circulator. However, it is recommended that future work concentrate on verifying system performance by a complete transient analysis of the entire system. Further assessment of any increase in system complexity and cost penalty is also recommended.

17. GCFR ALTERNATE FUELS: CORE DESIGN (189a No. 00759)

17.1. PRELIMINARY STUDY

A preliminary study of alternate fuel cycles for the GCFR (Ref. 17-1) was made to provide data for evaluation of the proliferation resistance and energy production capability of various fuel cycles. In the first part of the study the fuel cycles of interest were identified, and the characteristics of an operating GCFR on each cycle were calculated; Table 17-1 lists the fuel cycles investigated. The cycles start with the traditional plutonium/uranium cycle with all-uranium blankets and moves away from plutonium production and utilization toward thorium and U-233. As expected from the basic nuclear data, the breeding ratio tends to decrease with decreasing plutonium utilization. Table 17-1 lists the breeding ratio and specific power for those cycles investigated. A comparison of cases 1 through 3 shows that the breeding ratio and specific power of a GCFR are relatively insensitive to the fertile species employed in the blanket. Thus, a GCFR could be used to produce either plutonium or U-233 in the blankets with approximately the same fuel efficiency.

If thorium is substituted for uranium as the core fertile material, as in case 4, the breeding ratio decreases by approximately 0.10 to 0.20 as a result of decreased fertile fissions. A significant increase in core inventory is also required. The breeding ratio for U-233/Th fueled fast reactors (case 5) will be limited to approximately 1.10 in the absence of significant advances in fuel materials and core design. The smaller number of neutrons per absorption from U-233 reduces the breeding ratio by approximately 0.15. In any case, the doubling time for U-233 fueled breeders will be much longer than current estimates for plutonium-fueled systems. The data from case 6 suggest that U-235 fueled fast reactors have limited advantages over U-235 fueled thermal systems.

TABLE 17-1
POTENTIAL GCFR FUEL CYCLES

Case	Core Material		Axial Blanket	Radial Blanket	Breeding Ratio[a]	Specific Power[a,b] [MW(t)/kg-fissile]
	Fissile	Fertile				
1	Pu	U-238	U-238	U-238	1.41	0.98
2	Pu	U-238	U-238	Th	1.39	0.95
3	Pu	U-238	Th	Th	1.37	0.93
4	Pu	Th	Th	Th	1.27	0.80
5	U-233/U-238	Th	Th	Th		
5a	∿14% enriched					
5b	∿20% enriched				1.07	0.93
5c	∿40% enriched					
5d	∿100% enriched				1.02	0.80
6	U-235/U-238	Th	Th	Th		
6a	∿20% enriched					
6b	∿40% enriched					
6c	∿93% enriched				0.73	0.49
7	U-233/U-235/U-238	Th	Th	Th		
7a	∿30% enriched					
7b	∿50% enriched					
7c	∿100% enriched					

(a) For unoptimized designs with 20% fuel volume fractions.

(b) Excluding U-235 from tails.

The characteristics of each cycle are more apparent when the equilibrium mass flow requirements for the cases investigated are reviewed. Table 17-2 lists production by fissile species. By changing the radial blanket from U-238 to Th-232 the total excess fissile production [300 kg per GW(e)/yr] can be converted from plutonium to U-233. Employing Th-232 in both blankets enables the GCFR to produce nearly twice as much U-233 and to consume nearly 300 kg per GW(e)/yr of fissile plutonium. The GCFR with all-thorium blankets then becomes an effective plutonium consumer and U-233 producer. Of course, the plutonium/thorium core with all-thorium blankets represents the ultimate machine for conversion of plutonium to U-233. Another important point illustrated in Table 17-2 is the fact that the low-enriched U-233/Th fueled GCFR is a significant U-233 consumer and produces almost as much plutonium as the plutonium/uranium core with uranium blankets.

The mass flow requirements presented in Table 17-2 have been employed to investigate a number of fuel cycle and reactor strategies which might be utilized in the future. To develop a common basis for evaluation, it was necessary to make several assumptions regarding the uranium supply and the rate of construction of the LWR. These assumptions were

1. The economically recoverable domestic supply of uranium is approximately 2 million short tons.

2. Approximately 400 GW(e) of LWRs will be on line by the year 2000.

Since both assumptions are well within the range of current expert opinion, they provide a framework within which to evaluate alternative strategies.

As a starting point, the traditional all-breeder plutonium/uranium fuel cycle was evaluated. Figure 17-1 illustrates this strategy, in which the plutonium from the 400 LWRs is stored until approximately 2000, at which time it is employed to start up a number of breeders. The amount of energy which can be generated is maximized thereafter by minimizing the

TABLE 17-2
UNOPTIMIZED GCFR MASS FLOWS FOR VARIOUS FUEL CYCLES

	Case						
	1	2	3	4	5b	5d	6c
Fuel cycle							
Core	Pu/U	Pu/U	Pu/U	Pu/Th	U-233/U-238/Th	U-233/Th	U-235/Th
Axial blanket	U	U	Th	Th	Th	Th	Th
Radial blanket	U	Th	Th	Th	Th	Th	Th
Fissile inventory [kg/GW(e)]							
U-235	250	80	40		30		
U-233					2990	3430	5650
Pu-239 + Pu-241	2850	2920	2970	3490			
Net yearly fissile production [kg/GW(e)]							
U-235	-20	-15					-931
U-233		300	540	960	-188	8	644
Pu-239 + Pu-241	320		-260	-770	270		8
Specific power [MW(t)/kg-fissile]	0.98	0.95	0.93	0.80	0.92	0.81	0.49
Breeding ratio	1.41	1.39	1.37	1.27	1.07	1.02	0.73

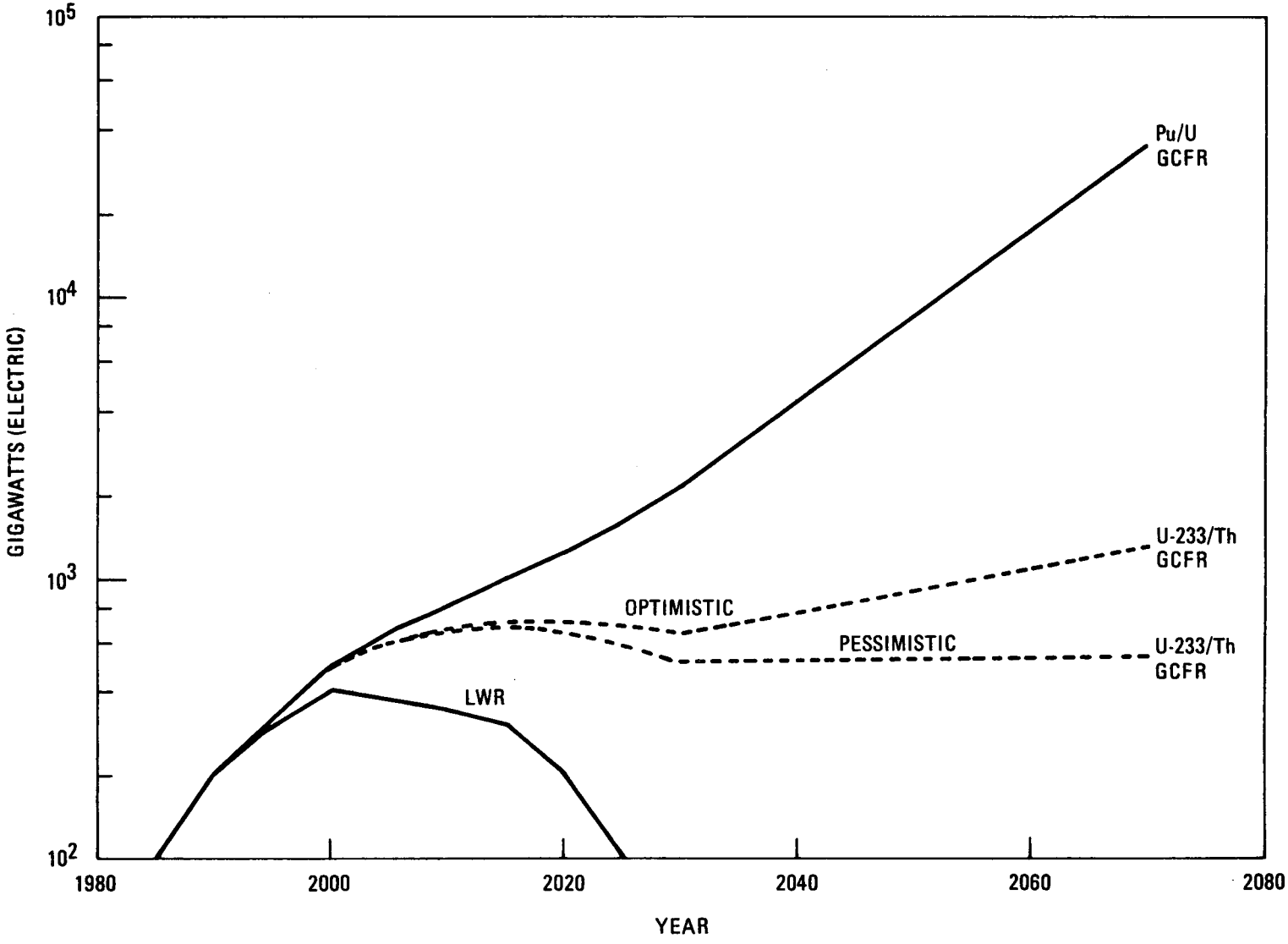

Fig. 17-1. Comparison of energy available from the U-235/U-238/Pu and U-235/Th/U-233 fuel cycles

quantity of fissile plutonium not in use. Figure 17-1 shows that by using a plutonium/uranium GCFR (or comparable high-gain breeder), 2 million short tons of uranium can produce approximately 2000 GW(e) of breeder energy by 2030. A continuing annual growth rate of more than 6% can be sustained thereafter without additional uranium mining.

Since the most recent re-examination of the fuel cycle was prompted by proliferation concerns directed primarily at the use of plutonium, there is an immediate temptation to investigate fuel cycles which minimize or avoid plutonium utilization. Such a strategy would require a number of basic changes in the future, the most difficult being the conversion of current and planned LWRs to the thorium cycle by the early 1980s. In addition, some means of avoiding proliferation difficulties with highly enriched U-233 would have to be found. The energy available from this highly enriched U-233/Th fuel cycle is also illustrated in Fig. 17-1. As can be seen, the energy potential of such a strategy is significantly lower than that of the plutonium/uranium cycle. Considering the attendant problems, it appears unlikely that a fuel strategy based on exclusive use of U-233/Th in both thermal and fast reactors will be attractive from any of the varying viewpoints now being put forth.

Strategies which restrict rather than eliminate plutonium utilization in the GCFR have also been studied. One class of strategies would involve using GCFR to supply fuel for advanced converter reactors, thereby restricting plutonium utilization to breeders alone. Such symbiotic systems are attractive since they allow plutonium (the best fast reactor fuel) to be employed in fast reactors and U-233 (the best thermal reactor fuel) to be employed in thermal converter reactors. Figure 17-2 shows the energy availability from a symbiotic system employing GCFRs with a plutonium/uranium core and uranium or thorium blankets supporting various numbers of low-enriched U-233 fed HTGRs. As can be seen, increasing the relative number of thermal converters decreases the energy which will be available in future years. If high-enriched U-233 can be employed in the satellite converters, then the energy availability increases as shown in Fig. 17-3.

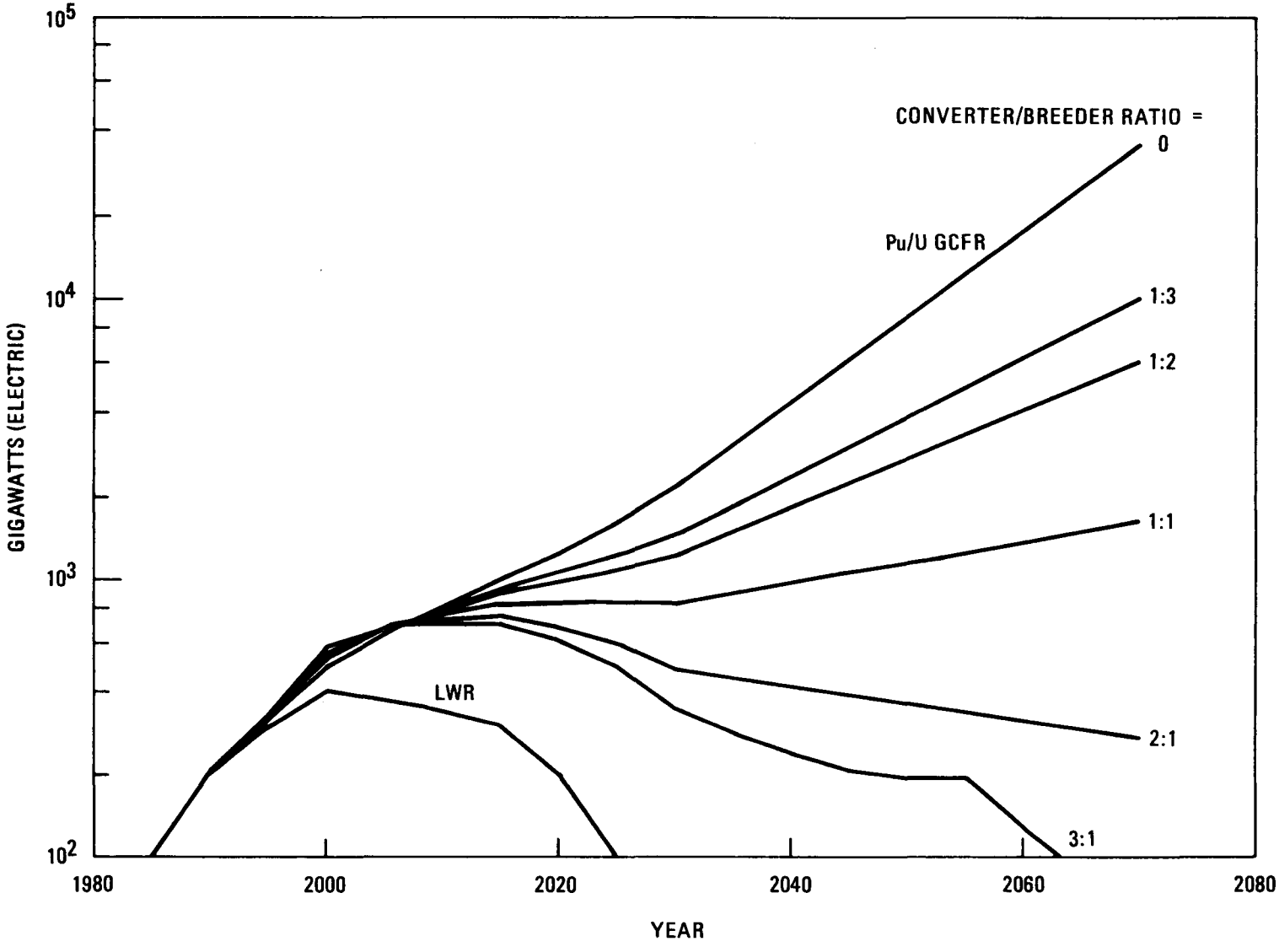

Fig. 17-2. Energy production capability using the Pu/U cycle within an energy park, assuming a 0.80 conversion ratio factor (denatured HTGR) outside the park

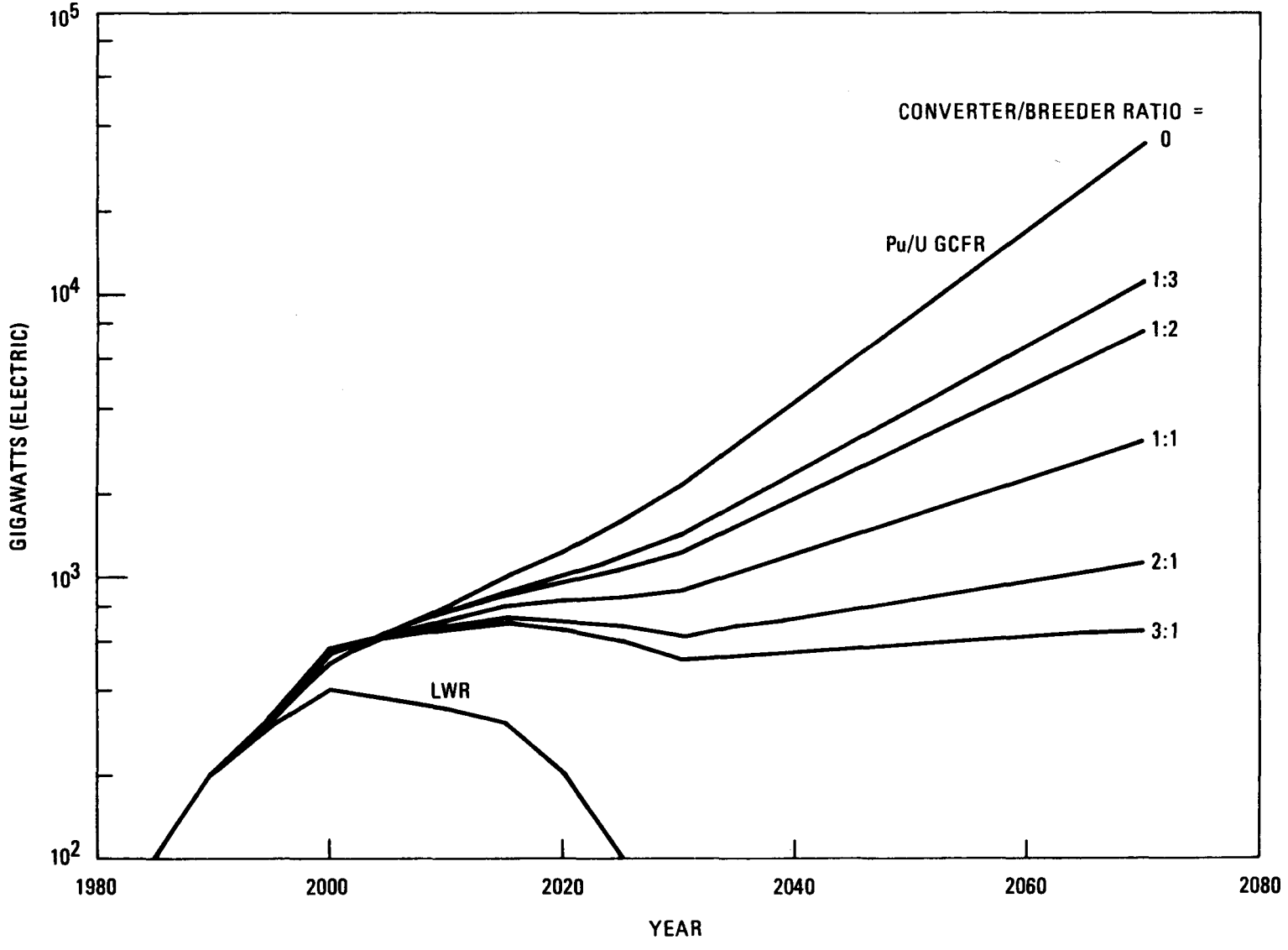

Fig. 17-3. Energy available from various combinations of Th/U-233 converter and U-238/Pu breeders with some Th blankets

The information in Figs. 17-2 and 17-3 clearly suggests that if nuclear energy growth rates of less than 6% are forecast, a compromise involving restriction of plutonium to secured energy centers can reduce proliferation risks while providing adequate potential for expansion of the nuclear energy supply.

Another system which appears attractive involves use of a plutonium/thorium GCFR in a symbiotic relationship with a low-enriched U-233/Th GCFR. Such an all-breeder system is capable of minimizing the number of plutonium-utilizing facilities required for a given nuclear energy growth rate. Figure 17-4 illustrates the energy growth potential of this system. With only about 25% of the plants employing plutonium, a 4% growth rate can be attained in the absence of additional uranium mining.

The preliminary study also demonstrated that the GCFR is the most fuel-efficient reactor when plutonium is used in the core and that all nuclear energy strategies which appear promising require plutonium utilization in the breeder. The traditional advantage of the GCFR, i.e., the higher breeding ratio, is not diminished by current proliferation concerns. On the contrary, the higher (out of core) breeding ratio of the GCFR may be a major advantage for future nuclear energy strategies which consider proliferation to be a major concern.

Based on these preliminary calculations, a more detailed evaluation of three fuel cycles for the GCFR is under way. These cycles are

1. Plutonium/uranium core with uranium or thorium blankets.
2. Plutonium/thorium core with all-thorium blankets.
3. Low-enriched U-233/Th core with all-thorium blankets.

Whether an optimized core design for these cycles will significantly affect the intended role of the GCFR will be studied.

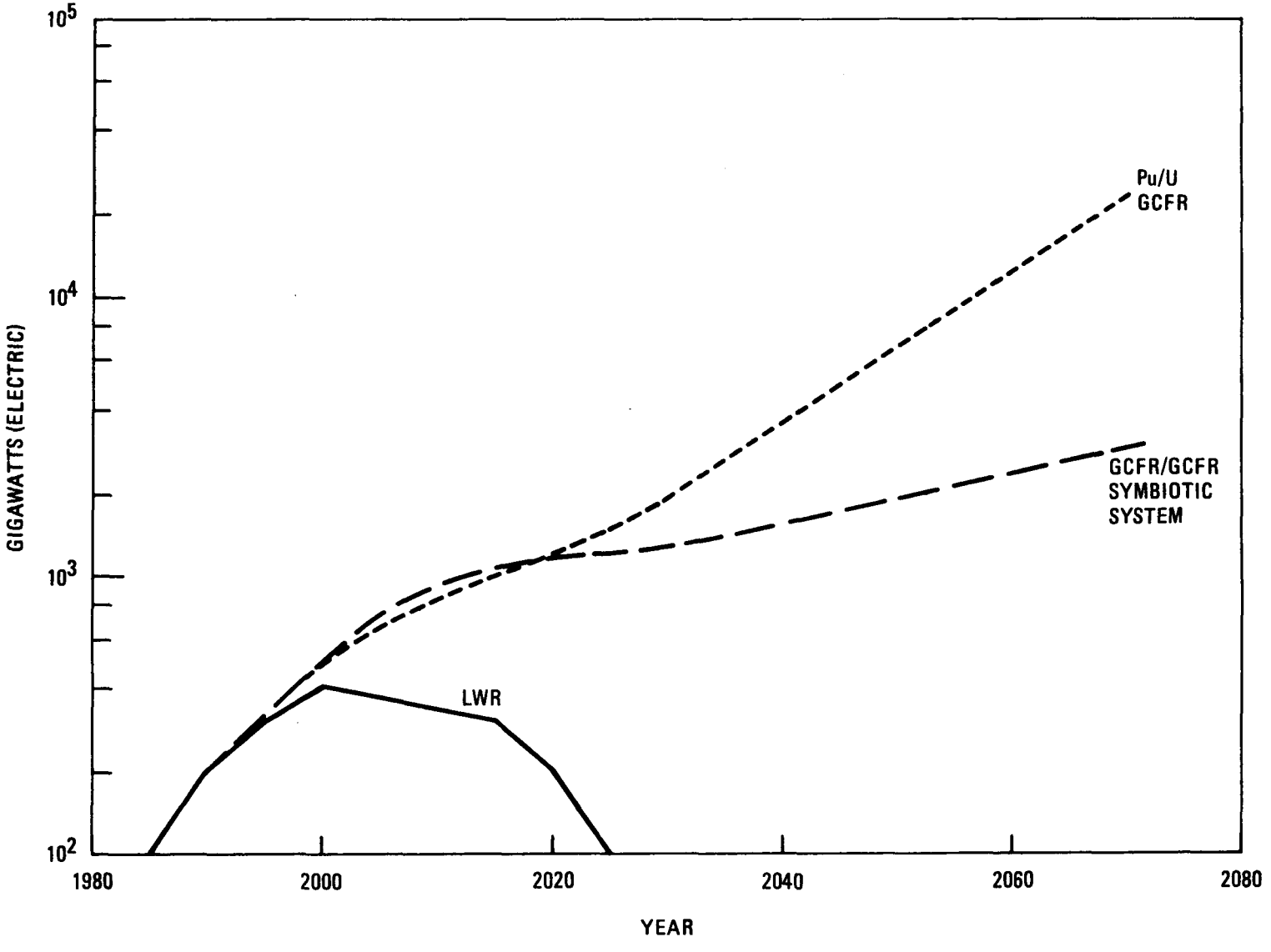

Fig. 17-4. Energy production capability for a denatured GCFR supplemented with a Pu/Th GCFR

17.2. FUEL CYCLE ADVANTAGES OF ADVANCED MATERIALS IN THORIUM CYCLES

A short study was carried out to provide information for ORNL's nonproliferation fuel cycle study (Ref. 17-2). Six alternate GCFR fuel cycles selected by ORNL for a 1500-MW(e) GCFR were studies to provide fuel cycle data and mass flow information for a typical large GCFR operating on the proposed fuel cycles. Starting with the same basic core configuration, a methodology was developed for calculating mass flows. No attempt was made to optimize the fuel cycles studied. The brief time frame of the study required that existing calculational techniques be employed. Reference 17-2 provides a detailed presentation of the mass flows, fission products, breeding ratios, and annual requirements for the following GCFR fuel cycles:

	Core and Axial Blanket		Radial Blanket
Case	Fissile	Fertile	Fertile
1	PuO_2	U-238/O_2	U-238/O_2
2	PuO_2	U-238/O_2	ThO_2
3	U-233/O_2	ThO_2	ThO_2
4	PuO_2	ThO_2	ThO_2
5	U-233/C	ThC	ThC
6	U-233 (alloy)	Th	Th (metal)

Since these calculations are so closely related to the alternate fuels task, some additional efforts were made to determine the more important conclusions which could be drawn from the data prepared for ORNL. First, the data presented for several of the cases represent somewhat more accurate calculations. Generally, the results are consistent with the preceding preliminary study (Ref. 17-1). Second, by comparing cases 3, 5, and 6, it is possible to estimate the advantages of advanced materials, i.e., carbides and alloys, in U-233/Th systems. Table 17-3 presents a brief characterization of the cases analyzed. As can be seen, the breeding ratio increases from 1.01 to 1.08 when the higher-density carbide is substituted for oxide (cases 3 and 5). Although this is not an insignificant increase, it still does not produce a system which can compete favorably with a plutonium/uranium core with thorium blankets for U-233 production. Similarly, the

TABLE 17-3
GCFR ALTERNATE FUEL CYCLES: SUMMARY[a]

	Case					
	1	2	3	4	5	6
Core	$Pu/U-O_2$	$Pu/U-O_2$	$U/Th-O_2$	$Pu/Th-O_2$	U/Th-C	U/Th (alloy)
Axial blanket	UO_2	UO_2	ThO_2	ThO_2	ThC	Th (alloy)
Radial blanket	UO_2	ThO_2	ThO_2	ThO_2	ThC	Th (alloy)
Enrichment (%)	14.7	15.0	19.0	19.5	17.5	16.0
Inventory [kg/MW(e)]						
U-233	--	--	3.255	--	3.642	4.011
U-235	0.252	0.078	0.126	--	0.141	0.156
Pu-239 + Pu-241	2.857	2.928	--	3.547	--	--
Th-232	--	65.29	94.047	93.487	106.32	117.48
U-238	101.77	31.69	--	--	--	--
Net yearly requirements [kg/MW(e)-yr]						
U-233	--	-0.292	0.002	-0.926	-0.075	-0.097
U-235	0.020	0.014	-0.007	--	-0.006	-0.004
Pu-239 + Pu-241	-0.313	0.0	--	0.778	--	--
Th-232	--	0.299	0.794	0.997	0.870	0.883
U-238	1.156	0.839	--	--	--	--
Specific power [MW(t)/kg-fissile]	0.97	0.95	0.82	0.78	0.73	0.67
Breeding ratio (beginning of initial cycle)	1.40	1.39	1.01	1.22	1.08	1.11

[a] Capacity factor = 80%; conversion efficiency = 36%; core enrichment = kg fissile Pu/total heavy metal or kg fissile U/total heavy metal.

use of thorium alloys produces a slight increase in breeding ratio, but does not result in a breeder which can produce significant amounts of excess U-233. Basically, the use of thorium carbides or alloys will enhance the breeding ratio of current U-233/Th fast reactors, but will not produce systems which can produce fissile materials at a rate which begins to rival the production rate of plutonium-fueled breeders.

REFERENCES

17-1. Hamilton, C. J., "A Preliminary Study of Alternate Fuel Cycles for the Gas-Cooled Reactor," ERDA Report GA-A14536, General Atomic, August 1977.

17-2. Baylor, K. J., W. M. Joseph, and M. Z. Nagel, "GCFR Fuel Cycle Information for the ORNL Nonproliferation Study," DOE Report GA-A14753, General Atomic, to be published.